Numerical simulation of collisionless kinetic plasma turbulence

Daniel W. Crews

A dissertation
submitted in partial fulfillment of the
requirements for the degree of

Doctor of Philosophy

University of Washington

2022

Reading Committee:

Uri Shumlak, Chair

Justin Little

Eric Meier

Program Authorized to Offer Degree:
Aeronautics & Astronautics

University of Washington

Abstract

Numerical simulation of collisionless kinetic plasma turbulence

Daniel W. Crews

Chair of the Supervisory Committee:
Uri Shumlak
Department of Aeronautics & Astronautics

Hot plasma dissipates energy on scales comparable to the modes of collective oscillation through a turbulent cascade of the distribution function in its phase space. This phase space turbulence is responsible for augmenting fluid transport coefficients beyond predictions from collisional theories, a phenomenon termed anomalous transport." This work studies collisionless kinetic phase space turbulence using spectral and high-order discontinuous Galerkin numerical methods to produce highly resolved simulations of the kinetic equation. Based on these simulations intuition is built for the physics of anomalously enhanced transport, critical studies are performed on reduced models such as quasilinear theory, and mechanisms are identified by which macroscopic plasma properties are altered by microscopic turbulence. Novel results on discontinuous Galerkin method can be found within, such as a new way of thinking about the discrete differential operators of finite element methods as partial sums of orthogonal polynomial completeness theorems. Phase space eigenfunctions are studied in detail for both the electrostatic and electromagnetic pictures in the unmagnetized and strongly magnetized regimes, and utilized in a novel way to produce the initial conditions of continuum kinetic simulations. The nonlinear phase space structures of electron cyclotron instabilities are studied for loss-cone distributions. In addition, highly resolved simulations are presented for Langmuir and Weibel turbulence in two-dimensional configuration space.

ACKNOWLEDGMENTS

I express my sincere gratitude to the mentors who encouraged my interest in plasma kinetics, namely Professors Uri Shumlak and Justin Little, as well as Professor Bernard Deconinck for his skilled teaching of the mathematics of wave theory. I also thank sincerely all of the faculty and staff of the William E. Boeing Department of Aeronautics and Astronautics for supporting me with many teaching assistant appointments where I had the opportunity to develop as a teacher. From that I also thank all of the students I received the joy of teaching throughout graduate school for giving me something other than plasma physics to worry about. In addition, I thank all of my family and friends for their patience with the number of times I talked to them about the phase space.

DEDICATION

To every one along the way and to come.

TABLE OF CONTENTS

LIST OF FIGURES

Figure Number Page

Chapter 1

INTRODUCTION

Superiora de inferioribus, inferiora de superioribus.

Unknown

This work is a study of turbulent kinetic processes in plasmas resulting from saturated linear instability when away from thermal equilibrium. As an effectively dissipative process this turbulence influences macroscopic scales through transport coefficients such as electrical resistivity. These turbulent processes are notoriously difficult to understand and to describe in a consistent manner so their influence is referred to as "anomalous" transport. The turbulence occurs in the phase space of the plasma, an abstract geometric space joining spatial coordinates with ones of momentum. The difficulty of a consistent description of anomalous processes in plasma is in part due to it being a blanket term for many possible specific mechanisms of transport-enhancing physics. Beyond this general ambiguity there is the problem that theoretical approaches to anomalous transport require a great deal of information on the statistics of the microscopic state, namely correlation functions between the fluctuating plasma and its fluctuating fields. Usually engineers are presented with practically *no* microscopic state information. However, through numerical simulations of microscopic processes one can obtain *intuition* for the physics of anomalously-enhanced transport, study the performance of *reduced models* describing dynamics given incomplete knowledge, and identify the *mechanisms* by which macroscopic properties are altered by small-scale dynamics.

To conduct these simulations a significant part of this work is devoted in Chapter 2 to the numerical methods used to solve plasma kinetic equations. Here a new way of thinking about the discrete differential operators of finite element methods is presented, namely as partial sums of orthogonal polynomial completeness theorems. Within Chapter 3 a great deal of the theory of kinetic plasma instability is then reviewed and extended to novel results for the simplest case of electrostatic fluctuations in unmagnetized plasma. Intuition for multidimensional Langmuir turbulence is built through numerical simulation of an electron two-stream instability in two-dimensional configuration space. Chapter 4 subjects the classic reduced model of phase space turbulence, the quasilinear kinetic theory (QLT), to a critical study including a consideration of its validity by comparison to unreduced theory. It is found that QLT is valid in predicting the asymptotic microscopic state, yet does not describe time-dependent behavior well due to weakly nonlinear effects. Chapter 5 then reviews the theory of linear electrostatic phase space modes in strongly magnetized plasma and extends well-known results for Maxwellian distributions to ring (or loss-cone) distributions of an arbitrary ring parameter. The linear eigenfunctions of the electron Bernstein modes are visualized in the phase space perpendicular to the magnetic field, and a technique is demonstrated to selectively excite electron cyclotron instabilities of various harmonics to study their saturation in isolation from other modes. Chapter 6 considers electromagnetic instability in unmagnetized plasma, namely the Weibel instability resulting from thermal anisotropy. The dispersion function for a bi-Maxwellian distribution is constructed for arbitrary angles of propagation. Simulations of the nonlinear saturation of Weibel instability in one- and two-dimensional configuration space are presented and studied. The one-dimensional simulation is a single-mode simulation in order to visualize the phase space structure of magnetic trapping, while the two-dimensional simulation consists of many modes to demonstrate the isotropization of the spatially-averaged distribution function. Finally, Chapter 7 considers the electromagnetic problem in strongly magnetized plasma and proposes the emission of parallel-propagating whistler waves by loss cones as a Vlasov-Maxwell test case.

1.1 The turbulence problem

Theory describes equilibrium very well. For instance, thermodynamics describes transitions between energetic equilibria and static mechanics predicts the distribution of balanced forces such as the trusses of a bridge or the toroidal magnetic field of a magnetohydrodynamic fluid.

In practice most engineering systems do not operate in equilibrium. Mechanics is the theory of evolution of complex systems given their initial state and boundary conditions. In principle, the details of dynamics away from equilibrium should be predictable by mechanics. Yet when far from equilibrium systems with many degrees of freedom display complicated dynamics lacking the special symmetries that allow simple mathematical explanations. Often the exact details of the process vary per experimental realization even with experimental conditions controlled as tightly as possible, meaning they display sensitivity to initial conditions, a famous syndrome of chaos theory. The problem of understanding the behavior of physical systems with many degrees of freedom far from equilibrium is called turbulence.

1.2 Interactions in plasma physics

Plasmas are composed of many individual parts making up a collective whole. On one level they are made up of individual free charge carriers, usually negatively charged electrons and positively charged ions. There are so many charges that the plasma is effectively a continuum on macroscopic scales relative to the scale of the free charges. Collective excitations of this continuum can be understood as individual parts themselves called quasiparticles. Now, in physics an *interaction* is a process through which parts exchange energy and/or momentum. A three-fold division of interactions in a plasma is then apparent: individuals with individuals (*e.g.* Coulomb collisions), individual/whole (*e.g.* wave-particle interaction), and whole/whole (*e.g.* wave-wave interactions, vortex behavior, etc.)

The three categories of interactions each have a role to play in kinetic plasma turbulence. The first division, particle-particle interactions, are actually turbulent themselves from the point of view of tracking each particle's precise state relative to others. This mental exercise illustrates the asymptotic time behavior of turbulent mixing in the usual cascade picture: a return to equilibrium. Although the Coulomb force is long-range, Debye screening limits inter-particle interactions to be effectively local on plasma scales. Because of the great number of simulataneously interacting particles, correlations are mixed on the collisional time-scale. The initial configuration is inextricably tangled and upon coarse-graining entropy is observed to increase. The result is a drive of the particle distribution function towards thermal equilibrium. Yet the individual/whole interactions (wave-particle interactions) occur at the plasma frequency $\omega_p^2 = \frac{ne^2}{\epsilon_0 m}$, the magnetic gyration (cyclotron) frequency $\omega_c = \frac{eB}{m}$, or their harmonic combinations. As well, the fastest Coulomb collision frequency, the electron-electron Coulomb interaction frequency ν_{ee}, is estimated as a small parameter multiplying the plasma frequency,

$$\nu_{ee} = \frac{\log(\Lambda)}{\Lambda}\omega_{pe} \tag{1.1}$$

where $\Lambda = \frac{4}{3}\pi\lambda_D^3 n$ is the (inverse) plasma parameter[1] and ω_{pe} is the electron plasma frequency. Then $\nu_{ee} \ll \omega_{pe}$ and wave-particle interactions occur on a time-scale separated by several orders of magnitude from the Coulomb interactions.

The central result is that upon coarse-graining of the *plasma* time- and length-scales, the same trends are observed as in the more intuitive collisional picture. That is, the initial configuration is inextricably tangled and upon coarse-graining entropy is observed to increase. An important difference is that waves are not localized like particles, and so wave-particle interactions can be either resonant or non-resonant. The resonant interactions occur only within the range of particle velocities accessible by phase waves, and relax the distributions towards thermal equilibrium while releasing energy in the form of plasma fluctuations sustained by the non-resonant particles. The state of turbulence supported by the relaxed plasma is called *microturbulence* because it takes place on the plasma's smallest length-scales and fastest time-scales. This work is focused almost exclusively on plasma microturbulence in the kinetic description. Finally, the interactions of the continuum with itself, through wave-wave interactions or vortex motion, describe the macroscopic aspects of turbulence. It should be stressed that in hot plasmas the boundary between microscopic and macroscopic is especially blurry compared to the matter of everyday experience where microscopic dissipation processes are extremely well-separated in scale from observable, macroscopic phenomena.

---

[1] The plasma parameter estimates the number of simultaneously interacting discrete particles in a plasma, where $\lambda_D = v_t/\omega_p$ is the Coulomb interaction screening length and v_t is the characteristic velocity of the particle ensemble. In the theory of ionized gases one is in the plasma regime when $\Lambda \gg 1$.

Chapter 2

NUMERICAL METHODS FOR KINETIC EQUATIONS

> “6accdæ13eff7i3l9n4o4qrr4s8t12ux”, or:
>
> *“Data æquatione quotcunque fluentes quantitates involvente, fluxiones invenire; et vice versa.”*
>
> “Given an equation involving some flowing quantities, find the fluxes, and vice versa,”
>
> or “It is useful to solve differential equations.”
>
> - *Isaac Newton*, loose translation by *V.I. Arnold*

2.1 Fourier spectral methods

Periodic boundary conditions are often used by physicists in numerical modeling of wave dynamics and instabilities. While the discontinuous Galerkin (DG) method is effective at spatial discretization in a manner agnostic to the domain boundary conditions, the aforementioned class of periodic problems possess a symmetry which makes single-domain spectral methods particularly effective [1]. Differential equations typically become algebraic problems in Fourier spectral space [2], and linear equations coupled to nonlinear ones, such as Poisson’s equation, may be solved exactly to be analytically eliminated as an unknown [3]. In addition, the calculation of a problem’s Fourier modes may be done to spectral accuracy below the Nyquist frequency by use of the discrete Fourier transform (DFT) provided that the function interpolated is analytic and periodic [4]. Further, the DFT is blessed with one of the world’s fastest and most widely used algorithms, the fast Fourier transform (FFT). These above factors make the pseudospectral method, where nonlinear spectral terms are calculated by FFT, very attractive for spatial discretization.

Spectral methods may also be used on infinite domains, with Hermite or rational Chebyshev basis functions. Yet their convergence is not as effective as the periodic Fourier modes. If the asymptotic behavior of the considered function does not match that of the basis then expansions generally require a very large number of modes [1]. This phenomenon limits the applicability of Hermite modes to discretization of velocity space in kinetic equations, as only near-Maxwellian distributions have a low-dimensional representation. The resolution of far-from-equilibrium distributions, which occur often in plasma kinetic theory, is thereby severely limited in Fourier-Hermite representations of the Vlasov-Poisson equations. For this reason the following notes study a discontinuous Galerkin discretization of velocity space coupled with a spatial Fourier representation. This method ensures spatial spectral accuracy with a very small number of nodes while velocity space can be highly resolved.

2.1.1 Mathematical preliminary: the discrete Fourier transform

This section summarizes the discussion of Ref. [4]. When a continuous function is expanded in Fourier series, its expansion coefficients are determined by calculating the Fourier integral

$$c_n = \frac{1}{L}\int_0^L f(x)e^{-ik_n x}dx. \tag{2.1}$$

The discrete Fourier transform sends a set of discrete ordinates $\{f_0, f_1, \cdots, f_{N-1}\}$ to the spectral domain by application of the DFT transform matrix

$$c_n = \frac{1}{N}\sum_{n=0}^{N-1} f_i e^{-i2\pi nx/N}. \tag{2.2}$$

2.1.2 The discrete Fourier transform as the trapezoidal rule

It is well-known in some circles that the DFT is a quadrature approximation of the continuous Fourier integral when the function $f(x)$ is sampled at N equally spaced points. The DFT is equivalent to computing the Fourier integral by an N-point trapezoidal rule

$$\int_a^b f(x)dx \approx \sum_{n=0}^{N-1}\frac{f(x_{k-1}) + f(x_k)}{2}\Delta x_k. \tag{2.3}$$

In total generality the trapezoidal rule is at least $\mathcal{O}\Big((\Delta x)^2\Big)$-accurate. However, application of the Euler-Maclaurin error formula to the DFT as a trapezoidal rule shows that the error for *periodic functions* is significantly lower than this.

Let a function $g(x)$ on $x \in [-\pi, \pi]$ be smooth up to order $2p+2$, *i.e.* in $C^{2p+2}[-\pi, \pi]$ for $p > 1$. The Euler-Maclaurin error for the N-point trapezoidal integration of $\int_{-\pi}^{\pi} g(x)dx$ is

$$E_N = \sum_{m=1}^{p} \Big\{ \Big(\frac{2\pi}{N}\Big)^{2m} \frac{B_{2m}}{(2m)!}[g^{(2m-1)}(\pi) - g^{(2m-1)}(-\pi)] \Big\} + 2\pi \Big(\frac{2\pi}{N}\Big)^{2p+2} \frac{B_{2p+2}}{(2p+2)!} g^{(2p+2)}(\xi) \tag{2.4}$$

where $\xi \in [-\pi, \pi]$ is a certain point in the interval and B_n are the Bernoulli numbers. This result states that the trapezoidal quadrature of $g(x)$ is acccurate up to the smoothness of $g(x)$ on the boundary when periodic. Clearly, something special happens for analytic and periodic functions.

2.1.3 Exactness of the discrete Fourier transform for analytic, periodic functions

Now let $g(x) = f(x)e^{inx}$ to consider the Fourier integral. Then the derivatives of $g^{(p)}(\xi)$ are given by repeated application of the product rule,

$$g^{(p)}(\xi) = e^{in\xi} \sum_{m=0}^{p} \binom{p}{m} (in)^m f^{(p-m)}(\xi). \tag{2.5}$$

Now consider some cases beginning with the first Fourier coefficient $n = 1$. The error is

$$E_N(1) \approx \Big(\frac{1}{N}\Big)^{2p+2} (2\pi)^{2p+2} \frac{B_{2p+2}}{(2p+2)!} f^{(2p+2)}(\xi) \tag{2.6}$$

where N is the number of points in the trapezoidal rule. The asymptotic expansion of the Bernoulli numbers is $B_p \leq 4\frac{p!}{(2\pi)^p}$ as $p \to \infty$. Thus, as $p \to \infty$,

$$\lim_{p\to\infty} E_N(1) \leq 8\pi \Big(\frac{1}{N}\Big)^{2p+2} f^{(2p+2)}(\xi) \to 0. \tag{2.7}$$

With increasing smoothness of $f(x)$ on the periodic boundary the integration becomes *exact* provided $N > 1$. Now consider the mode $n = N$. Then one has

$$E_N(N) \leq 8\pi f^{(2p+2)}(\xi). \tag{2.8}$$

The final error term no longer necessarily decreases with increasing smoothness. This is a manifestation of aliasing. Thus the discrete Fourier transform is *exact* for periodic, analytic functions interpolated on an N-point equally-spaced grid up to the aliasing point. This makes the DFT *optimal* versus other quadrature schemes provided that $f(x)$ is a C^∞ function.

2.1.4 Fourier discretization of the spatial coordinates

This section describes the discretization of phase space by joint Fourier/DG method. The discussion begins with Fourier series and Galerkin projection onto the Fourier modes. The discontinuous Galerkin, used to discretize velocity space, is discussed in the next section.

Fourier mode dynamics of the Vlasov-Poisson equations

Recall that the normalized Vlasov-Poisson equations for electron dynamics are given by

$$\frac{\partial f}{\partial t} + v\frac{\partial f}{\partial x} + \frac{\partial \varphi}{\partial x}\frac{\partial f}{\partial v} = 0, \tag{2.9}$$

$$\frac{d^2\varphi}{dx^2} = \int_{-\infty}^{\infty} f dv - 1. \tag{2.10}$$

For $f(x+L, v, t) = f(x, v, t)$, the distribution and potential can be expanded in Fourier series

$$f(x, v, t) = \sum_{n=-\infty}^{\infty} f_n(v, t) e^{ik_n x} \tag{2.11}$$

$$\varphi(x, t) = \sum_{n=-\infty}^{\infty} \varphi_n(t) e^{ik_n x} \tag{2.12}$$

with wavenumbers $k_n = \frac{2\pi}{L}n$, resulting in the transformed system of equations

$$\frac{\partial f_n}{\partial t} + ik_n v f_n + \partial_v F_n = 0, \tag{2.13}$$

$$-k_n^2 \varphi_n = \int_{-\infty}^{\infty} f_n dv - \delta_{n0}, \tag{2.14}$$

$$F_n(v, t) = \sum_{m=-\infty}^{\infty} ik_m \varphi_m(t) f_{n-m}(v, t) = -(E * f)_n \tag{2.15}$$

where $F_n(v,t)$, the velocity-space flux of the spatial Fourier coefficients, is the convolution of the electric field with the distribution function. The transformed Poisson equation may be solved analytically by imposing the gauge condition that $\varphi_0 \equiv 0$,

$$E_n = ik_n^{-1} \int_{-\infty}^{\infty} f_n dv, \quad n \neq 0 \tag{2.16}$$

so that the field variable is eliminated algebraically. This makes Eq. 2.13 a system of coupled, inhomogeneous first-order hyperbolic partial differential equations.

Galerkin projection onto Fourier modes

Let the Vlasov-Poisson equations be integrated against a set of test functions, specifically the Fourier modes $\psi_n = e^{-ik_n x}$ from $n = -N, -N+1 \cdots, N-1, N$. From this weak formulation, expand the distribution function in a finite Fourier series up to the chosen cut-off mode N. As the modes are orthogonal the mass matrix is diagonal, separating the modes into a coupled set of equations. This procedure is a Galerkin projection of the kinetic equation onto the first N Fourier modes, and formally results in the same set of coupled equations as the previous section [5]. However the system of coupled PDEs is now finite.

2.2 Domain decomposition and the discontinuous Galerkin method

Consider the conservation law for a scalar $u = u(t, x_i)$ and its flux $F^j = F^j(x_i, u)$,

$$\partial_t u + \partial_j F^j = 0. \tag{2.17}$$

Throughout this section the up/down summation notation is used. Equation 2.17 also describes vector-valued u and higher-order derivatives reduced to first-order systems. The DG method splits the domain Ω into finite elements Ω_α with boundary $\partial\Omega_\alpha$, and projects the weak or variational form of Eqn. 2.17 onto a polynomial basis of each element, resulting in an approximate solution $\widetilde{u}^\alpha$. A set of nodes is chosen $\{\xi_j\}_{j=0}^{n-1}$ within each element which are interpolated by the Lagrange polynomials

$$\ell_j(\xi) = \prod_{\substack{k=0 \\ k\neq j}}^{n-1} \frac{\xi - \xi_k}{\xi_j - \xi_k}. \tag{2.18}$$

The element basis is defined as these polynomials $\ell_j(\xi)$. Rectilinear d-dimensional elements Ω are built up by tensor products of the one-dimensional line element $\mathcal{L}$, so that $\Omega = \mathcal{L}_d \otimes \mathcal{L}_{d-1} \otimes \cdots \otimes \mathcal{L}_1$. The node set of Ω is correspondingly a tensor product of each line's node set, so the d-dimensional Lagrange functions can be factorized into products of the Lagrange polynomials in each dimension. To avoid a proliferation of indices, define an index β_i to range through the nodes $\{\xi_j\}_{j=0}^{n-1}$ in the line element $\mathcal{L}_i$, and then let $\beta = \{\beta_0, \beta_1, \cdots, \beta_{d-1}\}$ be the multi-index collecting the nodal index of each dimension. Additional discussion on ordering of a multi-index for tensor-product geometry constructions can be found in [6]. The Lagrange polynomial of Ω is then

$$L_\beta(x_0, x_1, \cdots, x_d) = \ell_{\beta_0}(x_0)\ell_{\beta_1}(x_1)\cdots\ell_{\beta_d}(x_d) \tag{2.19}$$

with x_i the i'th coordinate. In the projection of the approximation onto the basis functions L_β the expansion coefficients $u^{\alpha,\beta}$ may be labelled by the same multi-index,

$$\widetilde{u}^\alpha(t, x) = \sum_\beta u^{\alpha,\beta}(t) L_\beta(x). \tag{2.20}$$

Galerkin projection of Eq. 2.17 leads to inner products $\langle\cdot|\cdot\rangle_{\Omega_\alpha}$ over the basis functions. Specifically, Eq. 2.17 is integrated on the domain against the basis functions L_γ,

$$\langle \partial_t u | L_\gamma \rangle_{\Omega_\alpha} + \langle \partial_j F^j | L_\gamma \rangle_{\Omega_\alpha} = 0, \tag{2.21}$$

and the basis expansion Eq. 2.20 is substituted. The resulting projected integral form is

$$\frac{du^{\alpha,\beta}}{dt} \langle L_\beta | L_\gamma \rangle_{\Omega_\alpha} + \langle \partial_j F^{\alpha,j} | L_\gamma \rangle_{\Omega_\alpha} = 0. \tag{2.22}$$

Information must be passed between elements Ω_α in the form of a flux, or else the elements would decouple and the discretization would not be consistent. This is done by integrating the flux term $\langle \partial_j F^{\alpha,j} | L_\gamma \rangle_{\Omega_\alpha}$ by parts and taking the boundary term to be a function of both the local state and that of the neighbor, *i.e.* $F^\alpha|_{\partial\Omega_\alpha} \equiv \mathcal{F}(\partial\Omega_\alpha^-, \partial\Omega_\alpha^+)$ where $\partial\Omega_\alpha^-$ is the state interior to the element and $\partial\Omega_\alpha^+$ the state exterior. The function $\mathcal{F}$, termed numerical flux, is chosen so that Eq. 2.17 is discretized consistently. The requirement for consistency means $\mathcal{F}$ is related to the nature of information propagation in the system. The single integration by parts results in the DG weak form, and one further integration by parts in the strong form, given respectively by

$$\frac{du^{\alpha,\beta}}{dt} \langle L_\beta | L_\gamma \rangle_{\Omega_\alpha} = F^{\alpha,\beta,j} \langle L_\beta | \partial_j L_\gamma \rangle_{\Omega_\alpha} - \mathcal{F}^{\alpha,\beta,j} \langle L_\beta | L_\gamma \rangle_{\partial\Omega_\alpha^j}, \tag{2.23}$$

$$\frac{du^{\alpha,\beta}}{dt} \langle L_\beta | L_\gamma \rangle_{\Omega_\alpha} + F^{\alpha,\beta,j} \langle \partial_j L_\beta | L_\gamma \rangle_{\Omega_\alpha} = (F^{\alpha,\beta,j} - \mathcal{F}^{\alpha,\beta,j}) \langle L_\beta | L_\gamma \rangle_{\partial\Omega_\alpha^j} \tag{2.24}$$

These inner product matrices are termed the mass M, face mass Γ, advection $\mathcal{A}$, and stiffness S matrices by analogy with continuum mechanics, and their short-hand definitions are

$$M^\alpha_{\beta\gamma} \equiv \langle L_\beta | L_\gamma \rangle_{\Omega_\alpha}, \qquad \Gamma^{\alpha,j}_{\beta\gamma} \equiv \langle L_\beta | L_\gamma \rangle_{\partial\Omega_\alpha^j}, \tag{2.25}$$

$$\mathcal{A}^{\alpha,j}_{\beta\gamma} \equiv \langle L_\beta | \partial_j L_\gamma \rangle_{\Omega_\alpha}, \quad S^{\alpha,j}_{\beta\gamma} \equiv \langle \partial_j L_\beta | L_\gamma \rangle_{\Omega_\alpha}. \tag{2.26}$$

To solve for the expansion coefficients, define elementwise operators

$$\Upsilon^{\alpha,\beta}_{\gamma,j} \equiv (M^{-1})^{\alpha,\beta\epsilon} \mathcal{A}^\alpha_{\gamma\epsilon,j}, \qquad \Xi^{\alpha,\beta}_{\gamma,j} \equiv (M^{-1})^{\alpha,\beta\epsilon} \Gamma^\alpha_{\gamma\epsilon,j}, \qquad D^{\alpha,\beta}_{\gamma,j} \equiv (M^{-1})^{\alpha,\beta\epsilon} S_{\gamma\epsilon,j}, \tag{2.27}$$

to obtain the weak and strong form semi-discrete equations per element,

$$\frac{d}{dt} u^{\alpha,\beta} = \Upsilon^{\alpha,\beta}_{\gamma,j} F^{\alpha,\gamma,j} - \Xi^{\alpha,\beta}_{\gamma,j} \mathcal{F}^{\alpha,\gamma,j} \tag{2.28}$$

$$\frac{d}{dt} u^{\alpha,\beta} + D^{\alpha,\beta}_{\gamma,j} F^{\alpha,\gamma,j} = \Xi^{\alpha,\beta}_{\gamma,j} (F^{\alpha,\gamma,j} - \mathcal{F}^{\alpha,\gamma,j}). \tag{2.29}$$

Considering the weak form, Eqn. 2.28, the first term represents fluxes due to internal degrees of freedom within an element, and the second term boundary fluxes. The strong form operator $D^{\alpha,\beta}_{\gamma,\mu}$ is a direct gradient discretization called the derivative matrix, while the operator $\Upsilon^{j,\alpha}_{k,\mu}$ approximates the gradient in integral form. In both cases $\Xi^{\alpha,\beta}_{\gamma,\mu}$ discretizes the surface integrals between elements. Explicitly, the multi-index α denotes the elements Ω_α, β the element's nodes, and j the coordinates.

The basis of element Ω_α is related to a reference element by an isoparametric transform and its Jacobian J^α_{ij}, so that only one set of matrices $\{\Upsilon^\beta_{\gamma,j}, \Xi^\beta_{\gamma,j}, D^\beta_{\gamma,j}\}$ need be determined. These reference operators are then related to element-wise ones by $\Upsilon^{\alpha,\beta}_{\gamma,\nu} = J^{\mu,\alpha}_\nu \Upsilon^\beta_{\gamma,\mu}$. The following will consider operations with only the reference operators by taking elements to have an identical Jacobian. Equations 2.28 & 2.29 represent ODEs whose right-hand side is given by a tensor product contracting the multi-index γ and the coordinates j. The following section shows that for rectilinear elements these contractions simplify into a sum over products with the one-dimensional matrices Υ, D, Ξ.

2.3 The curse of dimensionality and Cartesian tensor methods

Now consider rectilinear n-cube elements with the multi-index (α, β) as shown in Fig. 2.1. Substitution of the factorized basis polynomials defined by Eq. 2.19 into Eqs. 2.25-2.26 shows the element to be composed of products of the lower-dimensional constituents. Specifically, the mass matrix $M_{\beta,\gamma}$ with nodal indices β, γ decomposes into tensor products as

$$M_{\beta\gamma} = M_{\beta_{d-1},\gamma_{d-1}} \otimes M_{\beta_{d-2},\gamma_{d-2}} \otimes \cdots \otimes M_{\beta_0,\gamma_0}. \tag{2.30}$$

so that it may be termed the mass tensor for $d > 1$. It follows that the inverse mass tensor is $M^{-1}_{\beta\gamma} = M^{-1}_{\beta_{d-1},\gamma_{d-1}} \otimes M^{-1}_{\beta_{d-2},\gamma_{d-2}} \otimes \cdots \otimes M^{-1}_{\beta_0,\gamma_0}$. Thus the advection tensor $\mathcal{A}^j_{\beta\gamma} = \langle \partial_j L_\beta | L_\gamma \rangle_{\Omega_\alpha}$ has d components (ranging over index j) each given by the tensor products

$$\mathcal{A}^j_{\beta\gamma} = \begin{bmatrix} M_{\beta_{d-1},\gamma_{d-1}} \otimes M_{\beta_{d-2},\gamma_{d-2}} \otimes \cdots \otimes \mathcal{A}_{\beta_0,\gamma_0} \\ \vdots \quad\quad \vdots \quad\quad \vdots \\ M_{\beta_{d-1},\gamma_{d-1}} \otimes \mathcal{A}_{\beta_{d-2},\gamma_{d-2}} \otimes \cdots \otimes M_{\beta_0,\gamma_0} \\ \mathcal{A}_{\beta_{d-1},\gamma_{d-1}} \otimes M_{\beta_{d-2},\gamma_{d-2}} \otimes \cdots \otimes M_{\beta_0,\gamma_0} \end{bmatrix} \tag{2.31}$$

with analogous results for the face mass Γ and stiffness matrices S. The components corresponding to the sub-indices of the multi-indices β, γ are seen to be the lower-dimensional matrices themselves. Due to the tensor product mixed-product property $(A \otimes B)(C \otimes D) =$

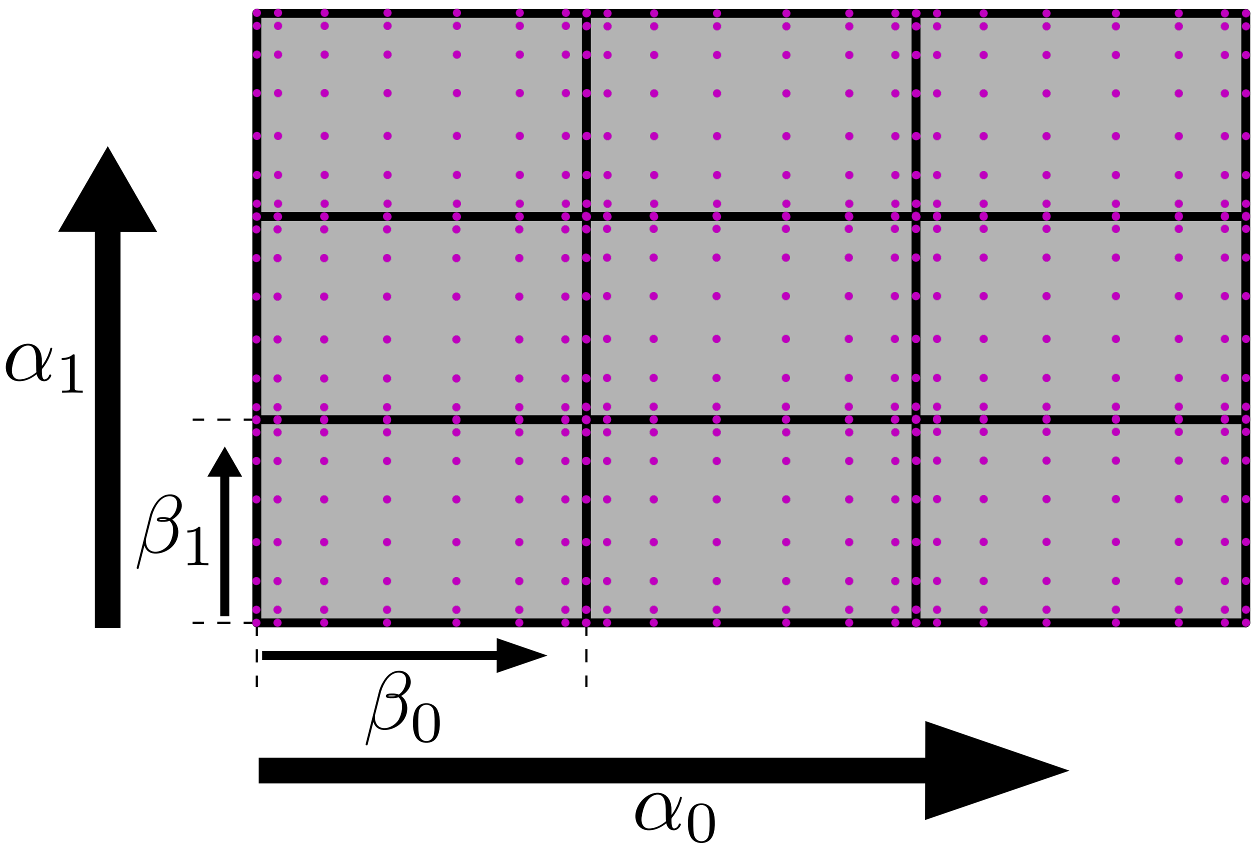

Figure 2.1: Structured grids have a natural tensor product structure which is illustrated by the use of multi-indexes. Shown is a two-dimensional example with an eight-node Legendre-Gauss-Lobatto (LGL) node set, where the elements in directions $(0, 1)$ are indexed by α_0, α_1 and the nodal sub-elements by β_0, β_1. Any node's index consists of its tuple $(\alpha_0, \beta_0, \alpha_1, \beta_1)$.

$(AC)\otimes(BD)$, the internal flux tensor $\Upsilon^{\mu}_{\mathcal{D}} = M^{-1}_{\mathcal{D}} A^{\mu}_{\mathcal{D}}$ has the d components,

$$\Upsilon^{j}_{\beta\gamma} = \begin{bmatrix} I_{\beta_{d-1},\gamma_{d-1}} \otimes I_{\beta_{d-2},\gamma_{d-2}} \otimes \cdots \otimes \Upsilon_{\beta_0,\gamma_0} \\ \vdots \qquad\quad \vdots \qquad\quad \vdots \\ I_{\beta_{d-1},\gamma_{d-1}} \otimes \Upsilon_{\beta_{d-2},\gamma_{d-2}} \otimes \cdots \otimes I_{\beta_0,\gamma_0} \\ \Upsilon_{\beta_{d-1},\gamma_{d-1}} \otimes I_{\beta_{d-2},\gamma_{d-2}} \otimes \cdots \otimes I_{\beta_0,\gamma_0} \end{bmatrix}, \tag{2.32}$$

each consisting of $(d-1)$ tensor products with the identity. The numerical flux tensor $\Xi^{j}_{\beta\gamma}$ follows an identical pattern, with component k $I_{\beta_{d-1},\gamma_{d-1}} \otimes I_{\beta_{d-2},\gamma_{d-2}} \otimes \cdots \otimes \Xi_{\beta_k,\gamma_k} \otimes \cdots \otimes I_{\beta_0,\gamma_0}$.

Equation 2.32 means that the flux of direction j only needs to be contracted with the corresponding one-dimensional matrix of direction j. To illustrate, consider the case of a $d = 3$ flux F^j with a rectilinear discretization. Separate the element multi-index α into directional indices a, b, c and β into sub-element nodal indices p, q, r so that $F^{\alpha}_{j,\gamma} \equiv F^{abc}_{j,pqr}$. The internal flux product is then

$$\Upsilon^{\gamma,j}_{\beta} F^{\alpha}_{j,\gamma} \equiv (I_2)^p_n (I_1)^q_m (\Upsilon_0)^r_\ell F^{abc}_{0,pqr} + (I_2)^p_n (\Upsilon_1)^q_m (I_0)^r_\ell F^{abc}_{1,pqr} + (\Upsilon_2)^p_n (I_1)^q_m (I_0)^r_\ell F^{abc}_{2,pqr} \tag{2.33}$$

$$= (\Upsilon_0)^r_\ell F^{abc}_{0,nmr} + (\Upsilon_1)^q_m F^{abc}_{1,nq\ell} + (\Upsilon_2)^p_n F^{abc}_{2,pm\ell} \tag{2.34}$$

by carrying through each identity product. By similar reasoning, having formed a numerical flux array $\mathcal{F}$ for the two faces of each sub-element axis, the boundary flux product is

$$\Xi^{j,\gamma}_{\beta} \mathcal{F}^{\alpha}_{j,\gamma} = (\Xi_0)^{\gamma_r}_\ell \mathcal{F}^{abc}_{0,nm\gamma_r} + (\Xi_1)^{\gamma_q}_m \mathcal{F}^{abc}_{1,n\gamma_q r} + (\Xi_2)^{\gamma_p}_n \mathcal{F}^{abc}_{2,\gamma_p m\ell} \tag{2.35}$$

where $\gamma_i = \delta_{0i} + \delta_{i(n-1)}$ picks out the boundary nodes of the sub-element index.

Equation 2.34 demonstrates that orthogonal elements reduce the number of calculations needed to evaluate the right-hand side of the semi-discrete equation. The gain increases with dimension versus using full basis tensors. With full tensors, Υ is a $\mathbb{R}^{d\times N\times N}$ array for $N \approx n^d$ the total number of nodes in the element and n the nodes per sub-element. In contrast, with a rectilinear discretization only the d one-dimensional matrices $\Upsilon \in \mathbb{R}^{n\times n}$ are needed. Unless a non-orthogonal mesh is required for particular domain geometry, an orthogonal grid provides significant simplification.

In some cases non-orthogonal elements are desired in certain dimensions of a problem while other dimensions are free to use orthogonal discretization [7]. For example the collisionless Boltzmann equation (*i.e.* Vlasov equation) is an advection equation in $d = (D+V)$-dimensional phase space consisting of D configurational (spatial) dimensions and V velocity dimensions. As irregular boundaries will occur only in spatial dimensions, one is free to discretize velocity space orthogonally. In this case a blended element basis E may be built up from tensor products of the simplex element basis Δ and V copies of the line element $\mathcal{L}_i$, *i.e.* for $D = V = 2$ one has $E \equiv \Delta \otimes \mathcal{L}_1 \otimes \mathcal{L}_2$. In this case

$$\Upsilon_E^j = \begin{bmatrix} I_2 \otimes I_1 \otimes \Upsilon_\Delta \\ I_2 \otimes \Upsilon_1 \otimes I_\Delta \\ \Upsilon_2 \otimes I_1 \otimes I_\Delta \end{bmatrix} \tag{2.36}$$

and similarly for the numerical flux array. The multi-index is naturally composed of unstructured spatial element information, velocity-space grid indices a, b, and sub-element nodal indices p, q. Equation 2.34 then generalizes to the blended case.

2.4 Theory of interpolation and Gaussian quadrature

The objective of this section is to obtain expressions for the DG flux divergence operators while emphasizing the interrelatedness of the theories of discrete integration, polynomial interpolation, and systems of orthogonal polynomials. These theories are often presented independently of one another but a considerate study of each topic reveals their inherent harmony. In this section the theory of DG matrices using Gauss-Lobatto quadrature points is considered according to the method of Refs. [8, 9] and extended to the particular form expressed in Section 2.2. The results are both explicit and interpretable to arbitrarily high order. The reader may skip to the results given in Eqs. 2.67, 2.70, and 2.71.

2.4.1 Orthogonal polynomials

The Weierstrass approximation theorem states that continuous functions on the interval $[a, b]$ are uniformly approximated by polynomials, and it is always convenient to express a linear object as a combination of orthogonal components. Orthogonal polynomials are the generalization of this concept to the vector space of polynomials Π_n up to degree n on the interval $[a, b]$ endowed with the inner product

$$\langle f|g\rangle = \int_a^b w(x)f(x)g(x)dx \tag{2.37}$$

for $f,\ g \in L^2[a, b]$ and $w(x)$ is a strictly positive, integrable weighting function[1]. A set of polynomials p_j is orthogonal if $\langle p_i|p_k\rangle = 0$ for $i \neq k$. It is worthwhile to review the properties of these functions [10]. For a given $w(x)$ and interval $[a, b]$, the set of orthogonal polynomials is uniquely defined by recursion through Gram-Schmidt orthogonalization from the monomial basis $1, x, x^2, \cdots$. However it is more instructive to define the orthogonal polynomials through the generalized Rodrigues formula

$$p_n(x) = \frac{1}{A_n w}\frac{d^n}{dx^n}(ws^n) \tag{2.38}$$

where A_n is a constant and $s(x)$ is a characteristic polynomial of degree 2 or less such that $w(a)s(a) = w(b)s(b) = 0$. It can be shown from this definition that $\frac{d^m}{dx^m}(ws^n) = 0$ for $m < n$. Then by repeated integration by parts it follows that $\langle f_k|p_n\rangle = 0$ for any polynomial f_k of degree $k < n$, so $\{p_0, p_1, \cdots, p_n(x)\}$ is a family of orthogonal polynomials. This family defines an orthogonal basis for the space Π_n so that any polynomial f_n may be expanded as

$$f_n(x) = \sum_{i=0}^{n} c_i p_i(x). \tag{2.39}$$

Further, because $s(x)$ is of degree two or less the polynomials so defined all satisfy Sturm-Liouville differential equations

$$\frac{d}{dx}\left(ws\frac{dp_n}{dx}\right) = w\lambda_n p_n(x) \tag{2.40}$$

where the eigenvalues λ_n depend on coefficients of $p_1(x)$ and $s(x)$. So the orthogonal polynomials arise naturally in the study of physical phenomena in various geometries. The Legendre

---

[1] The weighting function plays many roles, generally relating the polynomials to some sort of underlying geometry. Examples include the relation of Chebyshev polynomials to the semicircle and Hermite polynomials to the Gaussian.

polynomials $P_n(x)$ are in a sense the simplest such orthogonal family, with weight functions $w(x) = 1$ on the interval $[-1, 1]$ with $s(x) = x^2 - 1$ and normalization $A_n = 2^n n!$. That is,

$$P_n(x) = \frac{1}{2^n n!}\frac{d^n}{dx^n}(x^2 - 1)^n \tag{2.41}$$

which have the orthogonality property

$$\langle P_n|P_m\rangle = \frac{1}{2n+1}\delta_{nm}. \tag{2.42}$$

Orthogonal polynomials have the property that their roots are all real and distinct, an important fact in the theory of Gaussian quadrature.

2.4.2 Gaussian quadrature and interpolation polynomials

Each family of orthogonal polynomials is associated with a method of exact integration called Gaussian quadrature [11]. Consider integration of a polynomial $f(x)$ of degree $2n-1$ or less

$$\langle f(x)|1\rangle = \int_a^b w(x)f(x)dx \tag{2.43}$$

against the weight function of the previous section. Without loss of generality represent it as $f(x) = p_n(x)q(x) + r(x)$ where $p_n(x)$ is the n-th order orthogonal polynomial under the inner product Eqn. 2.37 and $q(x)$, $r(x)$ are some polynomials of degree $n-1$ or less. Expand each in terms of orthogonal polynomials,

$$q(x) = \sum_{k=0}^{n-1} a_k p_k(x), \qquad r(x) = \sum_{k=0}^{n-1} b_k p_k(x)$$

and note that

$$\langle p_n|q\rangle = 0 \qquad \langle r|1\rangle = \langle r|p_0\rangle = b_0\langle p_0|p_0\rangle.$$

Therefore

$$\langle f|1\rangle = \langle p_n|q\rangle + \langle p_0|r\rangle = b_0\langle p_0|p_0\rangle.$$

Now consider $f(x)$ evaluated at any root x_i of the polynomial $p_n(x)$, i.e. $f(x_i) = r(x_i)$. This means that the sum

$$\sum_{i=0}^{n-1} w_i f(x_i) = \sum_{i=0}^{n-1} w_i r(x_i) = \sum_{k=0}^{n-1} b_k\Big(\sum_{i=0}^{n-1} w_i p_k(x_i)\Big)$$

depends on the function $r(x)$ alone for some set of constants w_i. If the constants w_i are specified as the solution of the system of equations

$$\sum_{i=0}^{n-1} w_i p_k(x_i) = \begin{cases} \langle p_0 | p_0 \rangle & k = 0, \\ 0 & k \geq 1, \end{cases} \tag{2.44}$$

then this sum is equal to $b_0 \langle p_0 | p_0 \rangle$. The system Eqn. 2.44 is guaranteed to have a unique solution due to the linear independence of the orthogonal polynomials p_k and that the n roots of p_n are all real and distinct. Therefore the integral of an polynomial of degree $2n-1$ or less against a weighting function $w(x)$ (from e.g., a Sturm-Liouville system) may be expressed exactly as a weighted sum on the roots of the corresponding orthogonal polynomial,

$$\int_a^b w(x) f(x) dx = \sum_{i=0}^{n-1} w_i f(x_i). \tag{2.45}$$

Such a scheme is called Gaussian quadrature. The simplest case is Legendre-Gauss quadrature for $w(x) = 1$ and $[a, b] = [-1, 1]$, corresponding to quadrature on the n roots of the Legendre polynomial $P_n(x)$. The Legendre-Gauss quadrature weights are given by

$$w_i = \frac{2}{(1 - x_i^2)(P_n'(x_i))^2}. \tag{2.46}$$

Gaussian quadrature sets do not contain the end-points, and often the boundary information is given. Quadrature including the boundaries is called Gauss-Lobatto quadrature, and by similar reasoning its rule is given by

$$\int_a^b f(x) dx = w_1 f(a) + \sum_{i=1}^{n-2} w_i f(x_i) + w_n f(b) \tag{2.47}$$

which, including only $n-2$ free points, is exact only up to degree $2n-3$. For the Legendre case ($[a, b] = [-1, 1]$ and $w(x) = 1$), quadrature points are given as the n roots of the polynomial $(1 - x^2) P_{n-1}'(x)$ and the weights by

$$w_{0,n-1} = \frac{2}{n(n-1)}, \quad w_i = \frac{2}{n(n-1)(P_{n-1}(x_i))^2}. \tag{2.48}$$

This scheme is called Legendre-Gauss-Lobatto (LGL) quadrature.

Intuitively Gauss-Legendre quadrature is of unit weighting because the measure of a spherical surface projects uniformly onto an interval (its axis) due to a theorem of Archimedes [12]. As Legendre polynomials are those harmonics invariant under rotations of the polar axis, the quadrature shares their completeness properties, *i.e.* the relation [10]

$$\sum_{s=0}^{\infty}\Big(s+\frac{1}{2}\Big)P_s(x)P_s(y) = \delta(y-x), \qquad -1 \le x, y \le 1. \tag{2.49}$$

Section 2.4.3 shows the interpolants $\ell_j(\xi)$ through n Gauss-Legendre nodes satisfy

$$\ell_j(\xi) = w_j \sum_{s=0}^{n-1}\Big(s+\frac{1}{2}\Big)P_s(\xi_j)P_s(\xi), \qquad \text{and} \qquad \ell_j(\xi_i) = \delta_{ij} \tag{2.50}$$

with $\{w_j\}_{j=0}^{n-1}$, $\{\xi_j\}_{j=0}^{n-1}$ the quadrature weights and nodes respectively. Considering the summation $\lim_{n\to\infty}\sum_{j=0}^{n-1}\ell_j(\xi)f(\xi)$ suggests that the interpolation polynomial plays a role in discrete integration as if it were a δ-sequence on $[-1,1]$ in the sense of distributions [13]. The LGL interpolant is identical to Eq. 2.50 with a reweighted largest eigenvalue $(s+1/2) \to (s/2)$ [8]. With this, the gradient matrices in the LGL basis may be found explicitly [8, 9].

2.4.3 Basic patterns in the Gauss-Legendre basis

It's useful to first review the result for full Gauss-Legendre quadrature as the steps are simple and the patterns recur in the Lobatto basis. The situation is simple in full Gaussian quadrature, but evaluation of the numerical fluxes is simplified by Lobatto quadrature through including the endpoints [14]. Denoting nodes by the n quadrature points $\{\xi_j\}_{j=0}^{n-1}$, in addition to continuous orthogonality the polynomials P_n are discretely orthogonal [15, 11] ,

$$\sum_{s=0}^{n-1} w_s P_k(\xi_s)P_\ell(\xi_s) = \frac{1}{k+\frac{1}{2}}\delta_{k\ell} \tag{2.51}$$

with w_s the quadrature weights. This follows from the order $2n-1$ quadrature property as the sum equals the integral $\int_{-1}^{1} P_k(x)P_\ell(x)dx$. Expansions in the Lagrange basis of Eqn. 2.18 and in the Legendre basis are linearly related due to the interpolation property $\ell_j(\xi_i) = \delta_{ij}$,

$$f(\xi) = \sum_{j=0}^{n-1} f_j\ell_j(\xi) = \sum_{k=0}^{n-1} c_k P_k(\xi), \qquad \implies \qquad f_j = \mathcal{V}_j^k c_k \tag{2.52}$$

where $\mathcal{V}_j^k = P_k(\xi_j)$ is termed the generalized Vandermonde matrix. The inverse transform follows from Eqn. 2.51 as $(\mathcal{V}^{-1})_j^k = w_j P_k(\xi_j)(k + \frac{1}{2})$. In particular, the Lagrange function is

$$\ell_j(\xi) = w_j \sum_{s=0}^{n-1} \Big(s + \frac{1}{2}\Big) P_s(\xi_j) P_s(\xi) \approx w_j \delta(\xi - \xi_j) \tag{2.53}$$

making the interpolation polynomial a weighted partial sum of the completeness relation. As the $P_j(\xi)$ are orthogonal, the mass matrix $M_{ij} = \int_{-1}^{1} \ell_i(\xi)\ell_j(\xi)d\xi = \omega_i \delta_{ij}$ is diagonal, with inverse $M_{ij}^{-1} = \omega_i^{-1}\delta_{ij}$. The advection and stiffness $S = \mathcal{A}^T$ matrices follow from evaluating the integrals by quadrature, *e.g.*

$$\mathcal{A}_{ij} = \omega_i \ell_j'(\xi_i) = \omega_i \omega_j \sum_{s=0}^{n-1} \Big(s + \frac{1}{2}\Big) P_s(\xi_i) P_s'(\xi_j). \tag{2.54}$$

Then the weak and strong form internal flux operators are partial sums of the delta derivative,

$$\Upsilon_j^i = w_j \sum_{s=0}^{n-1} \Big(s + \frac{1}{2}\Big) P_s(\xi_i) P_s'(\xi_j) \approx w_j \delta'(\xi - \xi_i)\big|_{\xi=\xi_j}, \tag{2.55}$$

$$D_j^i = w_j \sum_{s=0}^{n-1} \Big(s + \frac{1}{2}\Big) P_s'(\xi_i) P_s(\xi_j) \approx w_j \delta'(\xi - \xi_j)\big|_{\xi=\xi_i}, \tag{2.56}$$

in the distributional sense. For example, the product $\Upsilon_j^i F^j$ integrates the flux term

$$\Upsilon_j^i F^j = \sum_{j=0}^{n-1} w_j F_j \sum_{s=0}^{n-1} \Big(s + \frac{1}{2}\Big) P_s(\xi_i) P_s'(\xi_j) \approx \sum_{j=0}^{n-1} w_j \nabla(F(\xi - \xi_i))\Big|_{\xi=\xi_j} \approx \int_{-1}^{1} (\nabla F^i) d\xi \tag{2.57}$$

by quadrature within the element.

2.4.4 DG matrices in the Lobatto basis

Lobatto type quadrature includes interval end-points, so that boundary information is localized to a single interpolation basis function. The Legendre-Gauss-Lobatto (LGL) quadrature scheme is expressed by, for $\int_{-1}^{1} f(\xi)d\xi \approx \sum_{j=0}^{n-1} w_j f(\xi_j)$, the nodes $\{\xi_j\}_{j=0}^{n-1}$ and weights $\{w_j\}_{j=0}^{n-1}$ according to

$$\{\xi_j | (1 - \xi_j^2) P_{n-1}'(\xi_j) = 0\}, \qquad w_j = \frac{2}{n(n-1)} \frac{1}{(P_{n-1}(\xi_j))^2}. \tag{2.58}$$

The above rule integrates polynomials of degree $\leq 2n-3$ [11].

From the perspective of linear algebra, the orthogonality of classical orthogonal polynomials under Gaussian quadrature follows from the orthogonality of the eigenvectors of the defining recurrence relation represented as a tri-diagonal Jacobi matrix [15]. In the case of Lobatto quadrature, a consequence of this modified Jacobi matrix eigenvalue problem is that the Legendre polynomials remain discretely orthogonal under LGL quadrature,

$$\sum_{s=0}^{n-1} w_s P_k(\xi_s) P_\ell(\xi_s) = \gamma_k \delta_{k\ell}, \qquad \gamma_k \equiv \begin{cases} \frac{2}{2k+1} & k < n-1, \\ \frac{2}{n-1} & k = n-1 \end{cases} \tag{2.59}$$

where the final eigenvalue is modified from $(k+\frac{1}{2})^{-1}$ to $(k/2)^{-1}$. Equation 2.59 also follows by direct calculation as in Ref. [8], where all but the final case follows from quadrature and the final value γ_{n-1} follows from the form of the boundary weights w_0, w_{n-1}.

Just as for Gauss-Legendre quadrature, the discrete orthogonality relation expresses the coefficients of the Vandermonde matrix and its inverse. That is, with the same expansion of Eqn. 2.52 the Vandermonde matrix elements are $\mathcal{V}_j^k \equiv P_k(\xi_j)$ with inverse components $(\mathcal{V}^{-1})_j^k = w_j \gamma_k^{-1} P_k(\xi_j)$ following directly from Eqn. 2.59. The spectral transform from the Lagrange to Legendre spectral basis is identical in form to full Gauss-Legendre quadrature. In particular the modal form of the Lagrange basis functions themselves is of the same form,

$$\ell_j(\xi) = (\mathcal{V}^{-1})_j^k P_k(\xi) = w_j \sum_{s=0}^{n-1} \gamma_k^{-1} P_s(\xi_j) P_s(\xi) \approx \omega_j \delta(\xi - \xi_j) \tag{2.60}$$

and expresses a re-weighted partial summation of the completeness theorem due to the Lobatto weighting of the last term in the series, γ_{n-1}.

As discovered in [8], the Lagrange function spectral form of Eqn. 2.60 reveals the Lobatto basis mass matrix to be diagonal with a rank-one update. This makes it explicitly invertible. To review the quoted result, let $A_m \equiv \int_{-1}^{1} P_m(\xi) P_m(\xi) d\xi$. Noting that $A_m = \frac{2}{2m+1} = \gamma_m$ of

Eqn. 2.59 for $m < n-1$, the mass matrix integrates to

$$M_{ij} = \int_{-1}^{1} \ell_i(\xi)\ell_j(\xi)d\xi = \sum_{k,m=0}^{n-1} \frac{w_i w_j}{\gamma_k \gamma_m} P_k(\xi_i)P_m(\xi_j)\int_{-1}^{1} P_k(\xi)P_m(\xi)d\xi \tag{2.61}$$

$$= w_i \sum_{k=0}^{n-1} \frac{w_j}{\gamma_k} P_k(\xi_i)P_k(\xi_j) + \frac{A_{n-1}-\gamma_{n-1}}{\gamma_{n-1}^2} w_i w_j P_{n-1}(\xi_i)P_{n-1}(\xi_j) \tag{2.62}$$

$$= w_i(\delta_{ij} - \alpha w_j P_{n-1}(\xi_i)P_{n-1}(\xi_j)) \tag{2.63}$$

as the first sum equals $\ell_i(\xi_j)$ and where $\alpha = (\gamma_{n-1} - A_{n-1})\gamma_{n-1}^{-2} = \frac{n(n-1)}{2(2n-1)}$. The mass matrix is full, but differs from the diagonal Gauss-Legendre result by a rank-one matrix. Applying the identity $(I - uv^T)^{-1} = I + \frac{uv^T}{1-v^Tu}$ inverts the mass matrix as

$$M_{ij}^{-1} = \frac{1}{w_i}\delta_{ij} + \frac{n}{2}P_{n-1}(\xi_i)P_{n-1}(\xi_j). \tag{2.64}$$

The DG matrices in the Lobatto basis follow from Eqn. 2.64. Fortunately, the face mass matrix Γ, advection matrix A and stiffness matrix S follow more easily than the mass matrix. For the interval $[-1, 1]$ the face mass matrix Γ is a Kronecker delta picking out the boundary nodes, while the advection matrix $\mathcal{A}$ is maximal order $2n-3$, so by quadrature

$$\mathcal{A}_{ij} = \langle \ell_i(\xi)|\partial_\xi \ell_j(\xi)\rangle = w_i \ell_j'(\xi_i), \tag{2.65}$$

with the stiffness matrix its transpose $S_{ij} = \mathcal{A}_{ij}^T = w_j \ell_i'(\xi_j)$. Using the projection matrices M^{-1}, $\mathcal{A}$, and S, and the Lagrange function of Eqn. 2.60, the DG operators follow as

$$\Upsilon_k^j = \frac{w_k}{w_j}\ell_j'(\xi_k) + \frac{n}{2}w_k P_{n-1}(\xi_j)P_{n-1}'(\xi_k), \tag{2.66}$$

$$\Xi_{\gamma^k}^j = \frac{1}{w_j}\delta_{j\gamma^k} + \frac{n}{2}P_{n-1}(\xi_j)P_{n-1}(\xi_{\gamma^k}), \tag{2.67}$$

$$D_k^j = \ell_k'(\xi_j) \tag{2.68}$$

Here, the numerical flux array Ξ is simply the first and last columns of the inverse mass matrix where the index $\gamma^k = \delta_{k0} + \delta_{k(n-1)}$ denotes the interval end-points. The term $P_{n-1}'(\xi_k)$ in Υ_k^j expressing the rank-one difference from the Gauss-Legendre result arises from the identity

$$\sum_{s=0}^{n-1} P_{n-1}(\xi_s)\ell_s'(\xi_j) = P_{n-1}'(\xi_j) \tag{2.69}$$

which follows from the orthogonality relation Eqn. 2.59. The result for D^j_k is found by accounting for boundary terms after a discrete integration by parts and canceling the remainder. By then applying Eqn. 2.60 the weak form operator Υ becomes simply

$$\Upsilon^j_k = w_k \sum_{s=0}^{n-1} \Big(s + \frac{1}{2}\Big) P_s(\xi_j) P'_s(\xi_k). \tag{2.70}$$

This form of the internal flux operator clearly demonstrates it as a flux discretization, that is, as a partial derivative of the Legendre completeness relation. In the limit of many quadrature nodes the internal flux operator approaches $\sim \omega_k \delta'(\xi - \xi_j)\big|_{\xi=\xi_k}$, picking out the flux gradient as $\Upsilon^j_k F^k \sim \sum_k w_k \delta'(\xi - \xi_j)|_{\xi=\xi_k} F^k \approx \nabla F^j$, just as Gauss-Legendre but of lower accuracy due to the reweighted value γ_{n-1}. Similarly, the derivative matrix is seen to be

$$D^j_k = w_k \sum_{s=0}^{n-1} \frac{1}{\gamma_s} P'_s(\xi_j) P_s(\xi_k) \tag{2.71}$$

so that, through integration by parts to return to the strong form, the components differ from the completeness relation by the last summation term [8]. This difference alters only the boundary values of D^j_k as $P'_{n-1}(\xi_j) = 0$ except for ξ_0 and ξ_{n-1}.

2.5 Approximate and consistent treatments of nonlinear fluxes in DG schemes

This short study examines the importance of exact integrations of nonlinear fluxes when the DG method is applied to conservation laws where the flux $F^j = F^j(u)$ is a nonlinear function of the conserved variable u. The simplest of such is the inviscid Burgers' equation for the nonlinear advection of a scalar variable $u = u(x,t)$,

$$\partial_t u + \partial_x \Big(\frac{1}{2} u^2\Big) = 0. \tag{2.72}$$

In a DG discretization of the above, the unknown variable $u(x,t)$ is interpolated between a set of known coordinates $\{\xi_j\}_{j=0}^{n-1}$ per finite element m on interpolation polynomials $\ell_j(\xi)$,

$$u(x,t) = \bigoplus_m \sum_{j=0}^{n-1} u^{mj} \ell_j(\xi_m(x)). \tag{2.73}$$

The nodes ξ_j are generally taken as an n-point Gauss-Lobatto quadrature scheme for a polynomial representation of order $n-1$. For Legendre quadrature of weights w_j, for example,

$$\ell_j(\xi) = w_j\Big\{\sum_{s=0}^{n-1}\Big(s+\frac{1}{2}\Big)P_s(\xi_j)P_s(\xi) - \frac{n}{2}P_{n-1}(\xi_j)P_{n-1}(\xi)\Big\} \tag{2.74}$$

$$\xi_m(x) = \frac{2}{(\Delta x)_m}(x-\bar{x}_m) \tag{2.75}$$

with $P_s(\xi)$ the Legendre polynomial of order s and $\bar{x}_m$ the midpoint of the m'th element.

2.5.1 The standard flux discretization supposes a known flux function

In the standard discretization the flux function $F(u)$ is considered to an interpolation of a known function on the nodes ξ_j, resulting in an order $n-1$ polynomial representation

$$F(u) = \bigoplus_m \sum_j F^{mj}\ell_j(\xi_m(x)). \tag{2.76}$$

When both u and F are polynomials of order $n-1$ so interpolated the DG discretization is

$$\frac{du_{mj}}{dt} = \Upsilon^k_{mj}F_{mk} - \Xi^b_{mj}F^*_{mb} \tag{2.77}$$

where the flux divergence matrices follow from the Galerkin projections of u and F,

$$\Upsilon^k_j = \langle\ell_j|\ell^s\rangle^{-1}_{\Omega_m}\langle\ell'_s|\ell^k\rangle_{\Omega_m} = w_j\sum_{s=0}^{n-1}\Big(s+\frac{1}{2}\Big)P'_s(\xi_j)P_s(\xi_k), \tag{2.78}$$

$$\Xi^b_j = \langle\ell_j|\ell^s\rangle^{-1}_{\Omega_m}\langle\ell_s|\ell^b\rangle_{\partial\Omega_m} = \frac{1}{w_j}\delta_{jb} + \frac{n}{2}P_{n-1}(\xi_j)P_{n-1}(\xi_b). \tag{2.79}$$

In the standard application of the DG method, the nodal values of the known function $F(x)$ are approximated as the pointwise products of the actual polynomial values $u(x,t)$. For example, in the case of the quadratic flux in Burgers' equation

$$F(u) = \frac{1}{2}u^2 = \frac{1}{2}u^{mj}u^{nk}\ell_{mj}\ell_{nk} = \frac{1}{2}u^{mj}u^{mk}\ell_{mj}\ell_{mk} \tag{2.80}$$

$$\approx \frac{1}{2}(u^{mj})^2\ell_{mj}. \tag{2.81}$$

Thus the symmetric-in-(jk) coefficient matrix F^{mjk} of a matrix of polynomials $\ell_{mj}\ell_{mk}$ of order $2n-2$ is approximated as the point-wise coefficients F^{mj} of polynomials of order $n-1$.

2.5.2 Consistent divergence discretization of the quadratic flux function

If the approximation is carried out consistently and the flux coefficients taken in their matrix form, then the Galerkin projection results in the following matrices,

$$\text{Internal flux divergence } \langle \ell_j | \ell^s \rangle^{-1}_{\Omega_m} \langle \ell'_s | \ell^p \ell^q \rangle_{\Omega_m}, \tag{2.82}$$

$$\text{Boundary flux divergence } \langle \ell_j | \ell^s \rangle^{-1}_{\Omega_m} \langle \ell_s | \ell^p \ell^q \rangle_{\partial\Omega_m}. \tag{2.83}$$

To get an idea for the character of these matrices, consider the triple product integral

$$\langle \ell_s | \ell^p \ell^q \rangle_{\Omega_m} = w_s w_p w_q \sum_{x,y,z}^{n-1} \lambda_x \lambda_y \lambda_z P_x(\xi_s) P_y(\xi_p) P_z(\xi_q) \int_{-1}^{1} P_x(\xi) P_y(\xi) P_z(\xi) d\xi. \tag{2.84}$$

The Legendre triple product integral is known as the Wigner 3j-symbol

$$\int_{-1}^{1} P_x(\xi) P_y(\xi) P_z(\xi) d\xi = 2 \begin{pmatrix} x & y & z \\ 0 & 0 & 0 \end{pmatrix}^2 \tag{2.85}$$

from the study of the angular momentum of spherical systems. It is zero unless $|x - y| \leq z \leq x + y$ (*i.e.* x, y, and z can form a triangle) and the sum $x + y + z$ is even. Due to these symmetries many of the terms in the summation are zero.

Forms of the matrix operators

Despite the existence of the above formal analytic expression for the integral, it is not clear that the integral works out to a decent or intuitive solution as in the case of the simple formula for the weak form operator Υ^k_j. The matrix operator, which is a full matrix, can be computed exactly by a Gauss-Legendre quadrature of minimal order $\lceil 3n - 4 \rceil$,

$$\text{Internal flux divergence } Q^{pq}_{mj} \equiv \langle \ell_j | \ell^s \rangle^{-1}_{\Omega_m} \langle \ell'_s | \ell^p \ell^q \rangle_{\Omega_m}. \tag{2.86}$$

On the other hand, the boundary flux divergence operator is identical to the approximate form since the interpolation polynomials localize the integration onto the boundary as

$$\text{Boundary flux divergence } \langle \ell_j | \ell^s \rangle^{-1}_{\Omega} \langle \ell_s | \ell^p \ell^q \rangle_{\partial\Omega} = \langle \ell_j | \ell^s \rangle^{-1}_{\Omega} \delta^{pq}_s \delta^b_{pq} = \Xi^b_j. \tag{2.87}$$

Having defined this quadratic operator, the semi-discrete inviscid Burgers' equation is

$$\frac{du_{mj}}{dt} = J^n_m Q^{pq}_{nj}\left(\frac{1}{2}u_{np}u_{nq}\right) - J^n_m \Xi^b_{nj}\left(\frac{1}{2}u^2_{nb}\right)^* \tag{2.88}$$

where the quantity $\left(\frac{1}{2}u^2\right)^*$ is a numerical flux computed on an element interface, for example by the upwinding method.

2.5.3 Comparison of the approximate to consistently quadratic flux

Besides consistency, an important consideration in the viability of a numerical method is its computational cost. The approximate form of the flux costs $\mathcal{O}(n^2)$ operations per element to compute the internal flux divergence, while the consistent form costs $\mathcal{O}(n^4)$. Whether this is prohibitive or not depends on the resolution and polynomial order used for the method.

With the increased complexity of the tensor operation now known, it remains to see whether the consistent integration is worth it. To that end the inviscid Burgers' equation was solved with the initial condition $u(x,0) = \frac{1}{2}\sin(x)$ on a periodic domain of length $L = 2\pi$. Prior to the breaking time at $t = 2$, the exact solution of this nonlinear problem is

$$u(x,t) = \frac{1}{2}\sin(x - u(x,t)t). \tag{2.89}$$

This can be solved by Newton's method on a guess provided by the DG solution at a particular (x,t), as in Fig. 2.2. The problem was run to time $t = 1.5$ using the Shu-Osher SSPRK3 explicit time integrator with a sufficiently small Δt such that the error was spatial.

2.5.4 Numerical errors and conservation of energy

Figure 2.3 shows pointwise off-node errors on a higher-order GL node set comparing the aliased, or approximate flux, with the dealiased, or consistently-computed quadratic flux. Convergence was examined with an $n = 3$ (piecewise quadratic) basis set, with results shown below in Fig. 2.4. The principal result is that while quantities converge at the appropriate rate for the approximate flux, the result is significantly better for the consistently-computed flux. The difference between the methods depends on the relative importance of higher-order

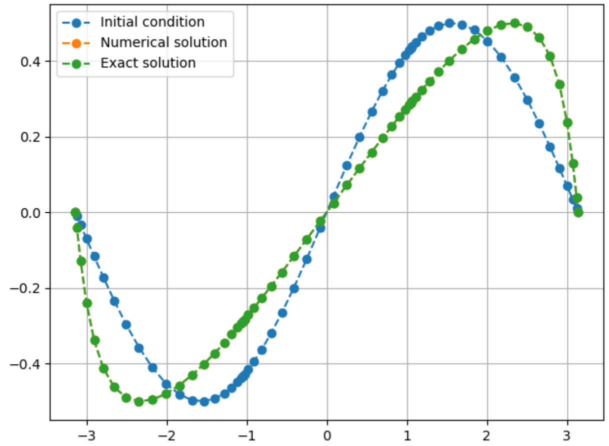

Figure 2.2: Initial condition with approximate and exact/numerical solutions to Burgers' equation for a three-element and twenty-point quadrature DG discretization. The numerical and exact solutions are indistinguishable at this scale.

terms; experiments with both high-order and highly resolved grids shows near identical errors and energy conservation, while high-order at low resolution shows a difference in energy conservation of up to 300 times.

2.5.5 Discretization of the kinetic equation with Lorentz force

This section discusses a method of DG discretization of velocity space when the momentum fluxes are due to forces of the form $\boldsymbol{E}+\boldsymbol{v}\times\boldsymbol{B}$. Consider the kinetic equation projected onto a truncated Fourier series. The Fourier coefficients $f_n(u,v,t)$ each satisfy

$$\partial_t f_n + ik_n u f_n + \partial_u(F_{x,n} + vF_{B,n}) + \partial_v(F_{y,n} - uF_{B,n}) = 0, \tag{2.90}$$

$$F_{x,n} \equiv \sigma(E_x * f)_n, \quad F_{y,n} \equiv \sigma(E_y * f)_n, \quad F_{B,n} \equiv \sigma(B * f)_n, \tag{2.91}$$

where $a * b$ is the convolution of a and b and $\sigma = q/|q|$. Let each velocity axis u and v be divided into finite elements, and let $f_n(u,v,t)$ be expanded onto a tensor product quadrature grid of the velocities, each with interpolation polynomial basis $\{\ell_i(\xi)\}$. In other words,

$$f_n(u,v) = \bigoplus_{p,q}\sum_{j,k} f_{n,pqjk}\ell^j(\xi(u)^p)\ell^k(\xi(v)^p) \tag{2.92}$$

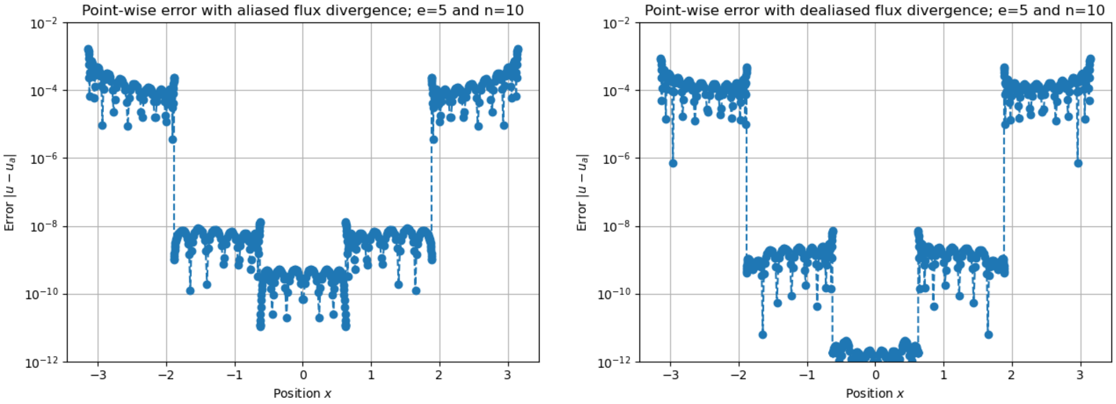

Figure 2.3: Pointwise errors at $n = 10$ and five elements, showing an improved solution when the flux is computed consistently (right) rather than approximately (left).

Performing the Galerkin projection suggests defining the operators

$$\Upsilon^j_r = \langle \ell_r|\ell^p\rangle^{-1}\langle \ell_p|(\ell')^j\rangle, \tag{2.93}$$

$$\mathbb{T}^k_s = \langle \ell_s|\ell^p\rangle^{-1}\langle \ell_p|x(\xi)\ell^k\rangle. \tag{2.94}$$

The operator Υ is a discretization of the flux divergence when the flux is a known function on the interpolation nodes. On the other hand, the operator $\mathbb{T}$ is needed whenever a term is linear in the coordinate x but does not appear inside a derivative. Terms linear in the velocity appear in Eq. 2.90 in two places: linear advection and the Lorentz force.

Neglecting to write the element index for clarity, the DG-discretization of Eq. 2.90 is

$$\begin{aligned}\frac{df_{n,rs}}{dt} = -ik_n\mathbb{T}^j_r f_{n,js} &+ \left\{\Upsilon^j_r(F_{x,n,js} + \mathbb{T}^k_s F_{B,n,jk}) - \Xi^j_r(F_{x,n} + vF_{B,n})^*_{n,js}\right\} + \\ &+ \left\{\Upsilon^k_s(F_{y,n,rk} - \mathbb{T}^j_r F_{B,n,jk}) - \Xi^k_s(F_{y,n} - uF_{B,n})^*_{n,rk}\right\}\end{aligned} \tag{2.95}$$

where Ξ^j_r is the boundary flux operator and F^* is a numerical flux. The net result is that the magnetic flux $F_{B,n} = \sigma(B * f)_n$ should be "preconditioned" by the operator $\mathbb{T}$. For example, if the term $v_s F_{B,js}$ is used instead of $\mathbb{T}^k_s F_{B,jk}$, then the momentum flux due to the magnetic field will be under-integrated in the Lobatto basis. However, this under-integration is minor and has been observed to not make a significant difference at high order.

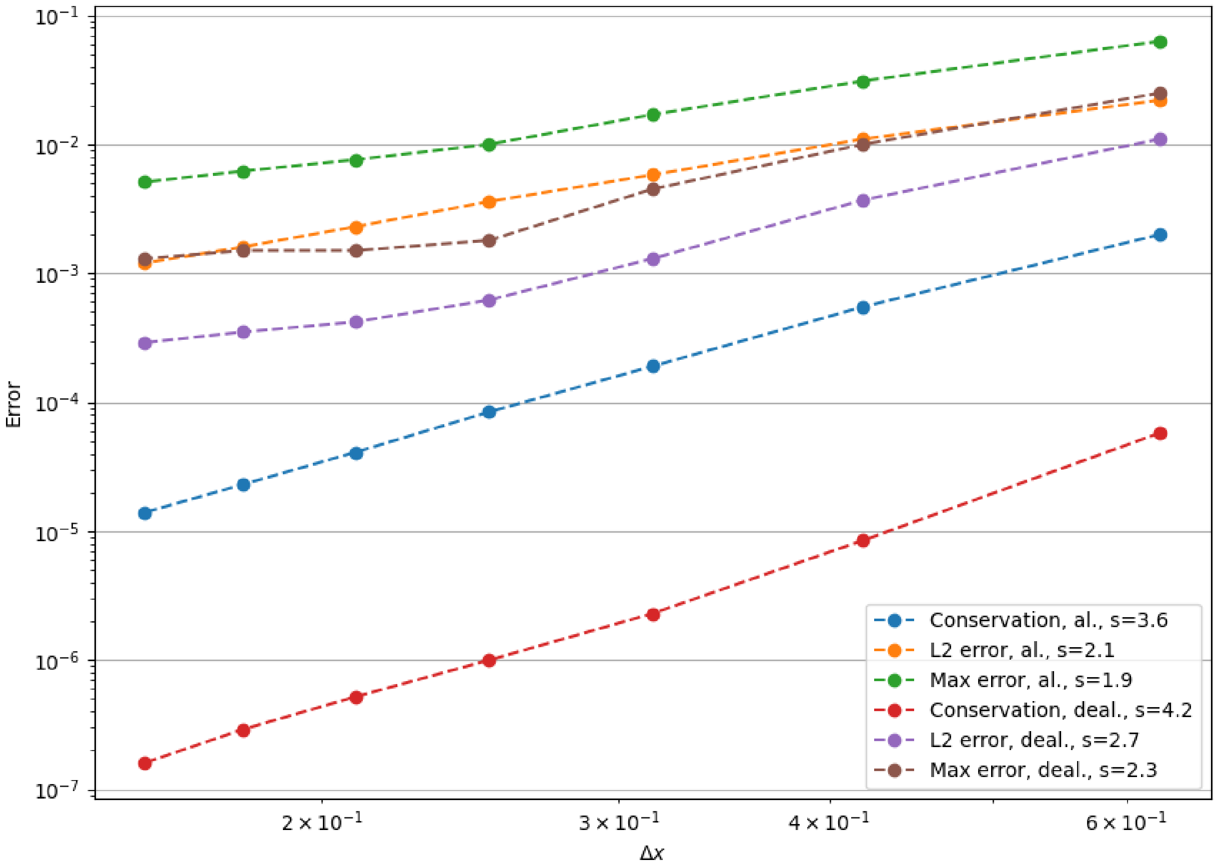

Figure 2.4: Convergence in energy conservation, L2 error, and max error for the "aliased" (approximated flux) with the "dealiased" (consistently computed flux) using an $n = 3$ basis set (piecewise quadratic polynomials). Using the consistent flux results in two orders of magnitude improvement in the conservation of energy, while the L2 error (a nonlinear quantity) is improved less than one order of magnitude. The quantity s means slope of the log-log line.

2.6 *Semi-implicit time integration for plasma kinetic equations*

Sections 2.1, 2.2, 2.3, and 2.4 presented numerical methods to discretize phase space where spatial dimensions are represented on a spectral basis (*i.e.* Fourier modes) and momental dimensions discretized with the discontinuous Galerkin method, a domain-decomposition technique. This section discusses a time-integration strategy for fast solutions of plasma kinetic equations, namely a semi-implicit integration to slow down the swiftest linear motions.

2.6.1 Time-step limitation of the kinetic equation

The kinetic equation in a phase space of one space and momentum dimension each is

$$\partial_t f + \partial_x(vf) + \sigma\partial_v(Ef) = 0 \tag{2.96}$$

with $\sigma = |q|/q$ the sign of the electric charge. The time-step Δt is limited by two factors: the maximum frequency of linear advection $\omega_a \equiv |kv|_\infty$ and the frequency of acceleration $\omega_f \equiv |E/\Delta v|_\infty$. Typically the time-step is limited by the phase fluid's spatial advection, $\Delta t \sim \omega_a^{-1}$, as the maximum velocity extent of the domain v_∞ conspires with good grid resolution k_∞ to require small Δt. Generally the spatial advection frequency is greater than field acceleration, $\omega_a \gg \omega_f$. However, limitation due to the electric field can occur in the saturated states of instabilities, or with small velocity-space elements. It would be useful to avoid resolving the maximum advection frequency, and retain only advections on scales of interest. This is possible using implicit time integration.

2.6.2 Mixed Fourier/DG phase space discretization

This section summarizes the discretization of the spatial and momental fluxes of Equation 2.96. Considering one periodic spatial dimension, the distribution function is expanded in Fourier series $f(x,v,t) = \sum_{n=-\infty}^{\infty} f_n(v,t)e^{ik_n x}$. Truncation at a maximum wavenumber k_n effects a Galerkin projection onto the Fourier basis with governing equations

$$\partial_t f_n + \partial_v F_n = -ik_n v f_n \tag{2.97}$$

with modal velocity flux $F_n(v, t) \equiv \sigma E * F$. Each equation for f_n is then discretized in v by the discontinuous Galerkin method into a weak-form system. The DG operator, capturing the momental flux F_n, is the difference in discretized internal and numerical flux divergence,

$$\mathcal{F}_{nmj} \equiv (\Upsilon F)_{nmj} - (\Xi F^*)_{nmj} \tag{2.98}$$

$$E_n \equiv -\sigma i k_n^{-1} \int_{-\infty}^{\infty} f_n dv \tag{2.99}$$

with Υ and Ξ the internal and numerical divergence operators. Explicitly, here the indices are ($n \sim$ Fourier mode), ($m \sim$ momental element), and ($j \sim$ elemental node). The flux F_n is computed pseudospectrally. Evidently the DG operation is *nonlinear* because the field equation is an integral of the distribution. The translation operator is discretized as

$$\mathbb{T}^k_{nmj} \equiv -ik_n\Big(\bar{v}_m I^k_j + J_m \langle \psi_j | \psi^s \rangle^{-1} \langle \xi \psi_s | \psi^k \rangle\Big) \tag{2.100}$$

with $\bar{v}_m$ the midpoint of the m'th element, J_m the element Jacobian, and ξ the reference element variable. Previously the spatial flux vf was slightly nonlinear, being the product of the distribution with a linear function. However, when represented in the weak form in this way the operation has become linear due to the integration, carried out in Eq. 2.100, which depends on an immutable coordinate. With all of this, the DG weak form is a sum of a nonlinear operation and a linear one,

$$\left(\frac{df}{dt}\right)_{nmj} = \mathcal{F}_{nmj} + \mathbb{T}^k_{nmj} f_{nmk}. \tag{2.101}$$

2.6.3 Semi-implicit time integration of the kinetic equation

Having reduced the kinetic equation to an ordinary differential equation consisting of the sum of a nonlinear and a linear operation, a time-stepping strategy can be chosen. Typical explicit schemes are the SSP-RK3 (Strong Stability-Preserving Runge-Kutta) and the AB3 (Adams-Bashforth) third-order methods. These explicit schemes suffer from time-step limitations according to the maximum frequencies discussed previously (i.e. $\Delta t \sim \min(\omega_a^{-1}, \omega_f^{-1})$). Yet the semi-discrete equation is the sum of a nonlinear and a linear function, suggesting two possibilities for time integration: (i) operator splitting and (ii) semi-implicit integration. Here the latter is investigated. Operating splitting is advantageous for multi-dimensional problems and discussed in a following section.

The usual semi-implicit time-integration strategy is to evolve the nonlinear terms explicitly but the linear terms implicitly [1]. The advantage of this is that the implicit solve is that only of a *linear system*, obviating the stiffness of linear terms but without any expensive nonlinear solves. A popular semi-implicit scheme is AB3 for $\mathcal{F}$ but Crank-Nicolson for $\mathbb{T}$:

$$\frac{f^{i+1}_{nmj} - f^{i}_{nmj}}{\Delta t} = \left\{\frac{23}{12}\mathcal{F}^{i}_{nmj} - \frac{4}{3}\mathcal{F}^{i-1}_{nmj} + \frac{5}{12}\mathcal{F}^{i-2}_{nmj}\right\} + \frac{\mathbb{T}^{k}_{nmj} f^{i+1}_{nmk} + \mathbb{T}^{k}_{nmj} f^{i}_{nmk}}{2} \tag{2.102}$$

also called the AB3CN method. Equation 2.102 is linear by design in f^{i+1}_{nmk}, so solving for it

$$f^{i+1}_{nmj} = (A_B^{-1})^{s}_{nmj}\Big(f^{i}_{nms} + \Delta t \mathcal{F}^{AB3}_{nms} + \frac{\Delta t}{2}\mathbb{T}^{k}_{nms} f^{i}_{nmk}\Big) \tag{2.103}$$

with the half-backward-advection-step inverse operator defined as

$$(A_B)^{k}_{nmj} \equiv I^{k}_{nmj} - \frac{\Delta t}{2}\mathbb{T}^{k}_{nmj} \tag{2.104}$$

and its inverse computed on one index only. This inverse operation can be thought of as computing a $j \times j$ inverse matrix for each pair (n, m) and can be computed by broadcasting using standard linear algebra libraries, *e.g.* `cupy.linalg.inv(A)` as shown in Fig. 2.5.

2.6.4 Beyond CFL-limited advection: operator splitting and fractional stepping

To conserve the distribution function and its functionals (such as momentum and energy) finite element schemes in phase space need to extend the maximum velocity boundary up to many thermal velocities. Explicit time-integration is then severely limited by the velocity ceiling even for long wavelengths according to the maximum advective frequency $|kv|_\infty$. In order to mitigate the curse of dimensionality time-advances beyond this limit are critical to continuum phase space treatments.

Section 2.6.3 presented a semi-implicit time-integration method to bypass this limitation by treating the spatial advective terms implicitly and the momentum flux due to fields explicitly. This section discusses a difficulty in the straight-forward extension of this idea to multi-dimensional advection, and proposes a time-integration method based on combining operator splitting (also called Strang splitting) with a fractional stepping algorithm. Operator splitting is used to separate quasilinear advection terms from truly nonlinear flux terms. The fractional stepping method is then used to simplify the implicit treatment of multi-dimensional advection.

Semi-implicit schemes for the multi-dimensional spectral kinetic equation

Consider the multi-dimensional collisionless kinetic equation,

$$\frac{\partial f}{\partial t} + \boldsymbol{v} \cdot \nabla_x f + \sigma \boldsymbol{F} \cdot \nabla_v f = 0 \tag{2.105}$$

where $\sigma = q/|q|$ is the sign of the charge and $\boldsymbol{F}$ is the self-consistent force field vector. Consider a two-dimensional problem expanded in spatial Fourier modes $(x, y) \to (k_n, k_m)$,

$$\frac{\partial f_{nm}}{\partial t} + ik_n u f_{nm} + ik_m v f_{nm} + \nabla_v \cdot (\boldsymbol{\mathcal{F}}_{nm}) = 0 \tag{2.106}$$

with $\boldsymbol{\mathcal{F}}_{nm}$ the vector of spectral momentum fluxes due to the fields $\boldsymbol{F}$. Now consider a finite element discretization of the velocity space $(u, v) \to (u_{jk}, v_{pq})$, with the (j, p) the element index and (k, q) the subelement index (collocation points or nodes). One obtains the semi-discrete equation as

$$\frac{df_{nmjkpq}}{dt} = \mathcal{N}_{nmjkpq}(f) + \mathcal{L}^{\ell r}_{nmjkpq} f_{nmj\ell pr} \tag{2.107}$$

where $\mathcal{N}$ represents the part of the discretized operator that is nonlinear in f and $\mathcal{L}$ the part of the semi-discrete operator linear in f. Originally the advection is quasilinear in f, but by defining an operator $\mathbb{T}$ by integrating the coordinates u or v over the basis functions ψ,

$$\mathbb{T}^{\ell}_{njk} \equiv -ik_n(\bar{v}_j I^{\ell}_k + J_m \langle \psi_k | \psi^s \rangle^{-1} \langle \xi \psi_s | \psi^{\ell} \rangle), \tag{2.108}$$

spectral advection is then represented by a linear operator defined as

$$\mathcal{L}^{\ell r}_{nmjkpq} f_{nmj\ell pr} \equiv \mathbb{T}^{\ell}_{njk} f_{nmj\ell pq} + \mathbb{T}^{r}_{mpq} f_{nmjkpr}. \tag{2.109}$$

Result of a naive semi-implicit time-integration algorithm

Consider a semi-implicit time discretization of Eq. 2.107 of time-step h as [1]

$$\frac{f^{n+1} - f^n}{h} = \mathcal{N}^E(f^n) + \mathcal{L}\frac{f^{n+1} + f^n}{2} \tag{2.110}$$

with $\mathcal{N}^E$ an explicit time-advance scheme of some order, such as SSP-RK3 or AB3. Then

$$f^{n+1} = \Big(I - \frac{h}{2}\mathcal{L}\Big)^{-1}\Big(\Big(I + \frac{h}{2}\mathcal{L}\Big)f^n + h\mathcal{N}^E(f^n)\Big). \tag{2.111}$$

Restoring all the discrete phase space indices, the half-backward advection linear operator is

$$(I - \frac{h}{2}\mathcal{L})^{\ell r}_{nmjkpq} \equiv I^{\ell}_{njk}I^{r}_{mpq} - \frac{h}{2}\mathbb{T}^{\ell}_{njk}I^{r}_{mpq} - \frac{h}{2}I^{\ell}_{njk}\mathbb{T}^{r}_{mpq}. \tag{2.112}$$

This operator consists of many $N^2 \times N^2$ matrices for each spectral pair (n, m) and element (j, p) (with elements of N collocation points). Its application is correspondingly more costly than the tensor product with many $N \times N$ matrices that arose in the one-dimensional semi-implicit treatment. It is advantageous to split the advection up step-by-step into a sequence of $\mathcal{O}(N^2)$ operations rather than one $\mathcal{O}(N^4)$ operation per element.

2.6.5 Second-order operator (Strang) splitting

Splitting an operation into sub-operations and applying the operators sequentially is called fractional stepping [1]. It works very well when the operators commute, which is the case for the advective operation $(\partial_t + \boldsymbol{v}\cdot\nabla_x)f = 0$ under consideration. However, the presence of the nonlinear term means that the operations *do not* commute if some part of $\mathcal{N}$ is applied at each sub-step. For this reason, the semi-discrete equation is first split into its linear and nonlinear parts using the method of operator (Strang) splitting.

When a differential equation can be represented as the sum of two operations,

$$\frac{df}{dt} = L_1 f + L_2 f \tag{2.113}$$

the splitting method considers separately the two equations

$$\frac{df}{dt} = L_1 f, \tag{2.114}$$
$$\frac{df}{dt} = L_2 f. \tag{2.115}$$

The complete solution and solutions of the separate problems are formally

$$\begin{aligned} f^{n+1} &= \exp\Big(\int_{t_n}^{t_{n+1}} (L_1 + L_2) dt'\Big) f^n \approx \exp((L_1 + L_2)h) f^n, \\ f^{n+1} &= \exp\Big(\int_{t_n}^{t_{n+1}} L_i dt'\Big) f^n \approx \exp(L_i h) f^n. \end{aligned} \tag{2.116}$$

Consider the two expansions

$$\begin{aligned} \exp(h(L_1 + L_2)) &= I + h(L_1 + L_2) + \frac{h^2}{2}(L_1 + L_2)^2 + \cdots \\ &= I + h(L_1 + L_2) + \frac{h^2}{2}(L_1^2 + L_1 L_2 + L_2 L_1 + L_2^2) + \cdots \\ \exp(hL_1)\exp(hL_2) &= (I + hL_1 + \frac{h^2}{2}L_1^2 + \cdots)(I + hL_2 + \frac{h^2}{2}L_2^2 + \cdots) \\ &= I + h(L_1 + L_2) + \frac{h^2}{2}(L_1^2 + 2L_1 L_2 + L_2^2) + \cdots \end{aligned} \tag{2.117}$$

Examining through second-order, the difference is

$$\exp(h(L_1 + L_2)) - \exp(hL_1)\exp(hL_2) = \frac{h^2}{2}(L_2 L_1 - L_1 L_2) + \mathcal{O}(h^3) \tag{2.118}$$

or is inaccurate through the commutator $[L_1, L_2]$. The second-order splitting method resolves this by alternating the formal solution of the two equations [16, 17],

$$\exp(h(L_1 + L_2)) = \exp\Big(\frac{h}{2}L_1\Big)\exp(hL_2)\exp\Big(\frac{h}{2}L_1\Big) + \mathcal{O}(h^3). \tag{2.119}$$

Note that each application of $\exp(hL)$ is really the formal solution of the split equations, each approximated as a linear problem.

Operator splitting for the spectral kinetic equation

Equation 2.107 writes the semi-discrete Vlasov equation as the sum of a linear and a nonlinear operation. Then consider the two operations to be separate problems as

$$\begin{aligned} \frac{df}{dt} &= \mathcal{N}f \\ \frac{df}{dt} &= \mathcal{L}f \end{aligned} \tag{2.120}$$

and apply the second-order operator splitting method as

$$f^{n+1} = \mathcal{S}[\mathcal{L}]^{h/2}\mathcal{S}[\mathcal{N}]^{h}\mathcal{S}[\mathcal{L}]^{h/2}f^{n} \tag{2.121}$$

where $\mathcal{S}[\cdot]$ represents evaluation of operator $[\cdot]$ by any method of approximation. Observe that the operator $\mathcal{S}[\mathcal{N}]$ is *evaluated* at f^n but *applied* following a half-step of advection.

Fractional stepping with the advection operator

The operation $\mathcal{S}[\mathcal{N}]$, when treated fully explicitly, is obtained by the DG method. Because f_{nm} is represented with a tensor-product basis in velocity space (u, v) the calculation of the semi-discrete equation consists of a sequence of $\mathcal{O}(N)$ operations by subsequent application of the flux matrices Υ and Ξ in each direction. When treated explicitly the advection operator $\mathcal{S}[\mathcal{L}]$ has the same property, yet when treated implicitly becomes an $\mathcal{O}(N^2)$ operation due to the inversion in Eq. 2.112. However, the linear advection is itself the sum of two operations,

$$\frac{df}{dt} = \mathcal{L}_u f + \mathcal{L}_v f \tag{2.122}$$

where the u- and v-advection operations $\mathcal{L}_u$, $\mathcal{L}_v$ commute. Evolving each separately by an implicit Crank-Nicolson advance maintains a second-order advection [1]

$$\left(\mathcal{S}[\mathcal{L}]^h\right)^{\ell r}_{nmjkpq} = \left(I^{\ell}_{njk} - \frac{h}{2}\mathbb{T}^{\ell}_{njk}\right)^{-1}\left(I^{\ell}_{njk} + \frac{h}{2}\mathbb{T}^{\ell}_{njk}\right)\left(I^{r}_{mpq} - \frac{h}{2}\mathbb{T}^{r}_{mpq}\right)^{-1}\left(I^{r}_{mpq} + \frac{h}{2}\mathbb{T}^{r}_{mpq}\right) \tag{2.123}$$

while dividing the $\mathcal{O}(N^2)$ operation per cell into two $\mathcal{O}(N)$ operations per cell. While the split advection is generally less accurate than the unsplit advection, both are $\mathcal{O}(h^2)$ accurate provided the operations commute.

The connection of Crank-Nicolson with rational (Padé) approximations

Finally, it's worth relating the Crank-Nicolson update to the notion of formal exponential solutions. The Euler forward or backward method is the first-order series

$$\exp(hL) = I + hL + \mathcal{O}(h^2) \tag{2.124}$$

while the first rational approximation, the "$[1,1]$ Padé approximant", is [1]

$$\begin{aligned} \exp(hL) &\approx (I - h/2L)^{-1}(I + h/2L) \\ &= I + hL + \frac{h^2}{2}L^2 + \mathcal{O}(h^3) \end{aligned} \tag{2.125}$$

shows it to agree with the non-rational Taylor series through the first three terms. This is the definition of a Pade approximation. Yet the largest eigenvalues of L are limited to the chosen time-advance, granting implicit stability compared to a forward Euler advance.

2.7 Techniques for efficient parallel implementation

This section details an efficient implementation of the DG method using GPU-accelerated Python libraries for CUDA devices. Any language which can efficiently compute tensor products of large arrays can implement DG well; this example utilizes Python and the CuPy library [18]. This library mimics NumPy data array structures and may be programmed in only a few lines of code to launch optimized kernels at execution for the tensor products appearing in the DG semi-discrete equations. Whichever library is used, its operations should occur entirely on device memory so that CPU-GPU transfers are only needed to save data. Such a GPU-centered DG implementation is shown schematically in Fig 2.6. Finally, the DG basis matrices are calculated via the Eqs. 2.67 and 2.70 in Section 2.4.4 using i) a scientific library with Legendre polynomials such as SciPy, and ii) tables of Legendre-Gauss-Lobatto quadrature nodes and weights available online, for example at [19].

2.7.1 Evaluating the semi-discrete equation with tensor products

As discussed in Section 2.3, when solving the semi-discrete equation on an orthogonal grid one need only contract the flux $F^{\alpha,\beta,j}$ of each direction j with its corresponding sub-element index. With a NumPy-like data array structure this is accomplished by structuring the array data $u^{\alpha,\beta}$ by its natural tensor-product structure. As in Fig. 2.1, each pair of indices for elements α_j and nodes β_j corresponds to the direction j, so a natural array ordering is $\mathtt{u}[\alpha_0,\,\beta_0,\,\alpha_1,\,\beta_1,\,\cdots,\,\alpha_{d-1},\,\beta_{d-1}]$ and fluxes $F^{\alpha,\beta,j} = F^j(u)$ index in the same manner per dimension j.

Structuring the data array by both element and sub-element indices allows the semi-discrete equation to be elegantly programmed using GPU-accelerated tensor product operations such as `cupy.tensordot(a, b, axes=)`, which compiles a just-in-time GPU kernel to compute a tensor product with contraction on specified axes like NumPy's `tensordot` function. For example, consider evaluating the internal flux product $\Upsilon^{\beta}_{\gamma,j}F^{\alpha,\gamma,j}$ in the DG weak-form of Eqn. 2.28. As the product decouples in an orthogonal discretization (Eqn. 2.34) it may be computed as a sum of tensor products for each direction using the `basis_product` function,

```
def basis_product(flux, basis_matrix, axis, permutation):
    return cupy.transpose(cupy.tensordot(flux, basis_matrix,
                                         axes=([axis], [0])), axes=permutation)
```

where `axis` gives the sub-element index of the direction of flux, and the function `transpose` returns a view to the original index order according to the tuple `permutation` as `tensordot` concatenates the tensor indices remaining after contraction of the specified axes.

Computing numerical fluxes

The function `basis_product` is also used to globally compute the numerical flux product $\Xi^{\beta}_{\gamma,j}\mathcal{F}^{\alpha,\gamma,j}$, by first arranging a numerical flux array $\mathcal{F}^{\alpha,\gamma,j}$ according to the tensor-product index ordering. The form of the function $\mathcal{F}$ depends on the chosen numerical flux scheme.

The upwind method, where $\mathcal{F}$ is a function of only one side of the interface, is well-suited for hyperbolic problems as it solves the underlying interface, or Riemann, problem [20]. As a unidirectional numerical flux the upwind method is also simple to adapt for the alternating fluxes used for parabolic problems [21].

The idea behind upwind flux is for information to flow across an element's boundaries in accordance with the PDE's dispersion relation. For example, in the problem $u_t + Vu_x = 0$ the dispersion relation is $\omega - Vk = 0$ and information flows to the right. Therefore information should be sent from left to right, and numerical flux would always be chosen as depending on values from the left.

Let R, L stand for right and left sides of an interface. Define auxiliaries $a^R = \max(a, 0)$ and $a^L = \min(a, 0)$ so the upwind flux for $F = au$ with speed a is

$$\mathcal{F}(u^R, u^L) = a^R u^L + a^L u^R. \tag{2.126}$$

```python
def adams_bashforth(self, distribution, elliptic, grid, prev_fluxes):
    # Compute Poisson constraint
    elliptic.poisson_solve_single_species(distribution=distribution, grid=grid)
    # Compute velocity flux
    self.flux.semi_discrete_rhs(distribution=distribution, elliptic=elliptic, grid=grid)
    # Update distribution according to explicit treatment of velocity flux and crank-nicholson for advection
    distribution.arr += self.dt * ((23 / 12 * self.flux.output.arr -
                                    4 / 3 * prev_fluxes[0] +
                                    5 / 12 * prev_fluxes[1]) +
                                   0.5 * self.flux.source_term_lgl_no_arr(distribution_arr=distribution.arr,
                                                                          grid=grid))
    # Do inverse half backward advection step
    distribution.arr = cp.einsum('nmjk,nmk->nmj', self.inv_backward_advection, distribution.arr)
    return [self.flux.output.arr, prev_fluxes[0]]

def build_advection_matrix(self, grid):
    """ Construct the global backward advection matrix """
    backward_advection_operator = (cp.eye(grid.v.order)[None, None, :, :] -
                                   0.5 * self.dt * -1j * grid.x.device_wavenumbers[:, None, None, None] *
                                   grid.v.translation_matrix[None, :, :, :])
    self.inv_backward_advection = cp.linalg.inv(backward_advection_operator)
```

Figure 2.5: Python implementation of a semi-implicit time advance of the kinetic equation.

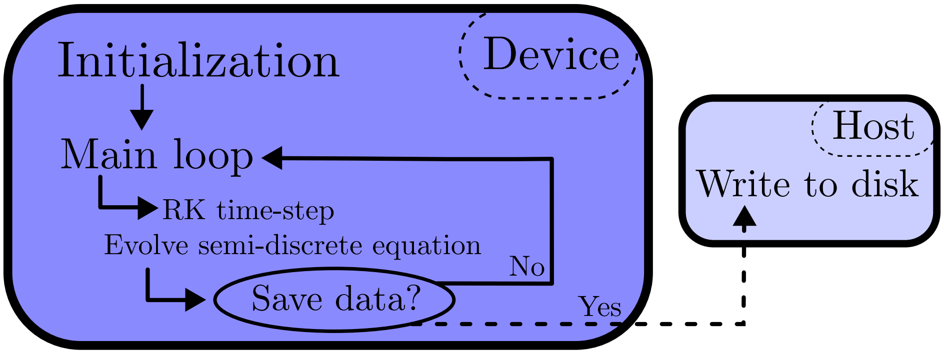

Figure 2.6: For performance of a parallelized DG implementation it's critical that all operations in the main time-stepping loop occur on the device (GPU). Device-host memory transfer should be minimized to the greatest extent possible. Transferring the array is only necessary at whichever time increments data is to be saved to the disk.

Chapter 3

UNMAGNETIZED ELECTROSTATIC MODES

3.1 Introduction to linear plasma kinetic theory

The fluctuations of a medium are inherently related to its energy transport and dissipation, *e.g.* through the well-known fluctuation-dissipation theorem, and to leading-order in amplitudes the fluctuations correspond with the linear modes. Therefore linear analysis of the coupled kinetic and field equations is essential to an understanding of the transport and dissipation of energy in a plasma. The vibrational modes and instabilities discovered through linear analysis give insight into the nature of a plasma's dissipative processes.

Analysis of linearized equations is important in just about every engineering discipline but there is a particular subtlety in plasma physics which deserves some commentary. Wave functions are often thought of as fluctuations in the three dimensions of spatial perception. However, plasma is composed of a distribution of relatively independent populations coupled to the lowest order through mean-field interactions. As a consequence the plasma fluctuates in a higher-dimensional *phase space*, while the electromagnetic field fluctuates in configuration space. Observable fluctuations are projections, or shadows, of the phase space fluctuation.

The relative momenta of the distinct parts of this distribution are understood geometrically by intertwining the intuitive spatial coordinates with the relevant coordinates of momentum. Momentum is initially understood as a vector originating from a point in space but a geometric space called momentum-space (or velocity-space) is generated by considering the coordinates of all the possible momentum vectors originating from that point. The union of spatial and momentum coordinates into one *phase space* is called "symplectization".

The simplest problem in kinetic plasma theory is for electrostatic modes in unmagnetized plasma and may be termed the one-dimensional scalar problem. The first two parts of this section consider the eigenvalue problem ($t \in (-\infty, \infty)$) and the initial-value problem ($t \in [0, \infty)$) for these electrostatic modes in a detailed manner that builds on top of standard textbook treatments of the problem. It is useful to work this theory out in detail in order to build intuition for the electromagnetic and magnetized problems of the latter sections where propagation of the initial data is algebraically cumbersome and a "quasi-analysis" is adopted for simplicity where the dispersion function, defined in the upper-half complex frequency plane, is analytically-continued to the lower-half plane, and damped modes are understood to not be true eigenfunctions. To reiterate, this intuition is that only instabilities represent normal (orthogonal) modes while dissipative modes, which appear only in the analytically continued dispersion function for reasons of causality, are composed of a sum of non-mutually orthogonal transient modes.

3.1.1 The eigenvalue problem for electrostatic modes in unmagnetized plasma

The study of eigenfunctions of collisionless and collisional plasma kinetic equations has a long history. Vlasov was the first to suggest a method to estimate the plasma oscillation frequencies by prescribing that the principal value be taken at the resonant velocity in the dispersion function. Bohm and Gross [22] side-stepped the resonant term by considering high-enough phase velocities that the distribution function was effectively zero there where the pole occurs. Following this, Landau [23] formally solved the linearized initial-value problem for Vlasov-Poisson dynamics using the Laplace transform method, discovering a discrete set of solutions for the Maxwellian plasma, with a potential damping in time. This collisionless decay phenomenon is called Landau damping.

Shortly after, van Kampen [24] and soon Case [25] considered the formal eigenvalue problem for the linearized kinetic equation. They discovered that the eigenfunctions of the linearized system are in fact distributions, or generalized functions. This is physically acceptable from the viewpoint of observables, or moments of the distribution function. Later work considered the addition of weak dissipation to the collisionless Vlasov equation, such as Lenard and Bernstein's simple drag-like operator [26]. Authors found numerically [27] and analytically [28] that as dissipation tended to zero, the system eigenfunctions, or collisional van Kampen modes, converged to the Landau modes rather than the collisionless eigenfunctions. This result suggests that, as dissipation introduces a singular perturbation to the collisionless dynamics, the Landau modes are in fact those observed in experiments. More recent work has numerically confirmed the limit of the collisonal eigenfunctions to the Landau modes [29].

It is significant that dissipation eliminates the continuous spectrum of the linearized operator, as numerical discretization schemes are almost guaranteed to be dissipative. However, it is still worthwhile to consider the formal eigenvalue problem as such a study sheds light on important subtleties. For example, one discovers that unstable Landau modes occur as the discrete part of the van Kampen spectrum. Therefore, unstable Landau eigenfunctions are in fact normal modes. In contrast, the infinite discrete spectrum of Landau damped modes are not orthogonal to one another. As previous notes discuss Landau's method, these notes summarize the Case-van Kampen modes and consider the role of dissipative terms in the kinetic equation.

The eigenvalue problem for linearized Vlasov-Poisson dynamics

Consider the normalized Vlasov-Poisson system for electron dynamics, given by the equations

$$\frac{\partial f}{\partial t} + v\frac{\partial f}{\partial x} + \frac{\partial \varphi}{\partial x}\frac{\partial f}{\partial v} = 0, \tag{3.1}$$

$$\frac{d^2\varphi}{dx^2} = \int_{-\infty}^{\infty} f dv - 1. \tag{3.2}$$

Linearization of the equations about a uniform background yields

$$\frac{\partial f_1}{\partial t} + v\frac{\partial f_1}{\partial x} + \frac{\partial \varphi}{\partial x}\frac{\partial f_0}{\partial v} = 0, \tag{3.3}$$

$$\frac{d^2\varphi}{dx^2} = \int_{-\infty}^{\infty} f_1 dv. \tag{3.4}$$

Fourier transforming the system in x and combining the equations yields the integral equation

$$\frac{\partial f_1}{\partial t} + ikvf_1 - ikF(v)\int_{-\infty}^{\infty} f_1(v')dv' = 0 \tag{3.5}$$

where $F(v) \equiv \zeta_p^2 \frac{\partial f_0}{\partial v}$. Following van Kampen, seek temporal modes $f_1 \sim e^{-i\omega t}$. Then

$$\zeta f_1 = vf_1 - F(v)\int_{-\infty}^{\infty} f_1(v')dv' \tag{3.6}$$

where $\zeta = \frac{\omega}{k}$ is the phase velocity. Equation 3.6 is an operator equation in eigenvalue form $\mathbb{V}f = \lambda f$ for the linearized Vlasov-Poisson operator defined as

$$\mathbb{V}f \equiv vf - F(v)\int_{-\infty}^{\infty} f(v')dv'. \tag{3.7}$$

Observe that $\mathbb{V}$ is not a differential operator but an integral operator. Further the eigenvalue problem depends, of course, on the background distribution $F(v) = \zeta_p^2 \partial_v f_0$.

Kinetic eigenfunctions: the Case-van Kampen modes

Van Kampen observed that the general solution of the operator equation was of the form

$$g_\zeta(v) = F(v)\Big(\mathcal{P}\frac{1}{v-\zeta} + \lambda(\zeta)\delta(v-\zeta)\Big) \tag{3.8}$$

and consists of generalized functions, where $\lambda(\zeta)$ may be specified by the normalization

$$\int_{-\infty}^{\infty} g_\zeta(v')dv' = 1 \qquad \Longrightarrow \qquad F(\zeta)\lambda(\zeta) = 1 - \mathcal{P}\int_{-\infty}^{\infty}\frac{F(v')}{v'-\zeta}dv'. \tag{3.9}$$

To verify this solution, consider the left and right sides of $(v-\zeta)f = F(v)\int_{-\infty}^{\infty} f dv'$:

$$\text{L:}\quad (v-\zeta)g_\zeta(v) = F(v) + F(v)\lambda(\zeta)(\zeta - v)\delta(\zeta - v) = F(v), \tag{3.10}$$

$$\text{R:}\quad F(v)\int_{-\infty}^{\infty} g_\zeta(v')dv' = F(v)\Big(\mathcal{P}\int_{-\infty}^{\infty}\frac{F(v')}{v'-\zeta}dv' + \Big[1 - \mathcal{P}\int_{-\infty}^{\infty}\frac{F(v')}{v'-\zeta}dv'\Big]\Big) = F(v), \tag{3.11}$$

showing equality by using $x\delta(x) = 0$. It was later shown by Case [25] that these functions are orthogonal and complete for functions on $\mathbb{R}$, in terms of the adjoint problem

$$\widetilde{\mathbb{V}}f = vf - \int_{-\infty}^{\infty} F(v')f(v')dv', \tag{3.12}$$

$$\widetilde{g}_\zeta(v) = \mathcal{P}\frac{1}{v-\zeta} + \lambda(\zeta)\delta(v-\zeta). \tag{3.13}$$

The continuous spectrum: Ballistic modes of real phase velocity ζ

Therefore, for each $\zeta \in \mathbb{R}$ there is an associated singular eigenfunction, and the operator $\mathbb{V}$ has an essential spectrum for the whole real axis of phase velocities. The continuous spectrum is due to the translation operator $\mathbb{T}f \equiv vf$ [29]. These singular eigenmodes are physically meaningful as only the observables (moments) of distributions are field sources.

A single van Kampen mode represents a purely ballistic motion. A perturbation to the distribution function of the form $f_1(v)$, without spatial structure, propagates without any interaction as there is no associated field. As they are a complete system of orthogonal functions they encode general perturbations such as the often-used plane wave $f_1 = e^{ikx}e^{-v^2}$.

The discrete spectrum: Unstable modes for which $\lambda = 0$

It is possible for the delta function scalar λ to vanish when ζ is a complex number. In order for this to occur, ζ must satisfy the dispersion relation

$$1 + \int_{-\infty}^{\infty} \frac{1}{v-\zeta}\frac{\partial f_0}{\partial v} dv = 0, \quad \mathrm{Im}(\zeta) \neq 0 \tag{3.14}$$

where the integral is *not* analytically continued into the lower half-plane. Note that the dispersion relation of Eq. 3.14 coincides with that obtained by the Landau contour only for unstable modes. When ζ_i is a simple root of Eq. 3.14, the van Kampen eigenmodes are analytic functions of the form

$$g_i(v) = \frac{F(v)}{v-\zeta_i} \qquad \Longrightarrow \qquad g_i(x,v,t) = \frac{e^{i(kx-\omega_i t)}}{v-\zeta_i}\frac{\partial f_0}{\partial v} \tag{3.15}$$

as the principal value sign is no longer needed. These discrete eigenfunctions represent kinetic instabilities and carry over to the initial-value problem.

Expansion in van Kampen modes

Expansion in the van Kampen modes of any zero-order distribution $f_0(v)$ is possible. Considering for simplicity the case of a stable $f_0(v)$ (no discrete spectrum) the expansion is

$$f(v) = \int_{-\infty}^{\infty} C(\zeta) g_\zeta(v) d\zeta \tag{3.16}$$

in terms of the spectrum $C(\zeta)$ of f in the van Kampen modes $g_\zeta(v)$. To invert the expansion, substitution of the eigenfunctions $g_\zeta(v)$ yields an integral equation to solve,

$$f(v) = F(v)\Big(\mathcal{P}\int_{-\infty}^{\infty} \frac{C(\zeta)}{\zeta - v} d\zeta + \lambda(v)C(v)\Big). \tag{3.17}$$

Equation 3.17 is called a singular integral equation for the unknown function $C(\zeta)$.

Interlude: the Riemann-Hilbert problem and the Hilbert transform

The solution of singular integral equations is the topic of what are called Riemann-Hilbert problems. In this case, one must consider the Riemann-Hilbert problem for the real line $\mathbb{R}$. The idea is to identify two functions g^+ and g^-, respectively holomorphic in the upper and lower half-planes, such that the difference of their limits as $x \to 0$ from above and below the real axis is equal to a given function $g(x)$, i.e. g^+ and g^- solve

$$g(x) = g^+ - g^-. \tag{3.18}$$

Fortunately, the Riemann-Hilbert problem on the real line is solved by a well-known operation in signal processing called the Hilbert transform, defined as

$$g^*(y) = \frac{1}{\pi}\mathcal{P}\int_{-\infty}^{\infty} \frac{g(x)}{x - y} dx. \tag{3.19}$$

An important theorem states that if g^+, g^- solve the Riemann-Hilbert problem of $g(x)$, then

$$ig^* = g^+ + g^- \tag{3.20}$$

is the Hilbert transform of g. In the case of the real line, the functions g^+ and g^- are the one-sided Fourier transforms of positive and negative frequency content, respectively [30].

Solution of the singular integral equation

In terms of the Hilbert transform, the integral equation may be written

$$f(v) = \pi F(v)C^*(v) + F(v)\lambda(v)C(v). \tag{3.21}$$

Further, by the normalization condition $F\lambda = 1 + \pi F^*$. Hence,

$$f(v) = \pi F C^* + \pi F^* C + C. \tag{3.22}$$

Now splitting into the components of the Riemann-Hilbert problem, one finds

$$f^+ - f^- = C^+(1 + 2\pi i F^+) - C^-(1 + 2\pi i F^-). \tag{3.23}$$

Thus, the function $C(\zeta)$ is reconstructed in terms of the positive and negative frequency components of the function to be represented,

$$C(\zeta) = \frac{f^+}{1 + 2\pi i F^+} - \frac{f^-}{1 + 2\pi i F^-}. \tag{3.24}$$

Simplifying the van-Kampen modes

The above summary uses a mixture of the notation used by van Kampen and Case in their separate work [24, 25]. On the other hand, another instructive form of the eigenfunctions can be written. For this, define Vlasov's dielectric function as

$$\varepsilon_V(k, \zeta) \equiv 1 - \zeta_p^2 \mathcal{P} \int_{-\infty}^{\infty} \frac{1}{v - \zeta} \frac{\partial f_0}{\partial v} \tag{3.25}$$

where $\zeta_p = \omega_p / k$ is the plasma phase velocity. The distributional part of the eigenfunction accounts for the free transport of particles. However, by requiring that the eigenfunction be a distribution ($\int_{-\infty}^{\infty} g_\zeta(v) dv = 1$), the constant λ is related to the plasma dielectric as

$$\frac{\partial f_0}{\partial v} \lambda = \varepsilon_P. \tag{3.26}$$

Therefore, the van Kampen mode can be written succinctly as

$$g_\zeta(v) = \zeta_p^2 \mathcal{P}\Big(\frac{1}{v - \zeta}\Big) \frac{\partial f_0}{\partial v} + \varepsilon_V(k, \zeta) \delta(v - \zeta). \tag{3.27}$$

Critically, this definition requires that the Landau contour not be used for integration of Eq. 3.25. This shows that the weighting of the singular part of the van Kampen mode is Vlasov's dielectric function evaluated at complex ζ. Vlasov's dielectric function is a non-analytic function with a branch cut along the real axis.

3.1.2 Dissipation as a singular perturbation of the collisionless problem

The addition of dissipation (collision models) changes the eigenfunctions from their collisionless forms. This has been shown with the simplest linear Fokker-Planck type operators, in the plasma literature called Lenard-Bernstein operators [27, 28, 29]. In the limit as $\nu \to 0^+$ the resulting damped eigenfunctions are *of the Landau type*, as the dissipation acts like a singular perturbation. Thus, the singular eigenfunctions of the preceding analysis are a purely collisionless phenomenon. The following considers an analysis of this weak dissipation.

Models of velocity-space diffusion

Coulomb collisions and other forms of direct interaction between plasma constituents lead to velocity space diffusion. These effects can be modeled using a Fokker-Planck operator,

$$\mathcal{C}[f] = \frac{\partial}{\partial v}\Big(\langle \Delta v\rangle f\Big) + \frac{\partial^2}{\partial v^2}\Big(\langle(\Delta v)^2\rangle f\Big). \tag{3.28}$$

One of the simplest such diffusion operators is known as the Lenard-Bernstein type [26],

$$\mathcal{C}_{LB}[f] = \nu\frac{\partial}{\partial v}\Big(vf + v_0^2\frac{\partial f}{\partial v}\Big) = \nu\frac{\partial}{\partial v}\Big(vf\Big) + \nu v_0^2\frac{\partial^2 f}{\partial v^2} \tag{3.29}$$

in terms of two constants ν, v_0. Physically, this operator states that particles experience a drag proportional to their velocity and a uniform diffusion in velocity. While very simple mathematically, it is a far cry from accurate descriptions such as the Lenard-Balescu operator. Nevertheless, the Lenard-Bernstein form is often used for analytical studies as it has the property that, if the constant $v_0 = 1$, its Hermite transform scales each mode uniformly,

$$f(v) = \sum_{n=0}^{\infty} c_n h_n(v) \implies \mathcal{C}_{LB}[f] = -\nu\sum_{n=0}^{\infty} c_n h_n(v). \tag{3.30}$$

Other choices of constant v_0 pass information between Hermite modes. To summarize, the linearized Vlasov-Poisson system with Lenard-Bernstein's dissipation model is

$$\frac{\partial f_1}{\partial t} + v\frac{\partial f_1}{\partial x} + \frac{\partial \varphi}{\partial x}\frac{\partial f_0}{\partial v} = \nu\frac{\partial}{\partial v}\Big(vf + v_0^2\frac{\partial f}{\partial v}\Big), \tag{3.31}$$

$$\frac{d^2\varphi}{dx^2} = \int_{-\infty}^{\infty} f_1 dv. \tag{3.32}$$

Uniform velocity-space diffusion and its influence on ballistic modes

As a simplest first case, consider a uniform diffusion without any spatial perturbation,

$$\frac{\partial f_1}{\partial t} + v\frac{\partial f_1}{\partial x} = \nu\frac{\partial^2 f_1}{\partial v^2}. \tag{3.33}$$

In this case, the spatiotemporal Fourier-transform results in the differential equation

$$-\zeta f_1 + v f_1 = -i\mu\frac{d^2 f}{dv^2} \tag{3.34}$$

where $\mu = \nu/k$. Rearranging, one has the second-order ordinary differential equation

$$\frac{d^2 f}{dv^2} - i\frac{v-\zeta}{\mu}f = 0. \tag{3.35}$$

Changing variable to $x = \frac{v-\zeta}{i\mu}$ results in a scaled Airy's equation,

$$\frac{d^2 f}{dx^2} - \mu^2 x f = 0. \tag{3.36}$$

Its general solution is expressed as a linear combination of Airy functions, an important family of wave functions exhibiting interference effects. The boundary conditions to be imposed are that $\lim_{|v|\to\infty} f(v) \to 0$ and $\int_{-\infty}^{\infty} f(v)dv = 1$. Due to the Stokes phenomenon, it is a complicated mathematical exercise to get the phases right in the appropriate combination of Airy functions. However, the important point is that the eigenfunctions are analytic and the spectrum of the operator is continuous. Pure velocity-space diffusion smoothes out the singular free-streaming van Kampen modes into analytic functions.

Regularity of the eigenfunctions under uniform dissipation

In the limit $\mu \to 0^+$, the Airy-like eigenfunctions will deform regularly into the singular van Kampen form. To see this, consider the velocity-space Fourier transform of Eq. 3.34,

$$\frac{d\widetilde{f}}{dq} + (\mu q^2 - i\zeta)\widetilde{f} = 0 \qquad \Longrightarrow \qquad \widetilde{f}(q) = Ce^{-\mu q^3/3}e^{iq\zeta}. \tag{3.37}$$

It is clear that as $\mu \to 0^+$, the eigenfunction deforms smoothly into $\widetilde{f}(q) = Ce^{iq\zeta}$, whose inverse transform is the distribution $C\delta(v-\zeta)$. Thus, pure velocity-space diffusion constitutes a regular perturbation of the linear transport equation's spectrum.

To consider the role of the electrostatic dynamics, note that the effect of incorporating the reaction on the background distribution results in the linear integral equation

$$-\zeta f + vf - F(v)\int_{-\infty}^{\infty} f(v')dv' = -i\mu\frac{d^2 f}{dv^2}. \tag{3.38}$$

Its velocity-space Fourier transform results in an inhomogeneous first-order ODE

$$\frac{d\widetilde{f}}{dq} + (\mu q^2 - i\zeta)\widetilde{f} = -i\widetilde{f}(0)\widetilde{F}(q). \tag{3.39}$$

By use of the homogeneous solution as an integrating factor, the general solution is implicitly

$$\widetilde{f}(q) = Ce^{-\mu q^3/3}e^{iq\zeta} - i\widetilde{f}(0)e^{\mu q^3/3}e^{-iq\zeta}\int_{q_0}^{q}\widetilde{F}(q')e^{-\mu q'^3/3}e^{iq'\zeta}dq'. \tag{3.40}$$

It's clear to see that as $\mu \to 0^+$ the smoothing kernel smoothly vanishes, returning to an implicit Fourier representation of the van Kampen modes.

Behavior of the eigenfunctions under a pure drag term

Now consider the opposite simple limit of the Lenard-Bernstein operator. Supposing that the constant $v_0 = 0$, the linearized kinetic equation takes the form

$$\frac{\partial f_1}{\partial t} + v\frac{\partial f_1}{\partial x} = \nu\frac{\partial}{\partial v}\Big(vf_1\Big). \tag{3.41}$$

Spatio-temporal Fourier transform results in the separable ODE

$$-\zeta f + vf = -i\mu\frac{d(vf)}{dv}, \tag{3.42}$$

$$\implies \frac{df}{f} = \frac{v-\zeta+i\mu}{-i\mu v}dv, \tag{3.43}$$

$$\implies f(v) = Ce^{iv/\mu}\frac{v^{-i\zeta/\mu}}{v}. \tag{3.44}$$

The solution is not defined around $v = 0$, and further are increasingly oscillatory as $\mu \to 0^+$. Thus, the isolated role of the drag term is associated with singular behavior as $\nu \to 0$. An alternative point of view is provided by the equation in the velocity-space Fourier domain,

$$\frac{d\widetilde{f}}{dq} + \frac{i\zeta}{1-\mu q}\widetilde{f} = 0. \tag{3.45}$$

Clearly as $\mu \to 0^+$ then $\widetilde{f} \to e^{-i\zeta q}$. Thus, while the solution is the ill-behaved

$$\widetilde{f}(q) = C(1-\mu q)^{i\zeta/\mu}, \tag{3.46}$$

in the limit as $\mu \to 0^+$, the solution formally reduces to $\exp(-i\zeta q)$. So in the case of pure drag too, the perturbation is "regular", though the solutions are ill-defined around $v = 0$. The addition of a smoothing term $\nu \frac{\partial^2 f}{\partial v^2}$ should smooth the solution.

Analysis of the full Lenard-Bernstein operator

Short and Simon have studied the behavior of the full Lenard-Bernstein operator in the dynamics of the linearized Vlasov-Poisson equation, and showed that the drag term results in the same singular behavior in the spectral velocity variable as $\nu \to 0^+$ [28]. They found a suitable dispersion relation by utilization of velocity space Fourier transforms, in terms of an incomplete gamma function. To summarize their findings, consider the linear equation

$$\frac{\partial f}{\partial t} + v\frac{\partial f}{\partial x} = \nu\frac{\partial}{\partial v}\Big(vf + \frac{\partial f}{\partial v}\Big) \tag{3.47}$$

with the right-hand term representing a balance of drag and diffusion. Fourier transformation in time and space results in the second-order ODE

$$i\mu\frac{d^2 f}{dv^2} + i\mu\frac{d}{dv}\Big(vf\Big) + (v-\zeta)f = 0. \tag{3.48}$$

To reduce to a first-order equation, Fourier transform in velocity $v \to q$ to find

$$\frac{d\widetilde{f}}{dq} - \frac{\mu q^2 - i\zeta}{1-\mu q}\widetilde{f} = 0. \tag{3.49}$$

The solution of this homogeneous equation is

$$\widetilde{f}(q) = Ce^{-q/\mu}e^{-\frac{1}{2}q^2}(1-\mu q)^{(i\mu\zeta-1)/\mu^2}. \tag{3.50}$$

Now according to Short and Simon, as one considers the limit $\mu \to 0^+$ of the inhomogeneous problem (that is, with self-consistent field) the inverse Fourier integral will not converge unless one chooses $C = 0$. However, it is possible to show the following limit,

$$\lim_{\mu\to 0} e^{-q^2/2}e^{-q/\mu}(1-\mu q)^{(i\mu\zeta-1)/\mu^2} = e^{-iq\zeta}. \tag{3.51}$$

Hence the linear solutions associated with the homogeneous problem should deform back into delta functions, the eigenfunctions of the translation operator $vf = \zeta f$. Therefore by choosing $C = 0$ Short and Simon artificially exclude the free-streaming ballistic modes from their analysis, which have deformed into decaying Airy-wavelike modes encoding initial data.

Summary of collisional dissipation as a singular perturbation

One way of understanding the central issue is that the van Kampen analysis decomposes the distribution function into marginally-stable ballistic modes without spatial variation [31]. These are necessarily time-symmetric, while Landau's Laplace transform analysis utilizes a one-sided Fourier transform. The analysis of van Kampen restricts decaying modes as eigenfunctions because the solutions must persist in both directions in time. Instead, the Landau damped solution for potential must be constructed through a superposition of marginally-stable modes. Their interference (phase mixing) leads to a decay of the potential.

In contrast, the addition of dissipation and the drag force breaks the symmetry of the problem and induces a preferred direction in time. This results in eigenfunctions perfectly capable of decaying due to both velocity-space dissipation and collective wave-particle interactions. The van Kampen and Landau modes are analytic in the case of weak dissipation.

Finally, it should be noted that as a complete system of orthogonal functions the van Kampen modes are a useful tool for the analysis of problems in kinetic plasma theory. Yet in any case, as the Landau modes solve the initial-value problem for the Vlasov-Poisson system, they are certainly better suited as initial conditions for numerical simulations than the Case-van Kampen modes. In addition, as generalized functions the Case-van Kampen modes cannot actually be represented numerically in the phase space.

3.2 The initial-value problem for electrostatic modes in unmagnetized plasma

There is a significant difference between unstable and damping plane waves of electrostatic potential, or plasma oscillations, in the solution of the linearized Vlasov-Poisson equations. By considering the initial value problem Landau showed that plasma oscillations are damped for a background distribution in thermodynamic equilibrium [23]. Further, unstable modes arise in Landau's analysis for certain non-equilibrium background distributions, suggesting that plasma oscillations play a key role in the physics of dissipative processes in plasma.

To reiterate, van Kampen and Case showed that the linearized kinetic equation has an eigenvalue spectrum with both continuous and discrete parts [25, 24]. The continuous part of the spectrum corresponds to marginally-stable ballistic modes, appearing as singular eigenfunctions of the form $g_\zeta(v) \sim \epsilon(k,\zeta)\delta(v-\zeta)$, while the discrete part of the spectrum corresponds to eigenfunctions of the form $g_\zeta(v) \sim \frac{1}{v-\zeta}\frac{\partial f_0}{\partial v}$. Discrete eigenvalues arise only for unstable solutions in complex-conjugate pairs. In the Case-van Kampen picture Landau damping arises due to phase mixing of these marginally-stable ballistic eigenfunctions.

This section considers Landau's method in detail. Then the evolution of special initial conditions describing a propagating, damping plane wave is considered. It is shown that when the plane wave is unstable it grows without any transients, but when the mode is damped it evolves along with a number of other transient oscillations.

3.2.1 One-sided temporal Fourier transform

Define the one-sided temporal Fourier transform as

$$f(\omega) = \int_0^\infty f(t)e^{i\omega t}dt, \tag{3.52}$$

with inverse transformation

$$f(t) = \frac{1}{2\pi}\int_{-\infty+is}^{\infty+is} f(\omega)e^{-i\omega t}d\omega \tag{3.53}$$

where the factor s keeps the contour above all poles of the integrand, in order that Eq. 3.52 converges. Provided that the transformed function $f(\omega)$ decays in the lower half-plane, the contour is then closed at infinity and the inverse transform given by the residue theorem as

$$f(t) = -i\sum \mathrm{Res}(f(\omega)) \tag{3.54}$$

with the sum over all poles of the response function $f(\omega)$.

3.2.2 Solution of the linearized kinetic equation

Considering the linearized Vlasov-Poisson equations for electron dynamics,

$$\frac{\partial f}{\partial t} + v\frac{\partial f}{\partial x} - \sigma\nabla\varphi\frac{\partial f_0}{\partial v} = 0, \tag{3.55}$$

$$\frac{d^2\varphi}{dx^2} = \int_{-\infty}^{\infty} f(v')dv', \tag{3.56}$$

with $\sigma = \mathrm{sgn}(q)$, two-sided spatial Fourier transform and one-sided time transform give

$$f(k,v,\omega) = \sigma\frac{\varphi(k,\omega)}{v-\zeta}\frac{\partial f_0}{\partial v} + i\frac{g(k,v)}{\omega - kv} \tag{3.57}$$

$$-k^2\varphi = \int_{-\infty}^{\infty} f(v)dv \tag{3.58}$$

with $g(k,v) \equiv f(k,v,t=0)$ the initial value of the distribution function and $\zeta = \frac{\omega}{k}$ the phase velocity. Now define a Cauchy integral of the initial condition as

$$g^*(k,\zeta) \equiv \int_{\mathcal{C}} \frac{g(k,v)}{\zeta - v}dv, \tag{3.59}$$

analytically continued with Landau's contour $\mathcal{C}$, and define the dielectric function $\varepsilon(k,\zeta)$,

$$\varepsilon(k,\zeta) = 1 + \frac{1}{k^2}\int_{\mathcal{C}} \frac{1}{\zeta - v}\frac{\partial f_0}{\partial v}dv. \tag{3.60}$$

Then combining the transformed kinetic equation and Poisson equation, the potential is

$$\varphi(k,\zeta) = \frac{i\sigma}{k^3}\frac{g^*(k,\zeta)}{\varepsilon(k,\zeta)}. \tag{3.61}$$

Landau then inverse-Laplace transforms this expression and concludes that the potential decays with modes given by the roots of $\varepsilon(k,\zeta)$. Inversion of the one-sided Fourier transform yields the solution as a sum of residues,

$$\varphi(k,t) = -i\sum \mathrm{Res}(\varphi(k,\zeta)). \tag{3.62}$$

In the event that each root of $\varepsilon(k,\zeta) = 0$ is simple and $g^*(k,\zeta)$ *is not singular*, then

$$\varphi(k,t) = \frac{\sigma}{k^3}\sum_j \frac{g^*(k,\zeta_j)}{\varepsilon_\omega(k,\zeta_j)}e^{-i\omega_j t}. \tag{3.63}$$

At this point one may conclude that plane waves decay provided that the roots of ε all lie in the lower half-plane (which they do, provided f_0 is in thermal equilibrium). Figure 3.1 shows the typical locations of the infinite set of zeros $\varepsilon(k,\omega) = 0$ in the lower-half frequency plane making up the Landau damping mode spectrum. Once the mode frequencies are determined, the amplitudes follow by computing the Cauchy transform of the initial condition.

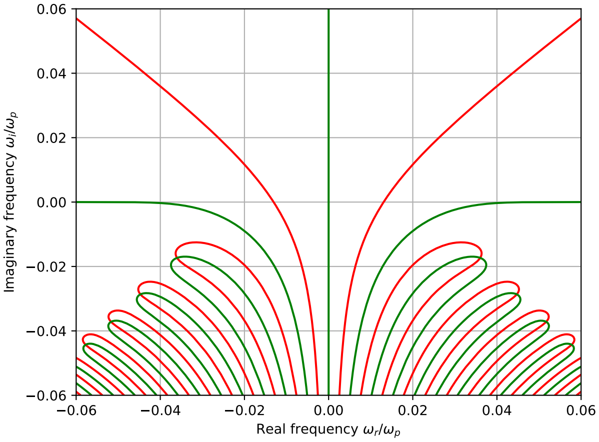

Figure 3.1: Locations of solutions to $\varepsilon(k,\omega) = 0$ showing contours of $\text{Re}(\varepsilon) = 0$ in red and $\text{Im}(\varepsilon) = 0$ in green given a Maxwellian background distribution $f_0(v)$ at short wavelength, $k\lambda_D = 0.5$. A solution to $\varepsilon(k,\omega) = 0$ occurs at an intersection of the real and imaginary zero-contours. The kinetic modes of greater magnitude in complex frequency represent transient oscillations which accompany any simulation of the kinetic equation which is not initialized with an eigenfunction.

Substitution of Eq. 3.61 solves for the perturbed distribution function,

$$f(k,\zeta) = i\frac{g(k,v)}{\omega - kv} - \frac{i}{k^2}\frac{g^*(k,\zeta)}{(\omega - kv)\varepsilon(k,\zeta)}\frac{\partial f_0}{\partial v}. \tag{3.64}$$

The first term inverts easily, while for the other one picks up both $\varepsilon(k,\zeta_j) = 0$ and $\omega = kv$,

$$f(k,v,t) = f(k,v,0)e^{-ikvt} - \frac{1}{k^2}\Big(\sum_j \frac{g^*(\zeta_j)e^{-i\omega_j t}}{(\omega_j - kv)\varepsilon_\omega(k,\zeta_j)} + \frac{g^*(v)e^{-ikvt}}{\varepsilon(k,v)}\Big)\frac{\partial f_0}{\partial v}. \tag{3.65}$$

The solution may be rearranged into a ballistic term undergoing phase-mixing, and an oscillatory term proportional to the perturbed potential,

$$f(k,t) = \Big(f(k,0) - \frac{1}{k^2}\frac{g^*(v)}{\varepsilon(k,v)}\frac{\partial f_0}{\partial v}\Big)e^{-ikvt} + \sigma\sum_j \frac{\varphi_j(k,t)}{\zeta_j - v}\frac{\partial f_0}{\partial v} \tag{3.66}$$

where each $\varphi_j(k,t) \equiv \frac{i}{k^3}\frac{f^*(\zeta_j)}{\varepsilon'(k,\zeta_j)}e^{-i\omega_j t}$ represents a plane-wave component of the potential. Landau's discussion notes that the potential responses all decay in time, so for long times the important remaining term is the free-streaming response.

3.2.3 Memory of the initial condition

Considering the solution evaluated at $t = 0$ gives a compatibility condition,

$$\frac{1}{k^2}\frac{g^*(v)}{\varepsilon(k,v)} = \sigma\sum_j \frac{\varphi_j(k,0)}{\zeta_j - v} \tag{3.67}$$

giving yet another form of the solution as

$$f(k,t) = \Big(f(k,0) - \sigma\sum_j \frac{\varphi_j(k,0)}{\zeta_j - v}\frac{\partial f_0}{\partial v}\Big)e^{-ikvt} + \sigma\sum_j \frac{\varphi_j(k,t)}{\zeta_j - v}\frac{\partial f_0}{\partial v}. \tag{3.68}$$

This equation states that the linearized distribution function retains a memory of the initial state of the electric potential, which persists even after the potential has Landau damped. These terms phase mix just as the initial condition does according to their velocity.

3.2.4 Behavior of special initial conditions

Observe that the response term for unstable solutions is similar to the Case-van Kampen eigenmode. To demonstrate this behavior, consider a special initial condition

$$g(k,v) = -\frac{\sigma}{k^2}\frac{1}{\zeta_n - v}\frac{\partial f_0}{\partial v} \tag{3.69}$$

where ζ_n is a solution to Landau's analytically-continued dielectric function, *i.e.* $\varepsilon(k,\zeta_n) = 0$.

Cauchy integral of the special initial condition

In the one-sided Fourier analysis, the following Cauchy-like integral must be calculated,

$$g^*(k,\zeta) = -\frac{\sigma}{k^2}\int_{\mathcal{C}} \frac{1}{(\zeta - v)(\zeta_n - v)}\frac{\partial f_0}{\partial v}dv. \tag{3.70}$$

To proceed, use a partial fraction expansion common to the theory of linear responses,

$$\frac{1}{(\zeta - v)(\zeta_n - v)} = \frac{1}{\zeta_n - \zeta}\Big(\frac{1}{\zeta - v} - \frac{1}{\zeta_n - v}\Big). \tag{3.71}$$

so that the transform is given by the formula

$$g^*(k,\zeta) = -\frac{\sigma}{\zeta_n - \zeta}\Big(\frac{1}{k^2}\int_{\mathcal{C}} \frac{1}{\zeta - v}\frac{\partial f_0}{\partial v}dv - \frac{1}{k^2}\int_{\mathcal{C}} \frac{1}{\zeta_n - v}\frac{\partial f_0}{\partial v}dv\Big). \tag{3.72}$$

Subtleties for Im$(\zeta) > 0$ *and Im*$(\zeta) < 0$

If the value ζ_n lies in the upper half complex velocity-plane, then it follows from Eq. 3.72

$$g^*(k,\zeta) = \sigma\frac{\varepsilon(k,\zeta) - \varepsilon(k,\zeta_n)}{\zeta - \zeta_n} \tag{3.73}$$

and further if a root of the dielectric function is examined, *i.e.* $\varepsilon(k,\zeta_n) = 0$, then one has

$$g^*(k,\zeta) = \sigma\frac{\varepsilon(k,\zeta)}{\zeta - \zeta_n}. \tag{3.74}$$

However, if the quantity ζ lies in the lower half-plane then only the first integral in Eq. 3.72 need be analytically continued into the lower half-plane. The reason is that in inverting the one-sided Fourier transform the contour only needs to deform around the variable of integration, namely ζ. To arrive at an analogous result to Eq. 3.73, the residue of the integrand at $v = \zeta_n$ must be added and subtracted to form $\varepsilon(k,\zeta_n)$. This gives

$$g^*(k,\zeta) = \frac{\sigma}{\zeta - \zeta_n}\Big(\varepsilon(k,\zeta) + \frac{2\pi i}{k^2}\frac{\partial f_0}{\partial v}\Big|_{v=\zeta_n}\Big). \tag{3.75}$$

This second component corresponding to the residue of the pole of the initial condition in the lower half-plane excites all damping kinetic modes. While the first component strongly excites the chosen mode the next section demonstrates that all modes remain excited.

Behavior of the electric potential

This section considers two cases; solutions to $\varepsilon(k,\zeta) = 0$ with $\mathrm{Im}(\zeta) > 0$ and then $\mathrm{Im}(\zeta) < 0$. In the first case, representing an unstable mode, the dielectric function cancels from the potential equation,

$$\varphi(k,\zeta) = \frac{i}{k^3}\frac{\varepsilon(k,\zeta)}{(\zeta-\zeta_n)\varepsilon(k,\zeta)} = \frac{i}{k^2}\frac{1}{\omega-\omega_n} \tag{3.76}$$

and the inversion is then given by the single mode

$$\varphi(k,t) = \frac{e^{-i\omega_n t}}{k^2}, \tag{3.77}$$

stating that the zeroth moment of the distribution function is a plane wave. Yet in the second case when the mode is damped, *i.e.* $\mathrm{Im}(\zeta) < 0$, then the potential equation is

$$\varphi(k,\zeta) = \frac{i}{k^2}\frac{1}{\omega-\omega_n} - \frac{2\pi}{k^2}\frac{1}{(\omega-\omega_n)\varepsilon(\zeta)}\frac{1}{k^2}\frac{\partial f_0}{\partial v}\bigg|_{v=\zeta_n}. \tag{3.78}$$

Equation 3.78 has a double pole at $\zeta = \zeta_n$ in the second term, and a simple pole at all other solutions $\varepsilon(\zeta_j) = 0$ with $j \neq n$. Inverting the solution obtains the expression

$$\begin{aligned}\varphi(k,t) = &\left\{1 + \frac{i\pi}{k^2}\frac{\epsilon_{\omega\omega}(\zeta_n)}{\epsilon_\omega^2(\zeta_n)}\frac{\partial f_0}{\partial v}\bigg|_{v=\zeta_n}\right\}\frac{e^{-i\omega_n t}}{k^2} \\ &+ \sum_{j\neq n}\left(\frac{1}{(\omega_n-\omega_j)\epsilon_\omega(\zeta_j)}\frac{1}{k^2}\frac{\partial f_0}{\partial v}\bigg|_{v=\zeta_n}\right)\frac{e^{-i\omega_j t}}{k^2}.\end{aligned} \tag{3.79}$$

It's evident that all modes are excited by this perturbation, yet the mode ω_n is so preferentially. Further, the amplitudes of the higher modes are all reduced by a factor of $\frac{1}{\omega_n-\omega_j}$.

Behavior of the distribution function

Now substitution of Eq. 3.76 into the expression for the distribution function gives

$$f(k,v,\omega) = \frac{i}{k^2}\frac{1}{(\zeta_n-v)(\omega-\omega_n)}\frac{\partial f_0}{\partial v} \tag{3.80}$$

after some algebra, which then inverts directly to

$$f(k,v,t) = \frac{1}{k^2}\frac{1}{\zeta_n-v}\frac{\partial f_0}{\partial v}e^{-i\omega_n t}. \tag{3.81}$$

Note that in contrast to the general solution for damping waves, Eq. 3.81 *has no phase mixing.* While Landau damping always involves phase mixing of the initial condition, unstable modes are true eigenfunctions and evolve without any oscillations or mixing in the distribution function. However, as will be seen from quasilinear analysis the growth of unstable modes does alter the dielectric function through reaction with the mean distribution.

3.2.5 Spectrum of the Maxwellian perturbation

A typical perturbation used in numerical simulations is Maxwellian in velocity space

$$g(v,x) = e^{ik_0 x}\frac{1}{\sqrt{2\pi}v_t}e^{-v^2/2v_t^2} \qquad \Longrightarrow \qquad g(v) = \frac{1}{\sqrt{2\pi}v_t}e^{-v^2/2v_t^2}. \tag{3.82}$$

Integration of $g(v)$ along the Landau contour gives the plasma dispersion function $Z(\zeta)$,

$$g^*(\zeta) = \frac{1}{\sqrt{2\pi}}\int_{\mathcal{C}}\frac{e^{-v^2/2v_t^2}}{\zeta - v}dv = \frac{1}{\sqrt{2}v_t}Z\Big(\frac{\zeta}{\sqrt{2}v_t}\Big). \tag{3.83}$$

Normalizing velocities such that $\sqrt{2}v_t = 1$ the potential response has the spectrum

$$\varphi(\zeta) = \frac{\sigma}{k^3}\sum_j \frac{Z(\zeta_j)}{\epsilon_\omega(\zeta_j)}e^{-i\omega_j t}. \tag{3.84}$$

In other words the zeroth moment is $n(x,t) = \sum_j A_j e^{ik(x-\zeta_j t)}$ with modal amplitudes

$$A_j \equiv \frac{Z(\zeta_j)}{\varepsilon'(\zeta_j)}. \tag{3.85}$$

A remark is in order regarding the physical meaning of the potential response. The quantity $\epsilon_\omega(\zeta_j)$ is proportional to the Brillouin factor for dielectric energy [31], $\omega_j\varepsilon_\omega(\zeta_j) = \frac{\partial(\omega\varepsilon)}{\partial\omega}\Big|_{\omega=\omega_j}$. Further, the higher Landau modes have frequencies of greater complex amplitude. This energy $\varepsilon_\omega(\zeta_j)$ increases with the frequency amplitude. Thus the response decays into its lowest energy state for $t \geq 0$ as the least-damped mode is also the lowest energy mode.

On the other hand, if the perturbation is the linear response then the solution is

$$\varphi(k,t) = \frac{1}{k^2}\Big\{\Big(1 - 2\pi i\frac{Z'''(\widetilde{\zeta}_n)}{(Z''(\widetilde{\zeta}_n))^2}\frac{\partial f_0}{\partial v}\Big)e^{-i\omega_n t} - 4\sqrt{2}\pi\frac{\partial f_0}{\partial v}\sum_{j\neq n}\frac{e^{-i\omega_j t}}{(\zeta_n - \zeta_j)Z''(\widetilde{\zeta}_j)}\Big\}. \tag{3.86}$$

Figure 3.2 compares the relative potential amplitudes of the damping modes for the Maxwellian background distribution at a wavenumber $k\lambda_D = 1$ for the Maxwellian perturbation and with the linear response Eq. 3.69 perturbation representing a right-propagating Langmuir wave. Here only the first ten modal amplitudes of negative and positive frequency are shown. While the fundamental plasma oscillation mode is primarily excited, the higher transient modes have amplitudes at most approximately 20% of the first modes.

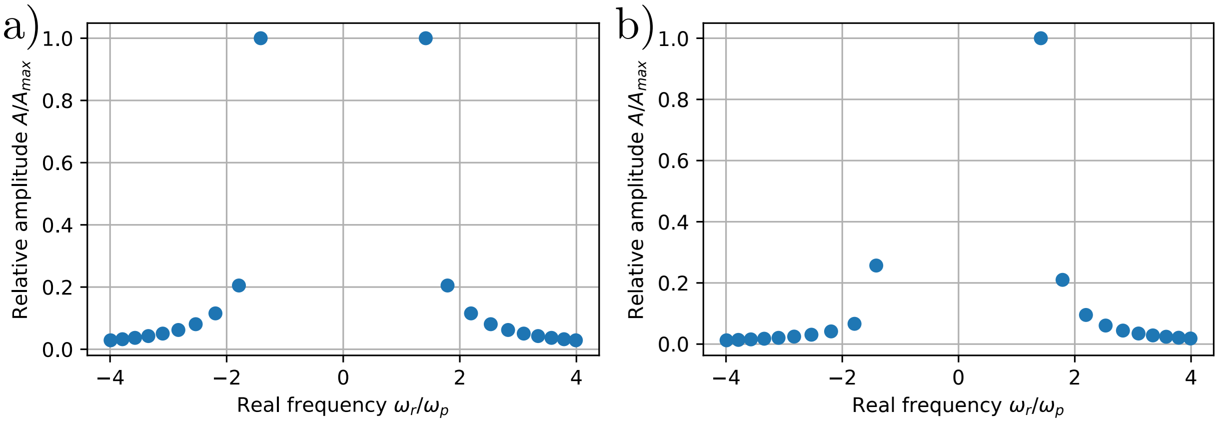

Figure 3.2: Relative potential amplitudes of the Landau damping spectrum for the first ±10 frequencies ω_j given a Maxwellian background distribution $f_0(v)$ with unit thermal velocity at $k\lambda_D = 0.5$ for a) the Maxwellian perturbation, and b) initial data as Eq. 3.69 with a single complex pole. Modes are ordered by the real part of their frequency. Higher modes are rapidly damped, as seen in Fig. 3.1. Here modal amplitudes are normalized to the largest amplitude in the spectrum. Part b) shows that while Eq. 3.69 can excite a propagating damping plane wave it is necessarily accompanied by a variety of transient oscillations, with initial amplitudes up to 20% of the primary mode.

3.2.6 Potential spectrum for initial conditions with an error in the eigenvalue

If a special initial condition of the form in Eq. 3.69 is chosen such that the phase velocity ζ_n is not a root of the dielectric function, *i.e.* $\varepsilon(k, \zeta_n) \neq 0$, then the response consists of a sum of plane waves of varying phase velocity. Specifically, substitution of the full Cauchy integral

$$g^*(k,\zeta) = \frac{\varepsilon(k,\zeta) - \varepsilon(k,\zeta_n)}{\zeta - \zeta_n} \tag{3.87}$$

of the initial condition into the equation for the perturbed potential gives

$$\varphi(k,\omega) = \frac{1}{ik^2}\frac{1}{\omega - \omega_n}\Big\{1 - \frac{\varepsilon(k,\zeta_n)}{\varepsilon(k,\zeta)}\Big\}. \tag{3.88}$$

Temporal inversion of this solution by the residue theorem gives

$$\varphi(k,t) = -\frac{1}{k^2}\sum_j \frac{\varepsilon(k,\zeta_n)}{\varepsilon_\omega(k,\zeta_j)}\frac{e^{-i\omega_j t}}{\omega_j - \omega_n} \tag{3.89}$$

with the sum j over all solutions of the dispersion relation $\varepsilon(k,\zeta) = 0$. This equation states that the zeroth moment of the distribution function consists of a sum over all excited modes, with the relative complex amplitude of each mode given by a classic resonance expression

$$A_j = \frac{\varepsilon(k,\omega_n)}{\varepsilon_\omega(k,\omega_j)(\omega_j - \omega_n)}. \tag{3.90}$$

Thus the closer the initialized eigenvalue ω_n is to the true solution the greater the relative amplitude of that component. If the eigenmode is the least-damped solution, or even a growing mode, then after a short period it will be the only solution observed.

In summary, Landau damping modes are not eigenfunctions of the Vlasov equation. If they are initialized and time is run either forward or backward they will damp as the initial condition phase mixes in either direction of time. On the other hand, unstable modes are true eigenfunctions and evolve without any transients in the distribution function.

3.3 Visualization of the simplest phase space eigenfunctions

This section explores a visual approach to the phase space eigenfunctions previously discussed mathematically. Figure 3.3 shows the zero-contours of the dielectric function $\varepsilon(\zeta,k)$ computed using the technique of Appendix A for a two-stream instability in the three-dimensional parameter space (ζ_r,ζ_i,k). An unstable solution where the real and imaginary zeroes intersect with $\zeta_i > 0$ represents an eigenvalue of the system, and the eigenfunction can be constructed as in the following.

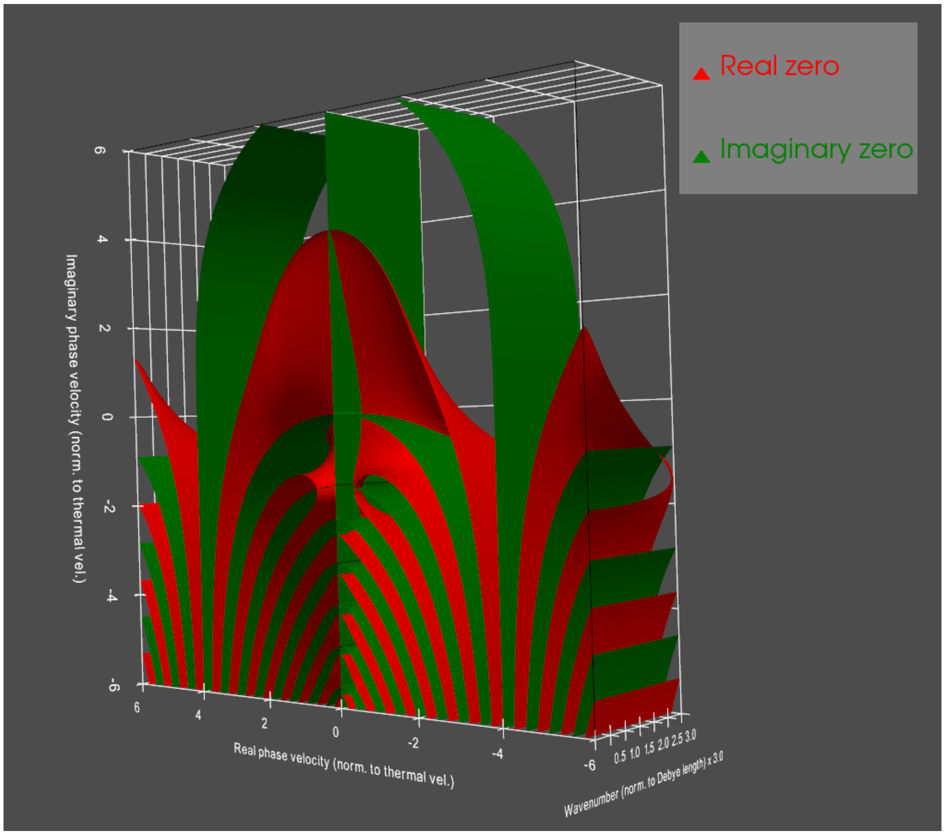

Figure 3.3: Valid solutions of $\epsilon(\omega, k) = 0$ for plane-waves in the Vlasov-Poisson system lie along intersections of the two families of surfaces shown here. This example is of two interpenetrating Maxwellians of drifts $\pm 4v_t$. Notice that the growth rate can not be directly interpreted from the imaginary phase velocity as it must be weighted by $\omega = \zeta k$.

3.3.1 Determining the corresponding eigenfunction of a solution to $\epsilon(\omega, k) = 0$

Once a solution pair (ω_0, k_0) (or as many pairs as desired) has been identified, one can then construct the corresponding perturbation to the distribution function by considering the Poisson equation. Therefore, the solution for the potential is

$$\widetilde{\Phi}_1(k, \omega) = \Phi_0 \delta(k - k_0) \delta(\omega - \omega_0). \tag{3.91}$$

Substitution into the linearized solution gives

$$\widetilde{f}_1 = \frac{e}{m} \Phi_0 \delta(k - k_0) \delta(\omega - \omega_0) \frac{1}{z - v} \frac{\partial f_0}{\partial v} \tag{3.92}$$

and inverse Fourier transforming gives the perturbation at $t = 0$ to be

$$f_1(x, v, 0) = \alpha \mathrm{Re}(\psi) \frac{\partial f_0}{\partial v} \tag{3.93}$$

$$\psi(x, v) \equiv \frac{e^{ik_0 x}}{z_0 - v} \tag{3.94}$$

where $\alpha \sim \frac{e}{m}\Phi_0$ is a constant proportional to the potential amplitude and $z_0 = \omega_0/k_0$. No solution to $\epsilon(\omega, k)$ has $\mathrm{Im}(\omega) = 0$, so the denominator of ψ is never zero and the inverse transform is well-defined. The delta function in ω of Eq. 3.92 is only for $\mathrm{Im}(\omega) > 0$. The complex function ψ is defined for convenience to account for all phase information in the perturbation and is an analytic function that is easily computed numerically. The perturbation can be interpreted as an instantaneous Cauchy transform of the distribution gradient.

Consider the unstable solution at $z = 0 + 2.77i$ in Fig. 3.4a. The wave-number is $k_0\lambda_D = 0.1$ and phase velocity $z_0 = 2.77i$, giving a growth rate $\omega_i = 2.77 \times 0.1\omega_p \sim 0.28\omega_p$. Therefore, the corresponding mode is given by the functions Eqs 3.93-3.94 with these values. Computing this, the resulting eigenmode is shown in Fig. 3.4b. While the perturbation is a two-dimensional wave in phase space the zeroth moment is a pure sine wave, resulting in an initial electric potential $\phi(x) = \Phi_0 \sin(x)$.

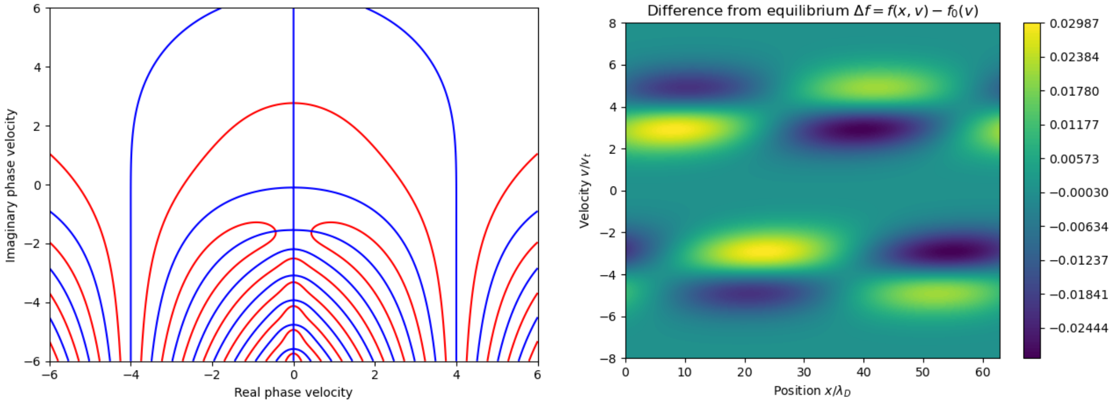

(a) Complex ζ-space at $k\lambda_D = 0.1$.

(b) $f_1(x, v, 0)$ with beam velocities $\pm 4v_t$.

Figure 3.4: The unstable solution at $\zeta = 2.77i$ indicates the two-stream mode. The eigenfunction, coupled plasma waves on each beam, has a pure sine wave as zeroth moment.

3.4 Transientless initialization using kinetic eigenmodes

This section makes the case that initialization of a continuum kinetic phase space simulation should be initialized with the analytic linear eigenfunction. The typical kinetic simulation philosophy is to excite instabilities by superposition of planar electrostatic or electromagnetic waves with Maxwellian phase space perturbations. But, the phase space structure of the unstable wave-like mode is not purely excited by the initial condition and a significant portion of the perturbation energy is divided amongst the Landau-damped modes of oscillation. Upon running the simulation a transient period of energetic reorganization takes place through the mechanism of linear Landau damping. On the other hand, an eigenfunction perturbation results in the same density plane wave as the Maxwellian perturbation yet seeds the instability without any transient oscillations.

There are several advantages to an eigenfunction initialization. The first is an economy of energy in the initial condition. Consider the distribution of potential amplitudes for the Maxwellian perturbation, given in Eq. 3.63 with $g^*(\zeta) = Z(\zeta)$. The plasma dispersion function $Z(\zeta_j)$ has a small modulus in the upper-half ζ-plane and asymptotes to zero there. However, due to the analytic continuation into the lower-half ζ-plane the modulus becomes unbounded there as $|\zeta| \to \infty$ for angles $225^\circ < \varphi < 315^\circ$. Because of this behavior of $Z(\zeta)$ in the complex ζ-plane the numerator of the unstable part of the Landau spectrum will typically be small because it lies in the upper-half plane. Therefore the initial energy distributed to the eigenfunction is just a few percent of the total initialized energy.

A second advantage of the eigenfunction perturbation is that the amplitude may be initialized just below the nonlinear threshold, cutting several instability e-folding times from the simulation. Because of the curse of dimensionality in continuum kinetic simulations, computational time and effort is at a premium. Yet large amplitude Maxwellian perturbations form nonlinear phase space structures as their transient oscillations decay. The problem initialized with eigenfunctions will saturate without these other structures. This earlier saturation can translate to a considerable computational cost savings for high-dimensional problems.

3.4.1 Example: The one-dimensional two stream instability

As a simple example of transientless initialization this section considers the two stream instability with both a Maxwellian in the velocity space and with the kinetic eigenfunction used as perturbations. The energy trace of the two simulations is compared for various amplitudes. An unstable distribution is given by counterstreaming electron beams,

$$f_0(v) = \frac{1}{2\sqrt{2\pi}v_t}\Big(\exp\Big\{-\frac{(v-v_d)^2}{2v_t^2}\Big\} + \exp\Big\{-\frac{(v+v_d)^2}{2v_t^2}\Big\}\Big). \tag{3.95}$$

When the perturbation structure matches the background distribution in the velocity space, such as $g(x,v) = \alpha f_0(v)e^{ikx}$ with α the perturbation amplitude, the potential amplitudes are

$$\varphi(k,t) = -2\alpha\sum_j \frac{Z(\zeta_{+,j}) + Z(\zeta_{-,j})}{Z''(\zeta_{+,j}) + Z''(\zeta_{-,j})}e^{-i\omega_j t} \tag{3.96}$$

where $\zeta_{\pm,j} \equiv (\zeta_j \pm v_d)/\sqrt{2}v_t$ are the beam-shifted phase velocities. Table 3.1 lists the first few modal amplitudes determined in this way, including the undamped plasma oscillations on each drifting beam and the coupled unstable mode of zero real frequency. Calculation of the potential amplitudes by Eq. 3.96 for a distribution of drift velocities $u_d = 5v_t$ at wavenumber $k\lambda_D = 0.5$ shows that the unstable mode is only the fifth-largest amplitude amongst the modes initialized in this way.

Figure 3.5 illustrates this concept by comparing the Maxwellian perturbation to the eigenfunction perturbation. When initialized at very small amplitude the type of perturbation does not make a difference; for example, the undamped plasma oscillation is too small amplitude by saturation to change the nonlinear dynamics. On the other hand, a perturbation may be seeded at large amplitude to save on computational time. The large amplitude perturbation in Fig. 3.5a has a different energy trace compared to the other simulations as the transient components undergo nonlinear Landau damping.

3.5 Simulation of a streaming instability in two-dimensional configuration space

Langmuir turbulence in an unmagnetized plasma is multi-dimensional. In the linear description it can be considered using preceding one-dimensional analysis as a spectrum of obliquely

Frequency ω_r/ω_p	$\pm$ 1.42	$\pm$ 0.0157	0	$\pm$ 1.10	$\pm$ 1.20	$\pm$ 1.29
Growth rate γ/ω_p	-3.2×10^{-7}	-0.341	0.335	-0.228	-0.377	-0.488
Relative amplitude $\lvert\varphi_j\rvert/\max(\lvert\varphi\rvert)$	1	0.710	0.335	0.0701	0.0581	0.0466

Table 3.1: Relative potential amplitudes of the first six linear modes contained in a perturbation of two counterstreaming thermal plasmas of drift velocities $u_d = \pm 5 v_t$ and at wavenumber $k\lambda_D = 0.126$ where the perturbation's velocity space structure matches the background distribution. For each non-zero frequency ω there is a pair of solutions. Due to these mode pairs the unstable mode (here of growth rate $\gamma/\omega_p = 0.335$) has only the fifth-largest relative amplitude in the initial condition.

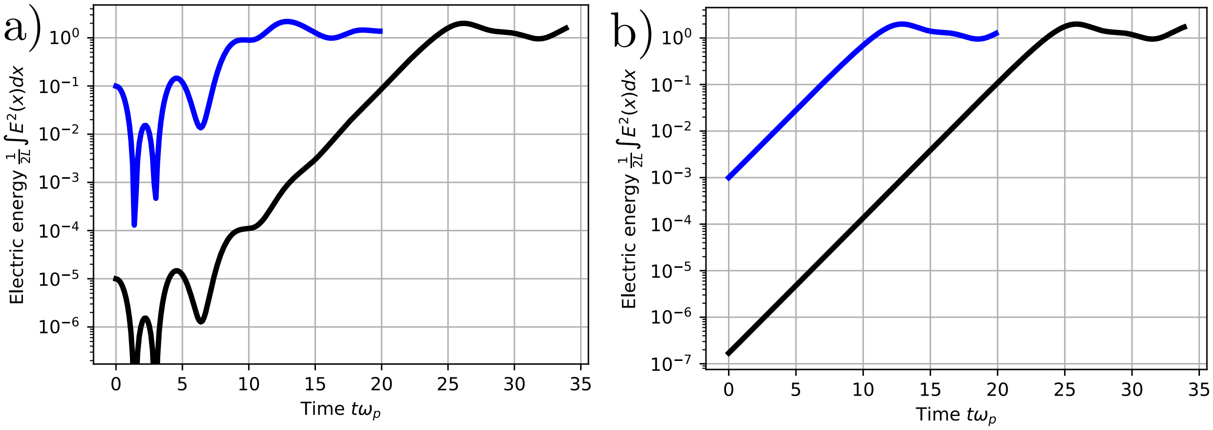

Figure 3.5: Comparison of energy traces for a single-mode two-stream instability of drifts $u_d = \pm 5 v_t$ at wavenumber $k\lambda_D = 0.126$ showing a) Maxwellian perturbations and b) eigenfunction perturbations. Two subcases are shown. The black trace represents a perturbation of small amplitude and the blue trace a large-amplitude perturbation. Large-amplitude perturbations save on computational time. However, the transient components of the large-amplitude Maxwellian perturbation decay through nonlinear Landau damping, polluting the solution. Yet the large-amplitude eigenmode saturates as if seeded from small amplitude.

propagating plane waves. This section considers the two-stream instability as an example of the methodology used to approach electrostatic dispersion analysis in multiple dimensions. Consider the Vlasov-Poisson system linearized around a homogeneous $f_0(\boldsymbol{v})$,

$$\frac{\partial f_1}{\partial t} + \boldsymbol{v} \cdot \nabla f_1 - \frac{q}{m}(\nabla_x \varphi) \cdot \nabla_v f_0 = 0 \tag{3.97}$$

$$\nabla^2 \varphi = \frac{q n_0}{\epsilon_0} \int f_1 d\boldsymbol{v} \tag{3.98}$$

The linear response and dielectric function are given by the formulas

$$f_1 = -\frac{q}{m}\varphi \frac{\boldsymbol{k} \cdot \nabla_v f_0}{\omega - \boldsymbol{k} \cdot \boldsymbol{v}} \tag{3.99}$$

$$\varepsilon = 1 + \frac{\omega_p^2}{k^2} \int \frac{\boldsymbol{k} \cdot \nabla_v f_0}{\omega - \boldsymbol{k} \cdot \boldsymbol{v}} d\boldsymbol{v} = 0. \tag{3.100}$$

For example, consider a thermal two-stream distribution with equal temperatures

$$f(u, v, w) = \frac{1}{(2\pi)^{3/2} u_t^3} e^{-\frac{v^2 + w^2}{2u_t^2}} \frac{1}{2}\Big(e^{-\frac{(u-u_d)^2}{2u_t^2}} + e^{-\frac{(u+u_d)^2}{2u_t^2}} \Big). \tag{3.101}$$

Assuming equal beam temperatures simplifies analysis. Let $\boldsymbol{k}$ lie in the (x, y)-plane and consider the dispersion integral. The z-velocity integrates out immediately, while the (x, y)-directed velocities must be rotated into the frame of the wavevector. Rotating counter-clockwise through an angle φ to coordinates $(v_\parallel, v_\perp)$, the distribution function becomes

$$\begin{aligned} f_\pm &\equiv \frac{1}{2\pi u_t^2} \exp\Big(- \frac{(v_\parallel \mp \cos(\varphi) u_d)^2}{2u_t^2} \Big) \exp\Big(- \frac{(v_\perp \pm \sin(\varphi) u_d)^2}{2u_t^2} \Big) \\ f(v_\parallel, v_\perp) &= \frac{f_+ + f_-}{2} \end{aligned} \tag{3.102}$$

The integral can then be evaluated for each drifting component $f_\pm$ as

$$\begin{aligned} \int \frac{1}{\zeta - v_\parallel} \frac{\partial f_\pm}{\partial v_\parallel} &= -\frac{1}{u_t^2} \int \frac{v_\parallel \mp \cos(\varphi) u_d}{\zeta - v_\parallel} f dv_\parallel dv_\perp \\ &= -\frac{1}{u_t^2} \frac{Z'(\zeta_\pm)}{2} \end{aligned} \tag{3.103}$$

where the phase velocity is shifted by the drift velocity as $\zeta_\pm \equiv \frac{\zeta \mp \cos\varphi u_d}{\sqrt{2} u_t}$. The dispersion function can then be written as [32]

$$\varepsilon(k, \zeta, \varphi) = 1 - \frac{1}{(k\lambda_D)^2} \frac{Z'(\zeta_+) + Z'(\zeta_-)}{2} = 0. \tag{3.104}$$

The effect of the rotation is to decrease the effective drift velocity by the cosine of φ. This leads to a maximum growth rate of longitudinal electrostatic waves parallel to the streaming velocity. However, the growth of transverse components seeds a two or three-dimensional turbulence, depending on the chosen dimensionality of the plasma configuration space.

3.5.1 Simulation geometry, initialization, and results

This problem considers two thermal distributions of electrons drifting through one another along the x-axis with beam velocities $\pm v_b$. Though the fastest growing eigenmode has a wavevector $\boldsymbol{k} = k_x\hat{x}$ aligned with the beam axis, eigenmodes with a long-wavelength transverse wavevector component $k_y \ll k_x$ have comparable growth rates to the fastest mode, as illustrated in Fig. 3.6. Thus for an unmagnetized plasma large compared to the Debye length streaming instabilities seed a multi-dimensional Langmuir turbulence as long-wavelength transverse components grow along with the modes on the beam axis. In most practical cases this is a three-dimensional phenomenon, but for computational tractability this section presents a simulation of the electrostatic streaming instability in phase space with two space dimensions and two velocity dimensions (2D2V).

To briefly summarize the numerical method, the Vlasov-Poisson system is discretized in configuration space by Galerkin projection onto a truncated Fourier basis $(x, y) \to (k_n, k_m)$. The system is discretized in velocity space by truncating the velocity domain and applying the discontinuous Galerkin method to yield a semi-discrete equation in time, which is then integrated numerically. The field equation is solved algebraically in spectral space and the velocity fluxes are computed by the pseudospectral method. The semi-discrete equation is advanced by second-order Strang splitting, with the explicit third-order Adams-Bashforth method used for the nonlinear flux and advection advanced implicitly to second order by fractional Crank-Nicolson stepping. These methods are discussed in detail in Chapter 2.

The domain is set with fundamental wavenumbers $k_x\lambda_D = 0.05$ and $k_y\lambda_D = 0.02$. The x-axis is divided into forty evenly spaced collocation nodes and the y-axis into fifty nodes. Velocity space is truncated at $v_{\max} = \pm 11.5 v_t$, and each axis divided into fourteen finite

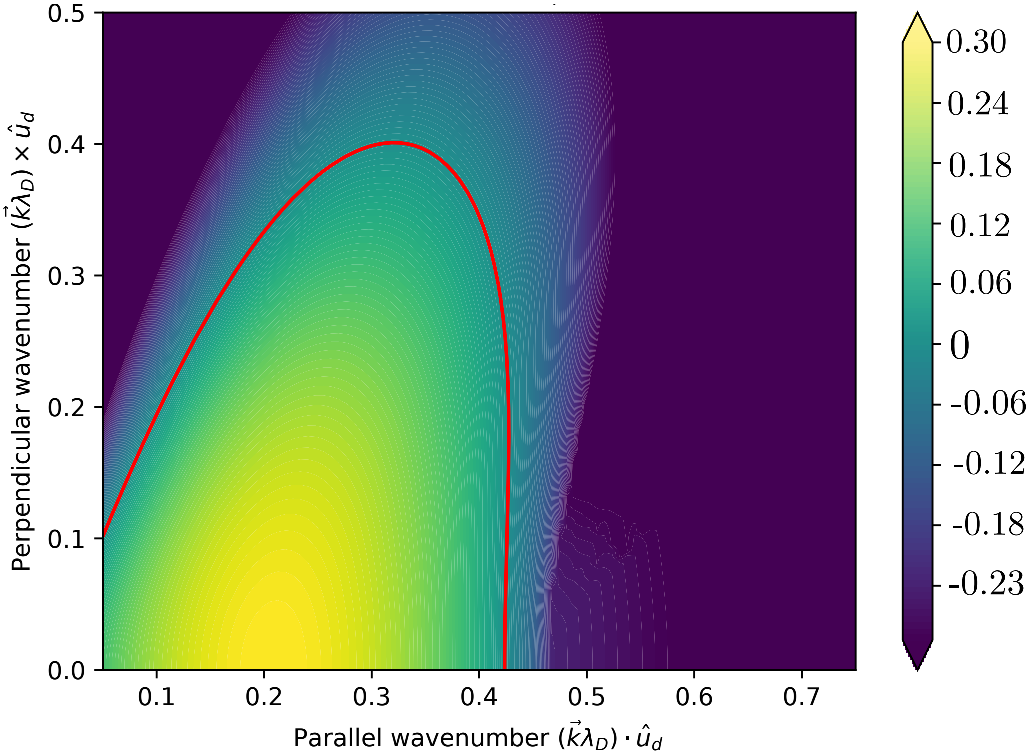

Figure 3.6: Growth rates of the electron two-stream instability as $\mathrm{Im}(\omega)/\omega_{pe}$ for two counter-streaming Maxwellians with relative velocity of six thermal velocities, *e.g.* $\Delta v = 6v_t$, in terms of parallel and perpendicular wavenumbers relative to the beam axis vector $\hat{u}_d$. The red contour indicates the line of marginal stability where $\mathrm{Im}(\omega) = 0$. While the fastest growing mode is aligned with the beam axis, modes of comparable growth rates occur with transverse wavelengths roughly five-to-ten times the unstable wavelength on-axis.

elements each of a seventh-order Legendre-Gauss-Lobatto polynomial basis. Ten elements are linearly clustered between $v \in (-7.5, 7.5)v_t$ and two elements into $v \in \pm(7.5, 11.5)v_t$. The beam velocity in Eq. 3.101 is set to $u_b = 3v_t$. Finally, a spatial hyperviscosity $\nu\nabla_x^4 f$ with $\nu = 10$ is added to the kinetic equation to mitigate spectral blocking with this low spatial resolution. Many modes of comparable growth rates are initialized, each with random spatial phase $\widetilde{\varphi}$ using the perturbations

$$f_1(x, y, u, v) = \frac{\alpha}{k}\mathrm{Re}\Big(\frac{k_x\partial_u f + k_y\partial_v f}{\omega(k_x, k_y) - k_x u - k_y v}\exp(i(k_x x + k_y y + \widetilde{\varphi}))\Big) \tag{3.105}$$

with α the amplitude, and where $\omega(k_x, k_y)$ is the unstable solution of the dispersion relation for the mode pair (k_x, k_y). A total of thirty-five modes are excited, with for each multiple of the x-fundamental $k_{n,x} = nk_{1,x}$ with $n = 2$, 3, and 4, multiples of the y-fundamental are excited with $k_{m,y} = mk_{1,y}$ with $m = 0$, ±1, ±2, ±3, ±4, and ±5. There is no symmetry of the perturbation in the y-direction as different random phases are used for the pairs $\pm m$. The simulation is run to a stop time of $t\omega_p = 30$ with amplitudes $\alpha = 0.01$. Figure 3.7 shows the simulation's energy trace; hyperviscosity with this spatial resolution leads to a domain energy loss of $\mathcal{O}(10^{-3})$ while electric energy saturates at $\mathcal{O}(10^{-1})$.

The instability causes wave energy to grow initially primarily along the beam-axis. Yet once amplitudes reach nonlinear levels the presence of random transverse components in the wave spectrum leads to the formation of two-dimensional nonlinear structures. This effect is illustrated by examining the electric potential in Fig. 3.8. The nonlinear phase of the simulation is marked by a significant increase of wave energy in the y-direction. A useful way of understanding this redistribution of wave energy is seen by examining the domain-averaged distribution function $\langle f\rangle_{(x,y)}(u, v)$ plotted in Fig. 3.9. In approaching a Penrose-stable double-humped distribution, the temperature transverse to the beam axis has clearly increased significantly. Plasma thermal and Langmuir wave energy on average scales are generally related by an energy equipartition [31]. Thus the turbulent redistribution of wave energy into the transverse direction is associated with the relaxation of $\langle f\rangle$ towards a double-humped distribution with a single characteristic thermal velocity.

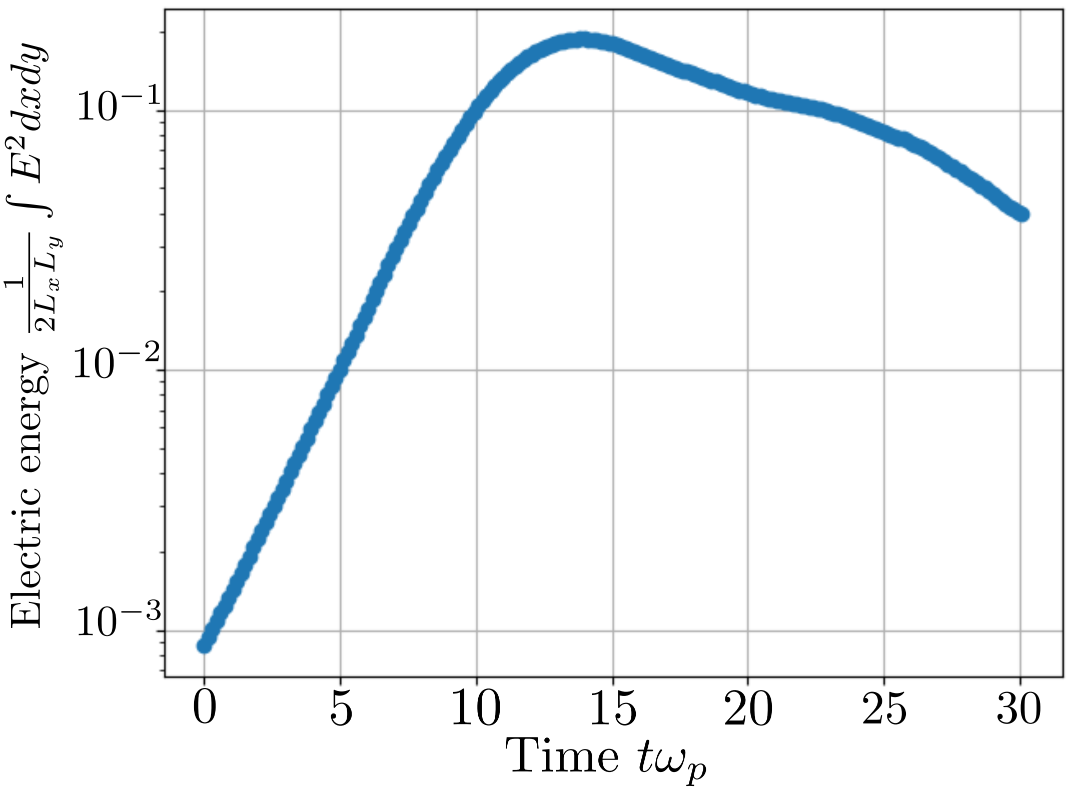

Figure 3.7: Electric energy evolution of the two-stream instability simulation in the restricted 2D2V phase space with thirty-five excited domain modes. The high spatial hyperviscosity of $\nu = 10$ leads to an energy loss of $\mathcal{O}(10^{-3})$ by the stop time. This is insufficient accuracy to study the fine details of phase space. However, the energy loss is well beneath the peak electric energy so that the result up to the stop time is a good approximation.

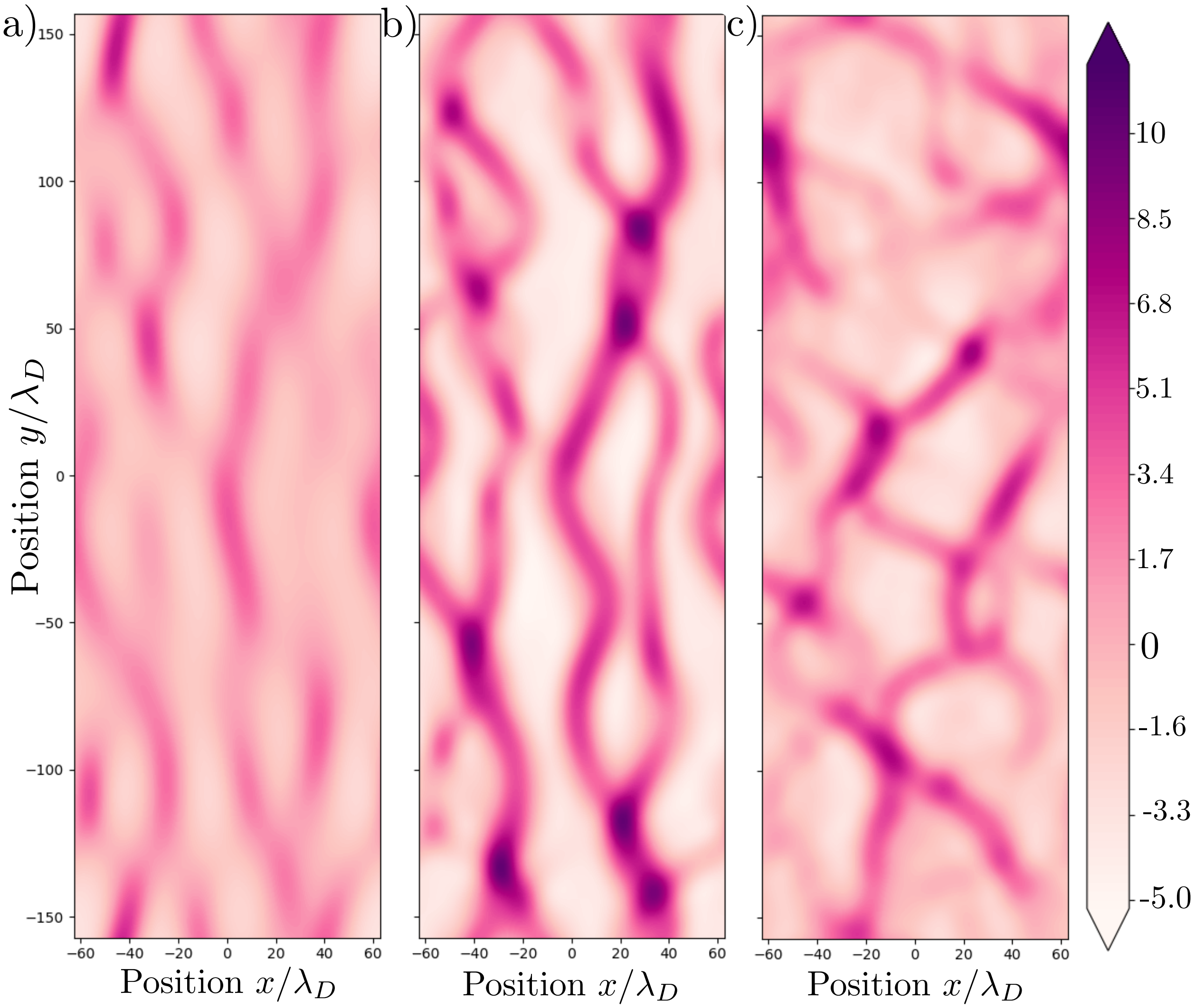

Figure 3.8: Electrostatic potential $\varphi(x, y)$ of the electron two-stream instability in a 2D2V phase space geometry for a) linear mode growth at $t\omega_p = 8$, b) beginning of nonlinearity at $t\omega_p = 18$, and c) heading towards isotropization at $t\omega_p = 27$. The instability is characterized by the formation of one-dimensional electron holes, or phase space vortex lines, transverse to the beam axis. These vortex lines then break up after nonlinear saturation into two-dimensional hole structures with more complex trapping orbits that maintain connection to one another through these vortex tubes by the conservation of phase space circulation in Vlasov dynamics. The lines of potential in this simulation can be understood as a projection into configuration space of the electron phase space vortex tubes.

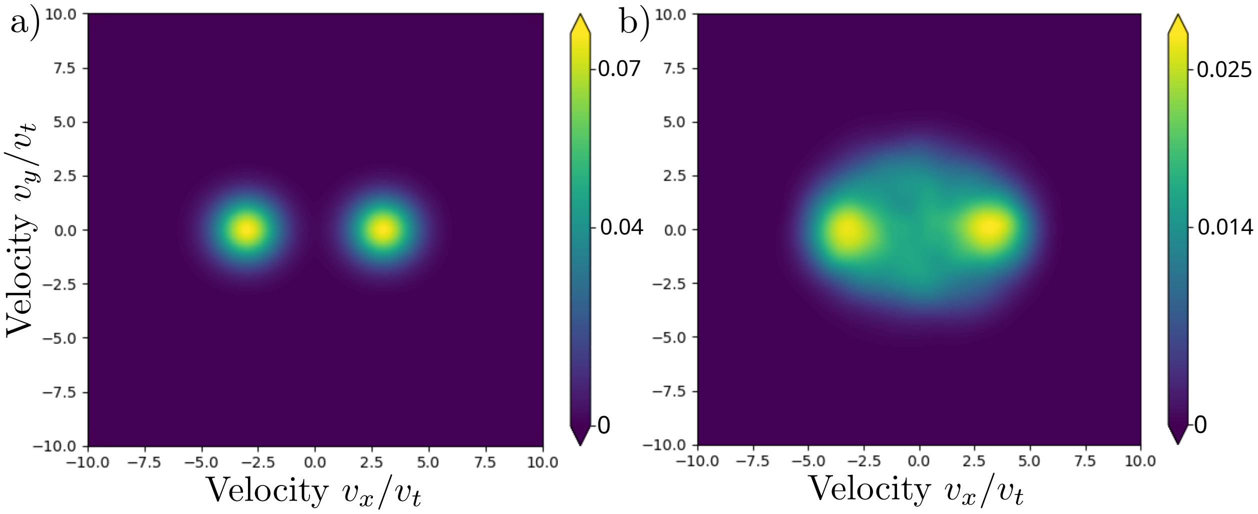

Figure 3.9: Domain-averaged distribution function $\langle f \rangle_{(x,y)}(v_x, v_y)$ showing relaxation to a Penrose-stable distribution on averaged scales due to multidimensional Langmuir turbulence, for a) the unstable initial condition at $t\omega_p = 0$ with beam velocities $\pm 3v_t$, and b) the stop time of the simulation at $t\omega_p = 30$. The average distribution becomes a single double-humped distribution and heats significantly in the direction transverse to the beam axis.

Chapter 4

QUASILINEAR THEORY OF ELECTROSTATIC INSTABILITY

Quasilinear theory (QLT) is the name given to the simplest closure in the hierarchy of equations resulting from separating the variables of a turbulent system into fluctuating and mean components. The scheme of the theory is as follows: a suitable method of averaging is defined, typically temporal, spatial, or ensemble averaging; the dynamical equation is averaged and the mean subtracted from the original equation to obtain the mean and fluctuating components of the system; lastly a closure hypothesis is made by neglecting the "second fluctuation" appearing in the fluctuating equation. The equation for the fluctuation becomes quasilinear and can be solved in spectral space. Substitution into the equation for the mean results in a diffusion equation, a second-order PDE.

4.1 Quasilinear diffusion theory

The quasilinear approximation is the first approximation to velocity-space diffusion in electrostatic turbulence and is a reduction from the Vlasov-Poisson theory [33, 34, 35, 36, 37]. It is mathematically similar to theories of Reynolds-averaging and eddy-viscosity in neutral fluid turbulence [38]. Consider a spatially-periodic domain of length L. Let $\langle f\rangle_L \equiv L^{-1}\int_0^L f dx$ be the spatially-averaged distribution and $\delta f \equiv f - \langle f\rangle_L$ the fluctuation. The kinetic equation is then spatially averaged and the resulting mean equation is subtracted out to obtain an equation for the fluctuation. The two equations for the mean and the fluctuation are then

$$\frac{\partial\langle f\rangle_L}{\partial t} = \frac{\partial}{\partial v}\langle E\delta f\rangle_L \tag{4.1}$$

$$\frac{\partial(\delta f)}{\partial t} + v\frac{\partial(\delta f)}{\partial x} = \frac{\partial}{\partial v}\Big(E\langle f\rangle_L + E\delta f - \langle E\delta f\rangle_L\Big). \tag{4.2}$$

Note that $E = \delta E$ for internal fields, and since the average of a fluctuation is zero, *i.e.* $\langle \delta(\cdot) \rangle = 0$, only the mean of a product of fluctuations contributes as a source to Eq. 4.1. The momentum flux of the fluctuation δf is composed of two terms: the flux from the mean distribution $E\langle f \rangle_L$ and the second fluctuation $E\delta f - \langle E\delta f \rangle_L$. The quasilinear closure is

$$\frac{\partial}{\partial v}\Big(E\delta f - \langle E\delta f\rangle_L\Big) \ll \frac{\partial}{\partial v}\Big(E\langle f\rangle_L\Big), \tag{4.3}$$

transforming Eq. 4.2 into a quasilinear PDE (one linear in its highest derivatives). The quasilinear equations are

$$\frac{\partial \langle f\rangle_L}{\partial t} = \frac{\partial}{\partial v}\Big\langle E\delta f\Big\rangle_L \tag{4.4}$$

$$\frac{d(\delta f)}{dt} = \frac{\partial}{\partial v}\Big(E\langle f\rangle_L\Big) \tag{4.5}$$

with $\frac{d}{dt} = \partial_t + v\partial_x$ the change along a zero-order trajectory. The momentum flux of the background distribution $\langle E\delta f\rangle_L$ is statistically the un-normalized field-particle correlation coefficient [39] and is a tool increasingly used independent of quasilinear theories in the analysis of energy transfer in collisionless plasmas [40, 41, 42, 43]. The quantity $\langle E\delta f\rangle_L$ also has a basic interpretation as the turbulent momentum flux, in analogy to a similar quantity arising in the averaged equation for advection of a passive scalar in a fluctuating velocity field [38]. These interpretations of $\langle E\delta f\rangle_L$ as a correlation coefficient and as a mean turbulent flux are independent of any closure assumptions.

The quasilinear closure amounts to assuming that the field-particle correlation has no variance, or in other words negligible structure inside the averaging box. This assumption is often stated as the random phase approximation as there are no wavepackets, or structure, in white noise. The fluctuating distribution and field are expanded in Fourier series to solve the linear equation for δf as

$$\delta f_n = \frac{iE_n}{\omega(k_n) - k_n v}\frac{\partial \langle f\rangle_L}{\partial v}. \tag{4.6}$$

The covariance $\langle E\delta f\rangle_L$ is converted to a spectral sum by Plancheral's theorem,

$$\langle E\delta f\rangle_L = \frac{1}{L}\int_0^L E\delta f dx = \sum_{n=-\infty}^{\infty} \delta f_n E_n^*. \tag{4.7}$$

Substituting Eq. 4.6 into Eq. 4.7 gives the turbulent momentum flux in the QL closure,

$$\langle E\delta f\rangle_L = \Big(\sum_{n=-\infty}^{\infty} \frac{i}{\omega(k_n) - k_n v}|E_n|^2\Big)\frac{\partial\langle f\rangle_L}{\partial v}. \tag{4.8}$$

As the left-hand side is the mean momentum flux, and the right-hand side proportional to the mean gradient, Eq. 4.8 defines a diffusivity as $\langle E\delta f\rangle_L = D(v)\partial_v\langle f\rangle_L$. In the sense that the quasilinear closure sets the turbulent flux as proportional to the mean gradient this specification of diffusivity is closely related to the eddy viscosity theory in physical space dating to Boussinesq [44]. Now, the simplest equation for the evolution of the spectrum $\mathcal{E}(k)$ is exponential growth (assuming no modal interactions and slow modulations), where the dispersion relation $\omega(k) = \omega_r(k) + i\omega_i(k)$ is taken as the solution to $\varepsilon(\omega, k) = 0$. From all this one arrives at the electrostatic quasilinear diffusion equations [33, 34, 35, 37, 45],

$$\frac{\partial\langle f\rangle_L}{\partial t} = \frac{\partial}{\partial v}\Big(D(v)\frac{\partial\langle f\rangle_L}{\partial v}\Big), \tag{4.9}$$

$$D(v) = \sum_{n=1}^{\infty}\frac{2|\omega_i|}{(\omega_r - k_n v)^2 + \omega_i^2}|E_n|^2, \tag{4.10}$$

$$\frac{d|E_n|^2}{dt} = 2\omega_i|E_n|^2, \quad \varepsilon(\omega, k_n) = 0, \tag{4.11}$$

with the absolute value $|\omega_i|$ following a one-sided time analysis, *i.e.* causality [45]. The equations are intrinsically nonlinear with a self-consistent determination of the dispersion relation key to the system's energy and momentum conservation properties [36]. The analytic solution of $\varepsilon(\omega, k) = 0$ as a complex root can be numerically expensive as $\langle f\rangle_L$ evolves from a sum of Maxwellians to a general form. The dispersion relation can be solved approximately on the real line using the well-known small growth-rate approximation, valid for $\omega_i \ll \omega_r$ [37],

$$\varepsilon_r(\omega_r, k) \equiv 1 + \frac{1}{k^2}\mathcal{P}\int_{-\infty}^{\infty}\frac{1}{\zeta_r - v}\frac{\partial\langle f\rangle_L}{\partial v}dv = 0, \tag{4.12}$$

$$\omega_i = \pi\frac{\partial\langle f\rangle_L}{\partial v}\Big(\frac{\partial\varepsilon_r}{\partial\omega_r}\Big|_{\omega=\omega_r}\Big)^{-1} \tag{4.13}$$

where $\zeta_r = \omega_r/k$ and $\mathcal{P}$ is the Cauchy principal value (P.V.), calculable by Hilbert transform.

4.1.1 The continuous spectrum limit

By defining a spectral density $\mathcal{E}(k) = k_0^{-1}|E(k_n)|^2$ with $k_0 = \frac{2\pi}{L}$ and considering the limit as $L \to \infty$, the quasilinear equations can be modeled with a continuous energy spectrum [37]

$$\frac{\partial f}{\partial t} = \frac{\partial}{\partial v}\Big(D(v)\frac{\partial f}{\partial v}\Big), \tag{4.14}$$

$$D(v) = \int_0^\infty \frac{2|\omega_i|}{(\omega_r - kv)^2 + \omega_i^2}\mathcal{E}(k)dk, \tag{4.15}$$

$$\frac{d\mathcal{E}(k)}{dt} = 2\omega_i\mathcal{E}(k), \quad \varepsilon(\omega, k) = 0. \tag{4.16}$$

The continuous-spectrum approximation is appropriate for large domains and for analysis of the resonant and non-resonant contributions to the diffusivity. A numerical advantage of using a continuous spectrum is that a high-order polynomial representation may be used for the spectral density $\mathcal{E}(k)$. The solution of the dielectric function on the spectral points k_n is typically the most expensive part of a numerical solution. With a high-order representation fewer interpolation nodes are required than the evenly-spaced lattice frequencies of the finite-interval problem. Fewer evaluations of $\varepsilon(\omega, k)$ speed the simulations considerably.

4.1.2 Resonant and non-resonant parts of the diffusivity

The diffusion coefficient is understood to be made up of resonant and non-resonant parts in the limit of slow modulation $\omega_i \to 0$ [35, 37, 46]. In a rather ad-hoc approach, one can apply the Plemelj relation to the linear response, Eq. 4.6, and consider it to be made up of two principal terms,

$$f_{1,n} \to \mathcal{P}\frac{i}{\omega_r - k_n v}E_n\frac{\partial f_0}{\partial v} + \pi\delta(\omega - k_n v)E_n\frac{\partial f_0}{\partial v}. \tag{4.17}$$

The first term represents the non-resonant contribution, the response of the main body thermal plasma particles in sustaining the wave motion (seen in Fig. 4.3(a) as the checkerboard pattern for $v \in (-3, 3)$), while the second term accounts for resonant energy transfer and is the primary contribution to the integration [45, 47]. Having consistently taken the small growth-rate limits, the quasilinear system is usually written as

$$\frac{\partial f}{\partial t} = \frac{\partial}{\partial v}\Big((D^r(v) + D^{nr}(v))\frac{\partial f}{\partial v}\Big), \tag{4.18}$$

$$\frac{d\mathcal{E}}{dt} = 2\omega_i \mathcal{E}, \tag{4.19}$$

$$D^r(v) = \pi \int_{-\infty}^{\infty} \delta(\omega_r - kv)\mathcal{E}(k)dk, \tag{4.20}$$

$$D^{nr}(v) = \text{``}\mathcal{P}\text{''} \int_{-\infty}^{\infty} \frac{\omega_i}{(\omega_r - kv)^2}\mathcal{E}(k)dk \tag{4.21}$$

with "$\mathcal{P}$" the principal value operator. Quotes are used because the principal value operation on the denominator, a term quadratic in a nonlinear function $\omega_r(k)$, is not necessarily well-defined. While it may be tempting to discard the non-resonant diffusivity and evolve only the resonant distribution as it is smaller than the resonant diffusivity by approximately ω_i/ω_r, it was well-phrased by Kadomtsev that the population of nonresonant particles is greater by this same factor and D^{nr} cannot be neglected [45]. The difficulty in a numerical implementation of the resonantly-split quasilinear equations lies in approximating the non-resonant diffusivity. For example, a typical approximation for D^{nr} is constant in velocity [35, 37]. For the problem under consideration there is no need to make this approximation. The numerical solution presented in this article is of the non-split QLT system in Eqs. 4.9 and 4.10.

The quasilinear theory presented and summarized in this section may be called classic QLT. It should be clear that the derivation of classic QLT is ad-hoc, in particular from the construction of the diffusion coefficient and the introduction of the equation for wave energy. Since the work of Ref [47]., where it was suggested that conservation of wave action was more primary than of wave energy, important contributions putting the theory on a rigorous foundation have been made [48, 49, 50]. When Eq. 4.42 is formulated as a wave action conservation law quasilinear theory is naturally connected to the theory of wave kinetics [51] by a transformation to oscillation-center coordinates [52]. In fact, approaches to considering saturated states of plasma turbulence beginning from wave kinetics have proven fruitful [53]. In simple situations the wave action differs from the energy by the factor $\partial_\omega \epsilon_r$, and this factor is approximately constant for the unstable Langmuir waves considered in this article.

For this reason classic QLT is an acceptable approach to the bump-on-tail instability in a homogeneous plasma.

4.1.3 On analytic prediction of the saturated spectrum

Note that as the growth-rate $\omega_i(k_n) \to 0$ the diffusivity corresponding to mode k_n becomes singular, *i.e.* $D(v = \zeta_r(k_n)) = \frac{2}{|\omega_i|}|E_n|^2 \to \infty$. As $\omega_i \propto \frac{\partial f_0}{\partial v}$ the dynamic equation *approaches* a singular diffusion equation in the region of resonant velocities, similar in form to

$$\frac{\partial f}{\partial t} \to \pi^{-1} \sum_{k_n} \partial_v \Big(\varepsilon_r' |E_{k_n}|^2 \frac{\partial_v f}{|\partial_v f|_{v=v_{\phi,k_n}}} \Big). \tag{4.22}$$

Such singular diffusion equations instantaneously flatten the diffusing variable [54], but the singular problem is approached asymptotically in QL theory. The singular behavior of the turbulent diffusivity does not require having taken the small-growth rate limit $\omega_i \to 0$ or having considered a resonant/non-resonant splitting of the diffusivity. From a numerical standpoint the transition from a regular diffusion equation with smooth diffusivity to a near-singular equation with delta-valued diffusivity peaks poses a serious challenge for a numerical time-dependent solution of the QL equations. This is not necessarily a problem for analysis.

A theory is sometimes discussed which analytically predicts the asymptotic state assuming dispersionless waves $\varepsilon = 1 - \omega_p^2/\omega^2$ and only resonant interaction, *i.e.* $D^{nr} = 0$ [45]. From this one can show that, with v_1 the lower limit of the asymptotically flat region,

$$|E_k|^2(t_\infty) = \zeta^3 \int_{v_1}^{\zeta} f(t_\infty, v') - f(t_0, v'))dv'. \tag{4.23}$$

The analysis leading to Eq. 4.23 must be cautioned as approximate because the neglect of non-resonant diffusivity means that the growth rate at the edges of the diffusing region is significantly overestimated, as illustrated in Fig. 4.1 for the considered bump-on-tail problem. Sharp gradients develop in the distribution near the “notch" and “hill" of the bump as seen in Fig. 4.1(a) which would be otherwise filled in by non-resonant diffusion. These sharp gradients correspond to near-singular instability growth rates, as shown in Fig. 4.1(b).

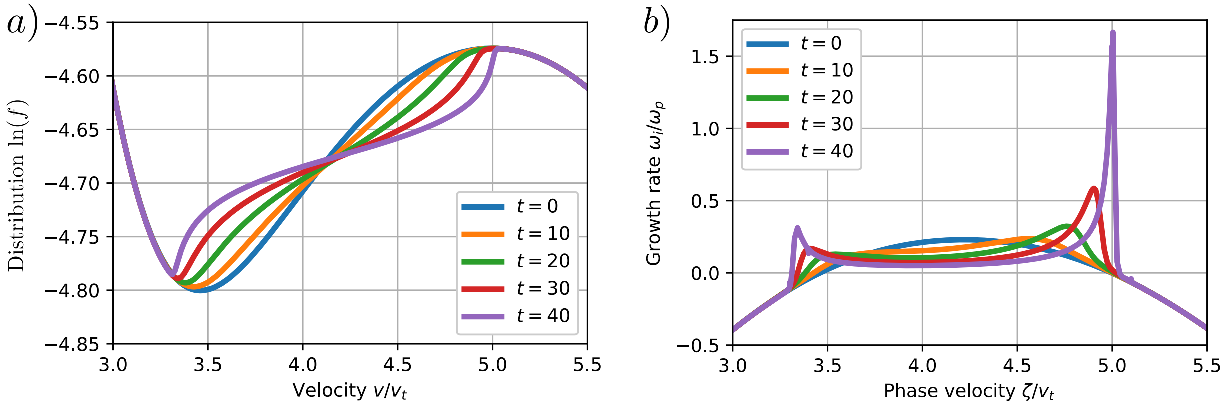

Figure 4.1: Solution of the quasilinear system using only the resonant diffusion coefficient and assuming $\omega = \omega_p$, showing: a) flattening of the distribution function in the region of $\partial_v f > 0$ and b) modal growth rates. Use of only resonant diffusion results in near-singular growth rates at the edges of the diffusing region as sharp gradients develop in the distribution. This means the growth rate is greatly overestimated, and the saturated spectrum is not correctly predicted by Eq. 4.23 across the full breadth of wavenumbers, specifically for non-initially-resonant phase velocities.

4.1.4 Conditions for validity of the QL approximation

A considerable amount of research has been conducted on the conditions under which QL theory should be valid [55, 56, 57], aptly summarized in Ref. [35] and briefly repeated here. The validity conditions center around whether the condition given by Eq. 4.3 is justified so that the fluctuation δf should satisfy a quasilinear equation. The second fluctuation $\delta(E\delta f)$ vanishes unless the wavefield has variance inside the averaging box, *i.e.* localized concentrations of wave energy within wavepackets. On the other hand, if the wave energy were consistently randomly phased then resonant electron trajectories would be random walks. Since some distribution of wavepackets from spectral superposition is inevitable, the condition is generally rephrased as to what extent particles undergo random walks in the wavefield [35]. The quantities of importance for this are: the electron bounce frequency $\omega_b \approx \sqrt{\rho_c}$ with ρ_c the normalized charge density; the wavepacket autocorrelation frequency $\tau_{ac}^{-1} \equiv |(\zeta - v_g)\Delta k|$ with ζ phase velocity, v_g group velocity, and Δk the wavepacket spectral width, describing the timescale on which phase waves remain within a wavepacket; and the distribution relaxation frequency $\tau_r^{-1} \equiv \langle f\rangle_L^{-1}\partial_t\langle f\rangle_L$.

With these quantities, the conditions for validity are that i) the bounce frequency be less than the autocorrelation frequency $\omega_b \ll \tau_{ac}^{-1}$, and ii) the growth rates lie between the relaxation and autocorrelation frequencies $\tau_r^{-1} < \omega_i < \tau_{ac}^{-1}$. Since the growth rates $\omega_i \to 0$, this second condition suggests that the QL theory should saturate asymptotically with $\tau_r \to \infty$. Instability saturation in a finite time violates this condition.

4.2 Quasilinear theory and anomalous resistivity

The origin of dissipation in physics is the correlation of fluctuating fields and sources. When plasma conditions lead to the accumulation of significant fluctuation energy there is a corresponding significant dissipation of energy, momentum, electric current, etc. This section summarizes a general approach to the dissipation of electrical energy in a plasma due to fluctuations and considers approaches to closure using quasilinear kinetic theory.

4.2.1 Macro/micro separation of the kinetic and field equations

In order to understand the dissipative nature of field-particle interactions, consider the collisionless kinetic and field equations for a multi-species plasma in electrostatic approximation,

$$\frac{\partial f_\alpha}{\partial t} + \boldsymbol{v} \cdot \nabla_x f_\alpha + \frac{q_\alpha}{m_\alpha} \boldsymbol{E} \cdot \nabla_v f_\alpha = 0, \tag{4.24}$$

$$\nabla_x \cdot \boldsymbol{E} = \epsilon_0^{-1} \sum_\alpha q_\alpha \int f_\alpha d\boldsymbol{v}. \tag{4.25}$$

Scale separation is considered by defining an average distribution $\langle f \rangle$ and a fluctuating distribution as $\delta f \equiv f - \langle f \rangle$. Averaging the equations in the quasilinear approximation,

$$(\partial_t + \boldsymbol{v} \cdot \nabla_x + \frac{q_\alpha}{m_\alpha} \langle \boldsymbol{E} \rangle \cdot \nabla_v) \langle f_\alpha \rangle = -\frac{q_\alpha}{m_\alpha} \nabla_v \cdot \langle \delta \boldsymbol{E} | \delta f_\alpha \rangle, \tag{4.26}$$

$$(\partial_t + \boldsymbol{v} \cdot \nabla_x + \frac{q_\alpha}{m_\alpha} \langle \boldsymbol{E} \rangle \cdot \nabla_v) \delta f_\alpha = -\frac{q_\alpha}{m_\alpha} \nabla_v \cdot (\delta \boldsymbol{E} \langle f_\alpha \rangle), \tag{4.27}$$

$$\nabla_x \cdot \langle \boldsymbol{E} \rangle = \epsilon_0^{-1} \sum_\alpha q_\alpha \int \langle f_\alpha \rangle d\boldsymbol{v}, \tag{4.28}$$

$$\nabla_x \cdot \delta \boldsymbol{E} = \epsilon_0^{-1} \sum_\alpha a_\alpha \int \delta f_\alpha d\boldsymbol{v}. \tag{4.29}$$

Already in Eqs. 4.24 and 4.25, $\boldsymbol{E}$ is the *mean field* of the plasma, namely an average over the true field whose source is a discrete ensemble of charged particles. In the same way f_α is an averaged or smoothed distribution over the discrete ensemble. Yet having defined this new average $\langle \bullet \rangle$ to accomplish a separation of scales, the averaged field $\langle \boldsymbol{E} \rangle$ may also be called a mean field, now existent on the defined large scale of the plasma. For example, if $\langle \bullet \rangle$ were an average over spatial scales large compared to the Debye length, or electrostatic screening length, then the mean field $\langle \boldsymbol{E} \rangle$ describes macroscopic fields due to macroscopic charge separation in the plasma, while the fluctuating fields $\delta \boldsymbol{E}$ consist of Langmuir and ion-acoustic wave fluctuations. In the general electrodynamic situation one has a full set of Maxwell's equations for both the macroscopic and microscopic (or scale-separated) fields.

4.2.2 The macro/micro moment equations

The correlation of the fluctuating field and plasma, namely $\langle \delta \boldsymbol{E} | \delta f_\alpha \rangle$, appears as a dissipative term on the right-hand side of Eq. 4.26. Therefore the equations describing the transport of mass, momentum, and energy on the macroscopic scale are needed to determine general expressions for the dissipation resulting from the fluctuation correlation. Considering just the equations for the macroscopic number $\langle n_\alpha \rangle$ and momentum densities $m_\alpha \langle n_\alpha \rangle \langle \boldsymbol{u}_\alpha \rangle$,

$$\partial_t \langle n_\alpha \rangle + \nabla \cdot (\langle n_\alpha \rangle \langle \boldsymbol{u}_\alpha \rangle) = 0 \tag{4.30}$$

$$m_\alpha \langle n_\alpha \rangle \frac{d\langle \boldsymbol{u}_\alpha \rangle}{dt} + \nabla \cdot \langle \mathbb{P}_\alpha \rangle = q_\alpha \langle n_\alpha \rangle \langle \boldsymbol{E} \rangle + q_\alpha \int \langle \delta \boldsymbol{E} | \delta f_\alpha \rangle d\boldsymbol{v} \tag{4.31}$$

where $(\langle \mathbb{P}_\alpha \rangle)_{ij} = \int (v_i - u_i)(v_j - u_j) \langle f_\alpha \rangle d\boldsymbol{v}$ is the macroscopic pressure tensor.

Macroscopic generalized Ohm's law

Now consider a two-component proton-electron plasma. The momentum equations are

$$m_e \langle n_e \rangle \frac{d\langle \boldsymbol{u}_e \rangle}{dt} + \nabla \cdot \langle \mathbb{P}_e \rangle = -e \langle n_e \rangle \langle \boldsymbol{E} \rangle - e \int \langle \delta \boldsymbol{E} | \delta f_e \rangle d\boldsymbol{v}, \tag{4.32}$$

$$m_i \langle n_i \rangle \frac{d\langle \boldsymbol{u}_e \rangle}{dt} + \nabla \cdot \langle \mathbb{P}_i \rangle = +e \langle n_i \rangle \langle \boldsymbol{E} \rangle + e \int \langle \delta \boldsymbol{E} | \delta f_i \rangle d\boldsymbol{v}. \tag{4.33}$$

Multiplying the electron equation by $-e/m_e$ and the ion equation by e/m_i, and adding the two together, one obtains the generalized Ohm's law. Approximating macroscopic quasineutrality $\langle n_e \rangle = \langle n_i \rangle \equiv n$, one has

$$\begin{aligned}\partial_t (en(\langle \boldsymbol{u}_i \rangle - \langle \boldsymbol{u}_e \rangle)) = \nabla \cdot (\frac{e}{m_e} \langle \mathbb{P}_e \rangle - \frac{e}{m_i} \langle \mathbb{P}_i \rangle) + \Big(\frac{e^2 n}{m_e} + \frac{e^2 n}{m_i} \Big) \langle \boldsymbol{E} \rangle \\ + \Big(\frac{e^2}{m_e} \int \langle \delta \boldsymbol{E} | \delta f_e \rangle d\boldsymbol{v} + \frac{e^2}{m_i} \int \langle \delta \boldsymbol{E} | \delta f_i \rangle d\boldsymbol{v} \Big).\end{aligned} \tag{4.34}$$

Making the typical MHD approximations of $m_i^{-1} \ll m_e^{-1}$, and letting $\boldsymbol{j} = en(\boldsymbol{u}_i - \boldsymbol{u}_e)$,

$$\partial_t \boldsymbol{j} = \frac{e^2 n}{m_e} \langle \boldsymbol{E} \rangle + \frac{e^2}{m_e} \int \langle \delta \boldsymbol{E} | \delta f_e \rangle d\boldsymbol{v} \tag{4.35}$$

as the generalized Ohm's law where the dissipative term is due to wave-particle interaction.

Two typical cases

In the case with mean field, in the steady state there must be

$$\langle \boldsymbol{E} \rangle = -\frac{1}{n} \int \langle \delta \boldsymbol{E} | \delta f_e \rangle d\boldsymbol{v}. \tag{4.36}$$

Postulating $\langle \boldsymbol{E} \rangle = \eta \boldsymbol{j}$, one has an expression for the anomalous resistivity [58],

$$\eta \boldsymbol{j} = -\Big\langle \delta \boldsymbol{E} \Big| \Big(\frac{\delta n_e}{n} \Big) \Big\rangle \tag{4.37}$$

On the other hand, without mean field (such as a periodic domain), current dissipates as

$$\partial_t \boldsymbol{j} = \epsilon_0 \omega_{pe}^2 \Big\langle \delta \boldsymbol{E} \Big| \Big(\frac{\delta n_e}{n} \Big) \Big\rangle. \tag{4.38}$$

This gives an expression for the rate of dissipation of current due to kinetic relaxation in a problem without external forcing or field.

The quasilinear approximation

The above discussion is true without approximation. However, the theory is not closed as there is no knowledge of the fluctuating fields, density, or their correlation. In the quasilinear closure (in the absence of mean field) one has from solving the fluctuating equations,

$$\langle \delta E | \delta f_e \rangle = \sum_{n=1}^{\infty} \frac{2|\omega_i|}{(\omega_r - k_n v)^2 + \omega_i^2} \partial_v \langle f_e \rangle \equiv D(v) \partial_v \langle f_e \rangle. \tag{4.39}$$

Therefore, the anomalous resistivity is given in terms of the total integrated diffusive flux,

$$\eta j = -\frac{1}{n} \int D(v) \partial_v \langle f_e \rangle. \tag{4.40}$$

In principle this can be calculated while solving a problem in QL theory.

4.3 Quasilinear theory as a first-order system

Numerical solution of diffusion equations can be cumbersome when the diffusivity becomes large. A drawback of QLT posed as a diffusion equation is that the diffusivity becomes infinitely large when considering the relaxation of an unstable system. This singularity arises in the theory around purely real frequencies, which are approached in the relaxed state. This brief study explores an alternative approach to the standard QLT by considering a numerical solution of the theory posed as a system of first-order equations. While there is no dimensionality reduction in this approach there remains a significant advantage over the fully-nonlinear theory in that there is a great reduction in required scale. Only the range of linearly unstable modes must be resolved because there is no turbulent cascade under the quasilinear closure. Neglecting the turbulent cascade is acceptable provided that the energy contained in the turbulent cascade is weak compared to the level of saturated energy in the linearly unstable modes. Under the closure the quasilinear equations are

$$\frac{\partial\langle f\rangle_L}{\partial t} = \frac{\partial}{\partial v}\Big\langle E\delta f\Big\rangle_L \tag{4.41}$$

$$\frac{d(\delta f)}{dt} = \frac{\partial}{\partial v}\Big(E\langle f\rangle_L\Big) \tag{4.42}$$

with $\frac{d}{dt} = \partial_t + v\partial_x$ the change along a zero-order trajectory. As was seen, typically analysis proceeds by a Fourier transformation of Eq. 4.42 and substitution into Eq. 4.41 to study the process as diffusion.

4.3.1 Formulation of the quasilinear equations as a first-order system

To explore an alternative approach to the quasilinear equations and avoid the difficulties discussed previously, consider the solution of Eqs. 4.41 and 4.42 as an initial-value problem for the first-order system. Consider the Fourier expansion of the distribution [2],

$$f(x,v,t) = \sum_{n=-\infty}^{\infty} f_n e^{ik_n x} = f_0 + \sum_{n=1}^{\infty}\Big(f_n e^{ik_n x} + f_n^* e^{-ik_n x}\Big). \tag{4.43}$$

We can identify the DC component as the average distribution, $f_0 = \langle f\rangle_L$ and the remaining Fourier coefficients as the Fourier spectrum of the fluctuation. Then under a Fourier transformation of Eqs. 4.41 and 4.42 the $\delta()$ and $\langle\rangle_L$ symbols may be dropped to write

$$\frac{\partial f_0}{\partial t} = \frac{\partial}{\partial v}\Big\langle Ef\Big\rangle_L, \tag{4.44}$$

$$\frac{\partial f_n}{\partial t} = -ik_n v f_n + \frac{\partial}{\partial v}\Big(E_n f_0\Big). \tag{4.45}$$

for $n \neq 0$. The instantaneous electric field $E(x)$ is determined from Gauss's law as

$$\frac{dE}{dx} = 1 - \int_{-\infty}^{\infty}(\langle f\rangle_L + \delta f)dv = -\int_{-\infty}^{\infty}(\delta f)dv \tag{4.46}$$

$$\implies E_n = \frac{i}{k_n}\int_{-\infty}^{\infty} f_n dv, \quad n \neq 0. \tag{4.47}$$

This system of first-order equations for $f_n(v,t)$ (with the above constraint for E_n) can now be discretized in the velocity v in some way.

4.4 Discretization of the first-order quasilinear equations

Let us discretize the equations of QLT formulated as a system of first-order coupled equations. First, the Fourier series is truncated at a chosen mode number. The x-grid is then identified as the evenly-spaced collocation nodes corresponding to the chosen frequency range. The spatial x-grid is then connected to the spectral k-grid through the fast Fourier transform (FFT). Now consider the two velocity fluxes in the Eqs. 4.44 and 4.45,

$$\mathcal{T}(v) \equiv \langle Ef\rangle_L = L^{-1}\int_0^L E(x)(\delta f(x,v))dx, \tag{4.48}$$

$$\mathcal{M}_n(v) \equiv E_n f_0 = \Big(ik_n^{-1}\int_{-\infty}^{\infty} f_n(v')dv'\Big) f_0(v). \tag{4.49}$$

The x-integration for the flux $\mathcal{T}(v)$ should be evaluated by the trapezoidal rule; because the two functions $E(x)$ and $\delta f(x,v)$ are both periodic functions their product is periodic and the trapezoidal rule acts as a trigonometric quadrature. Therefore $\mathcal{T}(v)$ is computed by trapezoidal rule on the inverse FFT of the two spectral coefficients E_n and $f_n(v)$. On the other hand, the fluxes $\mathcal{M}_n(v)$ depend only on the local field mode E_n and the mean distribution $f_0(v)$. The integral of the fluctuation $f_n(v)$ is found by a quadrature.

Now the v-axis of each equation for the modes f_n is discretized with the DG method. Denoting elements and nodes by indices (m, j), the resulting semi-discrete system is

$$\frac{df_{0,mj}}{dt} = \mathcal{D}\mathcal{T}_{mj} \tag{4.50}$$

$$\frac{df_{n,mj}}{dt} = \mathcal{D}\mathcal{M}_{n,mj} + \mathbb{T}^k_{n,mj} f_{n,mj} \tag{4.51}$$

where the discretized flux divergences are defined as the products

$$\mathcal{D}\mathcal{T}_{mj} \equiv J_m\Big((\Upsilon\mathcal{T})_{mj} - (\Xi\mathcal{T}^*)_{mj}\Big) \tag{4.52}$$

$$\mathcal{D}\mathcal{M}_{n,mj} \equiv J_m\Big((\Upsilon\mathcal{M}_n)_{mj} - (\Xi\mathcal{M}^*_n)_{mj}\Big) \tag{4.53}$$

through the internal and numerical flux divergence operators Υ^k_j and Ξ^k_j and the Jacobian J_m, and the linear translation operator $\mathbb{T}^k_{n,mj}$ discretizes the term $ik_n v f_n$ by quadrature.

Equation 4.51 is an ordinary differential equation consisting of a linear and a nonlinear term. Therefore it is integrated semi-implicitly by the explicit third-order Adams-Bashforth multistep method (AB3) on the nonlinear term and the implicit second-order Crank-Nicholson method on the linear term [1]. Define the half-forward or backward advection operator $A_{F,B}$ as

$$(A_{F,B})^k_{n,mj} = I^k_{n,mj} \pm \frac{\Delta t}{2}\mathbb{T}^k_{n,mj}. \tag{4.54}$$

Then the AB3CN time-marching scheme for the first-order QLT system is written as

$$f^{i+1}_{0,mj} = \Delta t(\mathcal{D}\mathcal{T}^{AB3}_{mj}) \tag{4.55}$$

$$f^{i+1}_{n,mj} = (A_B^{-1})^s_{n,mj}\Big((A_F)^k_{n,mj} f^i_{n,mk} + \Delta t(\mathcal{D}\mathcal{M}^{AB3}_{n,ms})\Big) \tag{4.56}$$

while the AB3 evaluation of a nonlinear operator $\mathcal{N}$ is defined through the present and past two iterations $\mathcal{N}^i$, $\mathcal{N}^{i-1}$, and $\mathcal{N}^{i-2}$ as

$$\mathcal{N}^{AB3} \equiv \Big\{\frac{23}{12}\mathcal{N}^i - \frac{4}{3}\mathcal{N}^{i-1} + \frac{5}{12}\mathcal{N}^{i-2}\Big\} \tag{4.57}$$

4.5 Numerical methods for quasilinear theory as a diffusion equation

The QL diffusion equation is discretized in velocity using the local discontinuous Galerkin (LDG) method [21] as high resolution and accuracy is needed in the region of resonant velocities when the diffusivity becomes highly peaked. A small modification in the LDG method is made to account for the nonlinearity of the system appearing as, defining $q \equiv \partial_v f$, the flux $F = D(v)q(v)$ being a product of two interpolated functions. The modification from the usual linear LDG method is that the Galerkin matrix elements on the right-hand side of the semi-discrete equation are computed by an exact quadrature of the products of the interpolation polynomial basis for both $D(v)$ and $q(v)$.

The grid nodes of high-order DG methods are not evenly spaced, so the Hilbert transform used to compute the principal-value integral in the small-growth rate approximation for $\varepsilon(k,\zeta)$ cannot be done using FFTs or most other methods discussed in the literature. Instead the principal value integral is determined by a quadrature approximation of the velocity Fourier coefficients to form the analytic signal, and the P.V. integral extracted as its imaginary part. This is not an optimal approximation but it works sufficiently well on the existing grid provided that the distribution is represented to high-enough velocity in the tail regions to be effectively zero. For this reason velocity-space is resolved from $v = (-20, 30)$ with one hundred finite elements. Each element contains a ninth-order polynomial basis on Lobatto quadrature node interpolants. Only twenty elements are used in the tails, with eighty elements spanning $v \in (2, 10)$. A Fourier-by-quadrature evaluation of the Hilbert transform is not computationally time-limiting as the P.V. integral needs to be evaluated only once per timestep. Rather, the nonlinear solution to $\varepsilon(k,\zeta) = 0$ for each lattice frequency k is typically the computational time-limiting factor.

With the P.V. integral determined, the dielectric function $\varepsilon(k,\zeta)$ is evaluated as a function of arbitrary phase velocity ζ via the Vandermonde matrix of the quadrature grid's interpolation polynomials. After solution with a nonlinear solver to obtain the phase velocity root to $\varepsilon(k,\zeta) = 0$ corresponding to the unstable wave branch, the gradient $\varepsilon'(k,\zeta)$ on the interpolated point is found using the local derivative matrix. Further computing the interpolated gradient of the distribution function, this determines the approximate linear growth rates $\omega_i(k)$ by Eq. 4.13. Since the velocity space is highly resolved the discretization is limited in accuracy by the $\mathcal{O}\left(\frac{\omega_i}{\omega_r}\right)$ expansion of ε.

As the distribution flattens and $\omega_i \to 0$ the diffusivity becomes highly peaked. Use of an implicit time integration scheme is necessary to avoid restrictive CFL-limited timestepping and avoid dispersive errors, as such oscillations feedback into the growth rate calculation. A second-order implicit midpoint method is used to evolve the diffusion equation. As the diffusivity nonlinearly depends on the distribution, a nonlinear global solve is avoided by taking an approximate explicit half-step in wave energy to the midpoint with a sufficiently small time-step. The diffusion equation is then solved by the implicit midpoint method. That is, with the semi-discrete QL system as

$$\frac{df}{dt} = A(E)f \tag{4.58}$$

$$\frac{dE}{dt} = 2\omega_i(\partial_v f)E \tag{4.59}$$

where A represents the discretized diffusion operator and $E = |E_k|^2$ the spectral energy,

$$E_{n+1/2} = E_n \exp(h\omega_i(\partial_v f_n)), \tag{4.60}$$

$$A_{n+1/2} \equiv A(E_{n+1/2}), \tag{4.61}$$

$$f_{n+1} = (I - \frac{h}{2}A_{n+1/2})^{-1}(I + \frac{h}{2}A_{n+1/2})f_n \tag{4.62}$$

where h is the time-step. The calculations use $h = 0.1\omega_{pe}^{-1}$ for the time-advance.

4.6 On the validity of quasilinear theory applied to the bump-on-tail instability

One-dimensional electrostatic turbulence is among the oldest model problems in plasma physics and stimulated the development of the quasilinear theory (QLT) of plasma diffusion [33, 34, 59]. Quasilinear diffusion theories are used to predict the statistical properties of turbulent energy and the plasma distribution function in the saturated state of high-dimensional dynamic processes such as velocity space instability with a reduced low-dimensional model. Quasilinear methods have been widely applied to model turbulent diffusion in both physical and velocity space (*e.g.* gyrokinetic modeling [60], rotating Couette flow [61], lower-hybrid drift instability [62], firehose instability [63], electron interaction with whistlers [64], etc.), often reproducing experimental phenomena beyond the theory's formal region of validity [65].

Quasilinear theory is concerned with the dynamics of macroscopic observables such as spatially-averaged quantities and the fluctuation power spectrum. It is applicable for weak turbulence, *i.e.* a broad spectrum of small-amplitude non-self-correlated linear waves in a homogeneous medium [66, 35]. In order that phase interference, or wave beating, not lead to nonlinearity it is also necessary to suppose random phasing of the waves [46]. However the random phase approximation is somewhat fictional because the spectral width of unstable wavenumbers is finite. Interference of finite spectral width produces a spatial distribution of wave energy (wavepackets) even for random phases. For example the two-species numerical study in [67] saw the late-time development of Langmuir cavitons from an initial ensemble of randomly-phased linear waves. The high amplitudes of wavepacket potentials lead to deviations from quasilinear predictions as linear waves grow from instability [68].

Nevertheless quasilinear theory makes accurate predictions of the saturated state of instability despite the breakdown of the random phase approximation. This article demonstrates by a direct simulation of an electron bump-on-tail instability for which quasilinear theory should be applicable that weak nonlinearity due to spatial structure in the distribution of wave energy enhances the rate of turbulent flux above quasilinear levels. However the effect of this discrepancy is to reach a similar saturated state as the quasilinear prediction, but in a finite time rather than asymptotically with corresponding corrections to the transient linear growth rates and with significant fluctuations in the probability distribution function atop the quasilinear equilibrium. The success of quasilinear theory is in prediction of the greatest amplitude part of the field spectrum as this portion is due to linear growth. On the other hand, the quasilinear prediction does not capture some aspects of the weak kinetic turbulence spectrum such as plasma wave harmonics and the eddy turbulence of resonant particles, *i.e.* phase space granulations.

Many numerical studies have been done comparing quasilinear analysis to solutions of the Vlasov equation using particle-in-cell (PIC) method [69, 70, 71]. Yet it is well-known that PIC methods are prone to errors due to statistically sampling the sensitive trajectories of the continuous distribution [72, 73, 74], so it is worthwhile to explore alternative kinetic modeling methods. In one such alternative the equation for the continuous distribution is solved by a demonstrably convergent and conservative finite element discretization of phase space, using for example discontinuous Galerkin methods [75, 76, 77]. This section uses a high-order discontinuous Galerkin method to sufficiently resolve the detailed phase flow up to and past saturation of the kinetic instability. From this point of view the turbulent nature of resonant electrons, and the distinct behavior of resonant and non-resonant electrons, can be clearly seen.

4.6.1 Initialization of many discrete linear modes

An unstable distribution which should meet the applicability conditions of quasilinear theory consists of a hot drifting Maxwellian through a main thermal population

$$\begin{split} f_0(v) = \frac{1}{(1+\chi)\sqrt{2\pi}}\Big\{\frac{1}{v_{t0}}\exp\Big(-\frac{v^2}{2v_{t0}^2}\Big)+ \\ \frac{\chi}{v_{tb}}\exp\Big(-\frac{(v-v_b)^2}{2v_{tb}^2}\Big)\Big\}. \end{split} \tag{4.63}$$

The bump-on-tail instability is the textbook example of a distribution with quasilinear evolution. According to Ref [37]., reasoning by the Bohm-Gross dispersion relation, instability development should be in the weak turbulence regime given a bump fraction $\chi = 0.05$, bump spread $v_{tb} = \chi^{1/3}v_b$, and beam velocity $v_b = 5v_{t0}$. Velocities are then normalized to $v_{t0} = 1$. Figure 4.2 shows the unstable branch of $\varepsilon(k,\zeta) = 0$ corresponding to the coupling of right-going oscillations of the main body and left-going oscillations on the drifting beam. The unstable spectrum somewhat corresponds to the expected mode content of the saturated instability, though both a spread of the unstable range and a shift in the highest growth-rate mode accompany relaxation of the bump-on-tail.

The Vlasov-Poisson simulation is initialized as a sum over the eigenmodes,

$$g(x,v) = f_0(v) + \sum_n \frac{\alpha_n}{k_n}\mathrm{Re}\Big(\frac{1}{\zeta_n - v}e^{i(k_n x+\theta_n)}\Big)\frac{\partial f_0}{\partial v} \tag{4.64}$$

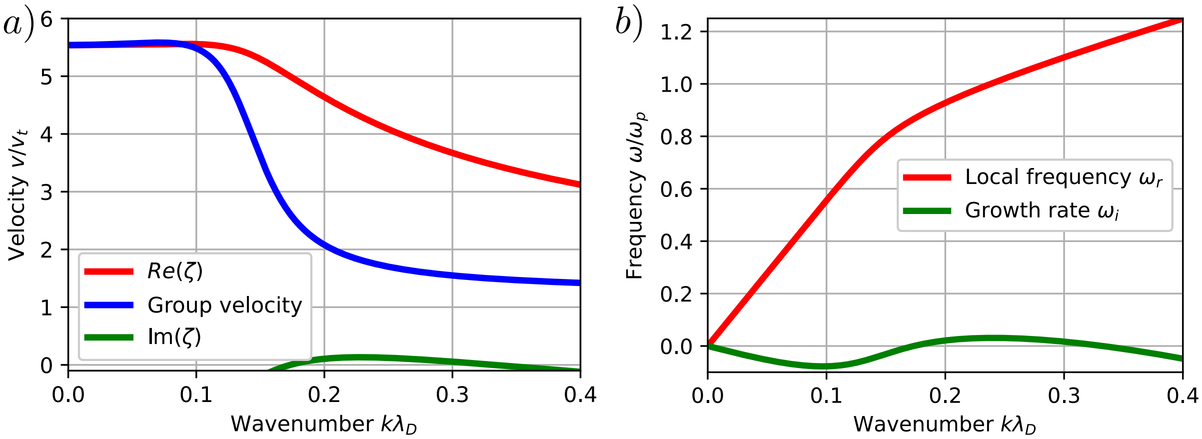

Figure 4.2: Bump-on-tail dispersion relation showing: a) wave velocities; and b) frequencies. The bump-on-tail distribution has an unstable branch of solutions with phase velocities bounded by the regions of $\frac{\partial f_0}{\partial v} > 0$ in the tail, in this case for $v \in (3,5)v_t$. The unstable solution is an electron-acoustic wave at the beam velocity for long wavelengths and an acoustic wave propagating at the bulk thermal velocity for short wavelengths. This unstable coupled acoustic wave is damped at both extremes and has maximum instability growth where the frequency $\omega \approx \omega_p$.

where each ζ_n with $\mathrm{Im}(\zeta_n) > 0$ is the solution to $\varepsilon(k_n, \zeta_n) = 0$, the factor θ_n is a random phase shift, and α_n is the field amplitude. The factor k_n^{-1} sets each initialized mode's field energy to $|E_n|^2 = \alpha_n^2$. Figure 4.3 shows the perturbation on a domain of $L = 5000\lambda_D$ initialized in this manner. The initial condition is chosen in this way to avoid exciting the other damped branches of $\varepsilon(k, \zeta) = 0$, as the quasilinear theory studies the unstable wave branch.

4.6.2 Analysis of quasilinear and nonlinear evolution of the bump-on-tail

Here the Vlasov-Poisson and quasilinear simulations are analyzed, and the discrepancy between the two simulations explored. Both results use the initial background distribution specified in Eq. 4.63 and suppose a domain length of $L = 5000\lambda_D$. Section 4.6.3 makes some comments on the choice of initial condition. A comparison of the turbulent flux is made in Section 4.6.4, along with a discussion on the fluctuations in the field-particle correlation $\langle \delta f E\rangle_L$ responsible for deviation from quasilinear diffusion. Section 4.6.5 analyzes the role of phase space structures in the solution of the Vlasov equation followed by an analysis of the validity conditions as discussed in Section 4.1.4.

4.6.3 On the choice of initial energy spectrum

The dynamic behavior of the quasilinear system as an initial value problem depends on the choice of initial condition, because the spatially-averaged distribution $\langle f\rangle_L$ and also the initial energy spectrum $|E_k|^2$ are free to be specified. All modes must be energized as change takes place only through linear growth or damping. A variety of choices exist for the initial distribution of spectral field energy $|E_k|^2$. A possible choice is a constant energy in all modes E_k with random phases, *e.g.* a white noise. Yet one cannot put energy into damped “eigenmodes" of the Vlasov-Poisson system without exciting the other branches of the kinetic dispersion relation, as Landau-damped modes are not true eigenfunctions [25]. If initialized, damped kinetic modes can couple into the dynamics of growing modes. For example, Fig. 4.4 shows the temporal change of domain-integrated electric and kinetic energies in the development of the instability. If perturbations other than eigenmodes are initialized then the

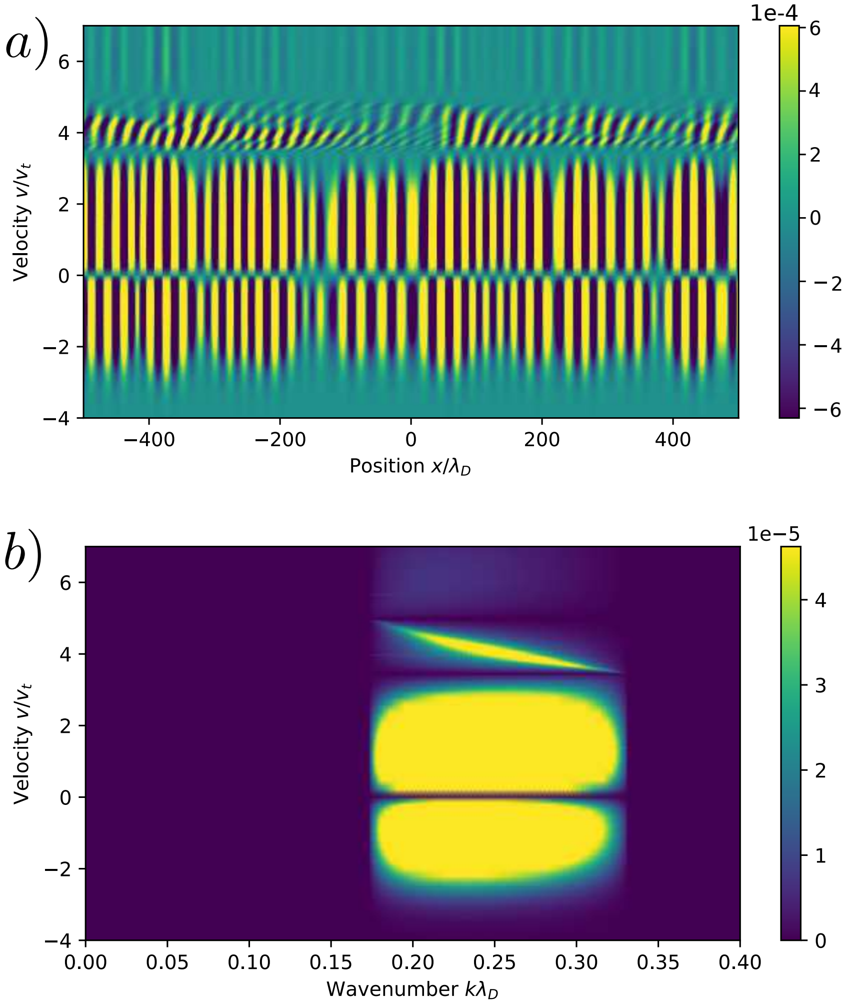

Figure 4.3: a) The perturbation is shown in phase space representation as a subset of the full domain, which has $5000\lambda_D$ length and spans velocities $v \in (-25, 25)$. The main thermal body ($v \in (-3, 3)$) supports coherent plasma oscillations while the modes in the resonant band ($v \in (3, 5)$) appear randomly phased. The unstable modes are rightward-propagating so the non-resonant distribution of positive velocity ($v \in (0, 3)$) oscillates with greater energy than the negative velocity part. Wavepackets in the initial condition are seen as regions of greater amplitude.

b) The Fourier amplitudes as $\log(1 + |f|)$ of the perturbation. Spectral energy is peaked along a coherent crescent shape bridging the band of unstable velocities.

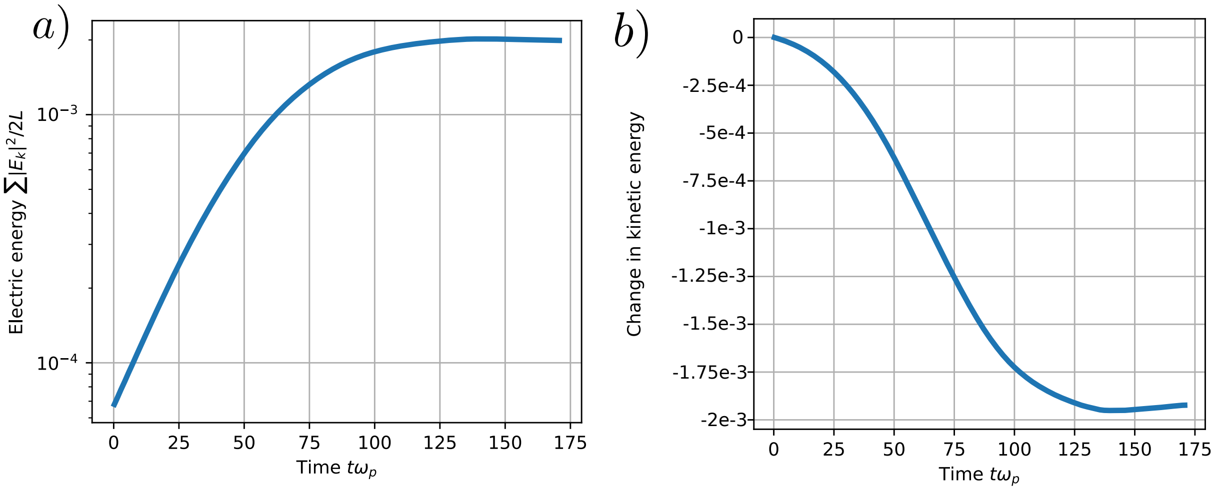

Figure 4.4: Domain-integrated energy traces for the length $L = 5000\lambda_D$ Vlasov-Poisson simulation of: a) electric field energy and b) change in kinetic energy. The bump relaxes as electrons release free kinetic energy. A typical feature of nonlinear saturation is an overshoot of equilibrium and slow nonlinear evolution, seen here as an increase in kinetic energy past saturation at $t\omega_p \approx 125$. An artificial hyperviscosity is applied for wavenumbers $k\lambda_D > 1$, but total energy per unit length is conserved to $\mathcal{O}(10^{-7})$.

domain-integrated energy will oscillate as it grows in time. The Vlasov-Poisson simulation is perturbed only by unstable modes for better comparison to quasilinear theory.

Initialization of constant energy across all modes results in a cusped diffusivity profile, nearly discontinuous at the edges of the resonant velocities, because some wavenumbers have near-zero growth rates. Because of this cusp effect the energy spectrum is initialized in both simulations to match a scaled version of the positive growth rates with the maximum $\alpha_n^2 = 10^{-6}$ in Eq. 4.64. In the quasilinear system the damped part of the spectrum is initialized to the minimum positive growth rate in order that the initial spectrum is continuous.

4.6.4 Comparisons of turbulent diffusivity and momentum flux

Primary quantities of interest in phase space turbulence are the velocity-space diffusivity and the turbulent momentum flux $\langle E\delta f\rangle_L$, in particular its profile and magnitude, in the regions of resonant and non-resonant velocities. Based on Eq. 4.8, a turbulent diffusivity can be estimated from the Vlasov-Poisson simulation by decomposing the distribution into a component that is averaged over physical space $\langle f\rangle_L$ and a component fluctuating about this average, $\delta f = f - \langle f\rangle_L$. Then diffusivity is estimated as

$$D_{\text{estimated}}(v) \equiv \frac{\langle E\delta f\rangle_L}{\partial_v \langle f\rangle_L} \tag{4.65}$$

as the turbulent momentum flux normalized to the gradient of the background distribution.

The variation of diffusivity with velocity is important for the change in $\langle f\rangle_L$ in the tail region, with the two simulations compared in Fig. 4.5 to an intermediate time in the simulation. The main thermal body is non-resonantly heated primarily in positive velocities. The “notch" or depression between the main thermal body and the bump in $\langle f\rangle_L$ is in this way filled in by diffusion from near-resonant, but not fully resonant, velocities.

Figure 4.6 shows the Vlasov-Poisson and quasilinear velocity-space diffusivities in the resonant (a-b) and non-resonant regions (c-d), demonstrating that quasilinear theory correctly predicts the shape and early development of the profile of turbulent diffusivity, but later presents an underestimate. By $t\omega_p = 50$ the velocity-space diffusivity is underestimated

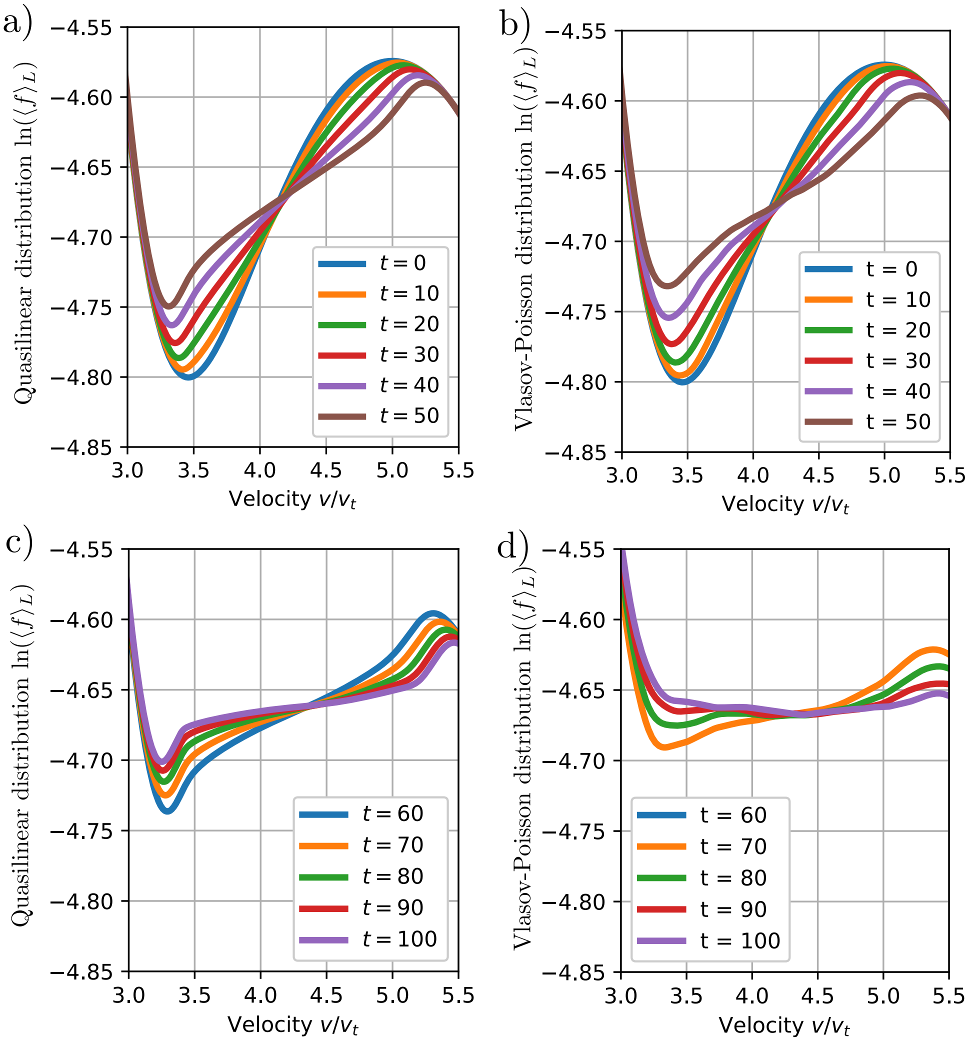

Figure 4.5: Diffusion of the distribution function in the tail region, (a), (c) in simulation of the quasilinear theory and (b), (d) in the Vlasov-Poisson simulation. Evolution up to time $t\omega_p = 50$ is shown in parts (a) and (b), while times up to $t\omega_p = 100$ are shown in parts (c) and (d). Up to time $t\omega_p = 30$ the quasilinear solution agrees closely with the Vlasov solution, though by $t\omega_p = 50$ the Vlasov-Poisson simulation has a noticeably smoother profile as the diffusivity has grown significantly greater than the quasilinear value. In later times the Vlasov evolution has a non-diffusive, fluctuating charater. By $t\omega_p = 90$ the Vlasov simulation has completely filled in the low-velocity notch, while the quasilinear simulation maintains a steep notch area.

by between 30–100%. Regarding the non-resonant diffusivity, Fig. 4.6(c-d) shows that this value varies by an order of magnitude across the positive velocities of the main thermal body, becoming smaller for negative velocities.

For later times in the Vlasov simulation fluctuations of $\langle f\rangle_L$ make the diffusivity estimate unreliable as its gradient oscillates. This happens to occur as the two models begin to diverge and the diffusive closure breaks down. A smoother quantity to compare is the covariance, or turbulent flux, $\langle E\delta f\rangle_L$. Figure 4.7 compares the quasilinear turbulent flux to that of the Vlasov-Poisson simulation. This figure shows that the flux in the region of non-resonant velocities close to the resonant region around $v \approx [3, 6]$ is underestimated by quasilinear theory. This enhanced turbulent flux flattens the extreme regions of the unstable distribution, meaning the "notch" and "bump" of the evolving tail. These two regions are flattened asymptotically in the quasilinear model. The effect of this enhanced diffusion is to quench the instability in a finite time, in contrast to quasilinear theory's asymptotic approach to quenching. This is seen as the saturation of electric energy in Fig. 4.4(a).

4.6.5 Analysis of phase space structures in the Vlasov-Poisson simulation

The beginning of the chapter reviewed quasilinear theory and highlighted parallels to models of eddy viscosity in the turbulence of an incompressible fluid. In such eddy viscosity models a passive scalar is mixed by its partial participation in an ensemble of fluid eddies, resulting in a diffusive character to the scalar's averaged profile. By observing the phase flow within the averaging box a similar structure of eddies is observed due to phase fluid resonantly interacting with phase waves.

Section 4.6.4 shows that the Vlasov simulation evolves in two phases, at first in agreement with quasilinear diffusion and later diverging as wave energy increases. Figure 4.8 shows the development of the fluctuation δf at an early time corresponding to quasilinear evolution for a domain of $L = 1000\lambda_D$. Phase fluid mixes without the formation of closed eddies. A shorter domain was chosen here to present a complete picture which can be reasonably viewed as a whole. The simulation in Fig. 4.8 uses 5000 spatial nodes and does not use spatial

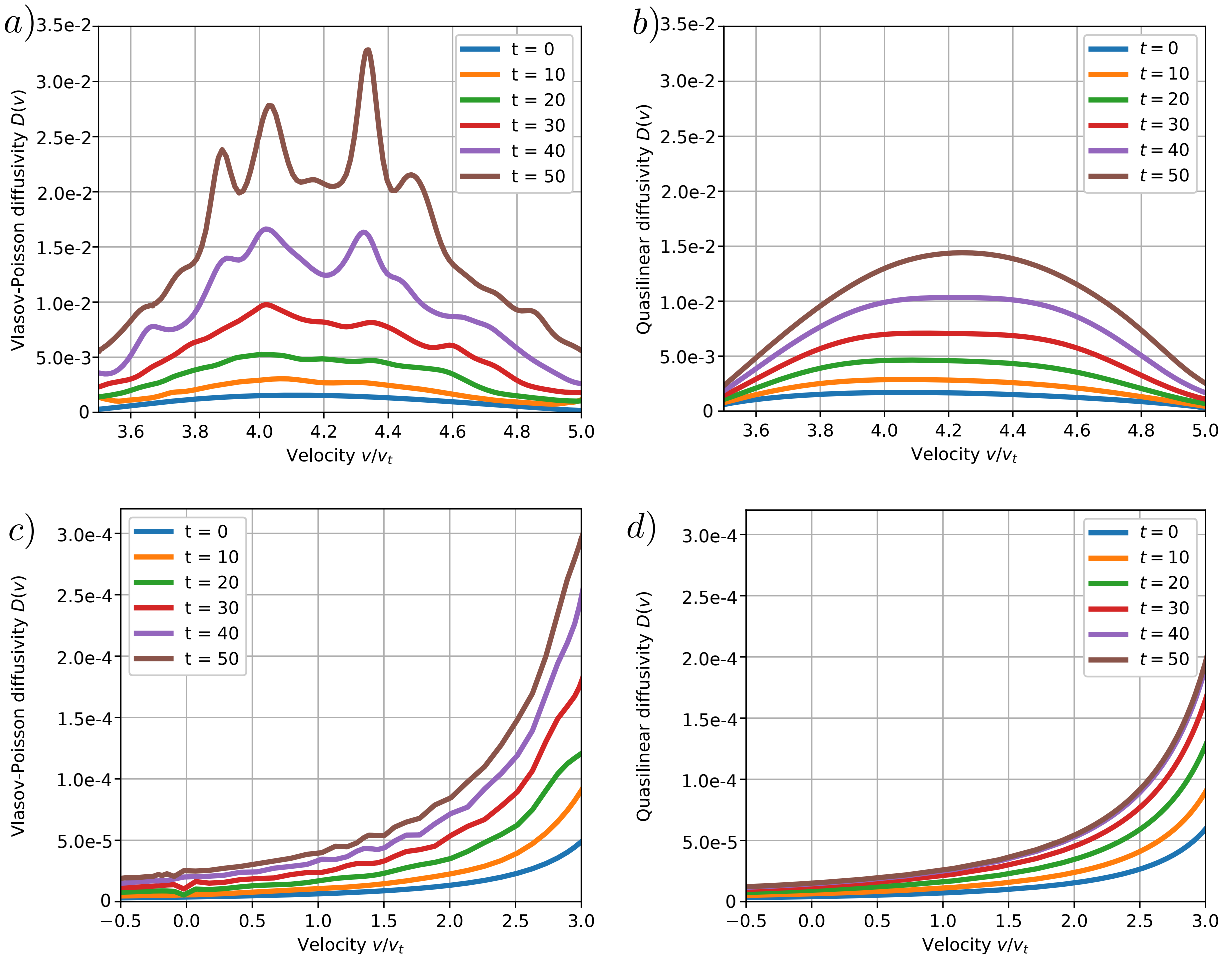

Figure 4.6: Evolution of diffusivity $D(v)$ in: (a-b) the region of resonant velocities; and (c-d) for non-resonant velocities in the main thermal body. The diffusivities agree well until around $t\omega_p = 40$, where they diverge significantly. A key difference is the width of the diffusing region, as the Vlasov simulation diffusivity at the resonant edges ($v = 3.5$ and $v = 5$) is twice as large as the quasilinear prediction. Note that wave energies, plotted in Fig. 4.4, are not yet at nonlinear levels. By $t\omega_p = 50$ non-resonant diffusivity of the Vlasov-Poisson simulation in (c) is roughly 30% greater than the diffusivity in (d) predicted by quasilinear theory for the $L = 5000\lambda_D$ interval. Diffusivity is not plotted beyond $t\omega_p = 50$ as the the Vlasov-Poisson diffusivity (estimated by Eq. 4.65) becomes incoherent when the simulation diverges from QLT.

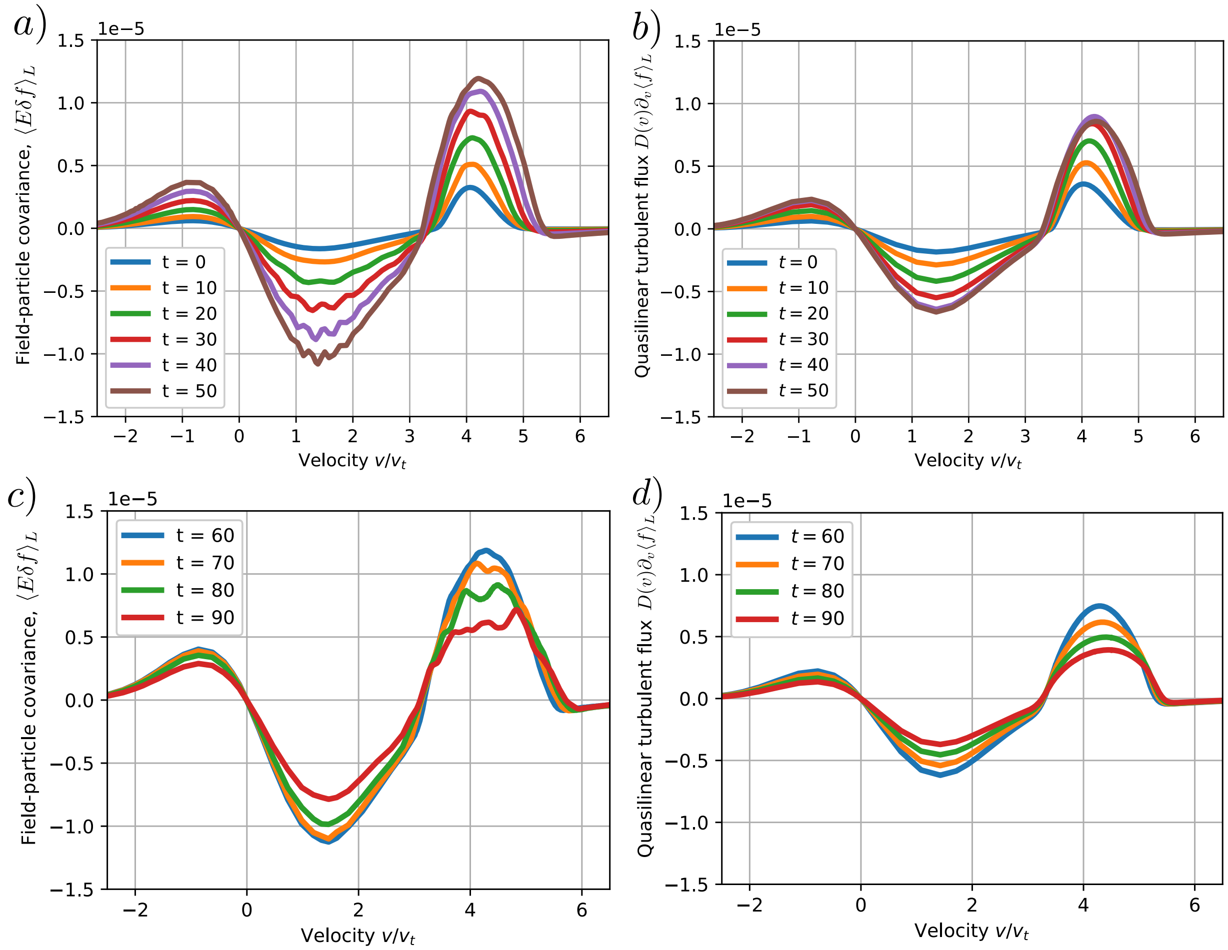

Figure 4.7: Time-evolution of the field-particle correlation, or equivalently turbulent momentum flux of the averaged distribution function, for (a, c) the Vlasov-Poisson solution and (b, d) the quasilinear solution. The turbulent flux of both systems peaks around $t\omega_p = 50$ for this initial condition, yet the observed flux of the Vlasov simulation is significantly greater than the quasilinear value for all times beyond $t\omega_p = 30$. The amplitudes of the functions E and δf both increase as the variance $\langle E\delta f\rangle_L$ of the functions spreads. In quasilinear theory the increase in this variance causes the increase in the fluctuating component of the distribution δf.

hyperviscosity. Note that the checkerboard pattern of the plasma oscillations is similar to the eigenmodes discussed in Section 3.1 and visualized in Fig. 4.3.

The Vlasov simulation begins to disagree with quasilinear theory as phase space eddies form. These eddies are also referred to as clumps or granulations and are a central ingredient of the theory of phase space structures [78, 79, 80]. These structures can be roughly divided into coherent (eigenmode-like) and incoherent (eddy-like) parts. This section discusses the dynamics of the eddy-like part of the fluctuation. An extensive textbook discussion of granulations and their role in phase space turbulence can be found in Chapter 8 of Ref [35]. Of course the analogy to eddy-viscosity models is only partial since phase space eddies account only for resonant diffusion; it is well-known from theory that coherent oscillations of the main thermal body are responsible for energy transfer at non-resonant velocities [47, 81].

Eddy analysis of the direct Vlasov simulation

One might expect each linear mode to evolve independently until terms nonlinear in the wave amplitude dominate the dynamics. Yet as seen in the Fourier spectrum of the fluctuating component of the distribution in Fig. 4.9(b), instability development leads to a broadening of the initialized coherent crescent shape in the distribution spectrum $f(k, v)$ and the gradual development of a power law in these Fourier coefficients around the resonant band of velocities. Initial broadening of the Fourier spectrum in the linear phase of the instability, representing evolution of fine structures in the band of resonant velocities from reaction on the mean momentum flux, is the essence of the quasilinear effect. However the power law seen in Fig. 4.9(a) represents turbulent features not captured by the quasilinear approximation.

An analysis of phase space eddies reveals how quasilinear closure breaks down as this resonant-velocity power law from turbulent eddy mixing develops. Eddies consist of electron phase fluid oscillating in a local potential well. The typical electron bounce frequency at saturation, measured as the rms charge density fluctuation, is $\omega_b \approx 0.1\omega_p$, extending to bounce frequencies of $\omega_b \approx 0.2$–$0.4\omega_p$ in the largest amplitude wavepackets. This gives a range of eddy turn-over times from $\tau_b\omega_p \approx 15$–$60$. Resonant particles do not experience a

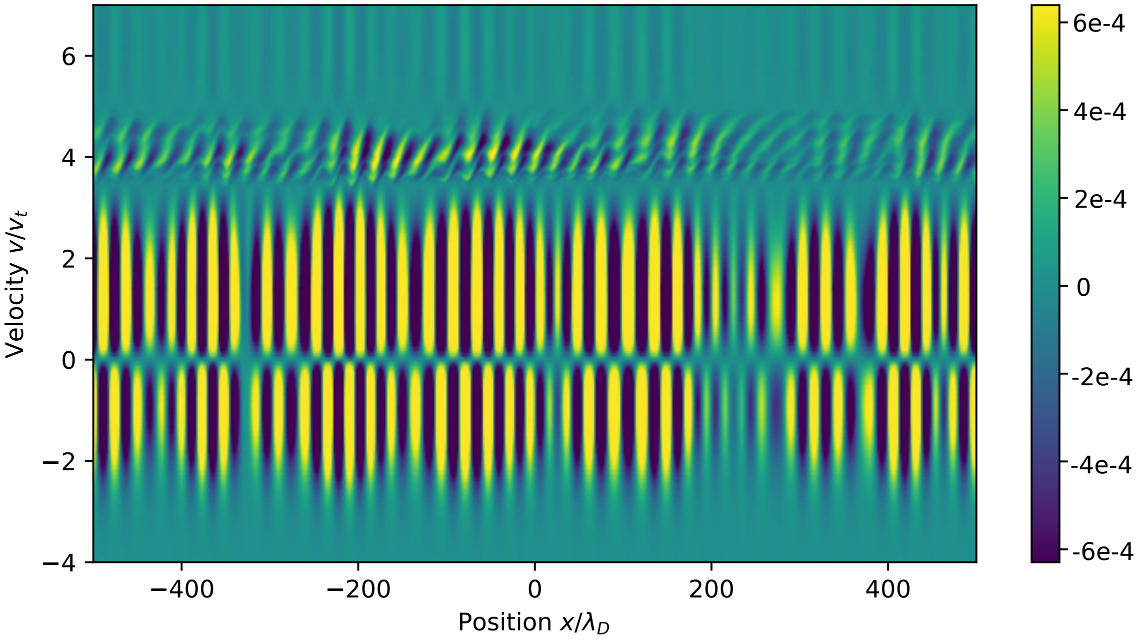

Figure 4.8: The fluctuation in the distribution function, $\delta f \equiv f - \langle f \rangle_L$, of a Vlasov simulation is plotted during the quasilinear phase of evolution at $t\omega_p = 10$. A short domain ($L = 1000\lambda_D$) is shown in order that the whole flow can be observable at once. A clear distinction can be made between resonant and non-resonant parts of the fluctuation. Non-resonant velocities undergo coherent oscillations (seen as the striped pattern) while phase fluid at resonant velocities ($v \in (3, 5)$) is accelerated by randomly-phased waves. These structures are consistent with quasilinear evolution.

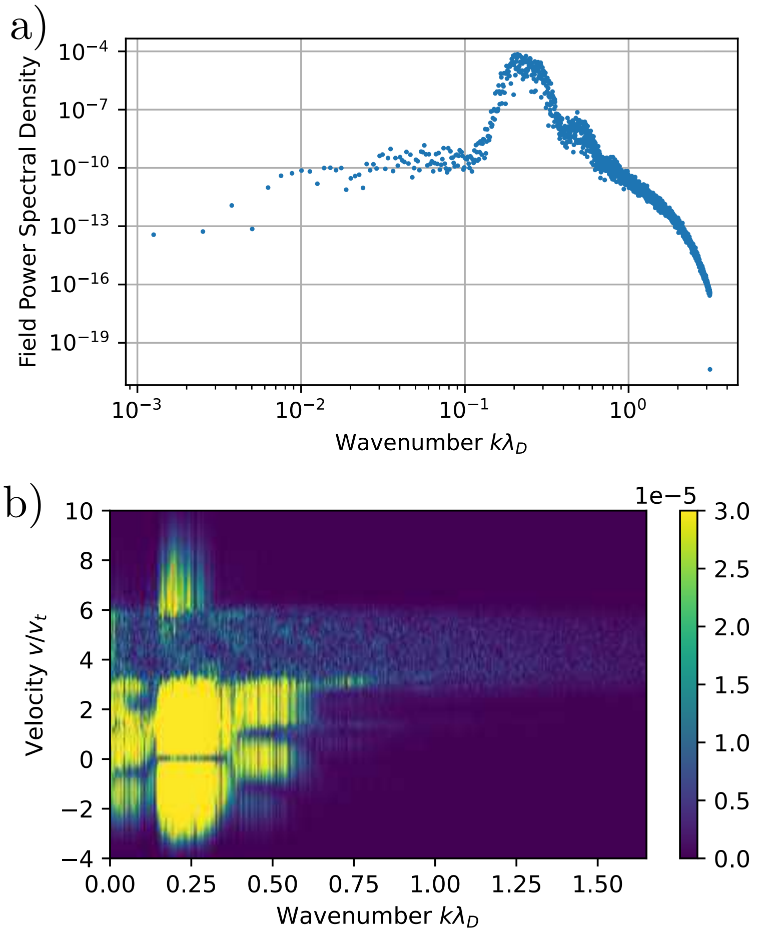

Figure 4.9: a) The field spectrum $|E_k|^2$ of the Vlasov simulation averaged from $t\omega_p = 140$–170, consisting of two peaks at $k\lambda_D \approx 0.25$ and 0.5, as well an inertial range-like power law for $k\lambda_D \gtrsim 0.6$. The primary peak is due to the saturated instability and the secondary peak to its first harmonic. The spectral knee and dissipation around $k\lambda_D = 2$ is due to the artificial hyperviscosity.

b) Fourier-decomposition of the distribution function at $t\omega_p = 170$, shown in logarithmic view as $\log(1 + |f|)$ and with the maximum of the colorbar set to 5% of the largest spectral amplitude. This demonstrates that the high-k power law is due to eddy turbulence of resonant electrons, while the energy-containing oscillations are present in the population of non-resonant electrons.

full period of bounce motion, as phase fluid transits each potential well in a time

$$\tau_{\text{transit}} \equiv \frac{\lambda}{v - v_g} \tag{4.66}$$

with v the local phase fluid velocity, v_g the wavepacket group velocity, and λ the width of a wavepacket potential trough. In the simulation considered the width of a wavepacket potential trough is roughly $\lambda \approx 10\lambda_D$, the group velocity of wavepackets roughly one thermal velocity, and the velocities of resonant particles $v \approx (3, 6)v_t$ (here estimated as greater than the original $v \in (3, 5)v_t$ as the resonant region expands with time). This gives transit times of $\tau_{\text{transit}}\omega_p = 2$–$5$. Thus groups of resonant particles in the mixing layer participate in between 3–30% of a typical phase space eddy motion per trough. However, since the potential profile is similar in each wavepacket trough, and the clump enters the trough approximately as it left, a rotating clump can turn over in the process of passing through multiple potential troughs. In this way a clump of phase fluid is progessively distorted by its passage through the potential profile of a wavepacket and trajectories randomized by the process of phase mixing in a nonlinear potential.

Visualization of phase space eddy turnover in a single-time snapshot

A recurrence effect allows this progressive eddy turnover to be visualized in a single-time snapshot of the phase flow. To understand the recurrence effect, consider the fluctuation's autocorrelation function $\langle \delta f(x, v, t)\delta f(x - v_g\tau, v, t - \tau)\rangle_L$ [35], plotted in Fig. 4.10 for resonant velocities during early quasilinear evolution and a later time when evolution deviates from quasilinear diffusion. During the quasilinear phase the autocorrelation signature is sinusoidal but during later evolution the signature changes to that of a structure repeating at the plasma frequency. The repeating signal corresponds to a temporal similarity in the phase flow. That is, one can approximately trace the past and future behavior of a phase space clump in a given potential well by looking at the neighboring potential wells because clumps transit between wells in approximately one plasma period. Figure 4.11b shows this effect in detail, tracing the approximate future state of a clump as it transits a wavepacket with a series of small circles. In the way visualized, resonant particle mixing becomes governed by progressive eddy turnover through the distinct potential wells of a wavepacket. The eddies visualized are not trapped in any particular potential well.

The phase fluid patterns have a long coherence time because the degree of phase mixing in a sinusoidal potential depends on the time spent participating in the eddy motion. Particle trajectories in a given clump slowly decorrelate, with a decorrelation time given by the decay of peaks in Fig. 4.10. The change from a sinusoidal signal to that of a repeating structure in the autocorrelation function at resonant velocities is concurrent with the time of disagreement of the turbulent flux from the quasilinear prediction. This is the time for which the particle bounce frequency (or equivalently, phase space eddy turnover time) becomes smaller than but comparable to the wavepacket autocorrelation and resonant particle transit times.

Wavepacket autocorrelation and quasilinear applicability

Besides its oscillation frequency a wavepacket is characterized by its autocorrelation time τ_{ac}, or the lifetime of the potential profile in the wavepacket, and the lifetime of the wavepacket τ_{life} as an amplitude envelope. The autocorrelation time, similar to the particle potential transit time, is estimated as $\tau_{ac} = 2\pi|(\zeta - v_g)\Delta k|^{-1}$ as in Section 4.1.4. The quantity Δk is the spectral width of the energy-containing oscillations, and can be estimated from the saturated spectrum, shown in Fig. 4.9(a), as $\Delta k \approx 0.1$. The phase velocities range from $\zeta \approx 3$–$5v_t$, so with $v_g \approx 1v_t$ the autocorrelation frequency is approximately $\omega_{\text{ac}} = 0.4$.

The importance of wavepacket lifetime can be estimated using the Hilbert transform to obtain the wave envelope ψ, and computing the group velocity-shifted autocorrelation function $\langle\psi(x,t)\psi(x - v_g\tau, t-\tau)\rangle_L$. When this shifted autocorrelation is compared against the unshifted autocorrelation of the envelope during the saturated state of the instability a stationary signal is observed. The slow evolution of the wavepacket envelope points to the robustness of the saturated state of oscillation.

Returning to the question of quasilinear applicability, the relaxation time is first estimated from finite differences of the Vlasov-Poisson averaged distribution $\langle f\rangle_L$ as $\tau_r^{-1} \approx \mathcal{O}(10^{-3})\omega_p$.

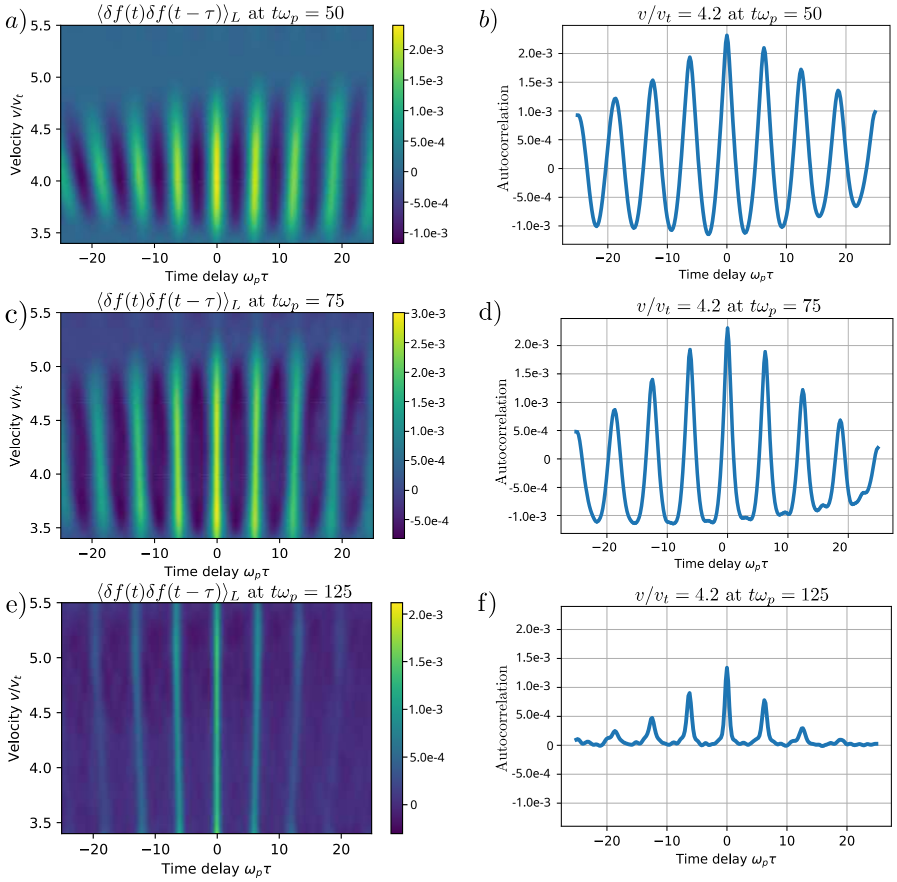

Figure 4.10: Autocorrelation $\langle \delta f(x,v,t)\delta f(x-v_g\tau,v,t-\tau)\rangle_L$ of the fluctuating distribution function in the Vlasov-Poisson simulation as a function of time-delay τ plotted for: (a), (b) $t\omega_p = 50$ during the quasilinear phase of instability evolution; (c), (d) $t\omega_p = 75$ the development of anomalously high diffusivity; and (e), (f) $t\omega_p = 125$ at instability saturation. A sinusoidal signal is indicative of an underlying oscillatory pattern, while a positively-peaked signal indicates a repeating pattern. Oscillation is observed during the quasilinear phase of evolution, while by saturation there is only recurrence at resonant velocities. Recurrence coincides the formation of phase space clumps and the increase of turbulent flux beyond the quasilinear value. The resonant fluctuation recurs at the plasma frequency, decorrelating into the past and future over about six plasma periods at $t\omega_p = 75$ and only two at $t\omega_p = 125$. The decay in autocorrelation peaks corresponds to the approximate coherence time of phase space clumps.

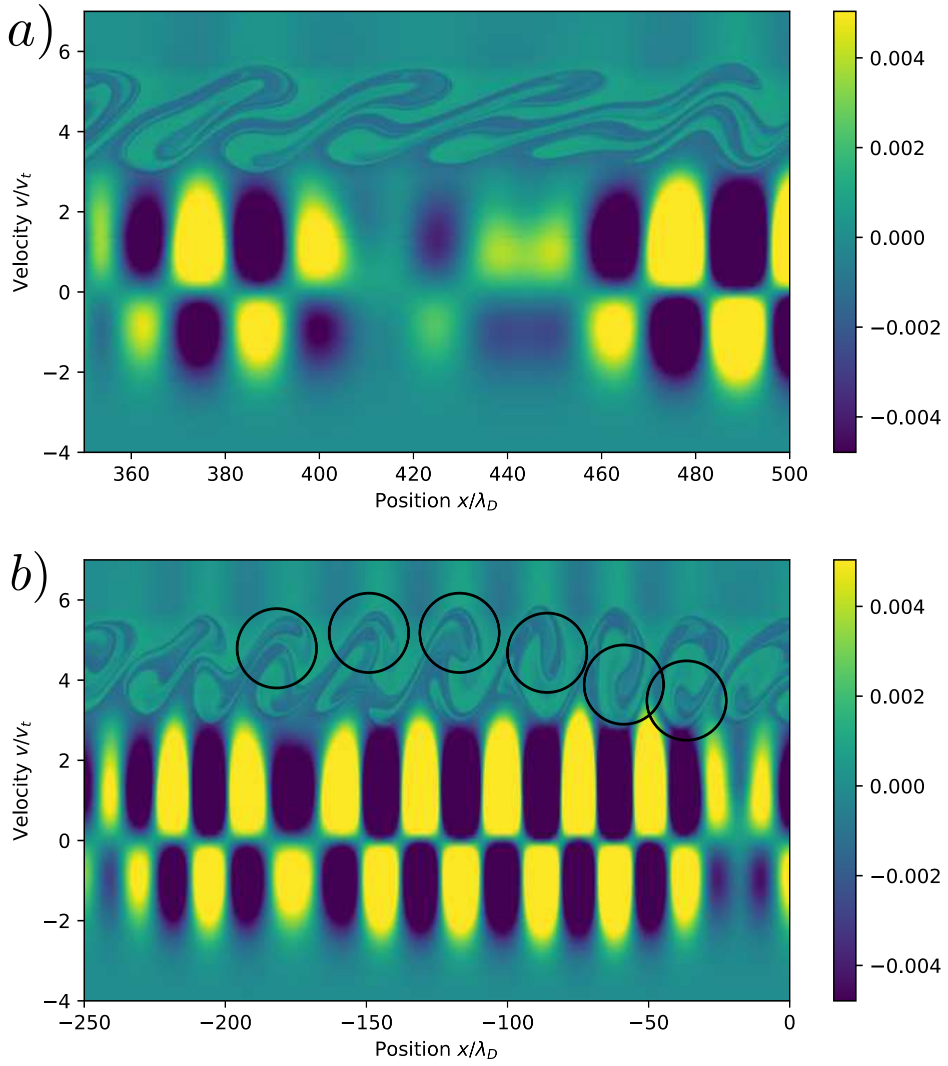

Figure 4.11: Detailed phase-space views of the fluctuation $\delta f \equiv f - \langle f \rangle_L$ in the Vlasov-Poisson simulation: a) outside a wavepacket; and b) within a wavepacket. Phase space is shown at $t\omega_p = 120$ for the $1000\lambda_D$ domain. Null-points between wavepackets can be determined from the phase-space view as the regions where the coherent plasma oscillation sustained by non-resonant electrons goes to zero amplitude. The mixing mechanism depends on the local potential structure. Outside wavepackets filaments mainly free-stream while within wavepackets eddies mix. The long decorrelation time of a clump is illustrated in (b) by a circle tracking a recurrent clump, demonstrating that an eddy can complete a turn as it propagates from trough-to-trough, even though the rotating clump is experiencing different potential amplitudes in each trough.

The maximum growth rate is initially $\omega_i \approx 0.03\omega_p$. Thus the inequality $\tau_r^{-1} < \omega_i < \tau_{ac}^{-1}$ is satisfied as $10^{-3} < 10^{-2} < 10^{-1}$. The rms bounce frequency of the perturbation is $\omega_b \approx 0.05\omega_p$, but by saturation the bounce frequency has grown to $\omega_b \approx 0.1\omega_p$ with maximum values of up to $\omega_b = 0.4\omega_p$ in the largest amplitude wavepackets. While the instability saturates at only 0.2% of the total thermal energy of the system this is enough to make the bounce frequency comparable to the autocorrelation frequency and the quasilinear flux is found to be modified [68] as discussed previously.

To quantify the quasilinear closure assumption, recall the ordering made in Eq. 4.3 comparing the fluxes in the equation for the fluctuation. This flux is made up of two terms, one due to the mean distribution $E\langle f\rangle_L$ and another due to the second fluctuation $\delta(E\delta f) = E\delta f - \langle E\delta_f\rangle_L$. This ordering is initially valid but begins to be weakly violated within wavepackets (where the amplitude of E is large) at resonant velocities. The velocity gradient scale of the mean flux $E\langle f\rangle_L$ is limited by gradients in $\langle f\rangle_L$, but the second fluctuation develops small gradient scales in the resonant velocity region. The smaller gradient scale of the second fluctuation makes the two flux divergences comparable despite the flux $E\langle f\rangle_L$ remaining much larger in amplitude than the second fluctuation. Figure 4.12 compares these two fluxes by following a wavepacket through a phase space view at three points in time, where the gradient scale of the second fluctuation is seen to be much smaller than the scale of the mean flux. The key observation in Fig. 4.12 is the difference in velocity gradient scale-lengths between the two fluxes. The amplitude of the neglected fluxes is comparable to but smaller than the amplitude of the mean flux at resonant velocities ($v \approx 3$–6), but the gradient scale-length of the neglected flux is much smaller than the mean flux with the development of phase space eddits. Because it is the divergence of the flux that matters this translates to a violation of the quasilinear closure at resonant velocities. The closure at non-resonant velocities is not violated, and its effect in the Vlasov-Poisson simulation is to pump energy into the oscillation harmonics. The harmonic peak in the power spectrum (Fig. 4.9) is observed to be small, in agreement with the conclusion that the closure is not violated at non-resonant velocities.

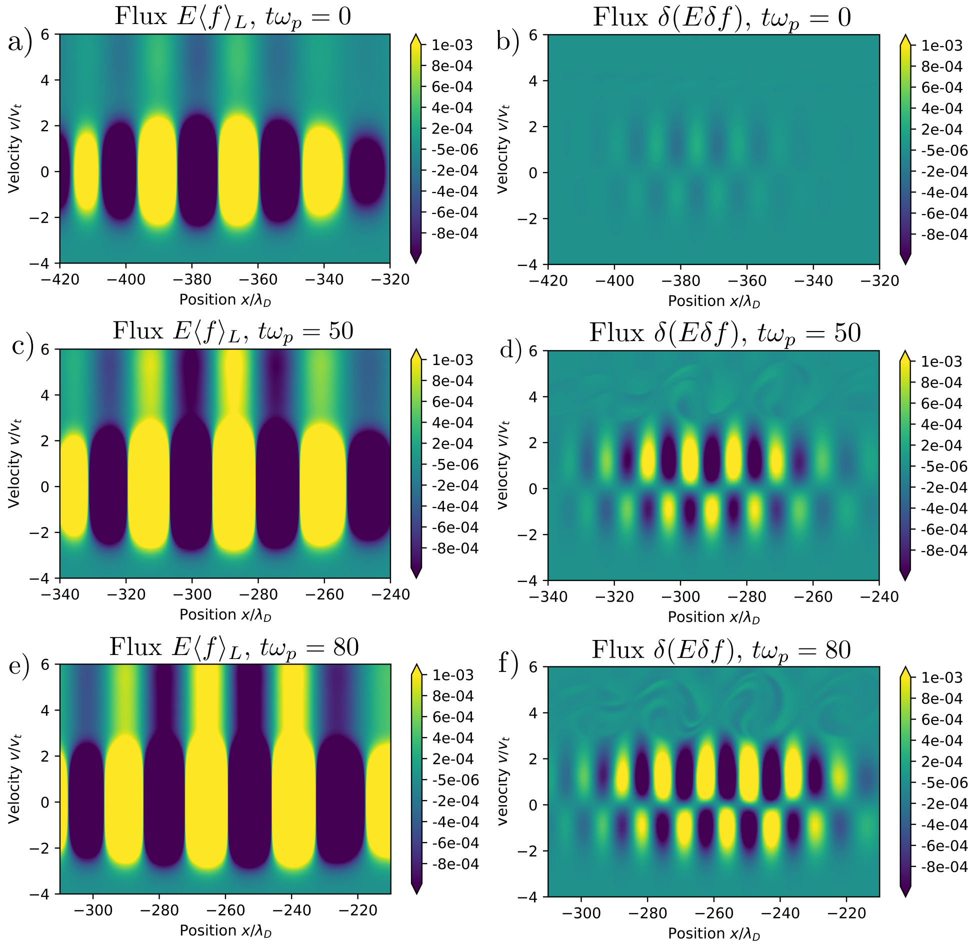

Figure 4.12: Quantification of the quasilinear closure assumption by comparison of the fluxes for the fluctuation δf in QLT, tracking a wavepacket over time in the $L = 5000\lambda_D$ simulation. The phase space is shown for (a, b) the initial condition $t\omega_p = 0$, (c, d) the beginning of anomalously high flux for the mean $\langle f\rangle_L$ at $t\omega_p = 50$, and (e, f) during the time of disagreement between QLT and the Vlasov-Poisson simulation at $t\omega_p = 80$. Parts (a), (c), and (e) show the flux due to the background distribution, $E\langle f\rangle_L$, while parts (b), (d), and (f) shows the remaining flux $\delta(E\delta f) = E\delta f - \langle E\delta f\rangle_L$. Initially the inequality $\partial_v(E\delta f - \langle E\delta f\rangle_L) \ll \partial_v(E\langle f\rangle_L)$ is satisfied, but by $t\omega_p = 50$ the divergence of $\delta(E\delta f)$ is comparable to the divergence of the mean flux in the region of resonant velocities as steep gradients form around phase space eddies. The closure assumption is violated in other wavepackets in the same way.

4.6.6 Summary of findings

This study revisited the bump-on-tail instability with a conservative high-order discontinuous Galerkin method applied to its quasilinear theory as well as to a direct simulation of the Vlasov-Poisson equations. The initial condition was chosen in the regime of beam parameters for which quasilinear theory should be applicable according to Ref [37]. It was found that QLT is initially in good agreement with the system evolution but underestimates the turbulent flux beginning at field energies halfway to instability saturation. The result of the correction beyond the quasilinear approximation is a quenching of the instability in a finite time and the development of a robust state of oscillation. This correction occurs as the phase space eddy turnover time in the largest amplitude wavepackets becomes comparable to the phase fluid transit time through the wavepacket potentials.

When these timescales become comparable, groups of correlated particles, *i.e.* phase space eddies, effectively turn over within wavepackets without being trapped in a single potential well. This effect is termed progressive eddy turnover because the eddies turn over while transiting wavepackets rather than turning over within a single potential well. Progressive eddy turnover transitions the mechanism of resonant electron scattering from diffusive random walks to effective nonlinear phase mixing in potential wells. The findings of this article support the theory of phase space density granulations [35, 78, 79] and shed light on the distribution of fluctuations with velocity in collisionless plasma turbulence.

Limitations of QLT have been known for some time. Theories to account for the discrepancies discussed in this article include resonance broadening theory and expansion to higher-order in the field amplitude [59, 46, 35]. These approaches can considerably complicate the analysis without a necessarily rewarding conclusion, as energy conservation in resonance broadening theory is still actively researched [59] and higher-order expansions may lead to misleading analysis for nonlinear Landau damping processes [82]. The findings of this study suggest that using QLT to predict plasma processes for all but the weakest instabilities should be considered as only order-of-magnitude accurate.

Chapter 5

STRONGLY MAGNETIZED ELECTROSTATIC MODES

> The nature of infinity is this: That every thing has its Own Vortex . . .
>
> *William Blake* in *Milton*

Electrostatic modes in a plasma with strong external magnetic field are longitudinal oscillations with characteristic frequencies at the plasma frequency ω_p, cyclotron frequency ω_c, and harmonic combinations of the two. The frequency spectrum is greatly dependent on the angle of the wave normal vector $\boldsymbol{k}$ with the magnetic field $\boldsymbol{B}$. Defining the wave obliquity as $\cos(\theta) = \hat{\boldsymbol{k}} \cdot \hat{\boldsymbol{B}}$, the parallel and perpendicular wavenumbers then follow as $\boldsymbol{k} = k_\parallel \hat{e}_\parallel + k_\perp \hat{e}_\perp = k\cos(\theta)\hat{e_\parallel} + k\sin(\theta)\hat{e_\perp}$. The spectrum is determined by the roots of the dielectric function $\varepsilon(\omega, k_\perp, k_\parallel) = 0$, conventionally for real wavenumbers and complex frequency. As the eigenmodes are solutions of the linear dynamics and linearization is done against a homogeneous background the spectrum depends on the thermal state of the plasma.

5.1 *The Harris dispersion relation*

Coordinates are chosen such that $\boldsymbol{B} = B\hat{z}$ and $\boldsymbol{k} = k_\perp\hat{x} + k_\parallel\hat{z}$ and the velocity space is expressed in cylindrical coordinates as $\boldsymbol{v} = v_\perp\cos(\varphi)\hat{v}_x + v_\perp\sin(\varphi)\hat{v}_y + v_\parallel\hat{v}_z$. In these coordinates the Vlasov equation linearizes around $f_0(v_\perp, v_\parallel)$ as

$$\frac{\partial f_1}{\partial t} + v_\perp\cos\varphi\frac{\partial f_1}{\partial x} + v_\parallel\frac{\partial f_1}{\partial z} - \omega_c\frac{\partial f_1}{\partial \varphi} = \frac{q}{m}\Big(E_x\cos\varphi\frac{\partial f_0}{\partial v_\perp} + E_z\frac{\partial f_0}{\partial v_\parallel}\Big). \tag{5.1}$$

The linearized equation is then Fourier transformed $(x, z, t) \to (k_\perp, k_\parallel, \omega)$ to yield

$$\frac{df_1}{d\varphi} + i\frac{\omega - k_\perp v_\perp\cos\varphi - k_\parallel v_\parallel}{\omega_c}f_1 = -i\frac{q}{m}\Phi\Big(k_\perp\cos\varphi\frac{\partial f_0}{\partial v_\perp} + k_\parallel\frac{\partial f_0}{\partial v_\parallel}\Big). \tag{5.2}$$

Equation 5.2 is a first order inhomogeneous equation in the cylindrical velocity-space angle φ and can be solved by the usual methods. Integrating the inhomogeneous term along the solution of the homogeneous equation yields

$$f_1(v_\perp, \varphi, v_\parallel) = -\frac{q}{m}\Phi(k)\exp(ik_\perp v_y/\omega_c)\Big[\frac{1}{v_\perp}\frac{\partial f_0}{\partial v_\perp}\Upsilon_1 + k_\parallel \frac{\partial f_0}{\partial v_\parallel}\Lambda_1\Big] \tag{5.3}$$

where the terms Υ_1 and Λ_1 are auxiliary wavefunctions defined as the polar Fourier series

$$\Upsilon_1 = \sum_{n=-\infty}^{\infty} \frac{n\omega_c}{\omega - k_\parallel v_\parallel - n\omega_c} J_n(k_\perp v_\perp/\omega_c)e^{in\varphi}, \tag{5.4}$$

$$\Lambda_1 = \sum_{n=-\infty}^{\infty} \frac{\omega_c}{\omega - k_\parallel v_\parallel - n\omega_c} J_n(k_\perp v_\perp/\omega_c)e^{in\varphi}. \tag{5.5}$$

The series Υ associated with the perpendicular terms decays one order slower than the parallel series Λ, meaning that high-order resonances are more important for the series related to the perpendicular wavenumber $k_\perp$. Equation 5.3 is the phase space linear response function for electrostatic fluctuations in a strongly magnetized plasma.

The self-consistent spectrum consists of all pairs $(\omega, k_\perp, k_\parallel)$ such that the zeroth moment of $f_1(\omega, k_\perp, k_\parallel, v_\perp, \varphi, v_\parallel)$ results in a potential of wavenumber $(k_\perp, k_\parallel)$. Integration of the phase space fluctuation gives the density fluctuation as

$$n_1(\omega, k_\perp, k_\parallel) = -i\frac{q}{m}\Phi \int_{-\infty}^{\infty}\int_0^{\infty} \Big[\frac{1}{v_\perp}\frac{\partial f_0}{\partial v_\perp}\Upsilon_2 + k_\parallel \frac{\partial f_0}{\partial v_\parallel}\Lambda_2\Big] 2\pi v_\perp dv_\perp dv_\parallel \tag{5.6}$$

where a set of additional series, analogs of Eqs. 5.4 and 5.5, are defined as

$$\Upsilon_2 = \sum_{n=-\infty}^{\infty} \frac{n\omega_c}{\omega - k_\parallel v_\parallel - n\omega_c} J_n^2(k_\perp v_\perp/\omega_c), \tag{5.7}$$

$$\Lambda_2 = \sum_{n=-\infty}^{\infty} \frac{\omega_c}{\omega - k_\parallel v_\parallel - n\omega_c} J_n^2(k_\perp v_\perp/\omega_c). \tag{5.8}$$

Substitution of the fluctuation n_1 into Poisson's equation gives Harris's dispersion relation

$$\varepsilon(\omega, k_\perp, k_\parallel) = 1 - \Big(\frac{\omega_p}{\omega_c}\Big)^2 \frac{1}{(k\lambda_D)^2}\int_{-\infty}^{\infty}\Big(\mathbb{V}_\perp f_\parallel + k_\parallel \mathbb{V}_\parallel \frac{\partial f_\parallel}{\partial v_\parallel}\Big)dv_\parallel = 0 \tag{5.9}$$

where the integration over perpendicular velocities is broken out into the two quantities

$$\mathbb{V}_\perp = \int_0^{\infty} \frac{1}{v_\perp}\frac{\partial f_\perp}{\partial v_\perp}\Upsilon_2(v_\perp, v_\parallel)2\pi v_\perp dv_\perp, \tag{5.10}$$

$$\mathbb{V}_\parallel = \int_0^{\infty} f_\perp \Lambda_2(v_\perp, v_\parallel)2\pi v_\perp dv_\perp, \tag{5.11}$$

and separability of the background $f_0(v_\perp, v_\parallel) = f_\perp(v_\perp) f_\parallel(v_\parallel)$ has been assumed for simplification.

5.1.1 Validity of linearization around zero-order cyclotron motion

Given a magnetic field beginning at zero order $B = \boldsymbol{B}_0 + \epsilon \boldsymbol{B}_1 + \cdots$ and small-amplitude electric field perturbations $\boldsymbol{E} = \epsilon \boldsymbol{E}_1 + \cdots$, the zero- and first-order kinetic equations are

$$(\boldsymbol{v} \times \boldsymbol{B}_0) \cdot \nabla_v f_0 = 0, \tag{5.12}$$

$$\partial_t f_1 + \boldsymbol{v} \cdot \nabla_x f_1 + \frac{q}{m}(\boldsymbol{v} \times \boldsymbol{B}_0) \cdot \nabla_v f_1 + \frac{q}{m} \boldsymbol{E}_1 \cdot \nabla_v f_0 = 0 \tag{5.13}$$

assuming a zero-order distribution $f_0 = f_0(\boldsymbol{v})$. The heart of this ordering is that the zero-order cyclotron acceleration is much greater than the electric wavefield acceleration at the most common (thermal) velocity v_{th}. Considering perpendicular waves ($k_\parallel = 0$) for simplicity gives $E_1 \ll v_{th} B_0$ and estimating the field perturbation of wavenumber k by Gauss's law also gives $E_1 \sim \frac{q}{k\epsilon_0} n_1$. Combining these two estimates results in the condition

$$\frac{n_1}{n_0} \ll \left(\frac{\omega_c}{\omega_p}\right)(k\lambda_D) = \left(\frac{\omega_c}{\omega_p}\right)^2 (k r_L) \tag{5.14}$$

having estimated the Debye length λ_D and Larmor radius r_L as $v_t \sim \lambda_D \omega_p \sim r_L \omega_c$. Equation 5.14 gives the condition for validity of the linearization and means that density fluctuations n_1/n_0 must be small enough amplitude. When the inequality does not hold the dielectric function Eq. 5.9 is not valid. Typical cyclotron instabilities have $k r_L \sim 1$ or greater which limits the amplitudes of the linear modes considered in this section to $\delta n/n_0 \ll (\omega_c/\omega_p)^2$.

5.2 The dielectric function for loss-cone (ring) distributions

Standard textbook theory considers isotropic or bithermal Maxwellian plasmas by a series expansion around the cyclotron harmonics [83]. Recent analytical work centers around the use of kappa distributions [84], whose long tails are representative of observed space plasma distributions. On the other hand, ring distributions in the perpendicular velocity are entropy-maximizing for magnetized systems and commonly arise due to the loss cone mechanism of magnetic trapping. During the golden age of magnetic mirror research unstable modes in ring distributed plasmas were identified, now called Dory-Guest-Harris (DGH) instabilities. Analytical results were most easily obtained for perpendicular waves with $\theta = 90^\circ$. DGH-type instabilities were shown to have a greater growth rate for $\theta < 90^\circ$, though analytical work with smooth ring distributions was not pursued. This section analyzes the dielectric function for loss-cone distributions perpendicular to $\boldsymbol{B}$,

$$f_0(v_\parallel, v_\perp) = f_\parallel(v_\parallel) f_\gamma(v_\perp) \tag{5.15}$$

where $f_\parallel(v_\parallel)$ is a Maxwellian of thermal velocity v_t and $f_\gamma(v_\perp)$ is a ring distribution

$$f_\gamma(v) = \frac{1}{\pi\alpha^2}\frac{1}{\Gamma(\gamma+1)}\Big(\frac{v^2}{\alpha^2}\Big)^\gamma \exp\Big(-\frac{v^2}{\alpha^2}\Big) \tag{5.16}$$

of thermal velocity α and ring parameter γ. The function f_γ is a two-dimensional distribution,

$$\int_0^\infty f_\gamma(v) 2\pi v dv = 1, \quad \mathrm{Re}(\gamma) > -1 \tag{5.17}$$

yet is both a distribution and bounded at zero only for $\gamma \geq 0$. In the mathematical literature the distribution f_γ is called a χ-distribution, and is a two-temperature distribution. That is, recall that the Maxwellian distribution maximizes entropy subject to the constraint of having a certain temperature. The loss-cone distribution f_γ is entropy-maximizing for $v_\perp \in [0, \infty)$ subject to the two constraints $\langle v_\perp^2 \rangle = \big(\gamma + 1\big)\alpha^2$ and $\big\langle (v_\perp - \langle v_\perp \rangle)^2 \big\rangle \approx 2\alpha^2 + \mathcal{O}(\gamma^{-1})$ with the second expression a factorial expression in γ. By analogy, the physical meaning of γ is a boost in thermal energy in the frame of the magnetic field, while α is the thermal velocity in the mean frame of gyration. For the following note that the distribution satisfies a recurrence relation in γ (and that $f_{-1} = 0$),

$$\frac{1}{v}\frac{df_\gamma}{dv} = \frac{1}{\alpha^2}\frac{f_{\gamma-1} - f_\gamma}{2}. \tag{5.18}$$

In the case of ring distributions of the form of Eq. 5.16, the integrals in both quantities $\mathbb{V}_\perp$ and $\mathbb{V}_\parallel$ involve only f_γ, in view of the recurrence in Eq. 5.18. The integration is given by defining

$$\mathbb{F}_{n,\gamma}(k) \equiv \int_0^\infty f_\gamma(v) J_n^2(kv) 2\pi v dv \tag{5.19}$$

which, as shown in Appendix B, is a type-${}_2F_2$ hypergeometric function with series representation [85]

$$\mathbb{F}_{n,\gamma}(x) = \frac{1}{\Gamma(\gamma+1)} \sum_{\ell=0}^{\infty} \frac{\Gamma(2n+2\gamma+2\ell+1)}{\Gamma^2(n+\ell+1)\Gamma(2n+\ell+1)} \frac{(-1)^\ell}{\ell!} x^{2(\ell+n)}. \tag{5.20}$$

It is possible to close the summation in the auxiliaries Eqs. 5.7 and 5.8 using the Lerche-Newberger summation theorem [86], and to determine the perpendicular velocity integrals in Eqs. 5.10, 5.11 in closed form as hypergeometric functions, as in Appendix C, for arbitrary $k_\parallel$. However, the integration over parallel velocities must then proceed by a series expansion around the poles of these hypergeometric functions. On the other hand, the power series developed in this section maintains separability of terms containing the parallel velocity $v_\parallel$. Proceeding to the integration over parallel velocities, with the parallel distribution $f_\parallel(v_\parallel)$ taken as a Maxwellian distribution, the two integrals are

$$\int_{-\infty}^{\infty} \frac{n\omega_c}{\omega - k_\parallel v_\parallel - n\omega_c} f_\parallel dv_\parallel = -\frac{n}{k_\parallel} Z(\zeta_n) \tag{5.21}$$

$$\int_{-\infty}^{\infty} \frac{\omega_c}{\omega - k_\parallel v_\parallel - n\omega_c} \frac{\partial f_\parallel}{\partial v_\parallel} dv_\parallel = \frac{1}{2k_\parallel} Z'(\zeta_n) \tag{5.22}$$

where $Z(\zeta)$ is the plasma dispersion function and the cyclotron harmonic-shifted phase velocity is defined as $\zeta_n \equiv \frac{\omega - n\omega_c}{\sqrt{2}k_\parallel v_t}$. Thus the dielectric function for loss-cone distributions is

$$\begin{aligned} \varepsilon(\omega, k) = 1 - \left(\frac{\omega_p}{\omega_c}\right)^2 \frac{1}{(kr_L)^2} \sum_{n=-\infty}^{\infty} \Big[& Z'(\zeta_n)\mathbb{F}_{n,\gamma}(k_\perp r_L) \\ & + \frac{n}{k_\parallel r_L} Z(\zeta_n) \Big\{ \mathbb{F}_{n,\gamma-1}(k_\perp r_L) - \mathbb{F}_{n,\gamma}(k_\perp r_L) \Big\} \Big]. \end{aligned} \tag{5.23}$$

Note that Eq. 5.23 reduces to the standard series for a Maxwellian plasma ($\gamma = 0$) by the identity $\mathbb{F}_{n,0}(k) = e^{-k} I_n(k)$ where $I_n(k)$ is the modified Bessel function of the first kind.

5.3 Propagation purely perpendicular to the magnetic field

In the limit $k_\parallel \to 0$ of perpendicular propagation the series Eq. 5.23 in the cyclotron harmonics simplifies as the terms incorporating parallel propagation vanish. Further, by use of the Lerche-Newberger summation theorem two alternatives to the power series for the perpendicular cyclotron wave dielectric function may be developed which incorporate the contributions from the cyclotron harmonics to all orders. The derivation of these expressions may be found in Appendix C. The first is a closed form, a hypergeometric function with complex poles at the cyclotron resonances,

$$\begin{aligned}\varepsilon(\omega,k_\perp) = 1 + \left(\frac{\omega_p}{\omega_c}\right)^2 \frac{1}{(k_\perp r_L)^2}\Big\{ {}_2F_2\left[\begin{matrix}\frac{1}{2}, & \gamma+1\\ 1+\omega/\omega_c, & 1-\omega/\omega_c\end{matrix}\right](-2(k_\perp r_L)^2)\\ - {}_2F_2\left[\begin{matrix}\frac{1}{2}, & \gamma\\ 1+\omega/\omega_c, & 1-\omega/\omega_c\end{matrix}\right](-2(k_\perp r_L)^2)\Big\} = 0\end{aligned} \tag{5.24}$$

and where the second is a representation of Eq. 5.24 as a trigonometric integral [87, 88]

$$\varepsilon(\omega,k) = 1 + \left(\frac{\omega_p}{\omega_c}\right)^2 \frac{1}{\sin(\pi\omega/\omega_c)} \int_0^\pi \sin(\theta)\sin(\theta\omega/\omega_c) L_\gamma(\beta)\exp(-\beta)d\theta \tag{5.25}$$

with $\beta \equiv 2\cos^2\big(\theta/2\big)(k_\perp r_L)^2$ and where $L_\gamma(\beta)$ is the Laguerre polynomial of order γ. Similar hypergeometrics to Eq. 5.24 have been obtained for the Maxwellian plasma and for kappa-distributions [84, 89]. Equation 5.25 is particularly suited to accurate calculation by quadrature methods. Observe that Eqs. 5.24 and 5.25 are naturally functions of frequency and no longer of phase velocity as there is no ballistic contribution to the zero-order motion.

5.4 Visualization of the dispersion function and eigenmodes

Figure 5.1 plots the electrostatic dispersion function in the complex frequency plane for a loss-cone distribution of $\gamma = 6$. The plethora of solutions to the complex dispersion function $\varepsilon = 0$ are illustrated by the intersection of the lines of $\text{Re}(\varepsilon) = 0$ and $\text{Im}(\varepsilon) = 0$, which takes place at both solutions and poles. Complex poles occur only for the perpendicular function at the cyclotron harmonics, as evident from the cosecant function $\csc(\pi\omega/\omega_c)$ in Eq. 5.25. In this way solutions and simple poles can be clearly distinguished. It's clear that, given zero-order cyclotron orbits, oblique modes are Landau damped but perpendicular modes are not. When density amplitudes violate the inequality of Eq. 5.14 then perpendicular waves are also Landau damped and one may see streaming instabilities in numerical experiments in the moderately magnetized regime where the parameter $\omega_c \sim \omega_p$.

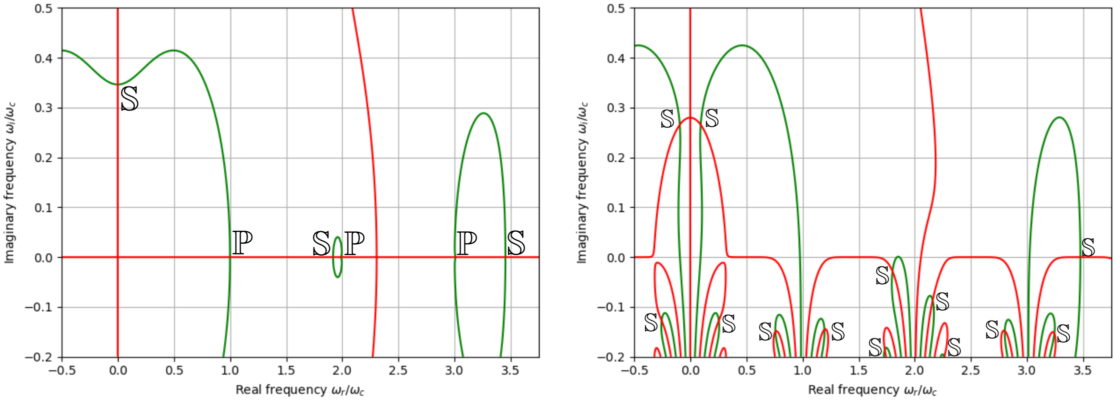

(a) Purely perpendicular. (b) Wave-vector at $\theta = 85°$.

Figure 5.1: Contours of $\mathrm{Re}(\varepsilon) = 0$ (green) and $\mathrm{Im}(\varepsilon) = 0$ (red) for electrostatic dispersion function of a loss cone-distributed plasma with $\omega_p = 10\omega_c$, $\gamma = 6$, and $k_\perp r_L = 0.9$ for (left) 90° propagation and (right) 85° propagation. Solutions to the dispersion relation $\varepsilon(\omega, k) = 0$ are labelled $\mathbb{S}$ while simple poles are labelled $\mathbb{P}$. There are no poles for $\theta < 90°$. Solutions correspond to the first few electron Bernstein modes. The dispersion function shows Gaussian-like responses in the lower-half plane for the oblique wave, associated with wave-particle resonance at the cyclotron harmonics.

Due to the absence of Landau damping for perpendicular propagation through strongly magnetized plasma, all modes are true eigenfunctions. The phase space structure associated with cyclotron waves (that is, Eq. 6.5) consists of helical modes in the perpendicular velocity space, since the primary phase component is $\exp(i(kx + n\varphi - \omega t))$ for a mode with frequency $\omega \sim n\omega_c$, with φ the cylindrical velocity space angle coordinate. The simplest example of such modes with a helical phase space structure are the electron Bernstein modes, which for $kr_L \sim 1$ are undamped oscillations with frequencies approaching the n'th cyclotron harmonic, $\omega \sim n\omega_c$. Figure 5.2 visualizes the eigenfunctions of the first and second cyclotron harmonics for a Maxwellian background distribution $f_0(v_\perp)$ in the phase space (x, u, v) with (u, v) the perpendicular velocity space and x the propagation coordinate perpendicular to the background magnetic field.

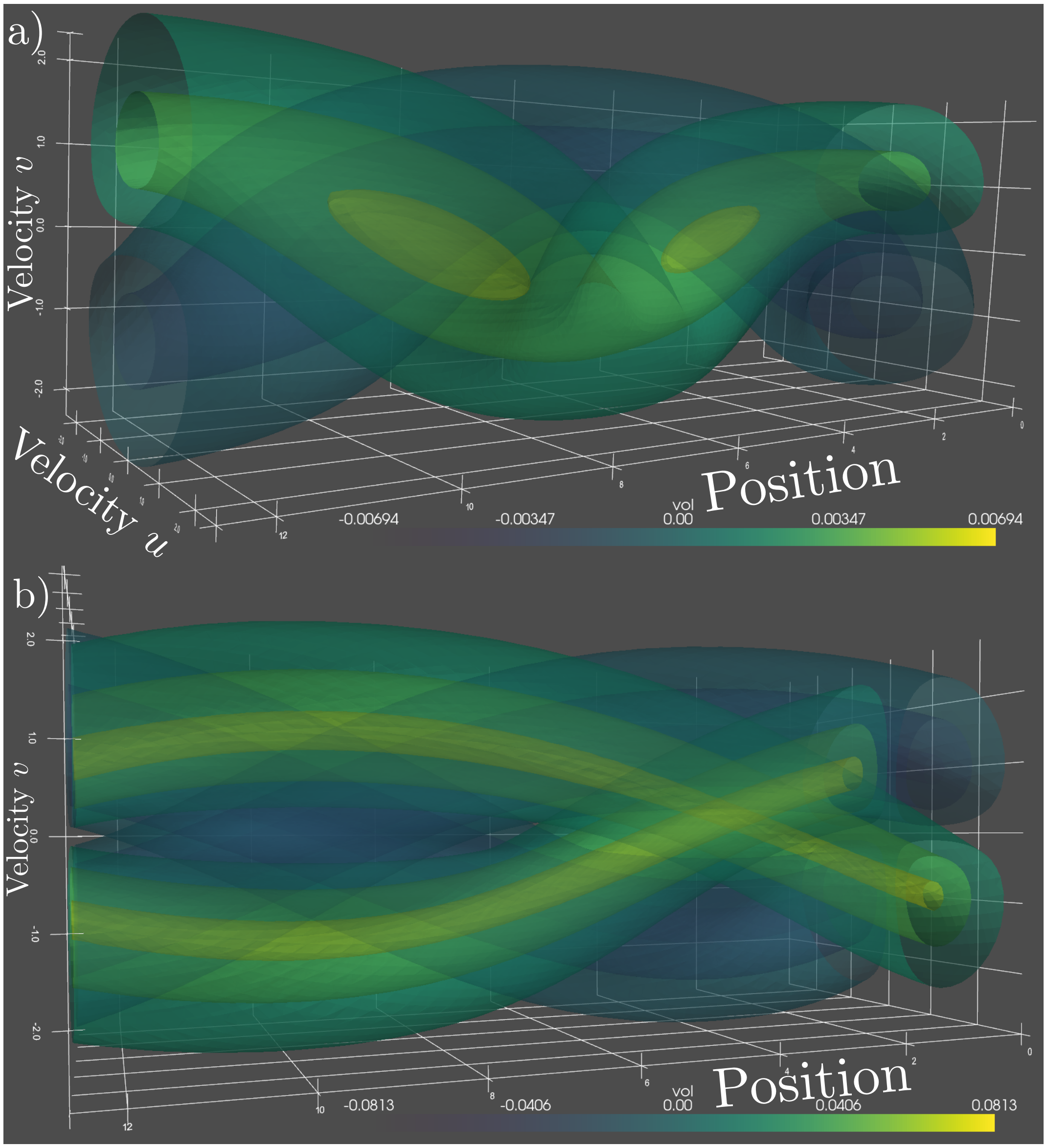

Figure 5.2: Eigenfunctions of a) the first, and b) the second cyclotron harmonic electron Bernstein waves propagating orthogonal to the magnetic field, visualized in the perpendicular phase space (x, u, v). The order of the cyclotron harmonic is equivalent to the number of strands of a given sign in the helix. In a fixed frame of reference these modes propagate along the x-coordinate. When observed from a particular position x the phase space mode rotates in the perpendicular velocity space. Counterpropagating modes oscillate as a standing wave.

5.5 *Simulation of perpendicular electron cyclotron loss-cone instabilities*

A useful model problem is the instability of a loss cone to perpendicular cyclotron waves [87]. Normalizing length to the Debye length λ_D, time to the inverse plasma frequency ω_p^{-1}, velocities to the thermal velocity $v_{th} = \lambda_D \omega_p$, and the fields by $E_0 = v_{th} B_0$ such that the plasma-cyclotron frequency ratio of the reference state is unity $(\omega_p/\omega_c)_0 = 1$, the Vlasov-Poisson equations are

$$\partial_t f + F^j \partial_j f = 0, \tag{5.26}$$

$$\partial_{xx}\Phi = \int_{-\infty}^{\infty} f dv - 1, \tag{5.27}$$

$$F = \Big[u, \quad \partial_x \Phi - vB_{\text{ext}}, \quad uB_{\text{ext}}\Big]^T \tag{5.28}$$

with coordinates (x, u, v). Here the external magnetic field B_{ext} is set such that the desired plasma-cyclotron frequency ratio is $\omega_p/\omega_c = B_{\text{ext}}^{-1}$ in normalized units. Two example simulations termed A and B are performed for Eqs. 5.26 and 5.27 conditions have $\omega_p = 10\omega_c$. using as perturbation eigenvalues the pairs $(k_A\lambda_D, \omega_A/\omega_c) \approx (0.886, 0.349i)$ and $(k_B\lambda_D, \omega_B/\omega_c) \approx (1.4, 1.182 + 0.131i)$, each solutions to the electrostatic dispersion function for perpendicular cyclotron waves. In this case the frequencies are found with Eq. 5.25 using a fifty point Gauss-Legendre quadrature. As a single-mode simulation the domain is set to $L = 2\pi/k$ in the each case and the velocity boundaries to $u_{\max}, v_{\max} = \pm 8.5$. Figure 5.3 shows the eigenfunctions corresponding to the pairs (k_A, ω_A), (k_B, ω_B) taken as the initial perturbations $f_1(x, u, v)$ at $t = 0$.

The problem is evolved numerically using discontinuous Galerkin (DG) method for phase space discretization with an element resolution $(N_x, N_u, N_v) = (25, 50, 50)$ and $n = 8$ nodal basis per dimension, while the Shu-Osher SSPRK3 method is used to integrate the semi-discrete equation. These instabilities grow on a slow time-scale relative to the plasma frequency; that is, they grow at a fraction of the cyclotron time-scale ω_c^{-1}, while time t is normalized to the plasma frequency ω_p^{-1}. As well, the initialized eigenfunction's amplitude must not exceed the limit imposed by Eq. 5.14, or the linear dynamics will fall into an inter-

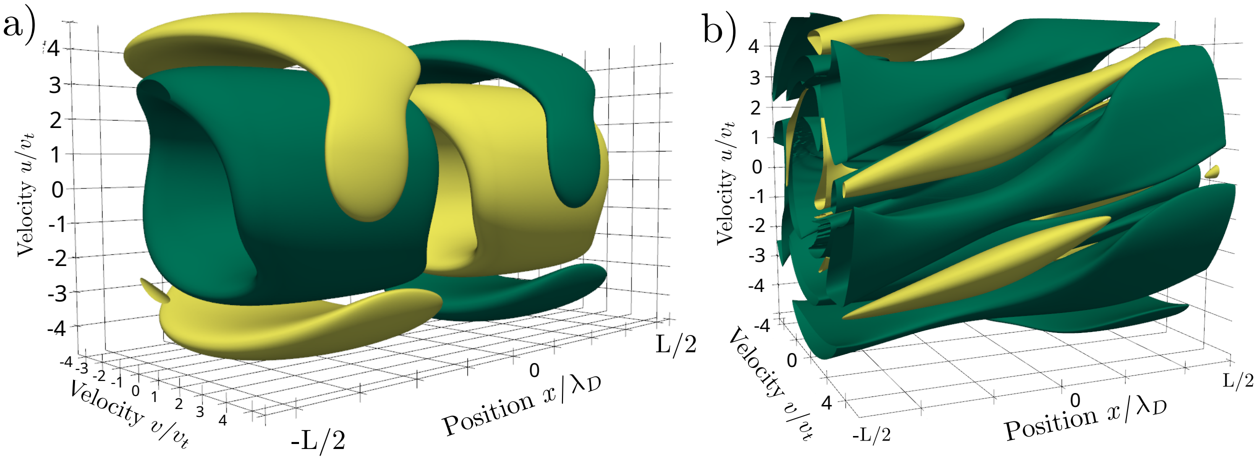

Figure 5.3: Shown here are the perturbations $f_1 \equiv f - f_0$ at time $t = 0$ for a) simulation A with $\omega_r = 0$ and b) simulation B with $\omega_r \neq 0$, each with iso-surfaces at 30% of the minimum (green) and maximum (yellow). The considered eigenfunctions $f_1(x, u, v)$ consist of twisting islands in the phase space, capturing the combined physics of translation, electric acceleration, and magnetic gyration. Translating modes ($\omega_r \neq 0$) are associated with a helical structure.

mediate regime between the limits of zero-order ballistic motion and cyclotron motion. Thus these instabilities take many plasma periods to reach nonlinear saturation beginning from amplitudes below the limit of Eq. 5.14. Simulation A reaches saturation around $t = 100$ and runs to $t = 175$ while simulation B saturates at around $t = 175$ and stops at $t = 200$. Each case requires approximately 50000 three-stage time steps to reach the stop time, with a machine run-time of several hours on an RTX 3090 GPU.

Three-dimensional isosurface plots were produced using PyVista, a Python package for VTK. To prepare the data, an average is taken of nodal values lying on element boundaries for smoothness, and the 8-nodes per element are resampled to 25 linearly-spaced points per axis and per element onto the basis functions of the DG method. These iso-contours are shown for simulations A and B in Figs. 5.4 and 5.5 respectively. Figure 5.6 shows the electric potentials $\Phi(x)$ in simulations A and B. In simulation A the wave potential $\Phi(x)$ is stationary with a weakly fluctuating boundary, so that part of the density $f(x, v)$ within the potential well executes trapped orbits. This results in a trapping structure with orbits tracing a nonlinear potential similar to that seen in electrostatic two-stream instability simulations where the potential is like that of a pendulum, *i.e.* $\Phi(x) = \sin(x)$, with its characteristic separatrix structure. In this case particles also execute cyclotron motion so that the separatrix of the potential in simulation A is similar in form to that shown by the isosurfaces.

On the other hand, the saturated wave potential $\Phi(x)$ of simulation B translates with positive phase velocity $v_\varphi \approx \omega_r/k$. The region of particle interaction translates along with the wave potential and forms a vortex structure in the phase space density $f(x, v_\perp, \varphi)$. The center of this kink continues to tighten as the simulation progresses, leading to progressively finer structures just as in simulation A. This effect is in agreement with the filamentation phenomenon and introduces simulation error as the structures lead to large gradients on the grid scale where discreteness produces dispersion error. For this reason the simulation is stopped at $t = 200$. In a state of cyclotron wave turbulence arising from an unstable loss-cone distribution, the translating instability at the first cyclotron harmonic grows more slowly and releases less energy than the mode with zero real frequency. This is demonstrated in Fig. 5.7 showing that simulation A saturates with a greater proportion of the plasma thermal energy than simulation B.

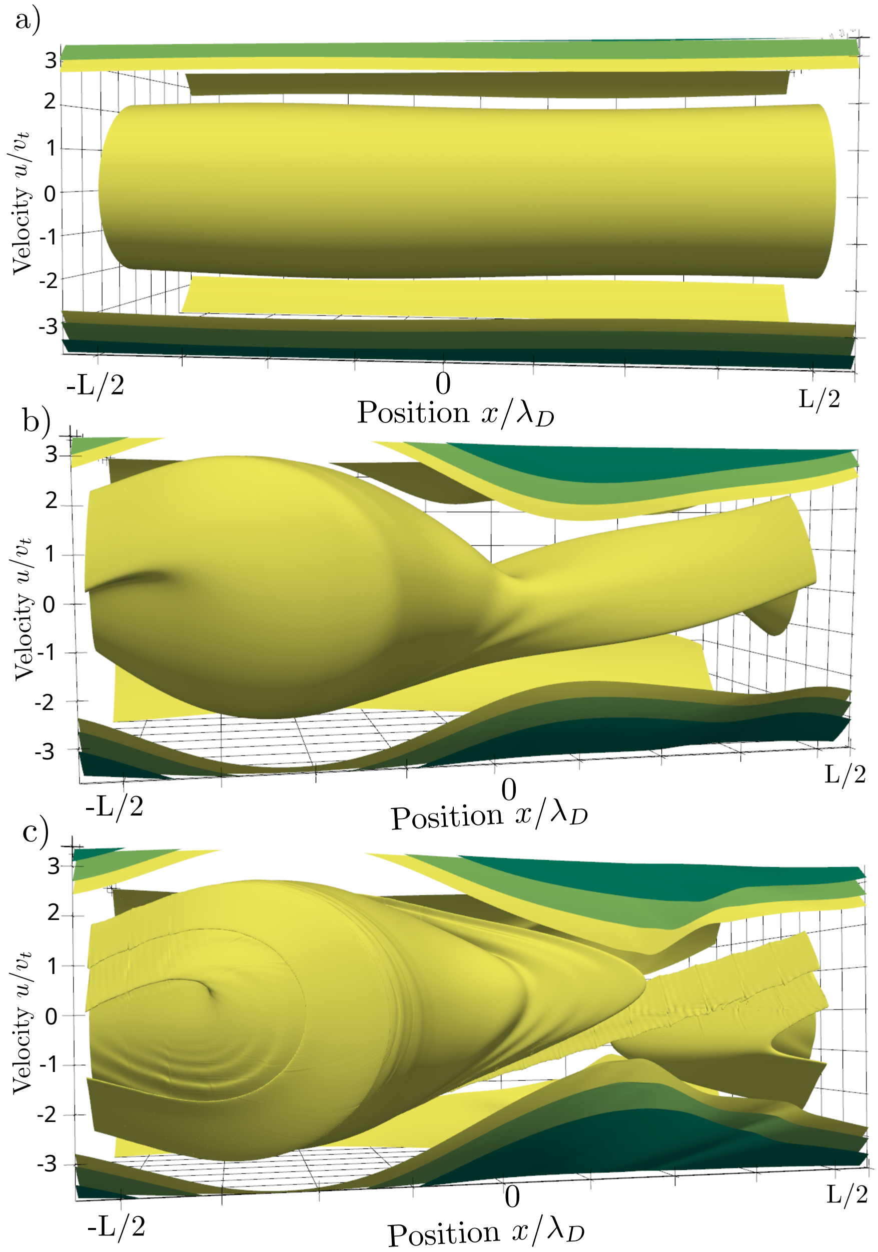

Figure 5.4: Phase space view (x, u, v) of simulation A focused on (x, u)-plane as iso-contours at 15% of $\max(f)$ shown in yellow, at times a) $t = 0$, b) $t = 80$, and c) $t = 120$. The inner domain is shown with $(u, v) \in (-4, 4)$ to focus on the trapping dynamics. The trapping structure consists of a ribbon of density winding around a separatrix, while the outer ring maintains passing trajectories from the original ring distribution. This saturation geometry is typical for potentials with external magnetic field as the magnetic force depends on the sign of the transverse velocity v/v_t.

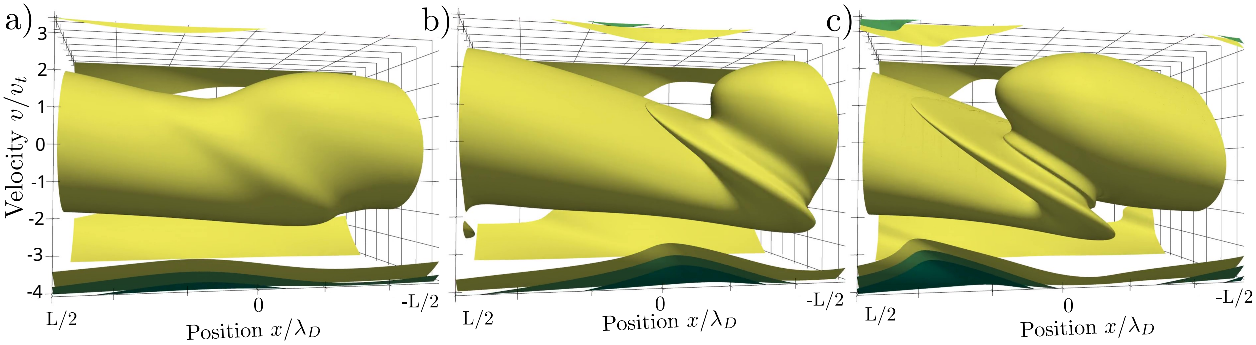

Figure 5.5: Phase space view looking on $(-x, v)$-plane of simulation B at 15% iso-contours of $\max(f)$ (yellow), with a) the nonlinear mode developing at $t = 100$, b) the developed vortex at $t = 160$, and c) the saturated vortex translating at $t = 180$. The mode is seen to be a growing, translating potential $\Phi(x)$ of positive phase velocity $v_\varphi = \omega_r/k$ with an underlying phase space vortex structure centered at $(u, v) = 0$. The vortex shape is explained by considering the trajectory of a test particle in the wave. That is, particles with a velocity close to that of the wave see a stationary potential and are accelerated to a high u-velocity. They then translate towards positive x while their velocity vector is rotated by the Lorentz force to $-u$ at a rate close to the wave frequency (as $\omega_r \approx 1.2\omega_c$). The particle then advects opposite the direction of wave propagation, before repeating the cycle.

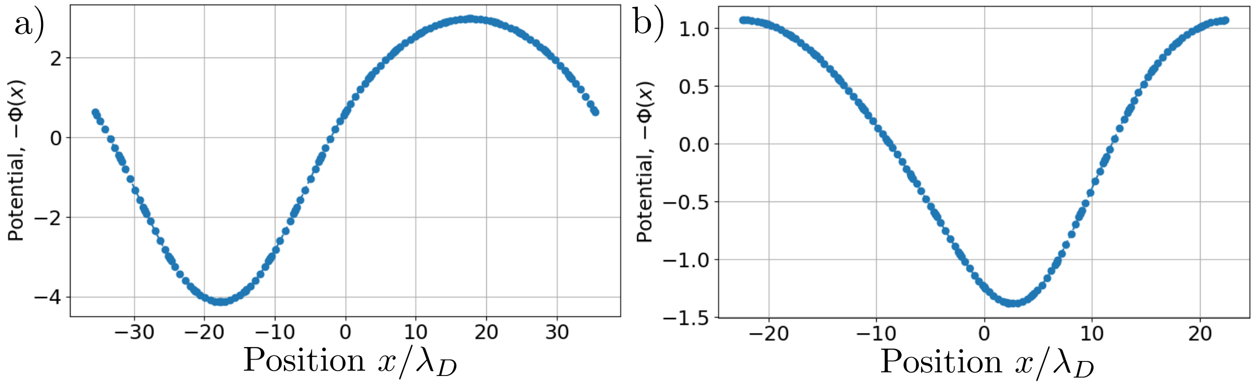

Figure 5.6: Electric potentials $\Phi(x)$ at saturation of the two studied cases, for a) simulation A at $t = 120$ and b) simulation B at $t = 180$. The potential of A is stationary while that of B is translating to the right. The negative of the potential $-\Phi(x)$ is shown in order to account for the electron's negative charge. In both cases particle trapping structures develop in the potential wells, or minimum regions, in $-\Phi(x)$.

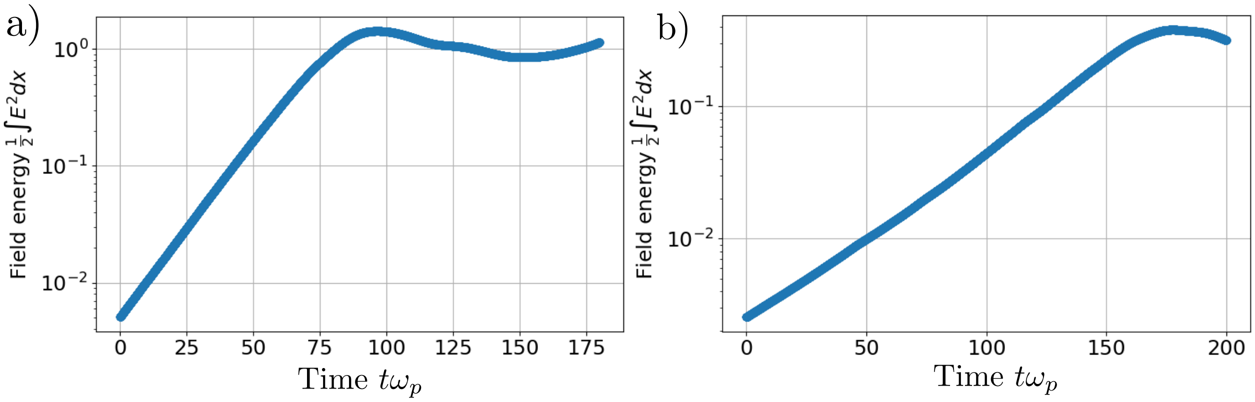

Figure 5.7: Domain-integrated field energy growth profiles for a) simulation A and b) simulation B. The thermal energy of the zero-order distribution is 0.25 per unit length with $\gamma = 6$ and $\alpha = 1$. In simulation A this corresponds to a domain-integrated thermal energy of $E_A \approx 17.8$ and in simulation B to $E_B \approx 11.2$. Therefore in both cases the instability saturates with an electric energy a few percent of the thermal energy, approximately 6% in A and 2.5% in B.

Chapter 6

UNMAGNETIZED ELECTROMAGNETIC MODES

This chapter presents the theory of electromagnetic instabilities in a plasma, based on linear theory where the magnetic field is considered weak enough relative to wave amplitudes such that the zero-order plasma motion can be considered ballistic. In addition to reproducing the streaming instabilities of the electrostatic theory in the limit $\zeta \ll c$, as discussed in Chapter 3, another class of instabilities arises due to the anisotropy of distributions. Just as broad a class of instability as the electrostatic streaming modes, these anisotropy-driven instabilities all fall under the label Weibel instability [90]. In this section the dielectric tensor components are determined for Weibel modes by considering, for simplicity, a two-sided Fourier analysis in time. The result of a one-sided time analysis is that only unstable modes are actual eigenfunctions of the system.

Consider the Vlasov-Maxwell equations linearized around a homogeneous equilibrium,

$$\partial_t f_1 + \boldsymbol{v}\cdot\nabla_x f_1 + \frac{q}{m}(\boldsymbol{E}+\boldsymbol{v}\times\boldsymbol{B})\cdot\nabla_v f_0 = 0, \tag{6.1}$$

$$\partial_t \boldsymbol{B} = -\nabla\times\boldsymbol{E}, \tag{6.2}$$

$$c^{-2}\partial_t\boldsymbol{E} = -\mu_0\boldsymbol{j}_1 + \nabla\times\boldsymbol{B}. \tag{6.3}$$

Faraday's equation gives $\boldsymbol{B} = \omega^{-1}\boldsymbol{k}\times\boldsymbol{E}$. Then the spectral Lorentz force is

$$\boldsymbol{E}+\boldsymbol{v}\times\boldsymbol{B} = \omega^{-1}\big((\omega-\boldsymbol{k}\cdot\boldsymbol{v})\boldsymbol{E} + (\boldsymbol{v}\cdot\boldsymbol{E})\boldsymbol{k}\big). \tag{6.4}$$

Therefore, a coordinate-independent form of the Vlasov linear response is

$$i\omega f_1 = \frac{q}{m}\boldsymbol{E}\cdot\nabla_v f_0 + \frac{q}{m}(\boldsymbol{v}\cdot\boldsymbol{E})\frac{\boldsymbol{k}\cdot\nabla_v f_0}{\omega-\boldsymbol{k}\cdot\boldsymbol{v}}, \tag{6.5}$$

and the spectral time-derivative of the perturbed current follows as

$$\mu_0(-i\omega\boldsymbol{j}_1) = \frac{\omega_p^2}{c^2}\Big(\boldsymbol{E} - \int \boldsymbol{v}(\boldsymbol{v}\cdot\boldsymbol{E})\frac{\boldsymbol{k}\cdot\nabla_v f_0}{\omega-\boldsymbol{k}\cdot\boldsymbol{v}}d\boldsymbol{v}\Big). \tag{6.6}$$

Note that the first term of the linear response, Eq. 6.5, has no resonant denominator and thus integrates out in the perturbed current, Eq. 6.6, in a manner independent of the distribution function. In this way, the first term of Eq. 6.5 constitutes the non-thermal response. This happens because the component of the Lorentz force orthogonal to the particle velocity vanishes in the frame of the electromagnetic wave, which exactly cancels the velocity-dependent propagation term $\omega - \boldsymbol{k}\cdot\boldsymbol{v}$. The second term of Eq. 6.5 encodes energy transfer between the plasma and its wavefield.

6.1 Tensor components for arbitrary Cartesian coordinates

Suppose one adopts orthogonal Cartesian coordinates (x,y,z) and considers a plane wave with wavevector $\boldsymbol{k} = k_x\hat{x} + k_y\hat{y} + k_z\hat{z}$. The dielectric tensor can then be written as [32]

$$\begin{aligned} \varepsilon_{ij}E_j &= 0 \\ \varepsilon_{ij} &= \delta_{ij} - \frac{c^2k^2}{\omega^2}\Big(\delta_{ij} - \frac{k_ik_j}{k^2}\Big) - \frac{\omega_p^2}{\omega^2}\Big(\delta_{ij} - \int v_iv_j\frac{\boldsymbol{k}\cdot\nabla_v f_0}{\omega - \boldsymbol{k}\cdot\boldsymbol{v}}d\boldsymbol{v}\Big) \end{aligned} \tag{6.7}$$

In a one-sided time analysis a vector of initial conditions appears on the RHS of the dispersion equation. The form appears simple enough, but evaluation of this general Cartesian form is usually difficult because the resonant denominator is $\omega - k_xv_x - k_yv_y - k_zv_z$, making the resulting integrals inseparable even for separable distributions of the form $f_0(\boldsymbol{v}) = f_{0x}(v_x)f_{0y}(v_y)f_{0z}(v_z)$. The way to proceed is to choose a frame such that one coordinate is aligned with the wave-vector so that the resonant denominator will appear only as $\omega - kv_{\parallel}$.

6.2 Electromagnetic susceptibility and the eigenvalue problem

The dispersion tensor defined by Eq. 6.7 may be reformulated as an eigenvalue problem. This is a useful operation when constructing the field eigenvectors for setting up numerical simulation of a kinetic instability as an initial value problem. Multiply by ω^2 and pull out the diagonal tensor $\omega^2\delta_{ij}$ containing the frequency. Defining the integral part of the self-consistent current source as

$$I_{ij} \equiv \int_{\mathcal{C}} v_iv_j\frac{\boldsymbol{k}\cdot\nabla_v f_0}{\omega - \boldsymbol{k}\cdot\boldsymbol{v}}d\boldsymbol{v} \tag{6.8}$$

where the integral is evaluated on the Landau contour $\mathcal{C}$, *i.e.* analytically continued to the lower-half complex ω-plane. The dielectric tensor system may then be rewritten as

$$\left\{\delta_{ij} - I_{ij} + (k\lambda_c)^2\left(\delta_{ij} - \frac{k_i k_j}{k^2}\right)\right\}E_j = \left(\frac{\omega}{\omega_p}\right)^2 E_i \tag{6.9}$$

where $\lambda_c = c/\omega_p$ is the inertial length. The resonant integrals are naturally functions of the phase velocity $\zeta = \omega/k$, so one can also express the system as

$$\frac{1}{(k\lambda_D)^2}\left\{\delta_{ij} - I_{ij} + (k\lambda_c)^2\left(\delta_{ij} - \frac{k_i k_j}{k^2}\right)\right\}E_j = \left(\frac{\zeta}{v_t}\right)^2 E_i \tag{6.10}$$

with v_t a normalization thermal velocity. Equation 6.10 casts the problem in eigenvalue form as the system of integral equations

$$\chi(k,\zeta)\vec{E} = \zeta^2\vec{E}. \tag{6.11}$$

Just like the scalar Poisson problem there are an infinite number of solutions ζ for a given k, obtained by determining a root of the characteristic function $D(k,\zeta) \equiv \det(\chi - \zeta^2 I) = 0$. As in the scalar problem only unstable solutions satisfying $\mathrm{Im}(\zeta) > 0$ constitute normal modes of oscillation. In an unmagnetized homogeneous plasma these modes are either streaming instabilities (*e.g.* two-stream, Buneman, ion-acoustic) or generalized Weibel instabilities. In either case their effect is thermalization on averaged scales by reducing relative velocities far from equilibrium. Note also that casting the dispersion tensor for a magnetized homogeneous equilibrium in eigenvalue form proceeds in exactly the same manner; the main difference is that the integral functions I_{ij} are sums over resonances at Doppler-shifted cyclotron harmonics and their calculation is tedious.

Having determined a particular characteristic value such that $D(k,\zeta_n) = 0$, the corresponding electric field mode $\vec{E}_n$ is found by solving for the eigenvector of the matrix $\chi_n = \chi(\zeta_n, k)$ with eigenvalue ζ_n^2. The other eigenvalues of the matrix χ_n are spurious and do not solve the system of Eq. 6.11. The magnetic part of the eigenmode is obtained through $\vec{B}_n = \zeta_n^{-1}\hat{k} \times \vec{E}_n$.

6.3 Dielectric tensor components for the bi-Maxwellian

A useful zero-order distribution function to illustrate the instability due to anisotropic pressure in a plasma with zero-order ballistic trajectories is the bi-Maxwellian, or two-temperature distribution. Two temperature, bi-Maxwellian distributions commonly arise in magnetized plasmas. In the limit of weak magnetic field the following analysis is applicable, where the zero-order plasma trajectories are ballistic. For a discussion of the limit of strong magnetization see Chapter 7. Let (x, y, z) and (u, v, w) be Cartesian coordinates in configuration space and velocity space respectively. Then the bi-Maxwellian with principal axes in the (x, y)-directions is given by

$$f_0 = \frac{1}{(2\pi)^{3/2} u_t v_t w_t} \exp\Big\{ -\frac{1}{2}\Big(\frac{u^2}{\theta_u^2} + \frac{v^2}{\theta_v^2}\Big)\Big\} \exp\Big\{ -\frac{w^2}{2\theta_w^2}\Big\}. \tag{6.12}$$

Let the wavevector lie in the (x, y) plane such that $\hat{z} = \hat{e}_b$ is the binormal direction. In this case the binormal direction does not contribute to the perturbed current in the (x, y) plane. This causes the transverse component in the $\hat{z}$-direction to decouple [91], and the dielectric tensor simplifies as

$$\begin{Bmatrix} \omega^2 - \omega_p^2(1 - I_{11}) & \omega_p^2 I_{12} & 0 \\ \omega_p^2 I_{12} & \omega^2 - c^2k^2 - \omega_p^2(1 - I_{22}) & 0 \\ 0 & 0 & \omega^2 - c^2k^2 - \omega_p^2(1 - I_{33}) \end{Bmatrix} \begin{Bmatrix} E_1 \\ E_2 \\ E_3 \end{Bmatrix} = 0. \tag{6.13}$$

In the coupled components I_{13}, I_{23}, etc., the z-velocity integrates out, leaving a distribution $f_0(u, v)$ such that lines of constant f_0 lie on ellipses in the (u, v) velocity plane. Assume that $\theta_v > \theta_u$ so that the semi-major axis of the ellipse is y-directed and the defining ellipse has eccentricity $e^2 = 1 - \theta_u^2/\theta_v^2$. Since propagation depends on the gradient of f_0 in the direction parallel to the electromagnetic wave, consider a rotation of the (x, y) frame through an angle φ defining $(v_\parallel, v_\perp)$ velocities. For any rotation not aligned with the principal axes the distribution is non-separable due to the presence of a cross-term. Rotation of the coordinates followed by completing the square on the variable $v_\perp$ shows the distribution to be

$$f_0(v_\parallel, v_\perp) = \frac{1}{2\pi\theta_\parallel\theta_\perp} \exp\Big(-\frac{v_\parallel^2}{2\theta_\parallel^2}\Big) \exp\Big(-\frac{(v_\perp - \alpha v_\parallel)^2}{2\theta_\perp^2}\Big) \tag{6.14}$$

where the rotated thermal and mean velocities are found to be

$$\theta_\parallel \equiv \theta_u \sqrt{\frac{1-e^2}{1-e^2\cos^2(\varphi)}}, \qquad \theta_\perp \equiv \theta_u \frac{1}{\sqrt{1-e^2\cos^2(\varphi)}}, \qquad \alpha \equiv \frac{e^2\sin^2(\varphi)\cos^2(\varphi)}{1-e^2\cos^2(\varphi)}. \tag{6.15}$$

The form of Eq. 6.14 shows clearly that the distribution is normal along both the longitudinal and transverse directions, yet for a choice of a particular $v_\parallel$ along the rotated axis the transverse normal distribution is shifted by an amount $\alpha v_\parallel$, as illustrated in Fig. 6.1. Thus for electromagnetic wave propagation in a plasma with anisotropic temperature, the integral $I_2 \neq 0$ because there exists an effective transverse current for particular velocities parallel to the wavevector, although there is zero net current in the fixed frame. This implies that longitudinal and transverse wave components are coupled for propagation angles not aligned with the principal axes of the distribution.

To evaluate the integrals I_{11}, I_{12}, and I_{22} for the distribution in Eq. 6.14 in the rotated coordinates, note the following integrals related to the plasma dispersion function $Z(\zeta)$:

$$\frac{1}{\sqrt{\pi}}\int_{-\infty}^{\infty} \frac{x}{\zeta - x} e^{-x^2/2a^2} dx = \frac{a}{\sqrt{2}} Z'(\widetilde{\zeta}), \tag{6.16}$$

$$\frac{1}{\sqrt{\pi}}\int_{-\infty}^{\infty} \frac{x^2}{\zeta - x} e^{-x^2/2a^2} dx = -\Big(\frac{a}{\sqrt{2}}\Big)^2 (Z''(\widetilde{\zeta}) + 2Z(\widetilde{\zeta})), \tag{6.17}$$

$$\frac{1}{\sqrt{\pi}}\int_{-\infty}^{\infty} \frac{x^3}{\zeta - x} e^{-x^2/2a^2} dx = \Big(\frac{a}{\sqrt{2}}\Big)^3 (Z'''(\widetilde{\zeta}) + 6Z'(\widetilde{\zeta})) \tag{6.18}$$

where $\widetilde{\zeta} = \zeta/\sqrt{2}a$. These formulas are found with the Hermite function relation $\psi_n(x) = \frac{d^n}{dx^n} e^{-x^2/2}$, and are put into alternative forms using the differential equation $Z(\zeta)' = -2(1 + \zeta Z(\zeta))$. The gradient of the distribution is then calculated as $\frac{\partial f}{\partial v_\parallel} = \Big(-\frac{v_\parallel}{\theta_\parallel^2} + \alpha\frac{v_\perp - \alpha v_\parallel}{\theta_\perp^2}\Big) f$. By

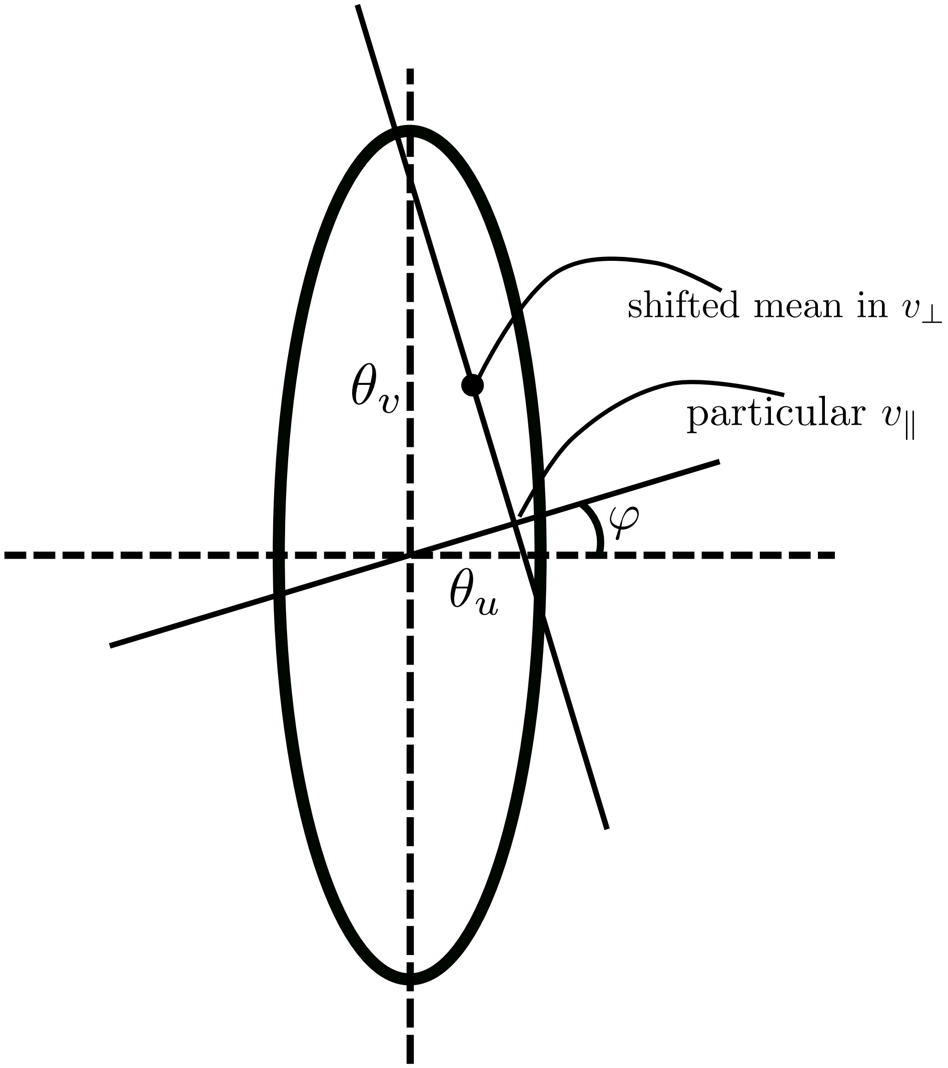

Figure 6.1: In a rotated frame relative to the principal axes of an anisotropic Maxwellian distribution, for any given $v_\parallel$ velocity there exists an effective mean velocity in the transverse direction. This results in nonzero mixed resonant moments $I_{ij} \neq 0$ for $i \neq j$ and couples together the electromagnetic wave branches.

this analysis, the velocity space integrals in the dielectric tensor components work out to

$$I_{11} = \frac{-1}{4}(Z'''(\widetilde{\zeta}) + 6Z'(\widetilde{\zeta})), \tag{6.19}$$

$$I_{12} = \frac{-\alpha}{4}(Z'''(\widetilde{\zeta}) + 6Z'(\widetilde{\zeta})), \tag{6.20}$$

$$I_{22} = \frac{-\alpha^2}{4}(Z'''(\widetilde{\zeta}) + 2Z'(\widetilde{\zeta})) - \frac{\theta_\perp^2}{\theta_\parallel^2}\frac{Z'(\widetilde{\zeta})}{2}, \tag{6.21}$$

$$I_{33} = -\frac{\theta_w^2}{\theta_\parallel^2}\frac{Z'(\widetilde{\zeta})}{2} \tag{6.22}$$

where $\widetilde{\zeta} \equiv \zeta/\sqrt{2}\theta_\parallel$. The two quantities $\theta_\perp^2/\theta_\parallel^2$ and $\theta_w/\theta_\parallel^2$ represent the degree of anisotropy perpendicular to the angle of propagation φ. Thus, both the coupled and decoupled components result in electromagnetic Weibel instability. From the expression for I_{33} it's clear that the effective parallel energy contributing to the anisotropic growth of a Weibel-type instability is $\theta_\parallel^2 = \theta_u^2\left(\frac{1-e^2}{1-e^2\cos^2(\varphi)}\right)$ for various angles of propagation. As discussed, the parameters appearing are functions of the elliptical geometry of the two-temperature distribution. In the perhaps unusual case of a three-temperature Maxwellian distribution, no component will decouple and the parameters will be functions of an ellipsoidal geometry. For $\varphi \to 0$ the parameters $\alpha, \beta \to 0$ and the longitudinal/transverse parts decouple as $I_{12} = 0$ and $\lim_{\varphi\to 0} I_{22} = -\frac{\theta_v^2}{\theta_u^2}\frac{Z'(\zeta/\sqrt{2}\theta_u)}{2}$ as expected.

6.3.1 Dispersion function for the classic Weibel instability

Focusing on the decoupled component in Eq. 6.13, namely $\varepsilon_{33}E_3 = 0$, leads to

$$\varepsilon_{33} = 1 - \left(\frac{\zeta}{c}\right)^2 + \frac{1}{(k\ell_s)^2}\left(1 - \langle v_\perp^2\rangle \int_{-\infty}^{\infty} \frac{1}{\zeta - u}\frac{\partial f_0}{\partial v_\parallel} dv_\parallel\right) = 0 \tag{6.23}$$

where here $\langle v_\perp^2\rangle$ is the mean-square velocity perpendicular to the direction of propagation, $\zeta = \omega/k$ is the phase velocity and $\ell_s = \omega_p/c$ the skin depth. Considering the special case of two electron beams of thermal velocities v_t and each of drift velocity $\pm v_b$ obtains the dispersion relation presented in Cagas [92]. On the other hand, for the bi-Maxwellian distribution the dispersion function is

$$\varepsilon_{33} = 1 - \Big(\frac{\zeta}{c}\Big)^2 + \frac{1}{(k\ell_s)^2}\Big(1 + \frac{\theta_\perp^2}{\theta_\parallel^2}\frac{Z'(\widetilde{\zeta})}{2}\Big) = 0. \tag{6.24}$$

If $\theta_\perp = \theta_\parallel$ then Eq. 6.24 reduces to to the expression for an isotropic Maxwellian, motivating

$$\varepsilon_{33} = 1 - \Big(\frac{\zeta}{c}\Big)^2 + \frac{1}{(k\ell_s)^2}\Big(1 + \frac{Z'(\widetilde{\zeta})}{2} + A\frac{Z'(\widetilde{\zeta})}{2}\Big) \tag{6.25}$$

where $A \equiv \theta_\perp^2/\theta_\parallel^2 - 1$ is the distribution anisotropy.

6.4 Single-mode saturation of Weibel instability in one spatial dimension

Just as electrostatic instability saturates by the trapping of plasma at resonant velocities in the electrostatic wavefield, magnetic trapping is often the means by which electromagnetic instability saturates. Simulation of a single unstable Weibel mode allows one to visualize the nonlinear phase space structure associated with magnetic trapping. This calculation was done previously by Cagas with a highly resolved continuum kinetic numerical approach using as zero-order distribution a pair of counter-streaming electron beams [92]. Beam initial conditions are typically used because Weibel instabilities are generated in the laboratory by colliding plasmas at high velocity [93, 94, 95, 96]. While beam plasmas are necessarily anisotropic, they are also potentially unstable to electrostatic streaming instability. Development of streaming instability was proposed by Cagas to explain the growth of electric energy along the beam axis as the Weibel mode approached saturation. There is no possibility of streaming instability when studying the saturation of Weibel instability from a zero-order bi-Maxwellian distribution. The bi-Maxwellian problem is considered here using the continuum kinetic method. Early simulations of the instability of bi-Maxwellians are found in the study of Davidson using particle-in-cell method [97].

This section summarizes a study of the Weibel instability in one spatial dimension using the mixed spectral-DG method presented in Chapter 2, where the space coordinate is represented using Fourier modes and the two velocity dimensions discretized using DG. The field equations are chosen as follows: Ampere's law and Faraday's law are used to evolve the transverse electrodynamic field, and Gauss's law is used to constrain the electric field along the axis of the wavevector. In this way only three field equations are necessary (one component each of the electrodynamic equations, and Gauss's law) when considering only a single spatial coordinate. The geometry is established by aligning the hot direction of the bi-Maxwellian with the y-coordinate, the growing magnetic field with the z-direction, and perturbing the distribution function with wavenumber in the x-direction. This necessitates two dimensions of velocity, v_x in the x-direction and v_y in the y-direction, for a 1D2V phase space geometry. Phase space is discretized using $N_x = 100$ evenly-spaced collocation nodes in the x-direction, and $N_{v_x} = N_{v_y} = 22$ finite elements in velocity, each of 11th polynomial order. Fourteen elements are evenly spaced between the velocity intervals $[-7, 7]v_t$, and four elements are evenly spaced from the velocity boundaries at $\pm 15v_t$ to the intervals $\pm 7v_t$ respectively. A spatial hyperviscosity $10^{-4}\nabla_x^4 f$ is used to prevent spectral blocking by the turbulent cascade saturation. The field equations are discretized by a standard Fourier spectral method.

The characteristic problem parameters are chosen such that $v_t/c = 0.3$ and anisotropy $A = 3$ (or ratio $\theta_y/\theta_x = 2$) with the zero-order distribution Eq. 6.12. Velocities are normalized to θ_x, time to ω_p^{-1}, and lengths to $\lambda_D = \theta_x/\omega_p$. The domain length is then specified by the chosen wavenumber $k_x\lambda_D = 0.1$. Solution of Eq. 6.24 gives the eigenvalue of the problem as the phase velocity $\zeta/v_t = 1.23i$. Using the eigenvalue, the bi-Maxwellian is perturbed using the linear response function:

$$f_1(x, v_x, v_y) = \mathrm{Re}\Big\{i\frac{\alpha}{k}\Big(\frac{v_y}{\zeta - v_x}\frac{\partial f_0}{\partial v_x} + \frac{\partial f_0}{\partial v_y}\Big)\exp(ikx)\Big\}, \tag{6.26}$$

and the initial transverse electrodynamic fields by

$$B_{z1} = \mathrm{Re}\Big(\alpha\exp(ikx)\Big), \tag{6.27}$$

$$E_{y1} = \mathrm{Re}\Big(\zeta\alpha\exp(ikx)\Big), \tag{6.28}$$

where the amplitude is set to $\alpha = 10^{-3}$. This initial condition is consistent in the sense that the zeroth moment of Eq. 6.26 is zero and its first moment is the source of B_{z1} and E_{y1}.

The simulation is run until $t\omega_p = 100$ using the time integration methods discussed in Chapter 2 using a time-step of $\Delta t = 2.0 \times 10^{-3}$. The change in time-integrated wave energies is shown in Fig. 6.2. Of note is that the transverse electric field oscillates following saturation, and the longitudinal electric energy trend follows that of the magnetic energy.

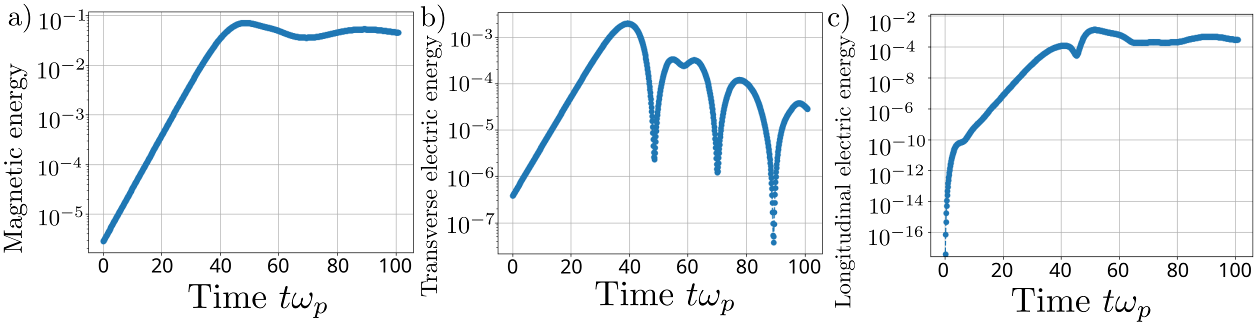

Figure 6.2: Evolution of domain-averaged wave energies past saturation of Weibel instability in one spatial dimension, namely a) the magnetic energy, b) the transverse electric energy of E_y, and c) the longitudinal electric energy of E_x, or energy along the axis of the wavevector. A nonlinear phase is reached at $t\omega_p = 40$, with peak magnetic energy around $t\omega_p = 50$. Longitudinal electric energy is observed to grow with a similar trend to the magnetic energy.

Figure 6.3 shows the time evolution of magnetic field and electron density in increments of $t\omega_p = 20$. As the magnetic energy grows, electrons of progressively lower velocity are trapped by the velocity-dependent force $v_y B_z$. The mechanism of nonlinear saturation is well-known as electron trapping within the effective potential wells of the electromagnetic field as the distribution function evolves towards a function of the constants of motion, namely the energy $E = \frac{1}{2}m(v_x^2 + v_y^2) - e\varphi(x)$ and components of canonical momentum $p_y = mv_y - eA_y(x)$, $p_x = mv_x$ [97]. Specifically, phase space trajectories are determined by the equation [98]

$$mv_x = \sqrt{2m(E + e\varphi(x)) - (p_y + eA_y(x))^2} \tag{6.29}$$

for any specific initial constants of motion $E = \frac{1}{2}m(v_{x0}^2 + v_{y0}^2)$ and $p_y = mv_{y0}$. Magnetic trapping is visualized in Fig. 6.4 showing a contour of the distribution function at 10% of the maximum value. Trapping and passing trajectories are seen at the right and left of the figure, respectively, for $v_y > 0$. Yet on the other side of phase space for $v_y < 0$, the positions of the trapping trajectories and passing trajectories are exchanged as the sign of the effective potential changes with that of $B_z(x)$.

Rather than a secondary electrostatic streaming instability, the growth of electrostatic energy observed in Cagas is a second-order phenomenon arising from space charge-generating density filamentation. This can be understood intuitively as being due to magnetic trapping, or as a coupling to the longitudinal field at second order in the transverse dynamic field. Trapping from either electric or magnetic fields is associated with local variations in the electron density, which manifests as space charge. Since the fraction of trapped electrons is proportional to the magnetic energy, with saturation when the characteristic magnetic bounce frequency reaches the growth rate [97], it follows that longitudinal electric fields will trend with the magnetic field. The development of space charge from magnetic pressure is anticipated in the discussion of Morse [98], and the longitudinal field is explained in an article of Taggart to arise at second-order from the coupling of two magnetic modes [99]. Since the magnetic field, plotted in Fig. 6.3, is observed to evolve into a multi-mode nonlinear wave resembling an elliptic cosine, mode pairs are indeed available to couple into the longitudinal field. Dynamic space charge in filamentation has been observed in modeling to modify growth rates, in both early and more recent studies [99, 100]. While the charge density is a second-order effect, the first-order effect of electrodynamic instability should be understood as the generation of electric currents to sustain the steadily growing magnetic mode.

6.5 Saturation of many unstable Weibel modes in two spatial dimensions

In reality the Weibel instability is multidimensional because wavevectors oblique to the principal anisotropy axes have growth rates comparable to the maximum, as was the case for the electrostatic streaming instability. Considering for example the dielectric tensor of the bi-Maxwellian in Eq. 6.13, one branch of instability exists satisfying the equation $\omega^2 - c^2k^2 - \omega_p^2(1 - I_{33}) = 0$. The transverse electromagnetic field of this branch is decoupled

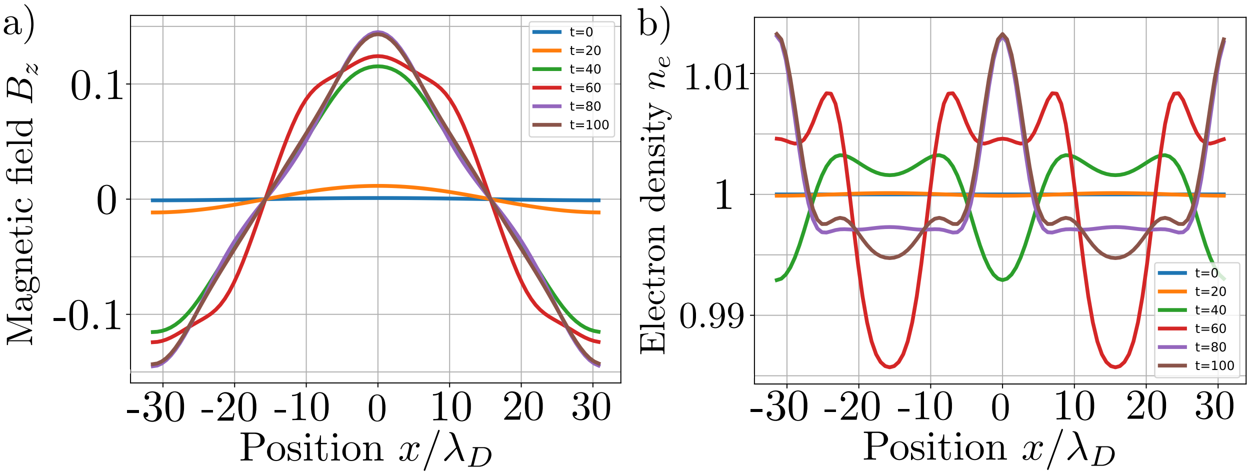

Figure 6.3: Evolution of a) magnetic field $B_z(x)$ and b) electron density $n_e(x)$, to nonlinear saturation of a single unstable Weibel mode. The mode saturates around $t\omega_p \approx 45$. Prior to saturation, the magnetic field has a spectrum consisting of only even mode numbers with an apparent power law in logarithmic amplitudes. Since the function is clearly analytic this spectrum is consistent with an elliptic cosine function up to time of saturation. The electron holes at saturation are bounded by the maxima of magnetic energy $B^2/2\mu_0$, or equivalently bounded by the potential wells $A_y(x)$.

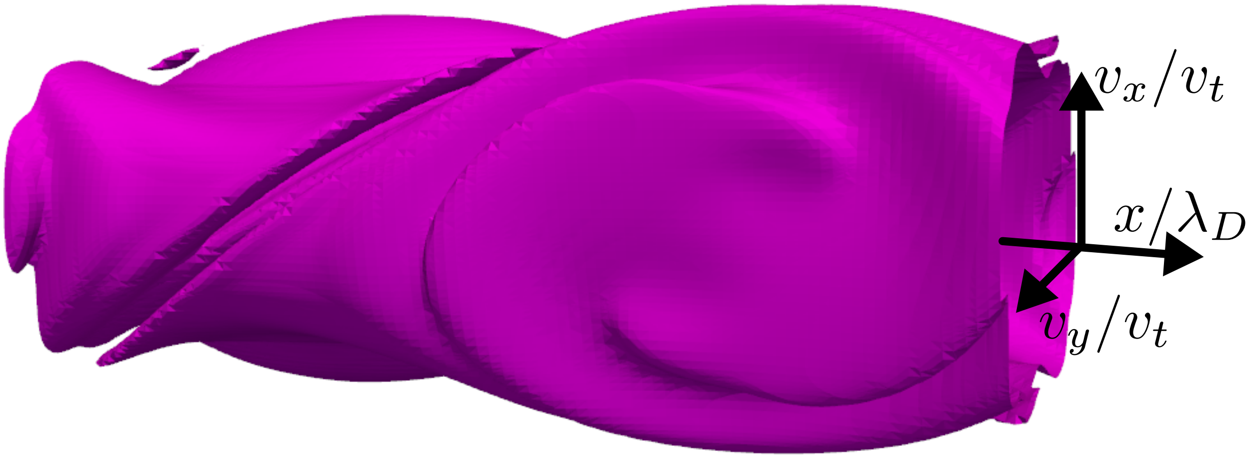

Figure 6.4: Phase space structure shown by contour at 0.1max(f) in the phase space (x, v_x, v_y) at saturation of a single Weibel mode. The middle of the domain in the x-coordinate corresponds to $x = 0$. The magnetic trapping phase space vortex is distinguished from the electrostatic vortex as velocity-dependent since the momentum p_y in Eq. 6.29 is linear in v_y. In this way the single-mode phase space vortex is symmetric, with vortex and passing orbits exchanging places as $v_y \rightarrow -v_y$.

from the other components and has magnetic field in the (x, y)-plane. The other branch consists of the solutions to the equation

$$(\omega^2 - \omega_p^2(1 - I_{11}))(\omega^2 - c^2k^2 - \omega_p^2(1 - I_{22})) - \omega_p^4 I_{12}^2 = 0 \qquad (6.30)$$

with magnetic field out of plane and transverse electric fields in-plane. The out-of-plane magnetic field allows a reduced 2D2V phase space geometry for more feasible continuum kinetic simulation [32]. It should be kept in mind, however, that the E_3 branch of the dielectric tensor is also unstable and means that the instability dynamics are truly three-dimensional, just as in Section 3.5. Figure 6.5 plots the growth rate as function of wavevector $\boldsymbol{k} = k_x\hat{x} + k_y\hat{y}$ of the unstable branch of Eq. 6.30 for a zero-order bi-Maxwellian distribution with anisotropy $A = 3$ and where $v_t/c = 0.3$.

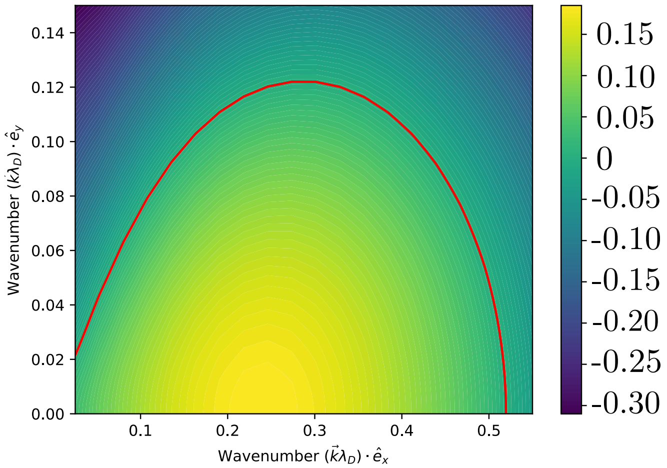

Figure 6.5: Growth rates of multidimensional Weibel instability as $\text{Im}(\omega)/\omega_{pe}$ for an anisotropic bi-Maxwellian with anisotropy $A = 3$ and $v_t/c = 0.3$. The red line is the marginal stability boundary.

6.5.1 Initialization and implementation of the two-dimensional problem

The numerical implementation is identical to the discussion in Section 3.5 except that Ampere's law and Faraday's law are used for the field equations, and are time-integrated in Fourier spectral space with the same third-order Adams-Bashforth multistep method used for the kinetic equation. However there is an important difference in initialization of the unstable modes. In the Vlasov-Poisson system the eigenfunctions are proportional to the scalar potential φ, yet in the Vlasov-Maxwell system the kinetic eigenfunctions are proportional to the components of the electric field $\boldsymbol{E}$. Thus when initializing with kinetic eigenfunctions in an electrodynamic problem these components must be consistent with an eigenvector of the equation $\chi\boldsymbol{E} = \zeta^2\boldsymbol{E}$ as in Section 6.2. For a given wavevector of angle θ in the (x, y)-plane, these eigenvectors are computed in the wavevector frame and then anti-rotated into the (x, y) frame with components $\boldsymbol{E} = E_x\hat{x} + E_y\hat{y}$. For each pair (k_x, k_y), this is procedure is used to apply a perturbation of the form

$$f_1 = \alpha\text{Re}\Big(\frac{q}{i\omega}\Big\{E_x\Big(\frac{\partial f_0}{\partial u} + \frac{v_x(\boldsymbol{k}\cdot\nabla_v f_0)}{\omega - \boldsymbol{k}\cdot\boldsymbol{v}}\Big) + E_y\Big(\frac{\partial f_0}{\partial v} + \frac{v_y(\boldsymbol{k}\cdot\nabla_v f_0)}{\omega - \boldsymbol{k}\cdot\boldsymbol{v}}\Big)\Big\}\exp(i(\boldsymbol{k}\cdot\boldsymbol{x} + \widetilde{\varphi}))\Big) \quad (6.31)$$

with $\widetilde{\varphi}$ a randomly chosen phase shift per perturbed wavevector and the amplitude $\alpha = 2\times10^{-3}$. The magnetic field is then initialized as $B_z = \zeta^{-1}\hat{k}\times\boldsymbol{E}$ where ζ is the eigenvalue. A higher amplitude than in the one-dimensional problem is chosen to reduce time to saturation.

The domain is specified by fundamental wavenumbers $k_x\lambda_D = 0.125$ and $k_y\lambda_D = 0.01$. Physical space is represented with $N_x = 32$ and $N_y = 128$ evenly-spaced collocation points, while velocity space is represented as a Cartesian tensor product of linear finite elements with eleven finite elements per (v_x, v_y) axis each of seventh-order polynomial basis spanning velocity space for each $(v_x, v_y) \in [-11, 11]\theta_x$. As in Section 3.5 a number of modes are excited; for each of the first two harmonics of the fundamental wavenumber, namely $nk_x\lambda_D$ with $n = 1, 2$, five transverse wavenumbers $\pm mk_y\lambda_D$ are excited with $m = 0, 1, 2$. The parameter $v_t/c = 0.3$ and the anisotropy is $A = 3$, as in the one-dimensional problem. The simulation is run to $t\omega_p = 40$ using a time-step of $\Delta t = 8\times10^{-3}$ with an added hyperviscosity $\nu\nabla_x^4 f$ with $\nu = 1$ to prevent spectral blocking. Due to the poor velocity-space resolution the energy is conserved only to $\mathcal{O}(10^{-4})$ by the simulation stop time. Resolution is limited by the memory of the NVIDIA RTX 3090 graphics card used to conduct these simulations.

6.5.2 Simulation results

Figure 6.6 shows the energy traces of the electrodynamic field during the linear phase and beyond instability saturation. Nonlinear saturation, as gauged by the transverse electric field E_y, occurs around $t\omega_p = 17$. The energy of the electric field E_x follows a similar trend as in the one-dimensional problem. Its growth is made up of two effects: linear growth from the initialized oblique modes, and the development of space charge with x-directed wavevector to second-order in the magnetic field as discussed in Section 6.4. Figure 6.7 illustrates the dynamics of multidimensional instability through streamlines of the current density $\boldsymbol{j}(x, y)$ and filled contours of its magnitude for three times in the simulation output. Trigonometric interpolation is used to visualize the current density by zero-padding the spectrum and inverse Fourier transformation, as the spectrum is properly resolved up to the chosen spectral cut-off. In Fig. 6.7b one can observe spiral current streamlines indicating the local production of space charge as the electrons form filaments. By the simulation stop-time nonlinear mixing has caused some of the filaments to rotate, indicating an isotropization on averaged scales. Inspection of Fig. 6.8, which plots the spatially-averaged distribution function $\langle f\rangle_{(x,y)}(v_x, v_y)$ at $t\omega_p = 0$ and $t\omega_p = 40$, shows the relaxation of the initially anisotropic distribution through the Weibel turbulence within the domain in Fig. 6.8a,b and the change of the anisotropy parameter A in time in Fig. 6.8c. The anisotropy is observed to decrease monotonically until $A = 1$. This observation should be confirmed with more highly-resolved studies.

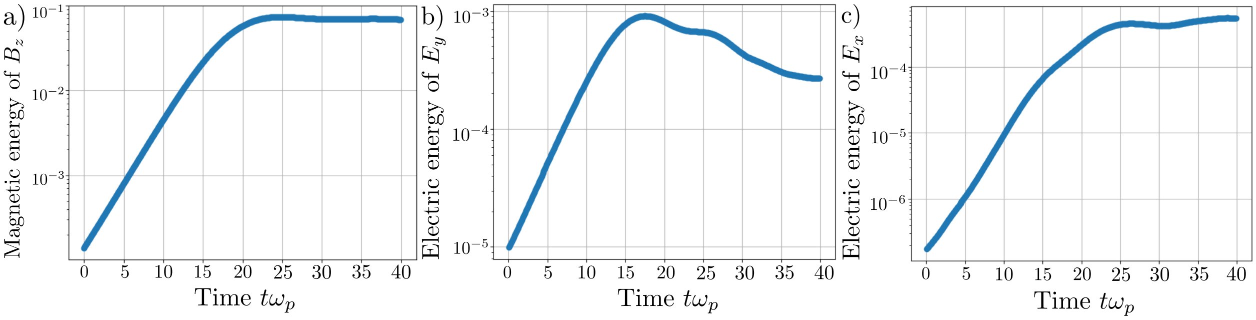

Figure 6.6: Time change in domain-averaged energy for a) the out-of-plane magnetic field B_z, b) the electric energy transverse to the maximum growth-rate axis, and c) the electric energy parallel to that axis (formerly the longitudinal field of the 1D problem). A difference from the one-dimensional simulation is a steadily decreasing transverse electric energy rather than an oscillation by the time of saturation. The x-directed electric energy increases at a rate faster than the growth of the linear modes due to the same space charge effects as in the single-mode simulation discussed in Section 6.4.

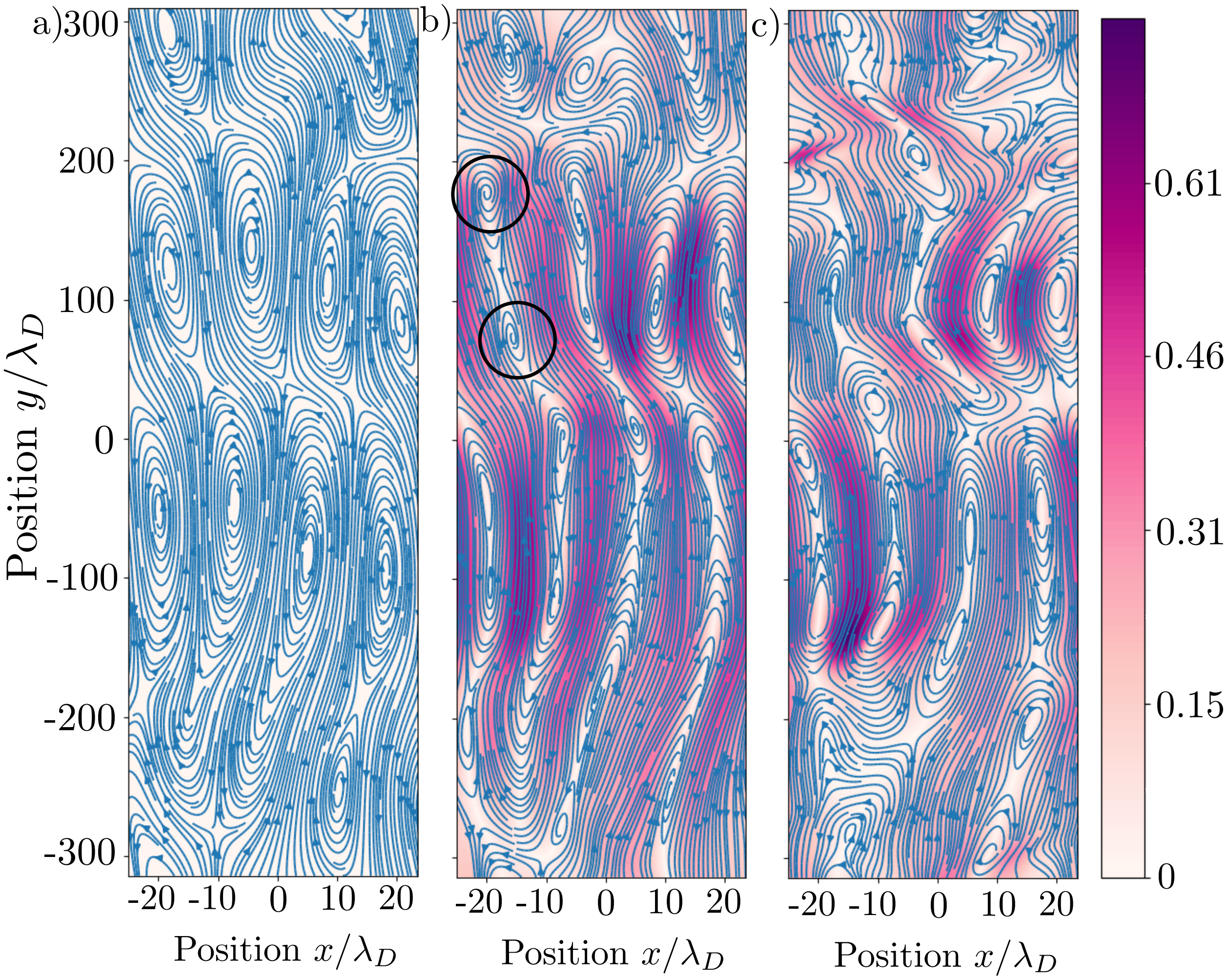

Figure 6.7: Evolution of current at times a) $t\omega_p = 0$, b) $t\omega_p = 25$, and c) $t\omega_p = 39.5$. Plotted are streamlines of $\boldsymbol{j}$ and its magnitude $|\boldsymbol{j}|$ as filled contours. Current tends to form closed paths at long wavelength in y. Note also that spiral vortexes in the streamlines, two examples here circled in black, indicate generation of space charge.

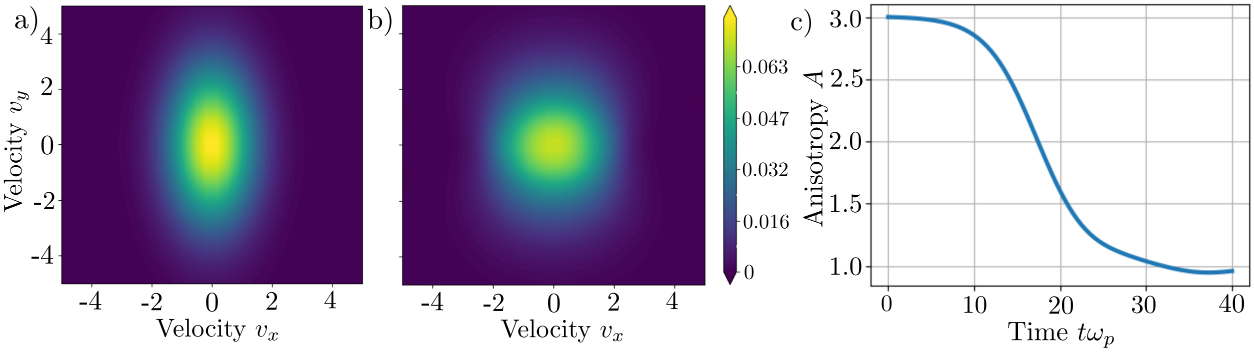

Figure 6.8: Shown is the relaxing spatially-averaged distribution function $\langle f\rangle_{(x,y)}(v_x, v_y)$ at two times, a) the initial condition $t\omega_p = 0$ and b) the stop-time $t\omega_p = 40$, and in addition c) the time evolution of the anisotropy parameter $A = \langle v_y^2\rangle/\langle v_x^2\rangle - 1$. The turbulence of magnetic trapping vortexes in the turbulent currents of the saturated instability relaxes the distribution function towards an isotropic distribution. Note that $A = 0$ corresponds to a fully isotropic distribution.

Chapter 7

STRONGLY MAGNETIZED ELECTROMAGNETIC MODES

This chapter reviews the theory of the dielectric tensor of plasma immersed in a homogeneous magnetic field, mainly to propose the emission of parallel-propagating whistler waves by an anisotropic distribution as an excellent 1D3V Vlasov-Maxwell test case.

7.1 Phase space linear response of electromagnetic cyclotron modes

This section summarizes the key points of the derivation of the dielectric tensor components and casts the linear response function in a form well-suited for numerical evaluation. The development follows that of Ref. [83] where a detailed derivation of the tensor components may be found. The same propagation geometry as the electrostatic analysis in Chapter 5 (that is, $\boldsymbol{k} = k_\perp \hat{x} + k_\parallel \hat{z}$) is assumed. This electrostatic analysis is combined with that of the first-order electromagnetic Lorentz force presented in Chapter 6 to find the linearized Vlasov equation as an ODE in the cylindrical velocity space angle φ analogous to Eq. 5.2,

$$\frac{df_1}{d\varphi} - i\frac{\omega - \boldsymbol{k}\cdot\boldsymbol{v}}{\omega_c} f_1 = \frac{1}{B_0\omega}((\omega - \boldsymbol{k}\cdot\boldsymbol{v})\boldsymbol{E} + (\boldsymbol{v}\cdot\boldsymbol{E})\boldsymbol{k}) \tag{7.1}$$

with B_0 the zero-order magnetic field and where $\boldsymbol{k}\cdot\boldsymbol{v} = k_\parallel v_\parallel + k_\perp v_\perp \cos\varphi$. Again integrating the inhomogeneous term along the zero-order cyclotron trajectory of the homogeneous solution, the spectral phase space response to an electromagnetic perturbation $(\boldsymbol{E}, \boldsymbol{B})$ is

$$\begin{aligned} f_1(\omega, k_\perp, k_\parallel, v_\perp, \varphi, v_\parallel) = \frac{i}{B_0}\Big\{&\Big(\frac{\partial f_0}{\partial v_\perp} + \frac{k_\parallel}{\omega}(\boldsymbol{v}\times\nabla_v f_0)_\varphi\Big)(\Upsilon_1 E_x + i\Delta_1 E_y) \\ &+ \Big(\frac{\partial f_0}{\partial v_\parallel}\Lambda_1 - \frac{k_\perp}{\omega}\frac{1}{\beta}(\boldsymbol{v}\times\nabla_v f_0)_\varphi \Upsilon_1\Big)E_z\Big\} \end{aligned} \tag{7.2}$$

with $(\boldsymbol{v} \times \nabla_v f_0)_\varphi = (v_\perp \partial_{v_\parallel} - v_\parallel \partial_{v_\perp}) f_0$, the auxiliaries Υ_1 and Λ_1 are as in Eqs. 5.4 and 5.5, and an additional polar Fourier series is defined as

$$\Delta_1 = \sum_{n=-\infty}^{\infty} \frac{\omega_c}{\omega - k_\parallel v_\parallel - n\omega_c} J_n'(\beta) e^{in\varphi} \tag{7.3}$$

and $\beta = k_\perp v_\perp / \omega_c$. Following the notation in Ref. [83], the conductivity tensor σ follows from combining the current of the linear response with Maxwell's equations as

$$\begin{aligned} \sigma = -i\epsilon_0 \omega_p^2 \int_{-\infty}^{\infty} \int_0^{\infty} \sum_{n=-\infty}^{\infty} & \frac{2\pi v_\perp dv_\perp dv_\parallel}{\omega - k_\parallel v_\parallel - n\omega_c} \\ & \times \begin{bmatrix} v_\perp A \frac{n^2 J_n^2(\beta)}{\beta^2} & i v_\perp A \frac{n J_n(\beta) J_n'(\beta)}{\beta} & v_\perp B \frac{n J_n^2(\beta)}{\beta} \\ -i v_\perp A \frac{n J_n(\beta) J_n'(\beta)}{\beta} & v_\perp A J_n'(\beta) J_n'(\beta) & -i v_\perp B J_n(\beta) J_n'(\beta) \\ v_\parallel A \frac{n J_n^2(\beta)}{\beta} & i v_\parallel A J_n(\beta) J_n'(\beta) & v_\parallel B J_n^2(\beta) \end{bmatrix} \end{aligned} \tag{7.4}$$

where $\beta = k_\perp v_\perp / \omega_c$ is the dimensionless Larmor radius parameter, auxiliaries are defined as

$$A \equiv \frac{\partial f_0}{\partial v_\perp} + \frac{k_\parallel}{\omega} (\boldsymbol{v} \times \nabla_v f_0)_\varphi, \qquad B \equiv \frac{\partial f_0}{\partial v_\parallel} - \frac{k_\perp}{\omega} \frac{n}{\beta} (\boldsymbol{v} \times \nabla_v f_0)_\varphi, \tag{7.5}$$

and $f_0(v_\parallel, v_\perp)$ is the magnetized zero-order distribution function. The dielectric tensor is then determined from the conductivity tensor components as $\varepsilon = I - \sigma/(i\omega\epsilon_0)$. While the integrals can be computed for a loss-cone distribution using the techinques of Appendix D, for a feasible computational geometry one can examine parallel-propagating waves.

7.2 Kinetics of parallel-propagating electromagnetic waves

Simulations of kinetic instability for general angles of wave propagation in a magnetized plasma require a 3D3V phase space geometry and are currently beyond reasonably available computational capacity. On the other hand, the limit of parallel propagation $k_\perp \to 0$ needs only a 1D3V geometry and is thus more accessible. The modes occurring in this regime are responsible for the emission of electron whistler waves [83] and are destabilized by pressure anisotropy. In this way the emission of whistler waves by a loss cone plasma can be thought of as a magnetized analog of the Weibel instability discussed in Chapter 6. In particular, this section discusses the nature of the whistler mode's eigenfunction in phase space for consistent initialization of kinetic simulations. Note the following limits as $k_\perp \to 0$:

$$J_n^2(\beta) \to \delta_{0n}, \qquad nJ_n^2(\beta) \to 0, \qquad J_n(\beta)J_n'(\beta) \to 0, \tag{7.6}$$

$$\frac{n^2}{\beta^2}J_n^2(\beta) \to \frac{1}{4}(\delta_{1n} + \delta_{-1n}), \quad \frac{n}{\beta}J_n(\beta)J_n'(\beta) \to \frac{1}{4}(\delta_{1n} - \delta_{-1n}). \tag{7.7}$$

Thus parallel waves are influenced only by the first cyclotron harmonic. Further, the electrostatic mode decouples from the electromagnetic modes [83]. The dielectric tensor is

$$\varepsilon = \begin{bmatrix} \varepsilon_{11} & i\varepsilon_{12} & 0 \\ -i\varepsilon_{12} & \varepsilon_{11} & 0 \\ 0 & 0 & \varepsilon_3 \end{bmatrix} \tag{7.8}$$

having simplified the components of the general dielectric tensor as

$$\varepsilon_{11} = 1 - \frac{c^2k^2}{\omega^2} + \frac{\omega_p^2}{\omega^2}\int_{-\infty}^{\infty} dv_\parallel \int_0^\infty 2\pi v_\perp dv_\perp \Big\{\frac{v_\perp \zeta A}{4}\Big(\frac{1}{\omega - k_\parallel v_\parallel - \omega_c} + \frac{1}{\omega - k_\parallel v_\parallel + \omega_c}\Big)\Big\}, \tag{7.9}$$

$$\varepsilon_{12} = \frac{\omega_p^2}{\omega^2}\int_{-\infty}^{\infty} dv_\parallel \int_0^\infty 2\pi v_\perp dv_\perp \Big\{\frac{v_\perp \zeta A}{4}\Big(\frac{1}{\omega - k_\parallel v_\parallel - \omega_c} - \frac{1}{\omega - k_\parallel v_\parallel + \omega_c}\Big)\Big\}, \tag{7.10}$$

$$\varepsilon_{33} = 1 + \frac{\omega_p^2}{k_\parallel^2}\int_{-\infty}^{\infty} dv_\parallel \int_0^\infty 2\pi v_\perp dv_\perp \frac{1}{\zeta - v_\parallel}\frac{\partial f_0}{\partial v_\parallel} \tag{7.11}$$

with $\zeta = \omega/k_\parallel$. Equation 7.11 reproduces the electrostatic dielectric function. The self-consistent modes then follow from the vanishing determinant $|\varepsilon| = 0$ as $(\varepsilon_1^2 - \varepsilon_2^2)\varepsilon_3 = 0$. Then the electromagnetic term is factored and its roots represented by those of the functions

$$\mathcal{D}_\pm = 1 - \frac{c^2k^2}{\omega^2} + \frac{\omega_p^2}{\omega^2}\int_{\mathcal{C}} \frac{G_0(v_\parallel)}{\zeta - v_\parallel \mp \zeta_c} dv_\parallel \tag{7.12}$$

by $\mathcal{D}_\pm = 0$. Here $\mathcal{C}$ is the Landau contour, $\zeta_c \equiv \omega_c/k_\parallel$ is the cyclotron phase velocity, and

$$G_0(v_\parallel) = \int_0^\infty \Big[(\zeta - v_\parallel)\frac{\partial f_0}{\partial v_\perp} + v_\perp \frac{\partial f_0}{\partial v_\parallel}\Big]\pi v_\perp^2 dv_\perp \tag{7.13}$$

is a reduced distribution defined as in Ref. [83]. Further, the phase space structure of the linear response, obtained by considering Eq. 7.2 as $k_\perp \to 0$, is

$$f_1 = \frac{iq}{m}\Big\{\Big(\frac{\partial f_0}{\partial v_\perp} + \frac{k_\parallel}{\omega}(\boldsymbol{v} \times \nabla_v f_0)_\varphi\Big)\frac{E_\perp}{2}\Big[\frac{e^{i(\varphi+\theta)}}{\omega - k_\parallel v_\parallel - \omega_c} + \frac{e^{-i(\varphi+\theta)}}{\omega - k_\parallel v_\parallel + \omega_c}\Big] + \frac{E_z}{\omega - k_\parallel v_\parallel}\frac{\partial f_0}{\partial v_\parallel}\Big\} \tag{7.14}$$

with $E_x + iE_y = E_\perp e^{i\theta}$ and θ the phase angle of the wave in the perpendicular plane. Considering the electromagnetic mode sets $E_z = 0$. For the electromagnetic mode, the phase space response of Eq. 7.14 can be understood by its two phase factors, $\exp(i(kx - \omega t \pm \varphi))/(\omega - kv_\parallel \mp \omega_c)$. The presence of a phase component in the cylindrical velocity-space angle gives the eigenfunction a naturally helical nature in the parallel phase space.

7.2.1 Simplification for the typical case of separable distributions

If the distribution is separable, *i.e.* $f_0(v_\parallel, v_\perp) = f_\parallel(v_\parallel)f_\perp(v_\perp)$, then the reduced distribution $G_0(v_\parallel)$ can be simplified into easily interpretable terms. First, observe

$$G_0(v_\parallel) = (\zeta - v_\parallel)f_\parallel \int_0^\infty \pi v_\perp^2 \frac{\partial f_\perp}{\partial v_\perp} dv_\perp + \frac{\partial f_0}{\partial v_\parallel}\int_0^\infty \Big(\frac{1}{2}v_\perp^2 f_\perp\Big) 2\pi v_\perp dv_\perp. \tag{7.15}$$

Integrating by parts in the first term shows $\int_0^\infty \pi v_\perp^2 \frac{\partial f_\perp}{\partial v_\perp} dv_\perp = -1$ as $f_\perp$ is a normalized distribution. The second term is the perpendicular energy $\langle \frac{1}{2}v_\perp^2\rangle$. Thus for any $f_\perp$,

$$G_0(v_\parallel) = \Big\langle \frac{1}{2}v_\perp^2 \Big\rangle \frac{\partial f_\parallel}{\partial v_\parallel} - (\zeta - v_\parallel)f_\parallel. \tag{7.16}$$

Substitution of Eq. 7.16 into Eq. 7.12 results in the simplified dispersion function

$$\mathcal{D}_\pm = 1 - \Big(\frac{\zeta}{c}\Big)^2 + \frac{1}{(k\ell_s)^2}\Big(1 - \Big\langle \frac{1}{2}v_\perp^2 \Big\rangle \int_{-\infty}^\infty \frac{1}{\zeta - v_\parallel \mp \zeta_c}\frac{\partial f_\parallel}{\partial v_\parallel} dv_\parallel \pm \int_{-\infty}^\infty \frac{\zeta_c}{\zeta - v_\parallel \mp \zeta_c} f_\parallel dv_\parallel\Big) \tag{7.17}$$

with $\ell_s = \omega_p/c$ the skin depth. In the limit $\zeta_c \to 0$ Eq. 7.17 reduces to Eq. 6.23, the kinetic dispersion function for the electromagnetic mode responsible for Weibel instability, by noting that $\langle v_\perp^2\rangle = 2\langle v_y^2\rangle$ if $f_\perp(v_y, v_z) = g(v_y)g(v_z)$ is separable. If $f_\parallel(v_\parallel)$ is Maxwellian, then

$$\mathcal{D}_\pm = 1 - \Big(\frac{\zeta}{c}\Big)^2 + \frac{1}{(k\ell_s)^2}\Big(1 + \frac{1}{4}\frac{\langle v_\perp^2\rangle}{v_t^2} Z'(\widetilde{\zeta}_\pm) \mp \zeta_c Z(\widetilde{\zeta}_\pm)\Big) \tag{7.18}$$

where the normalized phase velocity is $\widetilde{\zeta}_\pm \equiv (\zeta \mp \zeta_c)/\sqrt{2}v_t$. Equation 7.18 can be easily specialized to any perpendicular distribution by calculation of its mean square energy $\langle v_\perp^2\rangle$.

Chapter 8

SUMMARY AND FUTURE DIRECTIONS

It is hoped that this work will be useful to researchers who wish increase their understanding of fundamental plasma processes. Towards that end the results and contributions presented in the preceding chapters fall into two main categories: numerical methods for finite element discretization of plasma kinetic equations, and a presentation of plasma kinetic theory with an emphasis on building intuition for basic processes. Results which should be of interest to researchers in both discontinuous Galerkin methods and kinetic plasma turbulence can be found in each of the chapters of this work, ranging from analytical results to highly resolved simulations and prescriptions for numerical implementation.

A tremendous amount of work remains to be done in this field. First, the spectral slope of the phase space cascade power law must be studied à la Kolmogorov. Next, most plasma kinetic problems are tackled using the particle-in-cell method which is known to have a variety of issues (see Chapter 4). At the time of writing only restricted geometries (*e.g.* 2D2V) were feasible for high-resolution finite element discretizations on the computational resources available to the author. Yet in the recent past even these geometries were inaccessible to researchers. Therefore, the material has been presented at a level of abstraction allowing future researchers to extend these studies to more complex problems and phase spaces of full dimensionality. Studies which would nicely build on this work include studies of ion-acoustic turbulence in an unmagnetized current-carrying plasma, three-dimensional simulations of Langmuir, ion-acoustic, and Weibel turbulence, and studies of the electromagnetic modes of Chapter 7. In addition, this work has exclusively studied phase space turbulence in homogeneous plasmas. Drift wave instability from inhomogeneity is of great interest to experiment and its influence on dissipative phase space cascades should be studied in detail.

BIBLIOGRAPHY

[1] J. P. Boyd. *Chebyshev and Fourier Spectral Methods.* Dover, Second edition, 2000.

[2] C. Lanczos and J.P. Boyd. *Discourse on Fourier series.* SIAM, 2016.

[3] S.A. Orszag. Numerical Methods for the Simulation of Turbulence. *The Physics of Fluids*, 12, 1969.

[4] W.L. Briggs. *The DFT: An Owner's Manual for the Discrete Fourier Transform.* SIAM, 1995.

[5] S.A. Orszag. Numerical Simulation of Incompressible Flows within Simple Boundaries. I. Galerkin (Spectral) Representations. *Studies in Applied Mathematics*, 50, 1971.

[6] S. Olver, R.M. Slevinsky, and A. Townsend. Fast algorithms using orthogonal polynomials. *Acta Numerica*, 29:573–699, 2020.

[7] A. Ho, I.A.M. Datta, and U. Shumlak. Physics-based-adaptive plasma model for high-fidelity numerical simulations. *Front. Phys.*, 2018.

[8] S.A. Teukolsky. Short note on the mass matrix for Gauss-Lobatto grid points. *J. Comp. Phys.*, 312(333), 2016.

[9] S.A. Teukolsky. Formulation of discontinuous Galerkin methods for relativistic astrophysics. *J. Comp. Phys.*, 312, 2016.

[10] S. Hassani. *Mathematical physics: a modern introduction to its foundations.* Springer Science & Business Media, 2013.

[11] R. Bulirsch and J. Stoer. *Introduction to numerical analysis.* Springer, New York, 1991.

[12] G. Kuperberg. Numerical Cubature from Archimedes' Hat-box Theorem. *SIAM J. Numer. Anal.*, 44, 2006.

[13] I. Stakgold. *Boundary Value Problems of Mathematical Physics*, volume I. The Macmillan Company, 1967.

[14] J.S. Hesthaven and T. Warburton. *Nodal discontinuous Galerkin methods.* Springer, 2008.

[15] C. Dunkl and Y. Xu. *Orthogonal polynomials of several variables.* Cambridge University Press, Second edition, 2014.

[16] G. Strang. On the construction and comparison of difference schemes. *SIAM Journal on Numerical Analysis*, 5(3):506–517, 1968.

[17] L. Einkemmer and A. Ostermann. Convergence analysis of Strang splitting for Vlasov-type equations. *SIAM Journal on Numerical Analysis*, 52(1):140–155, 2014.

[18] R. Okuta, Y. Unno, D. Nishino, S. Hido, and C. Loomis. CuPy: A NumPy-Compatible Library for NVIDIA GPU calculations. In *Proceedings of Workshop on Machine Learning Systems (LearningSys) in The Thirty-first Annual Conference on Neural Information Processing Systems (NIPS)*, 2017.

[19] Nodes and Weights of Gauss-Lobatto Calculator. https://kesian.casio.com/, May 2021.

[20] R.J. LeVeque. *Finite Volume Methods for Hyperbolic Problems*, volume 31 of *Cambridge Texts in Applied Mathematics.* Cambridge University Press, 2002.

[21] B. Cockburn and C.W. Shu. The local discontinuous Galerkin method for time-dependent convection-diffusion systems. *SIAM Journal on Numerical Analysis*, 35(6):2440–2463, 1998.

[22] D. Bohm and E.P. Gross. *Phys. Rev.*, 75, 1949.

[23] L.D. Landau. On the vibrations of the electronic plasma. *J. Phys. USSR*, 10(26), 1946.

[24] N.G. van Kampen. On the theory of stationary waves in plasmas. *Physica*, 21(6-10):949–963, 1955.

[25] K.M. Case. Plasma oscillations. *Annals of physics*, 7(3):349–364, 1959.

[26] A. Lenard and I.B. Bernstein. *Phys. Rev.*, 112, 1958.

[27] C.S. Ng, A. Bhattacharjee, and F. Skiff. *Phys. Rev. Lett.*, 83, 1999.

[28] R.W. Short and A. Simon. *Phys. Plasmas*, 9, 2002.

[29] V. Bratanov, F. Jenko, D. Hatch, and S. Brunner. *Phys. Plasms*, 20, 2013.

[30] R. Penrose. *The road to reality: A complete guide to the laws of the universe.* Random House, 2005.

[31] D.R. Nicholson. *Introduction to plasma theory*, volume 582. Wiley New York, 1983.

[32] V. Skoutnev, A. Hakim, J. Juno, and J.M. TenBarge. Temperature-dependent saturation of Weibel-type instabilities in counter-streaming plasmas. *The Astrophysical Journal Letters*, 872(2):L28, 2019.

[33] W.E. Drummond and D. Pines. Nonlinear stability of plasma oscillations. *Nuclear Fusion Supplement*, 3:1049–1058, 1962.

[34] V.V. Vedenov, E.P. Velikhov, and R.Z. Sagdeev. Quaslinear theory of plasma oscillations. *Nuclear Fusion Supplement*, 2:465–475, 1962.

[35] P. Diamond, S. Itoh, and K. Itoh. *Modern plasma physics*, volume 1. Cambridge University Press, 2010.

[36] R. J. Goldston and P. H. Rutherford. *Introduction to plasma physics.* Taylor and Francis, 1995.

[37] K.S. Thorne and R.D. Blandford. *Modern classical physics: optics, fluids, plasmas, elasticity, relativity, and statistical physics.* Princeton University Press, 2017.

[38] U. Frisch. *Turbulence: the legacy of A.N. Kolmogorov.* Cambridge university press, 1995.

[39] N.G. van Kampen. *Stochastic processes in physics and chemistry.* Elsevier, third edition, 2007.

[40] G.G. Howes, K.G. Klein, and T.C. Li. Diagnosing collisionless energy transfer using field–particle correlations: Vlasov–Poisson plasmas. *Journal of Plasma Physics*, 83(1), 2017.

[41] T.C. Li, G.G. Howes, K.G. Klein, Y.H. Liu, and J.M. TenBarge. Collisionless energy transfer in kinetic turbulence: field–particle correlations in Fourier space. *Journal of Plasma Physics*, 85(4), 2019.

[42] K.G. Klein, G.G. Howes, J.M. TenBarge, and F. Valentini. Diagnosing collisionless energy transfer using field–particle correlations: Alfvén-ion cyclotron turbulence. *Journal of Plasma Physics*, 86(4), 2020.

[43] J. Juno, G.G. Howes, J.M. TenBarge, L.B. Wilson, A. Spitkovsky, D. Caprioli, K.G. Klein, and A. Hakim. A field–particle correlation analysis of a perpendicular magnetized collisionless shock. *Journal of Plasma Physics*, 87(3), 2021.

[44] F.G. Schmitt. About Boussinesq's turbulent viscosity hypothesis: historical remarks and a direct evaluation of its validity. *Comptes Rendus Mécanique*, 335(9-10):617–627, 2007.

[45] B. B. Kadomtsev. *Plasma turbulence.* Academic Press, 1965.

[46] R.C. Davidson. *Methods in nonlinear plasma theory.* Academic Press, 1972.

[47] R.L. Dewar. Oscillation center quasilinear theory. *The Physics of Fluids*, 16(7):1102–1107, 1973.

[48] A.N. Kaufman. Reformulation of quasi-linear theory. *Journal of Plasma Physics*, 8(1):1–5, 1972.

[49] S.W. McDonald, C. Grebogi, and A.N. Kaufman. Locally coupled evolution of wave and particle distribution in general magnetoplasma geometry. *Physics Letters A*, 111(1-2):19–21, 1985.

[50] H. Ye and A.N. Kaufman. Self-consistent theory for ion gyroresonance. *Physics of Fluids B: Plasma Physics*, 4(7):1735–1753, 1992.

[51] E.R. Tracy, A.J. Brizard, A.S. Richardson, and A.N. Kaufman. *Ray tracing and beyond: phase space methods in plasma wave theory.* Cambridge University Press, 2014.

[52] A.J. Brizard. Variational principles for reduced plasma physics. In *Journal of Physics: Conference Series*, volume 169, page 012003. IOP Publishing, 2009.

[53] D.E. Ruiz, M.E. Glinsky, and I.Y. Dodin. Wave kinetic equation for inhomogeneous drift-wave turbulence beyond the quasilinear approximation. *Journal of Plasma Physics*, 85(1), 2019.

[54] M.H. Giga, Y. Giga, and R. Kobayashi. Very singular diffusion equations. *Hokkaido University Preprint Series in Mathematics*, 461:1–28, 1999.

[55] D.F. Escande and F. Sattin. When can the Fokker-Planck equation describe anomalous or chaotic transport? *Physical Review Letters*, 99(18), 2007.

[56] N. Besse, Y. Elskens, D.F. Escande, and P. Bertrand. Validity of quasilinear theory: refutations and new numerical confirmation. *Plasma Physics and Controlled Fusion*, 53(2), 2011.

[57] Y. Elskens and D. Escande. *Microscopic dynamics of plasmas and chaos.* CRC Press, 2019.

[58] P.H. Yoon and A.T.Y. Lui. Quasi-linear theory of anomalous resistivity. *Journal of Geophysical Research: Space Physics*, 111(A2), 2006.

[59] J.A. Krommes. A tutorial introduction to the statistical theory of turbulent plasmas, a half-century after Kadomtsev's Plasma Turbulence and the resonance-broadening theory of Dupree and Weinstock. *Journal of Plasma Physics*, 81(6), 2015.

[60] R. Balescu. *Aspects of anomalous transport in plasmas.* CRC Press, 2005.

[61] S.M. Tobias and J.B. Marston. Three-dimensional rotating Couette flow via the generalised quasilinear approximation. *Journal of Fluid Mechanics*, 810:412–428, 2017.

[62] R.C. Davidson. Quasi-linear stabilization of lower-hybrid-drift instability. *The Physics of Fluids*, 21(8):1375–1380, 1978.

[63] J. Seough, P.H. Yoon, and J. Hwang. Simulation and quasilinear theory of proton firehose instability. *Physics of Plasmas*, 22(1):012303, 2015.

[64] O. Allanson, C. E. J. Watt, H. J. Allison, and H. Ratcliffe. Electron Diffusion and Advection During Nonlinear Interactions With Whistler-Mode Waves. *Journal of Geophysical Research: Space Physics*, 126(5):e2020JA028793, 2021.

[65] J.M. Albert. Diffusion by one wave and by many waves. *Journal of Geophysical Research: Space Physics*, 115(A3), 2010.

[66] J. Cardy, G. Falkovich, and K. Gawedzki. *Non-equilibrium statistical mechanics and turbulence.* London Mathematical Society, 2008.

[67] P. Henri, F. Califano, C. Briand, and A. Mangeney. Low-energy Langmuir cavitons: Asymptotic limit of weak turbulence. *EPL (Europhysics Letters)*, 96(5):55004, nov 2011.

[68] M. Vlad, F. Spineanu, J.H. Misguich, J.D. Reuss, R. Balescu, K. Itoh, and S. Itoh. Lagrangian versus Eulerian correlations and transport scaling. *Plasma physics and controlled fusion*, 46(7):1051, 2004.

[69] J. Seough, P.H. Yoon, and J. Hwang. Quasilinear theory and particle-in-cell simulation of proton cyclotron instability. *Physics of Plasmas*, 21(6):062118, 2014.

[70] T. Lafleur, R. Martorelli, P. Chabert, and A. Bourdon. Anomalous electron transport in Hall-effect thrusters: Comparison between quasi-linear kinetic theory and particle-in-cell simulations. *Physics of Plasmas*, 25(6):061202, 2018.

[71] R.S. Rajawat and S. Sengupta. Particle-in-cell simulation of Buneman instability beyond quasilinear saturation. *Physics of Plasmas*, 24(12):122103, 2017.

[72] B.I. Cohen, A.B. Langdon, D.W. Hewett, and R.J. Procassini. Performance and optimization of direct implicit particle simulation. *Journal of Computational Physics*, 81(1):151–168, 1989.

[73] J.U. Brackbill. On energy and momentum conservation in particle-in-cell plasma simulation. *Journal of Computational Physics*, 317:405–427, 2016.

[74] M. Horkỳ, W.J. Miloch, and V.A. Delong. Numerical heating of electrons in particle-in-cell simulations of fully magnetized plasmas. *Physical Review E*, 95(4):043302, 2017.

[75] R.E. Heath, I.M. Gamba, P.J. Morrison, and C. Michler. A discontinuous Galerkin method for the Vlasov–Poisson system. *Journal of Computational Physics*, 231(4):1140–1174, 2012.

[76] Y. Cheng, I.M. Gamba, and P.J. Morrison. Study of conservation and recurrence of Runge–Kutta discontinuous Galerkin schemes for Vlasov–Poisson systems. *Journal of Scientific Computing*, 56(2):319–349, 2013.

[77] J. Juno, A. Hakim, J. TenBarge, E. Shi, and W. Dorland. Discontinuous Galerkin algorithms for fully kinetic plasmas. *Journal of Computational Physics*, 353:110–147, 2018.

[78] T.H. Dupree. Theory of resistivity in collisionless plasma. *Physical Review Letters*, 25(12):789, 1970.

[79] T.H. Dupree. Theory of phase space density granulation in plasma. *The Physics of Fluids*, 15(2):334–344, 1972.

[80] T. Boutros-Ghali and T.H. Dupree. Theory of two-point correlation function in a Vlasov plasma. *The Physics of Fluids*, 24(10):1839–1858, 1981.

[81] J.R. Cary and A.N. Kaufman. Ponderomotive effects in collisionless plasma: A Lie transform approach. *The Physics of Fluids*, 24(7):1238–1250, 1981.

[82] C. Mouhot and C. Villani. On Landau damping. *Acta Mathematica*, 207(1):29–201, 2011.

[83] D.A. Gurnett and A. Bhattacharjee. *Introduction to plasma physics.* Cambridge University Press, Second edition, 2017.

[84] R.L. Mace and M.A. Hellberg. A new formulation and simplified derivation of the dispersion function for a plasma with a kappa velocity distribution. *Physics of Plasmas*, 16(7):072113, 2009.

[85] I.S. Gradshteyn and I.M. Ryzhik. *Table of Integrals, Series, and Products.* Academic Press, Seventh edition, 2015.

[86] B.S. Newberger. New sum rule for products of Bessel functions with application to plasma physics. *Journal of Mathematical Physics*, 23(7):1278–1281, 1982.

[87] G.V. Vogman, P. Colella, and U Shumlak. Dory–Guest–Harris instability as a benchmark for continuum kinetic Vlasov–Poisson simulations of magnetized plasmas. *Journal of Computational Physics*, 277:101–120, 2014.

[88] I.A.M. Datta, D.W. Crews, and U. Shumlak. Electromagnetic extension of the Dory–Guest–Harris instability as a benchmark for Vlasov–Maxwell continuum kinetic simulations of magnetized plasmas. *Physics of Plasmas*, 28(7):072112, 2021.

[89] R.L. Mace. Generalized electron Bernstein modes in a plasma with a kappa velocity distribution. *Physics of Plasmas*, 11(2):507–522, 2004.

[90] E.S. Weibel. Spontaneously growing transverse waves in a plasma due to an anisotropic velocity distribution. *Physical Review Letters*, 2(3):83, 1959.

[91] S.R. Sharma and T.N. Bhatnagar. Wave propagation along an arbitrary direction in a bi-Maxwellian plasma. *Plasma Physics*, 18(2):95, 1976.

[92] P. Cagas, A. Hakim, W. Scales, and B. Srinivasan. Nonlinear saturation of the Weibel instability. *Physics of Plasmas*, 24(11):112116, 2017.

[93] J.M. Hill, M.H. Key, S.P. Hatchett, and R.R. Freeman. Beam-Weibel filamentation instability in near-term and fast-ignition experiments. *Physics of plasmas*, 12(8):082304, 2005.

[94] W. Fox, G. Fiksel, A. Bhattacharjee, P-Y. Chang, K. Germaschewski, S.X. Hu, and P.M. Nilson. Filamentation instability of counterstreaming laser-driven plasmas. *Physical review letters*, 111(22):225002, 2013.

[95] C.M. Huntington, F. Fiuza, J.S. Ross, A.B. Zylstra, R.P. Drake, D.H. Froula, G. Gregori, N.L. Kugland, C.C. Kuranz, M.C. Levy, et al. Observation of magnetic field generation via the Weibel instability in interpenetrating plasma flows. *Nature Physics*, 11(2):173–176, 2015.

[96] N. Shukla, J. Vieira, P. Muggli, G. Sarri, R. Fonseca, and L.O. Silva. Conditions for the onset of the current filamentation instability in the laboratory. *Journal of Plasma Physics*, 84(3), 2018.

[97] R.C. Davidson, D.A. Hammer, I. Haber, and C.E. Wagner. Nonlinear development of electromagnetic instabilities in anisotropic plasmas. *The Physics of Fluids*, 15(2):317–333, 1972.

[98] R.L. Morse and C.W. Nielson. Numerical simulation of the Weibel instability in one and two dimensions. *The Physics of Fluids*, 14(4):830–840, 1971.

[99] K.A. Taggart, B.B. Godrey, C.E. Rhoades Jr, and H.C. Ives. Second-Order Effects in the Weibel Instability. *Physical Review Letters*, 29(26):1729, 1972.

[100] M. Tzoufras, C. Ren, F.S. Tsung, J.W. Tonge, W.B. Mori, M. Fiore, R.A. Fonseca, and L.O. Silva. Space-charge effects in the current-filamentation or Weibel instability. *Physical review letters*, 96(10):105002, 2006.

Appendix A

CALCULATING THE PLASMA DISPERSION FUNCTION

The Cauchy integral of a Maxwellian distribution appears ubiquitously in the dispersion analysis of plasma waves in kinetic theory, when considering resonances at the Doppler-shifted cyclotron harmonics, and is defined as

$$Z(\zeta) \equiv \frac{1}{\sqrt{\pi}} \int_{-\infty}^{\infty} \frac{e^{-z^2}}{\zeta - z} dz, \quad \mathrm{Im}(\zeta) > 0. \tag{A.1}$$

As a Cauchy integral, the function $Z(\zeta)$ has a jump along the real axis equal to the residue of e^{-z^2} at $z = \zeta$. In the initial-value (Landau) analysis, the integral is analytically continued into the lower half plane by adding this residue back in.

The function $Z(\zeta)$ can be shown to satisfy the inhomogeneous differential equation

$$\frac{dZ}{d\zeta} = -2(1 + \zeta Z(\zeta)) \tag{A.2}$$

which can be used to compute any derivative of $Z(\zeta)$. Further, a uniformly-valid solution in the complex ζ-plane is given by the function

$$Z(\zeta) = i\sqrt{\pi} e^{-z^2}(1 + \mathrm{erf}(iz)) \tag{A.3}$$

so that $Z(\zeta)$ is essentially a scaled complex error function. However, application of Eq. A.3 in all parts of the complex ζ-plane will quickly encounter numerical overflow and underflow.

A.1 Asymptotic expansions

In the case of small argument, the plasma dispersion function has power series

$$Z(\zeta) = i\sqrt{\pi} e^{-\zeta^2} - 2\zeta\Big(1 - \frac{2}{3}\zeta^2 + \frac{4}{15}\zeta^4 + \cdots\Big). \tag{A.4}$$

More likely, numerical overflow is encountered for $|\zeta| \gg 1$. This case occurs frequently in the analysis of magnetized plasma waves for $k_\parallel \to 0$, as the argument of $Z(\zeta)$ is $(\omega - n)/k_\parallel$ for each cyclotron harmonic. The asymptotic expansion for $|\zeta| \gg 1$ is

$$Z(\zeta) = i\sqrt{\pi}\sigma e^{-\zeta^2} - \zeta^{-1}\Big(1 + \frac{1}{2}\zeta^{-2} + \frac{3}{4}\zeta^{-4} + \frac{15}{8}\zeta^{-6} + \cdots\Big) \tag{A.5}$$

$$\sigma = \begin{cases} 0, & y > 0 \\ 1, & y = 0 \cdot \\ 2, & y < 0 \end{cases} \tag{A.6}$$

The Gaussian is added in only for the lower half-plane as it comes from the residue.

A.2 Continued fraction expansion

In the upper half-plane, numerical overflow occurs in Eq. A.3 even for an imaginary part $y \approx 3$, as the error function of complex argument takes on enormous values. However, the behavior of the error function is canceled out somewhat by the Gaussian function in the numerical value of $Z(\zeta)$. Fried and Conte found that an appropriate and rapidly convergent representation in the upper half-plane was given by a continued fraction,

$$Z(\zeta) = \frac{\zeta}{-\zeta^2 + \frac{1}{2} + \frac{(-1/2)}{-\zeta^2 + \frac{5}{2} + \frac{-3}{\cdots}}}. \tag{A.7}$$

The continued fraction converges in the entire complex plane besides the real axis, but convergence is very slow near the real axis. Fried and Conte discovered that the fraction converges quickly for $y > 1$. The fraction is best computed by the recursion relation

$$A_{n+1} = -a_{n+1}A_{n-1} + b_{n+1}A_n \tag{A.8}$$

$$B_{n+1} = -a_{n+1}B_{n-1} + b_{n+1}B_n \tag{A.9}$$

$$Z(\zeta) = \lim_{n\to\infty} \frac{A_n}{B_n} \tag{A.10}$$

with initial conditions $A_{-1} = 1, A_0 = 0$ and $B_{-1} = 0, B_0 = 1$, and the coefficients by

$$a_{n+1} = \frac{n(2n-1)}{2}, \quad n = 1, 2, \cdots \tag{A.11}$$

$$b_{n+1} = -\zeta^2 + 2n + \frac{1}{2}, \quad n = 0, 1, \cdots \tag{A.12}$$

$$a_1 = -\zeta. \tag{A.13}$$

A.3 Patched asymptotic representations

A numerical implementation of the plasma dispersion function avoiding overflow and underflow and convergent throughout the ζ-plane is given by the following representation:

$$Z(\zeta) = \begin{cases} \text{Continued fraction,} & \mathrm{Im}(\zeta) \geq 4 \\ i\sqrt{\pi}e^{-\zeta^2}(1 + \mathrm{erf}(i\zeta)), & |\zeta| < 15 \\ \text{Asymptotic } |\zeta| \gg 1, & |\zeta| \geq 15 \text{ and } \mathrm{Im}(\zeta) < 4 \end{cases} \tag{A.14}$$

The cutoff values $|\zeta| = 15$ and $y = 4$ are arbitrary but have been found empirically to work well. Ten terms are used in the continued fraction and four terms in the asymptotic relation.

Appendix B

POLAR FOURIER INTEGRALS OF LOSS-CONE DISTRIBUTIONS

This appendix integrates the ring distribution Eq. 5.16 over perpendicular velocities,

$$\mathbb{F}_{n,m,\gamma}(k) \equiv \int_0^\infty f_\gamma(v) J_n(kv) J_m(kv) 2\pi v dv \tag{B.1}$$

for integer n, m. By this theory one can also determine the integral of products, $J_n(v)J_n'(v)$ etc., by recursion of the derivatives $J_n'(z)$. The result is that Eq. B.1 is a type ${}_3F_3$ hypergeometric function,

$$\begin{aligned}\mathbb{F}_{n,m,\gamma}(k) = &\frac{\Gamma(\gamma + \frac{n+m}{2} + 1)(k\alpha)^{n+m}}{\Gamma(n+1)\Gamma(m+1)\Gamma(\gamma+1)} \times \\ &{}_3F_3\left[\begin{matrix}\frac{n+m}{2} + \frac{1}{2}, \frac{n+m}{2} + 1, \gamma + \frac{n+m}{2} + 1 \\ n+1, \quad m+1, \quad n+m+1\end{matrix}\right](-(2k\alpha)^2)\end{aligned} \tag{B.2}$$

which can be equivalently written as a power series with Gamma function coefficients,

$$\mathbb{F}_{n,m,\gamma}(k) = \frac{1}{\Gamma(\gamma+1)} \sum_{\ell=0}^\infty \frac{\Gamma(n+m+2\gamma+2\ell+1)}{\Gamma(n+\ell+1)\Gamma(m+\ell+1)\Gamma(n+m+\ell+1)} \frac{(-1)^\ell}{\ell!}(k\alpha)^{2\ell+n+m}. \tag{B.3}$$

Setting $n = m$ as required for electrostatic theory reduces to a more manageable ${}_2F_2$ function,

$$\mathbb{F}_{n,\gamma}(k) = \frac{\Gamma(\gamma+n+1)(k\alpha)^{2n}}{\Gamma^2(n+1)\Gamma(\gamma+1)} {}_2F_2\left[\begin{matrix}n+\frac{1}{2}, \gamma+n+1 \\ n+1, 2n+1\end{matrix}\right](-(2k\alpha)^2) \tag{B.4}$$

with the power series for practical computation given in Eq. 5.20.

B.1 Theorem for the product of integer-order Bessel functions

The product of integer-order Bessel functions is a generalized hypergeometric of type ${}_2F_3$,

$$J_n(z)J_m(z) = \frac{1}{n!m!}\left(\frac{z}{2}\right)^{n+m} {}_2F_3\left[\begin{matrix}\frac{n+m}{2} + \frac{1}{2}, \frac{n+m}{2} + 1 \\ n+1, m+1, n+m+1\end{matrix}\right](-z^2) \tag{B.5}$$

which for $n = m$ reduces to a type ${}_1F_2$ function,

$$J_n^2(z) = \frac{1}{(n!)^2}\Big(\frac{z}{2}\Big)^{2n} {}_1F_2\left[\begin{matrix} n+\frac{1}{2} \\ n+1, 2n+1 \end{matrix}\right](-z^2). \tag{B.6}$$

B.1.1 Proof of Equation B.5

Begin by multiplying term-by-term the power series of J_n, J_m and diagonalizing by $\ell = j+k$,

$$\begin{aligned} J_n(z)J_m(z) &= \Big(\frac{z}{2}\Big)^{n+m} \sum_{j,k=0}^{\infty} \frac{1}{\Gamma(n+k+1)\Gamma(m+j+1)} \frac{(-z^2/4)^{j+k}}{j!k!} \\ &= \Big(\frac{z}{2}\Big)^{n+m} \sum_{\ell=0}^{\infty} \Big[\sum_{k=0}^{\infty} \frac{1}{\Gamma(k+n+1)\Gamma(\ell-k+m+1)\Gamma(\ell-k+1)\Gamma(k+1)}\Big]\Big(\frac{-z^2}{4}\Big)^{\ell}. \end{aligned} \tag{B.7}$$

Using properties of Pochhammer symbols and Gauss's hypergeometric summation theorem,

$$\begin{aligned} &\sum_{k=0}^{\infty} \frac{1}{\Gamma(k+n+1)\Gamma(\ell-k+m+1)\Gamma(\ell-k+1)\Gamma(k+1)} \\ &= \frac{1}{\Gamma(n+1)\Gamma(\ell+1)\Gamma(\ell+m+1)} {}_2F_1\left[\begin{matrix} -\ell, -\ell-m \\ n+1 \end{matrix}\right](1) \\ &= \frac{\Gamma(n+m+2\ell+1)}{\Gamma(\ell+1)\Gamma(m+\ell+1)\Gamma(n+\ell+1)\Gamma(n+m+\ell+1)} \end{aligned} \tag{B.8}$$

one obtains a single summation for $J_n(z)J_m(z)$,

$$J_n(z)J_m(z) = \Big(\frac{z}{2}\Big)^{n+m} \sum_{\ell=0}^{\infty} \frac{\Gamma(n+m+2\ell+1)}{\Gamma(m+\ell+1)\Gamma(n+\ell+1)\Gamma(n+m+\ell+1)} \frac{(-z^2/4)^{\ell}}{\ell!}. \tag{B.9}$$

The numerator factorial is then written in Pochhammer symbols of order ℓ by the formulas

$$(x+\ell)_\ell = \frac{(x)_{2\ell}}{(x)_\ell}, \tag{B.10}$$

$$(x)_{2\ell} = 2^{2\ell}\Big(\frac{x}{2}\Big)_\ell\Big(\frac{1+x}{2}\Big)_\ell, \tag{B.11}$$

yielding a series identical to Eq. B.5 and proving the identity,

$$J_n(z)J_m(z) = \frac{1}{n!m!}\Big(\frac{z}{2}\Big)^{n+m} \sum_{\ell=0}^{\infty} \frac{\big(\frac{n+m}{2}+\frac{1}{2}\big)_\ell\big(\frac{n+m}{2}+1\big)_\ell}{(m+1)_\ell(n+1)_\ell(n+m+1)_\ell} \frac{(-z^2)^{\ell}}{\ell!}. \tag{B.12}$$

B.1.2 Integration of Eq. B.5 with a loss-cone distribution

Having developed the product of two Bessel functions in terms of a single entire function the integration over perpendicular velocities is now shown in this section to be Eq. B.2.

Proof of Eq. B.2

The distribution $f_\gamma(v)$ of Eq. 5.16 is combined with Eq. B.12 and integrated term-by-term,

$$\begin{aligned}\mathbb{F}_{n,m,\gamma}(k) = \frac{k^{n+m}}{n!m!\gamma!(\alpha^2)^{\gamma+1}}\left(\frac{k}{2}\right)^{n+m}\sum_{\ell=0}^{\infty}\frac{\left(\frac{n+m}{2}+\frac{1}{2}\right)_\ell\left(\frac{n+m}{2}+1\right)_\ell}{(m+1)_\ell(n+1)_\ell(n+m+1)_\ell}\frac{(-k^2)^\ell}{\ell!}\times \\ \int_0^\infty v^{2(\ell+\gamma+\frac{n+m}{2})}e^{-v^2/\alpha^2}2vdv.\end{aligned} \tag{B.13}$$

The interior integral is Euler's form of the Gamma function upon substitution $u = \frac{v^2}{\alpha^2}$; thus

$$\begin{aligned}\mathbb{F}_{n,m,\gamma} =& \frac{\Gamma(\gamma+\frac{n+m}{2}+1)}{\Gamma(n+1)\Gamma(m+1)\Gamma(\gamma+1)}(k\alpha)^{n+m}\times \\ &\sum_{\ell=0}^{\infty}\frac{\left(\frac{n+m}{2}+\frac{1}{2}\right)_\ell\left(\frac{n+m}{2}+1\right)_\ell(\gamma+\frac{n+m}{2}+1)_\ell}{(m+1)_\ell(n+1)_\ell(n+m+1)_\ell}\frac{(-4\alpha^2k^2)^\ell}{\ell!}.\end{aligned} \tag{B.14}$$

The series is a hypergeometric function of type ${}_3F_3$, demonstrating Eq. B.2. While the form of the integral as a type ${}_3F_3$ function reveals connections to the theory of special functions, in a practical power series computation the extra Pochhammer symbols are wasteful. By exchanging the Pochhammer symbols for Gamma functions the series is given by Eq. B.3. Finally by setting $n = m$ and simplifying the desired integral is determined.

Appendix C

THE DIELECTRIC FOR PERPENDICULAR WAVES IN LOSS-CONE PLASMAS

This appendix proves the results given in Eq. 5.24 and Eq. 5.25 for electrostatic modes in a magnetized plasma with loss-cone distributions, beginning from the Harris dispersion relation given in Eq. 5.9. The appendix begins by constructing the function in closed form as a hypergeometric function, and then considers a convenient trigonometric integral form by calculation of the loss cone's Hankel transform. These forms of the dielectric function $\varepsilon(\omega, k_\perp)$, which sum the contribution of the cyclotron resonances to all orders, enable precise numerics for use in continuum kinetic simulations.

C.1 The perpendicular wave dielectric function in closed form

This section proves Eq. 5.24 for the closed form of the dielectric function for perpendicular cyclotron waves in a loss-cone distributed plasma using the Lerche-Newberger summation theorem. This theorem sums the Bessel series in Eqs. 5.7 and 5.8 to all orders in the cyclotron harmonics, [86]

$$\Upsilon_2 = \sum_{n=-\infty}^{\infty} \frac{n}{\omega' - n} J_n^2(\beta) = \frac{\pi\omega'}{\sin(\pi\omega')} J_{\omega'}(\beta) J_{-\omega'}(\beta) - 1 \tag{C.1}$$

$$\Lambda_2 = \sum_{n=-\infty}^{\infty} \frac{1}{\omega' - n} J_n^2(\beta) = \frac{\pi}{\sin(\pi\omega')} J_{\omega'}(\beta) J_{-\omega'}(\beta) \tag{C.2}$$

with each sum limiting to a product of Bessel functions $J_z(\beta)J_{-z}(\beta)$ of complex order. Here the auxiliary quantities are $\omega' = (\omega - k_\parallel v_\parallel)/\omega_c$ and $\beta = k_\perp v_\perp/\omega_c$. The polar velocity-space integrals over the perpendicular direction $v_\perp$, when considering the closed forms expressed above in Eqs. C.1 and C.2, result in a generalized hypergeometric function,

$$\frac{1}{2^\gamma \alpha^{2\gamma+2}\Gamma(\gamma+1)}\int_0^\infty v^{2j+1}e^{-v^2/2\alpha^2}\frac{\pi\omega}{\sin(\pi\omega)}J_\omega(qv)J_{-\omega}(qv)dv = {}_2F_2\left[\begin{matrix}\frac{1}{2}, & \gamma+1\\ 1+\omega, 1-\omega\end{matrix}\right](-2(\alpha q)^2). \tag{C.3}$$

First note that with $k_\parallel = 0$ the Harris dispersion function is

$$\varepsilon(\omega, k_\perp) = 1 + \left(\frac{\omega_p}{\omega_c}\right)^2 \frac{1}{(k\lambda_D)^2}\int_0^\infty \frac{\Upsilon_2}{v_\perp}\frac{\partial f_0}{\partial v_\perp}2\pi v_\perp dv_\perp. \tag{C.4}$$

Using the integral identity in Eq. C.3, and the recurrence relation for $f_\gamma(v_\perp)$ Eq. 5.18, one obtains

$$\int_0^\infty \frac{\Upsilon_2}{v_\perp}\frac{\partial f_0}{\partial v_\perp}2\pi v_\perp dv_\perp = {}_2F_2\left[\begin{matrix}\frac{1}{2}, & \gamma+1\\ 1+\omega', 1-\omega'\end{matrix}\right](-2(k_\perp r_L)^2) - {}_2F_2\left[\begin{matrix}\frac{1}{2}, & \gamma\\ 1+\omega', 1-\omega'\end{matrix}\right](-2(k_\perp r_L)^2) \tag{C.5}$$

which was to be shown.

C.1.1 Proof of Eq. C.3

This section proves Eq. C.3. First, observe that multiplication of the power series for both J_ω and $J_{-\omega}$, and diagonalization of the double sum with $\ell = m + k$, leads to the expression

$$\frac{\pi\omega}{\sin(\pi\omega)}J_\omega(z)J_{-\omega}(z) = \sum_{m=0}^\infty\sum_{k=0}^\infty \frac{\Gamma(1+\omega)\Gamma(1-\omega)}{\Gamma(m+\omega+1)\Gamma(k-\omega+1)}\frac{(-1)^{m+k}}{m!k!}\left(\frac{z}{2}\right)^{2(m+k)} \tag{C.6}$$

$$= \sum_{\ell=0}^\infty \Big[\sum_{m=0}^\infty \frac{\Gamma(1+\omega)\Gamma(1-\omega)}{\Gamma(m+\omega+1)\Gamma(\ell-m-\omega+1)}\frac{1}{m!(\ell-m)!}\Big](-1)^\ell\left(\frac{z}{2}\right)^{2\ell} \tag{C.7}$$

having used Euler's reflection formula $\pi z\csc(\pi z) = \Gamma(1+z)\Gamma(1-z)$ with $\Gamma(z)$ the Gamma function. Recall the following identity for the rising factorial $(z)_n$ (or Pochhammer symbol),

$$(z)_n = \frac{\Gamma(z+n)}{\Gamma(z)} = (-1)^n\frac{\Gamma(z+1)}{\Gamma(z-n+1)} \tag{C.8}$$

as well as Gauss's hypergeometric summation theorem,

$${}_2F_1\left[\begin{matrix}a, b\\ c\end{matrix}\right](1) = \frac{\Gamma(c)\Gamma(c-a-b)}{\Gamma(c-a)\Gamma(c-b)}, \quad \mathrm{Re}(c) > \mathrm{Re}(a+b). \tag{C.9}$$

Application of Eqs. C.8 and C.9 shows that the inner summation becomes

$$\sum_{m=0}^{\infty} \frac{\Gamma(1+\omega)\Gamma(1-\omega)}{\Gamma(m+\omega+1)\Gamma(\ell-m-\omega+1)} \frac{1}{m!(\ell-m)!} = 2^{2\ell} \frac{(\frac{1}{2})_\ell}{(1+\omega)_\ell(1-\omega)_\ell} \frac{1}{\ell!}. \tag{C.10}$$

Therefore the function expressed by the Lerche-Newberger theorem is a hypergeometric,

$$\frac{\pi\omega}{\sin(\pi\omega)} J_\omega(z)J_{-\omega}(z) = \sum_{\ell=0}^{\infty} \frac{(\frac{1}{2})_\ell}{(1+\omega)_\ell(1-\omega)_\ell}(-1)^\ell \frac{z^{2\ell}}{\ell!} = {}_1F_2\left[\begin{matrix} \frac{1}{2} \\ 1+\omega, 1-\omega \end{matrix}\right](-z^2). \tag{C.11}$$

To compute the integral considered, the power series in Eq. C.11 is integrated term-by-term

$$\frac{1}{2^\gamma \alpha^{2\gamma+2}\Gamma(\gamma+1)} \int_0^\infty v^{2j+1} e^{-v^2/2\alpha^2} \frac{\pi\omega}{\sin(\pi\omega)} J_\omega(qv)J_{-\omega}(qv)dv = \tag{C.12}$$

$$= \frac{1}{2^\gamma \alpha^{2\gamma+2}\Gamma(\gamma+1)} \int_0^\infty v^{2\gamma+1} e^{-v^2/2\alpha^2} {}_1F_2\left[\begin{matrix} \frac{1}{2} \\ 1+\omega, 1-\omega \end{matrix}\right](-(qv)^2)dv \tag{C.13}$$

$$= \sum_{\ell=0}^{\infty} \frac{(\frac{1}{2})_\ell(\gamma+1)_\ell}{(1+\omega)_\ell(1-\omega)_\ell} \frac{(-2(\alpha q)^2)^\ell}{\ell!} \tag{C.14}$$

as the coefficients reduce to Euler's integral for the Gamma function, $\Gamma(1+z) = \int_0^\infty x^z e^{-x} dx$. This establishes Eq. C.3.

C.2 The trigonometric form of the dielectric function

The closed form representation as a hypergeometric function of complex order is of theoretical interest by connecting the calculation of characteristic frequencies to the theory of advanced special functions. However, at the present stage of development of scientific computing libraries there are limited options available for hypergeometric functions with complex series coefficients. For this reason the dielectric function is alternatively represented as a trigonometric integral [87]

$$\varepsilon(\omega, k) = 1 + \frac{\omega_p^2}{\omega_c^2} \int_0^\pi \frac{\sin(\theta)\sin(\theta\omega)}{\sin(\pi\omega)} \Big[\int_0^\infty f_\perp(v) J_0(\lambda(\theta)v) 2\pi v dv \Big] d\theta \tag{C.15}$$

with $\lambda = 2k\cos(\theta/2)/\omega_c$. The interior integration is an azimuthally-symmetric polar Fourier transform, also known as the zero-order Hankel transform $\mathcal{H}_0[f(r); k] = \int_0^\infty f(r)J_0(kr)dr$.

The Hankel transform has a Fourier-multiplier property with the radial Laplacian,

$$\mathcal{H}_0[r^{2n}f(r);k] = (-\nabla_k^2)^n \mathcal{H}_0[f(r);k]. \tag{C.16}$$

Further, radial Laplacians of the Gaussian are precisely the Laguerre functions,

$$(\nabla_k^2)^n[\exp(-\alpha^2k^2/2)] = (-2\alpha^2)^n L_n(\alpha^2k^2/2)\exp(-\alpha^2k^2/2). \tag{C.17}$$

Therefore the Hankel transform of the loss cone $f_\gamma(v)$ is the family of polar Hermite functions

$$\mathcal{H}_0[f_\gamma(v);q] = L_\gamma\Big(\frac{\alpha^2q^2}{2}\Big)\exp\Big(-\frac{\alpha^2q^2}{2}\Big). \tag{C.18}$$

Substitution of Eq. C.18 into Eq. C.15 gives Eq. 5.25, as was to be shown.

Appendix D

RING DISTRIBUTIONS AND THE DIELECTRIC TENSOR

Here the theorem demonstrated in Appendix B is used to compute the integrals over perpendicular velocity which appear in the electromagnetic theory in the case of zero-order cyclotron orbits. In electromagnetic theory the field sources are plasma currents so first moments of the distribution are needed. Thus, it's necessary to compute a more general integral with an index j corresponding to the desired moment,

$$\mathbb{F}_{n,m,\gamma,j}(k) \equiv 2\pi \int_0^\infty v^j f_\gamma(v) J_n(kv) J_m(kv) v dv. \tag{D.1}$$

with $j = 1, 2$ as the terms which appear in the susceptibility tensor from the linear response reacting with the background distribution.

D.1 Higher moment integrals over perpendicular velocities

The calculation is identical to Appendix B except that the term-by-term integration is

$$\frac{1}{\alpha^{2\gamma}} \int_0^\infty v^{2\gamma+2\ell+n+m+j} e^{-v^2/\alpha^2} \frac{2vdv}{\alpha^2} = \alpha^{2\ell+n+m+j} \Gamma(\gamma + \frac{j}{2} + \ell + \frac{n+m}{2} + 1). \tag{D.2}$$

Therefore, the function in Eq. D.1 can be written in either hypergeometric form

$$\begin{aligned} \mathbb{F}_{n,m,\gamma,j}(k) = \alpha^j &\frac{\Gamma(\gamma + \frac{j}{2} + \frac{n+m}{2} + 1)}{\Gamma(n+1)\Gamma(m+1)\Gamma(\gamma+1)} (k\alpha)^{n+m} \times \\ &{}_3F_3 \left[\begin{matrix} \frac{n+m}{2} + \frac{1}{2}, \frac{n+m}{2} + 1, \gamma + \frac{j}{2} + \frac{n+m}{2} + 1 \\ n+1, \quad m+1, \quad n+m+1 \end{matrix} \right] (-(2k\alpha)^2) \end{aligned} \tag{D.3}$$

or in the alternative power series form

$$\mathbb{F}_{n,m,\gamma,j}(k) = \frac{\alpha^j}{\Gamma(\gamma+1)} \sum_{\ell=0}^\infty \frac{\Gamma(n+m+j+2\gamma+2\ell+1)}{\Gamma(n+\ell+1)\Gamma(m+\ell+1)\Gamma(n+m+\ell+1)} \frac{(-1)^\ell}{\ell!} (k\alpha)^{2\ell+n+m}. \tag{D.4}$$

D.1.1 Each moment increases the effective ring index by one-half

An important conclusion is that each higher moment is a rescaling of the zeroth moment for a distribution with a ring index increased by one-half,

$$\mathbb{F}_{n,m,\gamma,j}(k) = \alpha^j \frac{\Gamma(\gamma + \frac{j}{2} + 1)}{\Gamma(\gamma + 1)} \mathbb{F}_{n,m,\gamma+\frac{j}{2},0}(k). \tag{D.5}$$

Note that higher ring parameters are typically destabilizing.

D.1.2 Integrals occurring in the uniform plasma susceptibility tensor

Following Stix, the necessary perpendicular velocity space integrals are

$$\mathcal{I}_1(k) = 2\pi \int_0^\infty J_n^2(kv) f_\gamma(v) v dv, \tag{D.6}$$

$$\mathcal{I}_2(k) = 2\pi \int_0^\infty v J_n(kv) J_n'(kv) f_\gamma(v) v dv, \tag{D.7}$$

$$\mathcal{I}_3(k) = 2\pi \int_0^\infty v^2 (J_n'(kv))^2 f_\gamma(v) v dv. \tag{D.8}$$

Each is evaluated using the derivative recursion relation for Bessel functions,

$$\frac{dJ_n(z)}{dz} = \frac{J_{n-1}(z) - J_{n+1}(z)}{2} \tag{D.9}$$

and the function $\mathbb{F}_{n,m,\gamma,j}$ as defined. The resulting functions are thus

$$\mathcal{I}_1(k_\perp) = \mathbb{F}_{n,n,\gamma,0}(k_\perp), \tag{D.10}$$

$$\mathcal{I}_2(k_\perp) = \frac{1}{2}\Big(\mathbb{F}_{n,n-1,\gamma,1}(k_\perp) - \mathbb{F}_{n,n+1,\gamma,1}(k_\perp)\Big), \tag{D.11}$$

$$\mathcal{I}_3(k_\perp) = \frac{1}{4}\Big(\mathbb{F}_{n-1,n-1,\gamma,2}(k_\perp) - 2\mathbb{F}_{n-1,n+1,\gamma,2}(k_\perp) + \mathbb{F}_{n+1,n+1,\gamma,2}(k_\perp)\Big). \tag{D.12}$$

Alternative representations are possible using derivative identities involving the $\mathbb{F}$ functions. However the above are sufficient to compute the elements of the susceptibility tensor for general ring parameters by use of the general power series of Eq. D.4. Note that these results reduce to the standard results for a Maxwellian plasma in the case $\gamma = 0$ by the identity

$$\mathbb{F}_{n,n,0,0}(\lambda) = e^{-\lambda} I_n(\lambda) \tag{D.13}$$

where $I_n(\lambda)$ is a modified Bessel function of the first kind.